ISBN 978-82-326-4810-8 (printed version)
ISBN 978-82-326-4811-5 (electronic version)
ISSN 1503-8181

Doctoral theses at NTNU, 2020:231

Ine L. Jernelv

Mid-Infrared Tuneable Laser Spectroscopy for Glucose Sensing

NTNU
Norwegian University of
Science and Technology
Faculty of Information Technology
and Electrical Engineering
Department of Electronic Systems

NTNU
Norwegian University of
Science and Technology

Doctoral theses at NTNU, 2020:231

NTNU

NTNU
Norwegian University of
Science and Technology

Ine L. Jernelv

Mid-Infrared Tuneable Laser Spectroscopy for Glucose Sensing

Thesis for the degree of Philosophiae Doctor

Trondheim, August 2020

Norwegian University of Science and Technology
Faculty of Information Technology
and Electrical Engineering
Department of Electronic Systems

NTNU
Norwegian University of
Science and Technology

NTNU
Norwegian University of Science and Technology

Thesis for the degree of Philosophiae Doctor

Faculty of Information Technology
and Electrical Engineering
Department of Electronic Systems

ISBN 978-82-326-4810-8 (printed version)
ISBN 978-82-326-4811-5 (electronic version)
ISSN 1503-8181

Doctoral theses at NTNU, 2020:231

Printed by Skipnes Kommunikasjon as

Abstract

Mid-infrared spectroscopy is a versatile analytical technique, with recent technological developments that enable further advancements towards miniaturised and portable sensor applications. Quantum cascade lasers (QCLs) are infrared lasers that are small, can be made tuneable, and can be engineered to cover a specific wavelength range. They therefore have high potential in a wavelength region where traditionally mainly spectrometers have been available. Mid-infrared spectroscopy targets the fundamental molecular vibrational levels, and measurements in this wavelength range can provide unique features useful for classification, identification, and quantification of many materials. This technique is therefore highly suitable for label-free and accurate measurements of an investigated sample.

The focus of this thesis is on biomedical applications of mid-infrared spectroscopy, specifically for glucose sensing. The aim is to develop an experimental setup and analytical methods for fast and accurate measurements of glucose in biological fluids. Glucose sensing is a critical tool for management of diabetes, and current commercially available devices that measure subcutaneously have shortcomings such as a lag time compared to the actual blood glucose level. Fluid measurements in the peritoneal cavity have been suggested as a possible replacement for subcutaneous monitoring. While previous research has investigated mid-infrared spectroscopy measurements for hospital settings or non-invasive monitoring, there has been less interest in solutions targeted towards portable sensing. This work has therefore concentrated on a fibre-coupled sensor system with a QCL source, with development towards a continuous glucose monitoring (CGM) device.

This thesis presents contributions on QCL-based spectroscopy and chemometric methods. The included papers document the development and characterisation of a fibre-coupled QCL setup. Additional investigation is done into signal-enhanced attenuated total reflection (ATR) spectroscopy, and a comprehensive study of multivariate analysis with convolutional neural networks and other chemometric methods is also included. Finally, the system is employed for measurements of physiological glucose levels in peritoneal fluid samples from animal trials. The presented results show that fibre-coupled setups in transmission and ATR configurations are both suitable for measurements of glucose in peritoneal fluid. This system has a high potential for further testing in animal trials, and may be realised as a CGM device for humans.

Acknowledgements

This thesis is a product of four years of hard work, and many people deserve mention because of their involvement. Firstly, I want to thank my supervisor, Astrid Aksnes, for giving me the chance to start a PhD in a field that was almost completely new to me. Astrid has always provided a realistic perspective and sound advice, and at the same time let me follow my own research ideas. I would also like to thank my co-supervisor, Dag Roar Hjelme, who has provided invaluable technical discussions throughout my studies, and has always taken a part in my project. My project has been a part of the APT group at NTNU, and through this group I have met many wonderful colleagues (ingen nevnt, ingen glemt), and the interdisciplinary discussions have given very helpful insights.

I am grateful for my research stay at Tohoku University in Sendai, where Professor Yuji Matsuura kindly opened his lab for me. Especially thanks to Dr. Saiko Kino, who instructed me on many instruments and taught me how to make optical fibres. The other students were also exceedingly welcoming, and the many lunchtime conversations ensured that my Japanese improved dramatically.

I would like to acknowledge the work by the master students that I co-supervised, who have devoted many hours on this project and made several valuable contributions. I want to thank Karina Strøm in particular, who made several forays into both software development and experimental work, and who kept working just as hard even when I went off to Japan.

I am appreciative of my many colleagues at Gløs, in particular Karolina Milenko whom I had the pleasure of sharing an office with for 3.5 years. She introduced me to the finer aspects of optical alignment, and gave helpful advice whenever I had issues with my experimental setup. I am also grateful for the company from the cybernetics lunch gang during our long treks in search of edible food on campus.

I want to thank my family for having me grow up in the best environment possible, and for having a place I could always come back to. Mum, thank you for always asking about my work. Dad, I wish you could have seen this. Lastly, thanks to my partner and best friend, Trygve Ræder, whose impact on my life is too big to put into words. *Giitu!*

Contributions

The work that constitutes this thesis was carried out at the Department of Electronic Systems, Norwegian University of Science and Technology (NTNU) in Trondheim, Norway, from May 2016 to May 2020. These studies have been performed under the supervision of Professor Astrid Aksnes (NTNU), and co-supervisor Professor Dag Roar Hjelme (NTNU). The work has been a part of the Artificial Pancreas Trondheim (APT) group at NTNU, with funding from the Research Council of Norway through grant numbers 248872 and 248810.

During the doctoral study I have been co-supervisor for three master students: Karina Strøm, Christian Furuseth, and Håvard Bakke Skjellerud. I have also had a three month research stay at the Matsuura Laboratory of the Graduate School of Biomedical Engineering at Tohoku University. During this research stay I did experimental work under the supervision of Professor Yuji Matsuura.

Publications

Paper I
I.L. Jernelv, K. Milenko, S.S. Fuglerud, D.R. Hjelme, R. Ellingsen, A. Aksnes, "A review of optical methods for continuous glucose monitoring," *Applied Spectroscopy Reviews*, Vol. 54(7), pp. 543-572, 2019.

I.L.J., R.E., D.R.H., and A.A. conceptualised this review article. I.L.J. wrote and prepared most of the original draft, K.M. and S.S.F. contributed one section each (Raman spectroscopy and near-infrared spectroscopy, respectively). All authors reviewed the original draft and contributed to the revision of the paper.

Paper II
I.L. Jernelv, K. Strøm, D.R. Hjelme, A. Aksnes, "Infrared Spectroscopy with a Fiber-Coupled Quantum Cascade Laser for Attenuated Total Reflection Measurements Towards Biomedical Applications," *Sensors*, Vol. 19(23), 5130, 2019.

All authors conceptualised and designed the experiments, I.L.J. and K.S. performed the experiments. K.S. performed the simulations. I.L.J. implemented the code for the analysis and analysed the results. I.L.J. wrote and prepared the original draft. A.A. and D.R.H. supervised the work. All authors reviewed the original draft and contributed to the revision of the paper.

Paper III

I.L. Jernelv, K. Strøm, D.R. Hjelme, A. Aksnes, "Mid-infrared spectroscopy with a fiber-coupled tuneable quantum cascade laser for glucose sensing," *Proceedings of SPIE 11233, Optical Fibers and Sensors for Medical Diagnostics and Treatment Applications XX*, 1123311, 2020.

All authors conceptualised and designed the experiments, and K.S. did initial experimental work. I.L.J. performed the experiments included in the paper. I.L.J. implemented the code for the analysis and analysed the results. I.L.J wrote and prepared the original draft. A.A. and D.R.H. supervised the work. All authors reviewed the original draft and contributed to the revision of the paper.

Paper IV

I.L. Jernelv, J. Høvik, D.R. Hjelme, A. Aksnes, "Signal enhancement in microstructured silicon attenuated total reflection elements with quantum cascade laser-based spectroscopy," *Proceedings of SPIE 11359, Biomedical Spectroscopy, Microscopy, and Imaging*, 113590A, 2020.

All authors conceptualised and designed the experiments. I.L.J. developed the experimental setup and performed the measurements. I.L.J. implemented the code for the analysis and analysed the results. J.H. did the simulation work. I.L.J. wrote and prepared the original draft. A.A. and D.R.H. supervised the work. All authors reviewed the original draft and contributed to the revision of the paper.

Paper V

I.L. Jernelv, D.R. Hjelme, Y. Matsuura, A. Aksnes, "Convolutional neural networks for classification and regression analysis of one-dimensional spectral data," *Preprint published on* `arxiv.org`, arXiv ID 2005.07530, 2020.

All authors conceptualised and designed the experiments. I.L.J. performed the measurements for the original dataset included in the study, and Y.M. supervised this experimental work. I.L.J. implemented the code for the analysis and analysed the results. I.L.J. wrote and prepared the original draft. A.A. and D.R.H. supervised the work. All authors reviewed the original draft and contributed to the revision of the paper.

Paper VI

I.L. Jernelv, D.R. Hjelme, A. Aksnes, "Infrared measurements of glucose in peritoneal

fluid with a tuneable quantum cascade laser," *Biomedical Optics Express*, Vol. 11(7), pp. 3818-3829, 2020.

All authors conceptualised and designed the experiments. I.L.J. developed the experimental setup and performed the measurements. I.L.J. implemented the code for the analysis and analysed the results. I.L.J. wrote and prepared the original draft. A.A. and D.R.H. supervised the work. All authors reviewed the original draft and contributed to the revision of the paper.

Software

SpecAnalysis: A Python software package for multivariate data analysis, with functionality for regression and classification analysis, as well as pre-processing and feature selection methods. Developed by I.L.J. with open source code freely available online.

Other Results

Other results and conference contributions during the doctoral studies not directly related to the thesis are:

1. I.L. Jernelv, K. Milenko, D.R. Hjelme, R. Ellingsen, S.M. Carlsen, A. Aksnes, "Optimising Multivariate Models for Glucose Measurements in an ATR-FTIR Spectrometer." ICAVS9 (2017).

2. I.L. Jernelv, K. Milenko, R. Ellingsen, D.R. Hjelme, A. Aksnes, "Improving Multivariate Analysis Mid-Infrared Spectroscopy for Biosensing." Optical Sensors, (2018) JTu2a-49. Optical Society of America.

3. K.B. Milenko, I. L. Jernelv, S.S Fuglerud, A. Aksnes, R. Ellingsen, D.R. Hjelme, "Towards Fiber-Optic Raman Spectroscopy for Glucose Sensing" Specialty Optical Fibers, (2018) JTu2a-49. Optical Society of America.

4. S.S. Fuglerud, K.B. Milenko, I. L. Jernelv, R. Ellingsen, A. Aksnes, D.R. Hjelme, "A miniaturized ball-lensed fiber optic NIR transmission spectroscopy-based glucose sensor" Specialty Optical Fibers, (2018) SeM3E-5. Optical Society of America.

Contents

List of Abbreviations

ANN	Artificial neural network
AP	Artificial pancreas
ATR	Attenuated total reflection
BGL	Blood glucose level
CGM	Continuous glucose monitoring
CNN	Convolutional neural network
CV	Cross-validation
CW	Continuous wave
DFB	Distributed feedback
DTGS	Deuterated triglycine sulfate
EC	External cavity
FEM	Finite element method
FP	Fabry-Pérot
FTIR	Fourier transform infrared
GOx	Glucose oxidase
HWG	Hollow-core waveguide
ICL	Interband cascade laser
ICU	Intensive care unit
IP	Intraperitoneal
IR	Infrared
IRE	Internal reflection element
ISF	Interstitial fluid
kNN	k-nearest neighbours
LV	Latent variable
MAE	Mean absolute error
MAPE	Mean absolute percentage error
MCT	Mercury cadmium telluride
MHF	Mode-hop-free
MIR	Mid-infrared
NIR	Near-infrared
OLS	Ordinary least-squares
PC	Principal component
PCA	Principal component analysis
PCR	Principal component regression

PLSR	Partial least-squares regression
POC	Point-of-care
QCL	Quantum cascade laser
RMSE	Root-mean-square error
SC	Subcutaneous
SE	Signal enhancement
SEIRA	Surface-enhanced infrared absorption
SEP	Standard error of prediction
SG	Savitzky-Golay
Si	Silicon
SMBG	Self-monitoring of blood glucose
SNR	Signal-to-noise ratio
SPR	Surface plasmon resonance
SVM	Support vector machine
TIR	Total internal reflection
TLS	Tuneable laser spectroscopy

Chapter 1

Introduction

There is an increasing demand for sensor technology targeted towards real-time and in situ monitoring of various chemical and biological species. This is the case for a wide range of applications, including food analysis, monitoring of hazardous gases or greenhouse gases, chemical process monitoring and control, and diagnostics in biomedicine. Optical spectroscopy techniques are a class of robust and reliable measurement methods for identification and quantification of analytes in complex surroundings. In many cases these methods have been restricted to bulky equipment with free-space optics and measurements in a laboratory setting. A combination of optical spectroscopy with fibre-optic sensing may remove these limitations and bring these methods into a new range of applications. Fibre-optic sensors are interesting for applications where the measurement site can be difficult to access, as the source and detector can be placed remotely. One such application is glucose sensing, which is paramount for monitoring and treatment of diabetes.

Mid-infrared (MIR) spectroscopy has been a standard laboratory technique for decades through the use of spectrometers for identification of organic and inorganic compounds. MIR spectroscopy is sensitive to fundamental vibrational transitions, and is consequently a technique with high specificity that can be used to identify, characterise, and quantify a large variety of molecular species. Molecules in gas/vapour, liquid, and solid phases can all be investigated with MIR spectroscopy. However, waveguide technology is less mature in the MIR range compared to the visible and near-infrared (NIR) wavelength regions, and MIR spectroscopy has therefore not enjoyed the same range of applications within e.g. process monitoring, environmental monitoring, or chemical/biomedical sensing. New developments such as commercially available tuneable MIR lasers and signal-enhanced waveguides may solve some of the current bottlenecks. These technologies enable miniaturisation and higher sensitivity, and thereby adaptation of MIR spectroscopy for various portable and real-time monitoring applications.

Sensing in biomedicine is a substantial area where new sensor technologies are required. Healthcare costs are rising rapidly in the world due to chronic and lifestyle diseases, as well as due to ageing populations, and this is expected to put a strain on the future economy [1, 2]. More efficient, improved, and cheaper biomedical sensors is one avenue to reduce costs and improve patient outcomes. Biomedical monitoring often involves extracting a sample from a patient, which is then measured in an external apparatus and later discarded. This can put an undue burden on the patient. One example is in intensive care units (ICUs) where patients often suffer from anaemia, which is detrimental to patient outcomes. Anaemia can be exacerbated by blood draws, as blood samples are collected multiple times per day in the ICU [3, 4]. Optical measurement methods can potentially replace many current biomedical applications, and can enable real-time and point-of-care (POC) monitoring. Optical spectroscopy also fulfils many other sensor requirements such as robustness, label-free sensing, fast response/measurement time, and a possibility for miniaturisation.

Glucose sensing is an important example of an application that is handled with POC monitoring by diabetic patients, and glucose sensors comprise 85% of the world market for biosensors [5]. Diabetic patients, especially those with type 1 diabetes, lose the ability to control their blood glucose level (BGL). Monitoring the BGL is therefore essential for diabetic patients in order to avoid low and high glucose levels. In 1964, Dextrostix was developed as the first semi-quantitive glucose test strip that could be employed for home use [6]. This test strip changed colour based on a reaction with the enzyme glucose oxidase, and glucose concentration was initially estimated by eye. Since then better sensors with built-in electronic glucose measurements have been developed as hand-held devices, and even implantable sensors for continuous glucose monitoring (CGM) have become more common. However, these electrochemical devices use an enzymatic reaction for glucose sensing, and the device lifetime in the body is limited to 1–2 weeks. Subcutaneous (SC) measurements have also been found to lag behind the BGL by 5–15 minutes, which can be detrimental to glucose control during rapid changes in glucose levels [7, 8]. Extensive effort has been expended on research and development of better alternatives, but so far no other options have come close to replacing the electrochemical sensors.

MIR spectroscopy has been suggested and studied for glucose monitoring, mainly through non-invasive sensing or measurements of blood samples from patients. Brandstetter et al. [9], as well as Vahlsing et al. [10], have demonstrated glucose

measurements of blood serum and micro-dialysate samples in free-space transmission setups intended for an ICU setting. Liakat et al. [11] showed that a MIR laser-based system could be used to determine glucose levels from reflection-mode measurements of skin, while Kino et al. [12] demonstrated spectrometer-based glucose sensing with measurements on the inner lip mucosa in humans. However, these non-invasive systems have lower sensitivity due to high water absorption in skin.

An implantable fibre-optic sensor in reflection mode could be suitable for real-time spectroscopy-based glucose monitoring, and would circumvent some of the challenges inherent to MIR spectroscopy due to high water absorption. MIR spectroscopy has several features that are advantageous for continuous glucose monitoring; reagent-free monitoring can increase the sensor lifetime, optical fibres are robust in biomedical environments as they can withstand temperature and pressure changes, and fibre-optic sensing allows for remote sensing into small sample volumes. MIR spectroscopy is also very selective, which is advantageous for quantitative determination of glucose in a complex biological environment. Today's implantable CGM sensors measure glucose subcutaneously, which could potentially be handled by a fibre-optic sensor. Another alternative is to do sensing in the peritoneal cavity, which is the space between organs in the abdomen, as this has been recently suggested as a better sensor site due to improved glucose dynamics [13]. Higher sensitivity might be needed in such environments, and this can be achieved with signal-enhancement techniques. Signal enhancement in infrared spectroscopy has been demonstrated with surface plasmon resonances in layers of metal nanoparticles, as well as with 3-layer dielectric or semiconductor structures [14,15]. These signal-enhancement methods may enable highly sensitive measurements with only one reflection in reflection-mode sensing, and thereby allow for miniaturised fibre probes.

This project has been a part of the research group Artificial Pancreas Trondheim, where the long-term goal has been to develop an automated system that combines CGM and insulin infusions in diabetic patients. This automated system would form a basis for an artificial pancreas (AP), where the efficacy of the automation heavily depends on a rapid response to changes in the glucose level, as well as fast uptake of insulin. The focus of the AP development has therefore been towards operation in the peritoneal cavity, as this has been suggested as an avenue to achieve normalised glucose levels.

1.1 Aim of the Thesis

Given the above-mentioned issues with electrochemical glucose sensors, this thesis aimed to develop an optical sensor system for measurements of glucose in peritoneal fluid. This sensor system was developed with in vivo operation in mind, and a fibre-coupled system was therefore the basis of this work. The optical system was based on mid-infrared tuneable laser spectroscopy using a quantum cascade laser (QCL).

The main contributions of this thesis are summarised as follows:

- Evaluation of several optical spectroscopy methods with regard to their applicability for biomedical sensing, specifically for continuous glucose monitoring. This work resulted in a review article that covered optical measurement methods for CGM.
- Design, construction, testing, and characterisation of a sensor system for glucose measurements in aqueous media. Initial measurements were done with aqueous solutions due to ease of access.
- Exploration of a signal enhancement technique as a means to minimise sensor size. Investigation of the signal enhancement effect in the QCL-based system, and whether or not any effective enhancement could be achieved.
- In-depth investigation of multivariate analysis methods for prediction of analyte concentrations, and application of convolutional neural networks to improve prediction accuracy. In-house development of a software package, SpecAnalysis, with source code made freely available online.
- Demonstration of sensor system performance on peritoneal fluid samples from pigs. Measurements of physiological glucose concentrations, with sufficient accuracy to maintain control of BGL.

The following chapters cover theoretical background related to the publications connected to this thesis, as well as the methods used for this work. The background covers infrared spectroscopy, components used in the mid-infrared wavelength region, measurement modalities and signal enhancement, as well as biomedical applications and multivariate data analysis. The chapter on methods describes the experimental setups used and the multivariate analysis of the spectral data. Following this are a summary of the included papers, an outlook on the presented work, and the publications included in this article collection.

Chapter 2

Background

This chapter covers relevant theoretical background for biomedical measurements of aqueous fluids with mid-infrared (MIR) spectroscopy. Included topics range from the fundamental physics behind infrared absorption, to the available optical components and measurement techniques in the mid-infrared wavelength range, to multivariate analysis used to investigate infrared spectral data.

2.1 Infrared Spectroscopy

Light can interact with matter in different ways, such as by scattering, transmission, reflection, and absorption. This section covers the physical origin of light absorption and how this property can be used for wavelength-dependent measurements of matter. Infrared spectroscopy uses light in the infrared wavelength region to identify and measure molecules, both qualitatively and quantitatively. Spectroscopy with infrared light can be used on many organic and inorganic materials, and is useful in many application areas such as food analysis, biomedical measurements, forensics, and environmental monitoring. Materials that have infrared-active vibrations can be measured directly without any need for reagents, and the measurement process is non-destructive.

2.1.1 Light Interaction with Matter

Light is electromagnetic radiation, and the interaction between light and matter is governed by how the electric and magnetic fields from incident radiation interact with electric charges in the matter. Specifically, incident light on some matter, for example a molecule, will lead to a displacement of electrons in the matter. The electrons will oscillate with this incident field, which causes a separation of positive

and negative charges, and hence a dipole is created [16]. For a material these smaller dipole moments can be added up to a net polarisation. The net polarisation, $\mathbf{P}$, in the matter is related to the incident electric field, $\mathbf{E}$, as:

$$\mathbf{P} = \varepsilon_0 \chi \mathbf{E} \tag{2.1}$$

where ε_0 is the permittivity constant of vacuum and χ is a tensor that describes the material's susceptibility, i.e. how much it reacts to an applied field, and may contain higher-order terms that depend on the electric field. The susceptibility is related to the relative permittivity as $\varepsilon_r(\omega) = 1 + \chi$. Relative permittivity is generally a complex value, which can be divided into a real and an imaginary part:

$$\varepsilon_r(\omega) = \varepsilon_r'(\omega) + i\varepsilon_r''(\omega) \tag{2.2}$$

Eq. 2.1 can be expanded into a Taylor series with increasing orders of $\mathbf{E}$ and associated constants, and the first term dominates at low field strength. Nonlinear effects arise at high field strengths, but optical nonlinear effects will not be considered further here and we refer the reader to Boyd [17] for more information. The effect of incident radiation on the displaced charges can be described as a damped harmonic oscillator in a linear system, see Fig. 2.1. Let us consider a single electron bound to a nucleus, with incident radiation at a single frequency. The total electric force for a linear system is then a sum of the forces acting on the charges:

$$m\frac{d^2\mathbf{x}}{dt^2} + k_s\mathbf{x} + \boldsymbol{\gamma}\frac{d\mathbf{x}}{dt} = e\mathbf{E} \tag{2.3}$$

In this system, a mass m oscillates with a displacement $\mathbf{x}$, and and a balancing counter-force is described by the spring constant k_s. The oscillations are dampened by energy loss, which is described by a damping coefficient, $\boldsymbol{\gamma}$, and the velocity of the object.

The expression in Eq. 2.3 is a differential equation, and the solutions of such equations are covered in many electromagnetics textbooks, e.g. by Saleh et al. [18]. A solution on the form $\mathbf{x} = \mathbf{x}_0 e^{-i\omega t}$ can be inserted into Eq. 2.3, and the result can be used in Eq. 2.1 to give an expression for the susceptibility, χ, as a function of ω. An expression for the relative permittivity, also called the dielectric constant, can then be found:

$$\varepsilon_r(\omega) = 1 + \frac{\omega_p^2}{\omega_0^2 - \omega^2 - i\boldsymbol{\gamma}\omega} \tag{2.4}$$

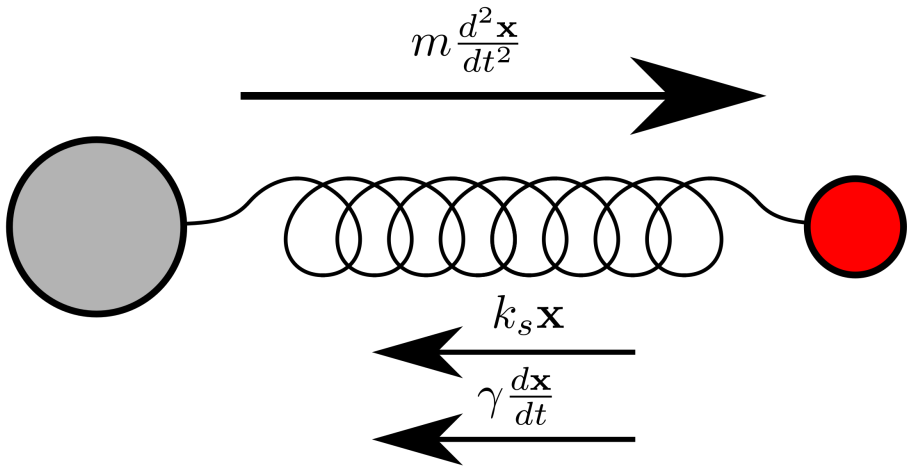

Figure 2.1: Forces acting on an oscillating dipole as a result of an incident field, modelled as a damped harmonic oscillator. An electron is displaced from its resting point by a force described by its mass and acceleration. This is countered by an elastic force described by the spring constant k_s, as well as a damping force described by γ and the velocity of the particle. These forces are also shown in Eq. 2.3.

where ω is the frequency of the incident radiation, ω_0 is the resonant frequency as defined by $\omega_0 = \sqrt{k_s/m}$, and ω_p is the plasma frequency. The plasma frequency quantifies the rate of electron oscillations in a medium and is defined as $\omega_p = \sqrt{N_e e/m\varepsilon_0}$, where N_e is the number of electrons per volume [19].

In electromagnetics, material properties are defined from the relative permittivity. Light absorption can be described as a part of the complex refractive index from Maxwell's equations [18]:

$$n(\omega) + i\kappa(\omega) = \sqrt{\varepsilon_r'(\omega) + i\varepsilon_r''(\omega)} \tag{2.5}$$

The real part of the refractive index, n, represents the propagation of light in a medium. The imaginary part, κ, which is called the extinction coefficient, determines the light attenuation, or absorption, in a medium. From the previous expressions it can be seen that the properties of a medium will depend on the frequency of the incident radiation. Frequency and wavelength, λ, are related as $\omega = c/\lambda$, where c is the speed of light in vacuum. Consequently, light interaction with matter is also wavelength-dependent, which is an important property for spectroscopy-based measurement techniques.

2.1.2 Absorption of Light

The previous section outlined how material properties are wavelength dependent in response to an electric field. In the same way, light itself will be affected as it interacts with matter, and here we will discuss the theory behind light absorption. Absorption is a process where light interacts with a medium and the electromagnetic energy is transformed into internal energy. For example, a molecule can take energy from the incident radiation if the energy of a photon equals the difference of two energy levels in the molecule. In the case where the photon energy does not match the difference between energy levels, the molecule will not absorb any of the incident radiation.

Fig. 2.2 shows a band diagram with electronic energy transitions for infrared spectroscopy, as well as for UV/visible and Raman spectroscopy for comparison. Electrons will typically be in the lowest energy state, E_0. When excitation light is introduced, an electron may absorb a photon and thereby be excited to a higher energy state. Infrared light, which has long wavelengths and thus low energy, can only excite vibrational and rotational states in a molecule. Relaxation back to the ground state usually occurs through release of energy in the form of heat.

Absorption bands are not equal in strength, and are characterised by the absorption cross section $\sigma(\lambda)$. The absorption cross section can be described as $\sigma(\lambda) = \kappa/N$, where N is the atomic number density and κ is the extinction coefficient, which was shown to be a wavelength-dependent parameter in the last section. The total absorption probability can then be quantified with the absorption coefficient, μ_a. The absorption coefficient is defined as:

$$\mu_a = C \times \sigma(\lambda) \tag{2.6}$$

where C is the concentration of the absorbing material. Light going through an absorbing material will then have an incremental change in intensity as described by:

$$\frac{dI}{I} = -\mu_a dx \tag{2.7}$$

Integrating this gives an exponential function:

$$I(x) = I_0 e^{-\mu_a x} \tag{2.8}$$

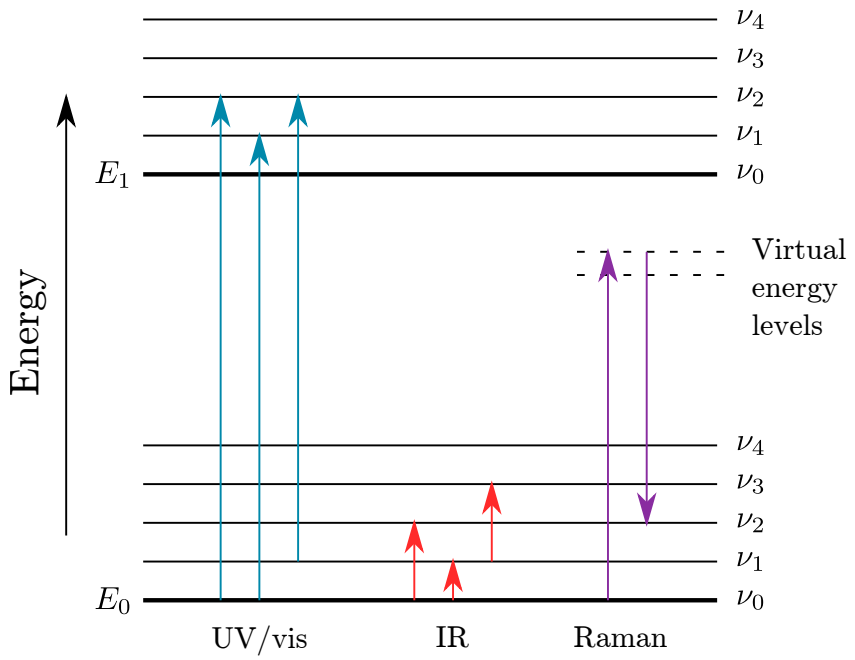

Figure 2.2: Band diagram of electronic transitions for UV/visible spectroscopy, infrared spectroscopy, and Raman spectroscopy. Two energy levels are shown, with several rotational/vibrational sublevels, as well as the virtual energy levels in Raman scattering.

which is called the Beer-Lambert law [20], where I is the light intensity and x is the pathlength. As shown by Eqs. 2.6 and 2.8, the absorption process also depends on wavelength and molecular concentration. The amount of absorbed light in the material can be expressed as a ratio between the incident, I_0, and transmitted, I, light through a sample:

$$A = -\log \frac{I}{I_0} \tag{2.9}$$

which is a dimensionless quantity called absorbance. An infrared spectrum can be created by transmitting light at several wavelengths through a material, as the absorbance will vary according to wavelength. Molecules can only absorb infrared light if the energy of the photon corresponds to a vibrational, rotational, or combination mode in the molecule. The exact composition of these vibrational, rotational, and combined modes is associated with the arrangement and constituent atoms within the molecule, and is therefore unique [21]. Infrared spectroscopy therefore

gives information which is unique to the particular material under investigation, and this can be used to investigate most kinds of organic or inorganic materials.

There are certain limitations to infrared spectroscopy. For some materials the sensitivity is quite low if the infrared activity is low, i.e. if the vibrational transition has a weak oscillatory dipole. In complex samples it can also be difficult to detect analytes with small concentrations, especially if they have absorption bands that overlap with other highly concentrated analytes. Infrared spectroscopy does not give any direct structural information on molecules, such as the position of functional groups and molecular weight. Other complicating factors make infrared spectra more difficult to interpret, such as line broadening, heavily overlapping bands, and shifts in absorption bands due to hydrogen bonds, especially when water is used as a solvent. Additional bands are created when two photons are absorbed simultaneously, called overtone and combination bands.

The infrared wavelength range is typically divided into three subranges: the near-infrared (0.78–3 μm), the mid-infrared (3–50 μm), and the far-infrared (50 μm–1 mm) [22], although different sources use somewhat different definitions [23]. Near-infrared spectra are products of overtone or combination bands which are typically less intense and broader than fundamental vibrational modes. Near-infrared spectroscopy is nevertheless a popular measurement method, in part due to the low price of optical components in that wavelength range. The mid-infrared wavelength range encompasses fundamental vibrational modes, in addition to skeletal vibrations, which are vibrational modes that couple over the entire molecule. Skeletal vibrations give a distinct spectral shape, and the region for skeletal vibrations (approximately 6.5–12 μm) is therefore called the fingerprint region. The fundamental and skeletal vibrational modes are sharper and higher in intensity than e.g. overtones, which gives mid-infrared spectroscopy an advantage for detection and quantification of materials. Far-infrared spectroscopy uses photons with very low energy, and is typically used to investigate stretching modes in molecules with heavy atoms or lattice vibrations in crystals. Since mid-infrared spectroscopy is the focus of this work, further sections will focus on spectroscopy in the mid-infrared wavelength range.

As a note on units, it is common in spectroscopy to use wavenumbers, which is the number of wavelengths per unit distance, $\tilde{\nu} = 1/\lambda$, typically given as cm^{-1}. In wavenumbers, the mid-infrared range is 3333–200 cm^{-1}, and the region of skeletal vibrations is approximately 1500–800 cm^{-1}.

2.2 Measurement Modalities

There are three main methods for direct MIR spectroscopy: transmission, internal reflection, and external reflection. Transmission and internal reflection will be discussed here, as these measurement modalities are widely used for applications relevant to this work.

2.2.1 Transmission Measurements

Transmission spectroscopy is done by transmitting radiation through a sample and detecting the transmitted light. The resulting spectrum can be represented as either absorbance or transmittance. The Beer-Lambert law as shown in Eq. 2.8 can be formulated to relate absorbance directly with the concentration, C, of an absorbing material, or the optical pathlength, l:

$$A = \varepsilon \cdot C \cdot l \tag{2.10}$$

where ε is the absorptivity of the material. The absorptivity is related to the absorption cross section as $\varepsilon = \frac{\log 10}{N_A}\sigma(\lambda)$, where N_A is Avogadro's number. All else being equal, this can be used for quantitative measurements, as an increase in concentration correlates linearly with the absorbance.

Many solid materials are opaque in the mid-infrared range, and extensive preparation is often necessary for transmission sensing. Qualitative measurements are facilitated by mixing or dissolving the material with an infrared-transparent matrix, and then either creating films from the mixture, or holding it between transparent plates. Liquids, solutions, and gases are typically easier to measure in transmission spectroscopy. Gas cells can be filled to a suitable partial pressure, and multi-reflection cells can be used in order to achieve a longer effective optical pathlength with higher absorbance. Liquids and solutions can be contained in liquid cells with two infrared-transparent windows. Samples with water can be challenging to measure since water absorbs very strongly in the mid-infrared, as shown in Fig. 2.3 [24]. For the 1250–1000 cm^{-1} (8–10 μm) wavelength range, which is the region with the strongest glucose absorption bands [25], water absorption is a constant background, but water still absorbs very strongly. Short pathlengths must therefore be used in order to transmit enough radiation, which decreases the absorbance by the analytes of interest.

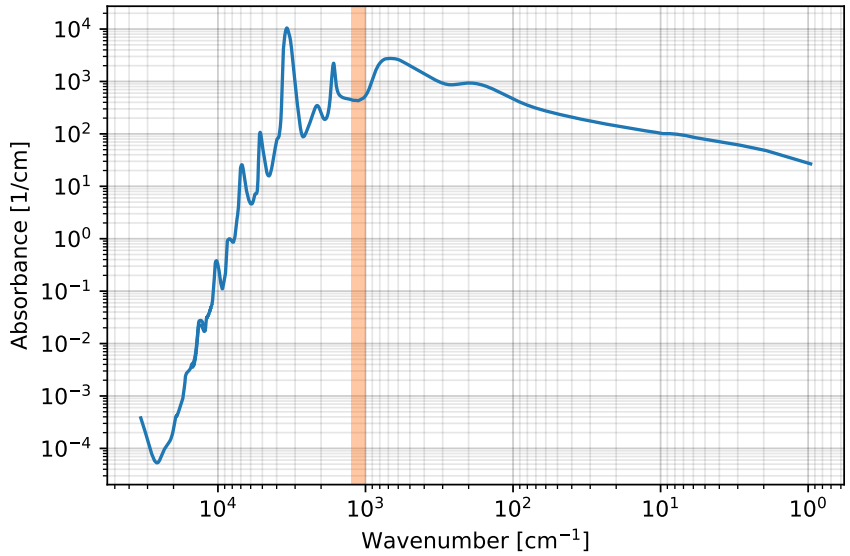

Figure 2.3: Water absorption in the visible to the far-infrared wavelength range. Water is most transparent for visible light, and the absorption increases in the infrared region. The region 1250–1000 cm^{-1} has been highlighted, and this region covers the strongest glucose absorption bands. Plot based on data from refs. [24, 26].

The noise level and optimal optical pathlength in transmission spectroscopy have been a point of discussion [27, 28]. It has been demonstrated that the optimal pathlength l_{opt} can be calculated as:

$$l_{opt} = \frac{l}{A_w \ln 10} \tag{2.11}$$

where A_w is the absorbance of the solvent, e.g. water, at a specific wavenumber [29]. For measurements around 9 μm wavelength this gives an optimal pathlength of approximately 20 μm with water as a solvent. However, Eq. 2.11 was derived for systems limited by detector noise, such as spectrometers. Systems where noise from the light source is a large factor, such as laser-based systems, can not necessarily use the same approach to estimate the optimal pathlength. Studies have shown optimal pathlengths of 135–200 μm for quantum cascade laser-based measurements of aqueous solutions, depending on the laser power [30, 31].

2.2.2 Attenuated Total Reflection Spectroscopy

Quantification of materials is not limited only to transmission measurements. Another common method in infrared spectroscopy is evanescent field sensing, where the material interacts with the evanescent field arising from total internal reflection (TIR) of light in a medium such as a crystal or an optical fibre, see Fig. 2.4. This method is called attenuated total reflection (ATR) spectroscopy. In this case the absorbance arises through interaction with only a fraction of the radiation, r, which can be quantified through:

$$A = -\left(\frac{I}{I_0}\right)r = (\varepsilon C l)r \tag{2.12}$$

For multiple reflections the measured absorbance increases approximately linearly with the number of reflections [32].

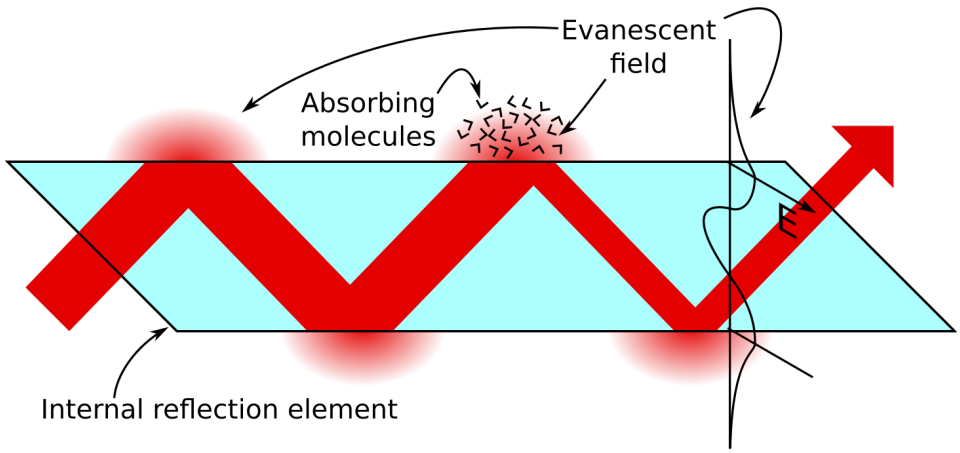

Figure 2.4: Illustration of total internal reflection (TIR) and the concomitant evanescent field in an internal reflection element (IRE). When a non-absorbing cladding is used, the light propagates in the IRE with minimal change. If a cladding is not used, materials close to the outside surface may interact with the evanescent field, and this effect can be used for absorption spectroscopy.

TIR occurs if light is reflected at a material interface at an angle larger than the critical angle:

$$\theta_c = \arcsin\frac{n_2}{n_1} \tag{2.13}$$

as determined from Snell's law. The interface must be between a material with high refractive index, n_1, such as an optical fibre or other waveguiding material, and a material with low refractive index, n_2, e.g. a sample matrix. The process of TIR carries with it a non-propagating component which extends into the neighbouring material, called the evanescent field. The intensity of the evanescent field decays exponentially from the material interface, as described by:

$$E = E_0 e^{-z/d_p} \tag{2.14}$$

where E is the electric field intensity at a distance z from the interface, and E_0 is the electric field intensity at the material interface. The penetration depth, d_p is given by:

$$d_p = \frac{\lambda_0}{2\pi n_1 \sqrt{\sin^2\theta - (n_2/n_1)^2}} \tag{2.15}$$

where λ_0 is the free-space wavelength and θ is the angle of incidence. Absorbing molecules close to the material interface may interact with the evanescent field, which creates an absorption spectrum, as mentioned previously. It has been shown that absorbance is proportional to the effective penetration depth, d_e [33, 34], rather than the penetration depth, which is calculated as:

$$d_e = \frac{n_{21}}{\cos\theta} \int_0^\infty E^2 dz = \frac{n_{21} E_0^2 d_p}{2\cos\theta} \tag{2.16}$$

where n_{21} is the ratio between n_2 and n_1.

Mid-Infrared Waveguides

Fourier transform infrared (FTIR) spectrometers can often be fitted with an ATR sensing unit, which is especially useful for materials and solutions with high water content that would otherwise require measurements through a very thin layer in transmission mode. These ATR units use crystal prisms made from various materials with single or multiple internal reflections, called internal reflection elements (IREs). Some materials that are typically used for ATR spectroscopy are diamond, zinc selenide, ZnSe, and zinc sulphide, ZnS [35]. Diamond is a resilient material and can today be fabricated industrially, however it is still a very expensive prism material. ZnSe is much cheaper, but very soft and toxic to humans, and is therefore not a good material choice for some applications. ZnS offers a good compromise as a prism material, as it is cheap, has a low refractive index (approx. 2.2 at 10 μm), and is non-toxic. Lower refractive index gives a longer

penetration depth, which increases the interaction volume outside of the IRE. This gives a higher absorbance and higher signal-to-noise ratio (SNR) as compared to IREs with high refractive index. Using a fibre-coupled system simplifies further sensor development with regard to portable sensing and reducing sensor form factor. A combination of ATR spectroscopy and fibre-coupling could be used in a probe design in a portable sensor.

Optical fibres can also be used for ATR sensing, after stripping away outside coating and alternatively the cladding [36]. The fibre can be looped several times to increase the sensing area in a liquid volume. Higher sensitivity can then be achieved in comparison to single bends or single-reflection prisms. However, evanescent sensing with fibres in the mid-infrared range has a few disadvantages. The fibres are usually several hundred micrometers in diameter, and a large bend radius must therefore be used. This can be a major drawback if the intended application is e.g. a biomedical sensor, where sensor footprint is a critical parameter. The fibre core can be pressed or tapered in order to reduce the dimensions and increase the evanescent field, but this also tends to put more mechanical strain on the fibre. Common optical fibre materials in MIR spectroscopy, such as silver halide materials, have also been found to be toxic as the fibres degrade and release particles in the surrounding environment over time. The issue with toxicity can potentially be solved by e.g. encasing the sensor in a semipermeable membrane which allows the analyte of interest to pass through [37]. This could potentially also improve sensing as it would allow for a preliminary filtering of the analyte of interest.

Another option is to use integrated waveguides for evanescent field sensing in the mid-infrared, in the interest of reduced form factor. Waveguides can be made with common techniques for microfabrication, resulting in a light-guiding structure on top of a substrate. This increases the fraction of light available for sensing as compared to ATR crystals or fibres and therefore also the measured signal. However, few transparent materials have been available as mid-infrared waveguides, and the fabricated structures are often quite lossy due to e.g. roughness at the waveguide-substrate interface. Liquid spectroscopy has been demonstrated with systems based on Ge and GaAs waveguides [38, 39]. Tantalum pentoxide is one potential waveguide material in the MIR range that has received recent research interest, and newer structures for gas sensing have been demonstrated [40]. Losses also occur when coupling light from a laser into a waveguide. So although increased signal can be achieved, this is often counteracted by an increase in noise, resulting in little or no improvement for the SNR.

For gas sensing, it is also possible to use the internal space of hollow-core fibres for spectroscopy. This is an improvement on traditional multi-pass gas cells, where the required volume varies from a few hundred millilitres to several litres. Compared to gas cells used for spectroscopy, hollow-core fibres also have more efficient interaction volume sizes and faster flow times for sample replacement. However, hollow-core waveguides are sensitive to vibrations, which can affect measurements in any sensing environment. Integrated hollow waveguides have been demonstrated by Wilk et al. [41], where a hollow waveguide was machined into an aluminium block for improved robustness.

2.2.3 Signal Enhancement

Surface-enhanced infrared absorption (SEIRA) is used in optical spectroscopy in order to increase the detected signal, and thereby the total sensitivity [42]. Enhancement can be achieved with surface plasmon resonances (SPRs), which occur when incident radiation induces a resonant oscillation of electrons in the conduction band of a material, see Fig. 2.5a. SPRs can only be induced at an interface between materials with negative and positive permittivity, such as a metal and a dielectric. This is typically realised by coating a surface with a layer of roughened metal or metal nanoparticles. Analytes close to the substrate are then typically measured with internal or external reflection. SPR-based sensors are commonly used in the visible/NIR range, as the technique can offer large sensitivity increases for optical methods that are otherwise not adequate. SPR-based sensors in the MIR range have been increasingly studied with enhancement from coated surfaces or deposited waveguides [14, 43, 44], as well as doped waveguide structures [45, 46]. SEIRA is usually reported to give enhancement factors of 10-100 for MIR spectroscopy.

Enhancement has also been demonstrated through an interference effect with micropillar silicon (Si) structures on Si wafer chips, and the principle is shown in Fig. 2.5b [15, 47]. The advantage of these microstructures for enhancement is that it is possible to use only one material for fabrication, and standard Si wafer technology can be used to produce the chips. This enhancement effect has been described several times previously for three-layer dielectric structures [48–50]. This measurement technique has been reported to give signal enhancement up to a factor of 10.

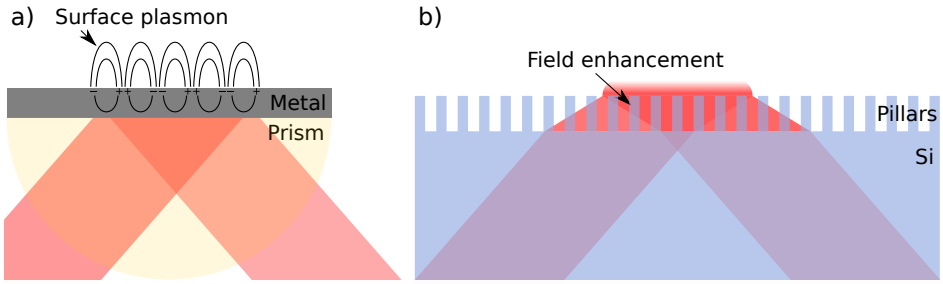

Figure 2.5: a) Signal enhancement through induction of surface plasmons using a metal layer or metal nanoparticles. b) Enhancement method using an interference effect in a three-layer dielectric, here exemplified with an Si IRE with micropillars.

Signal enhancement does not come without challenges. For SPR-based systems one common issue is sensor lifetime, as the thin metal layers or metal nanoparticles have a tendency to degrade over time. This leads to a decline in sensor performance. A release of nanoparticles from the sensor surface also poses potential risks with regards to environmental safety in many applications [51, 52]. Interference-based signal enhancement, on the other hand, has been shown to be associated with a simultaneous increase in noise, which can significantly reduce the achieved effective enhancement factor [47].

2.3 Systems for Mid-Infrared Spectroscopy

Technical systems for MIR spectroscopy are based on either spectrometers or tuneable laser spectroscopy, which have several fundamental differences. In order to appreciate how this can affect measurements in biomedical applications, the basic principles of these systems are detailed below.

2.3.1 FTIR Spectrometers

Fourier transform infrared (FTIR) spectroscopy has been a routine laboratory technique for mid-infrared spectroscopy for decades, and has taken the place of dispersive spectrometers [23]. Dispersive spectrometers are still commonly used for e.g. near-infrared spectroscopy. Commercially available FTIR spectrometers combine a light source, interferometer, sample stage, and detector for a complete system.

Michelson Interferometers

Michelson interferometers are the most common interferometers used in FTIR spectroscopy. As shown in Fig. 2.6, a Michelson interferometer consists of a beamsplitter, which is a semi-reflective film, and two perpendicular plane mirrors, one of which is moveable. The incident radiation travels towards the beamsplitter, where 50% of the beam is transmitted to one of the mirrors, while the remaining 50% of the beam is reflected to the other mirror. The beams are reflected at the mirrors, and then return to the beamsplitter where they recombine and interfere. The beam that emerges from the interferometer at 90° to the input beam is called the transmitted beam, and this is the beam (interferogram) detected in FTIR spectroscopy. Due to the nature of the beamsplitter, 50% of the total radiation reaches the sample, while 50% of the radiation is lost.

The optical path difference between the two arms of the interferometer is produced by the moving mirror. This path difference causes destructive and constructive interference between the beams, and results in an interferogram. The moving mirror is a critical part of the interferometer. It must be aligned accurately, and must be able to trace the distance consistently so that the path correlates with a known value. Most modern FTIR systems use a separate laser to measure the mirror position.

Fourier Transformation

FTIR spectroscopy works on the principle of Fourier transformation, which converts the interferogram measured by the detector into an infrared spectrum. The main development that enabled widespread use of FTIR spectrometers was the introduction of modern computers that were able to perform Fourier transform algorithms in real time. The Fourier transformation, as used in FTIR spectroscopy, can be written as:

$$I(\delta) = \int_0^\infty B(\bar{\nu}) \cos(2\pi\bar{\nu}\delta)\, \mathrm{d}\bar{nu}. \tag{2.17}$$

$$B(\bar{\nu}) = \int_{-\infty}^\infty I(\delta) \cos(2\pi\bar{\nu}\delta)\, \mathrm{d}\delta. \tag{2.18}$$

These equations relate the light intensity that reaches the detector, $I(\delta)$, to the spectral power density at a wavenumber $\bar{\nu}$, that is $B(\bar{\nu})$. Indeed, the equations show that it is possible to convert between $I(\delta)$ and $B(\bar{\nu})$. Eq. 2.17 shows how the power density varies as a function of difference in pathlength, which is the

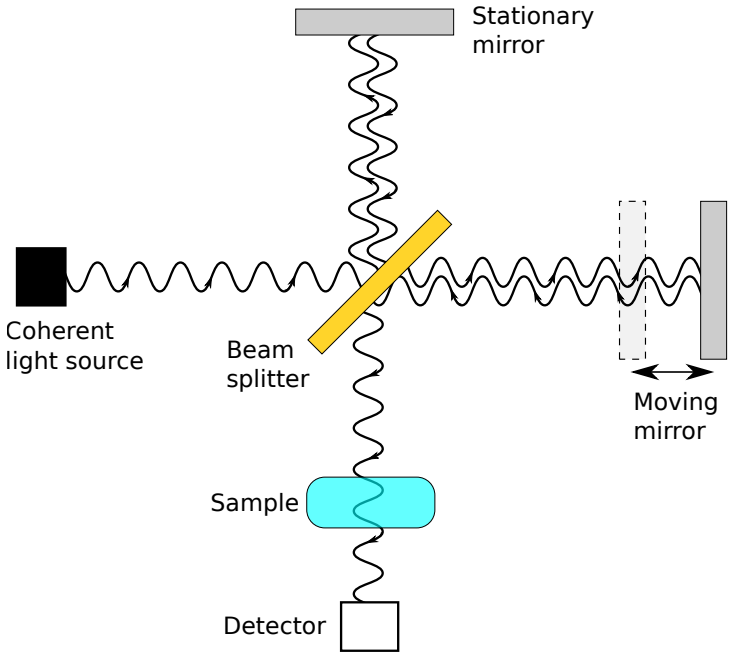

Figure 2.6: Sketch of the main components in a Michelson interferometer, showing a light source, beam splitter, stationary and moving mirrors, sample, and detector.

interference pattern on the detector. Eq. 2.18 shows the variation in light intensity as a function of wavenumber, which produces the infrared spectrum.

Advantages of FTIR Spectroscopy

FTIR spectroscopy as a research method has many advantages. These advantages are usually compared against dispersive spectrometers, as they in many cases have been displaced by FTIR instruments. The *Fellgett* advantage, also called the multiplex advantage, describes an improvement in SNR for a given measurement time because information is collected from all wavelengths at the same time. The *Jacquinot* advantage, also called the throughput advantage, results from most of the light from the coherent light source contributing to the measurement, so a large signal and higher SNR can be achieved [23]. This is in contrast to dispersive spectroscopy, where most of the light is stopped by entrance and exits slits in the

monochromator. FTIR spectroscopy also benefits from rapid scanning and the associated improvement in SNR is related to the number of scans as SNR $\propto \sqrt{n}$.

FTIR Light Sources

Different sources are used in FTIR spectrometers depending on the wavelength, and they are usually broadband thermal light sources. The most common source for the MIR region is a silicon carbide element, which is heated to around 1200 K. Tungsten-halogen lamps are used for NIR spectroscopy, as a higher temperature source is required to achieve the shorter wavelengths. Mercury lamps are needed to give a high output at the long wavelengths required for far-infrared spectroscopy. These are all blackbody sources that emit over a broad wavelength range, which means that many spectral features can be investigated at the same time. However, the spectral power density is quite limited, down to μW, which presents a challenge for the detection limit.

2.3.2 Tuneable Laser Spectroscopy

Tuneable laser spectroscopy (TLS) is an alternative to FTIR spectrometers and dispersive spectrometers. TLS has the advantage of much higher spectral power density than spectrometers using thermal emitters. This section will focus on quantum cascade lasers (QCLs) for MIR spectroscopy as a QCL laser was used for measurements in this thesis. QCLs were the first commercially available tuneable MIR semiconductor lasers capable of room-temperature operation.

Operation Principle of QCLs

The earliest semiconductor lasers made were interband semiconductor lasers, and they are ubiquitous today in many applications ranging from barcode readers, to telecommunications, to medical uses such as dentistry. These semiconductor lasers are based on stimulated emission from electron transitions between the conduction and valence bands in the semiconductor material, see Fig. 2.7 [53]. Interband semiconductor lasers are usually limited to visible and near-infrared wavelengths. A smaller bandgap is necessary for low-energy photons and longer wavelengths, and as the bandgap gets smaller the thermal effects become more dominant, until population inversion can no longer be achieved.

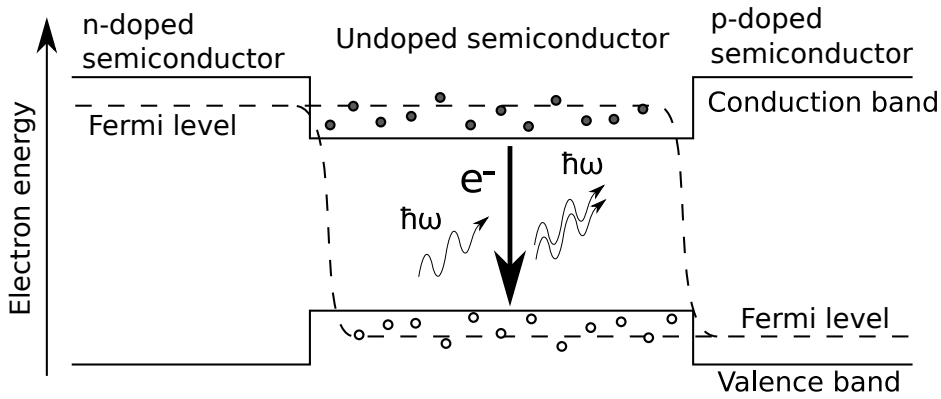

Figure 2.7: Simplified diagram illustrating stimulated emission in a semiconductor double heterostructure based on electron-hole recombination [54]. Lasing is achieved with forward biasing, and the optical field projects into the plane, with optical confinement ensured through a higher refractive index in the undoped layer. The energy of the Fermi level branches into quasi-Fermi levels for electrons and holes in the active undoped region.

QCLs differ from typical semiconductor lasers because they rely on intersubband transitions of electrons [55], which occur within the conduction band of the semiconductor. This is achieved by stacking alternating layers of semiconductor material with different bandgaps, which creates heterostructures. As long as the layers are thin enough, meaning on the scale of a few nanometres, they will behave as quantum wells, see Fig. 2.8. The electron wave function then becomes quantised, and the electrons can become trapped in the quantum wells. With a current applied over the QCL structure, the band diagram can effectively be tilted. Electrons can then transition from a high to a low energy level in the quantum well, and then couple into a lower quantum well through an injector region. Each electron undergoes these transitions typically around 40 times in a QCL, and therefore each electron gives rise to many photons. Since these transitions occur within the conduction band of the semiconductor, both the transition energy and the emission wavelength are completely independent of the bandgap. The emission wavelength of a QCL can therefore be chosen by engineering the thicknesses of the heterostructures.

Fig. 2.8 shows an energy diagram of a QCL heterostructure with three energy levels in the quantum wells in the active regions, and injector regions inbetween. In this simplified overview, electrons tunnel solely from the injector region to state 3 of the next active region, where a photon is emitted in the laser transition 3→2. Lasing is

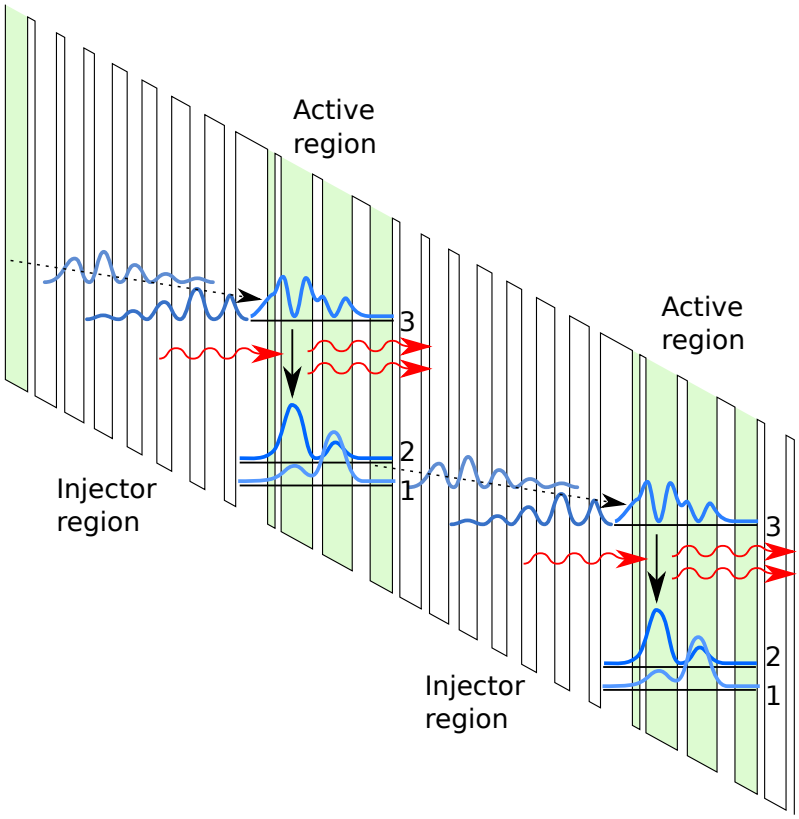

Figure 2.8: Band diagram of intersubband transitions in the conduction band of a quantum cascade laser, with three energy levels highlighted in the quantum wells. Stacked heterostructures of semiconductor materials form quantum wells where electrons can emit photons by stimulated emission.

achieved with population inversion between states 3 and 2, and electrons must exit from states 2 and 1 rapidly in order to maintain the population inversion. In reality other detrimental behaviours can occur, such as scattering directly from the injector to the lower states, or scattering from state 3 into the injector. Electrons may also be thermally excited or tunnel into the continuum from state 3, after which they do not contribute to lasing any further. These alternative paths contribute to leakage currents in the laser, which adds to the threshold current. QCLs also experience optical losses, such as outcoupling loss at the mirror facets and waveguide losses through absorption in the doped semiconductor regions [56]. The highest wall-plug efficiency demonstrated for QCLs at room temperature is 28% for a pulsed laser and 21% for continuous-wave operation [57, 58].

The first working QCL was demonstrated by Faist et al. at Bell Labs in 1994 [59], and the concept of intersubband transitions in the conduction band of lasers was already suggested by Kazarinov et al. in 1971 [60]. Precision on the level of atomic layers is necessary for growth of the QCL heterostructures, and this was enabled by development of the now staple tools in nanotechnology research, namely molecular beam epitaxy (MBE) and metal-organic vapour phase epitaxy (MOVPE).

Bandstructure engineering can also be implemented for interband transitions in so-called interband cascade lasers (ICLs) [61, 62]. These lasers follow the same principle as QCLs, where stacked heterostructures are used to form the gain element. Lasing in ICLs can be achieved at lower input powers than what is possible in QCLs. Currently 5.6 μm is the longest emission wavelength demonstrated at ambient conditions with CW operation [63].

QCLs and ICLs are important tools for research using mid-infrared wavelengths for spectroscopy. Previously, only spectrometers could cover large wavelength ranges in the mid-infrared, with very limited spectral power density. The other laser sources available were CO_2 lasers and lead-salt lasers, as well as light sources based on difference frequency generation or optical parametric oscillation. CO_2 lasers have found many uses in industrial applications, with power levels up to several hundred kWs. However, CO_2 lasers are bulky as they are gas lasers, and can usually only be used at a set few wavelengths. Lead-salt lasers can be made tuneable over small wavelength ranges, but have seen limited use as they often require cryogenic cooling for operation. Mid-infrared radiation based on frequency comb generation has also become available [64], and has demonstrated good results particularly for gas spectroscopy [65, 66]. Frequency comb generation usually requires femtosecond laser sources, which currently necessitates complex optical systems. Spectroscopy with frequency combs based on quantum cascade lasers has been demonstrated as a promising alternative, with potential for time-resolved spectroscopy [67, 68].

QCL Resonator Design

QCLs are classified according to their resonator design. The three resonators that are most commonly used are Fabry-Pérot (FP), distributed feedback (DFB), and external-cavity (EC).

An FP resonator design is achieved by cleaving the ends of the laser chip in order to make highly reflective end facets on the laser ridge. Light amplification is only

possible if the distance between the facets allows for constructive interference, in addition to the gain condition for the active material. FP-QCLs typically have multimode emission, as the standing wave condition in the cavity is fulfilled for up to several hundred longitudinal modes. The emission covers a large spectral range, up to 50 cm^{-1}, and the wavelength can be controlled by adjusting the chip temperature. As a result of the multimode emission, FP-QCLs are often unsuitable for most applications in spectroscopy, especially gas spectroscopy and other applications where single-mode emission is required. However, these QCLs have found use in analysis of liquids [69], and in heterodyne spectroscopy [70].

A QCL with a DFB resonator uses a Bragg grating that is integrated into the laser waveguide along the direction of light propagation. As a result, all modes except one will be lossy, and a single mode is chosen for emission. The emission wavelength can be tuned over a small range of approximately 5 cm^{-1} by changing the operation temperature or the injection current of the chip. DFB-QCLs have been used for gas spectroscopy [71, 72], as the single-mode emission enables accurate targeting of specific spectral lines. Multiple DFB-QCLs can also be joined in an array if a larger wavelength range is needed [73].

With an EC resonator design, an external diffraction grating is used for broadband spectral tuning, see Fig. 2.9 [74]. Tuning ranges of several hundred wavenumbers are enabled by adjusting the angle of the diffraction grating relative to the QCL chip. EC-QCLs are available with three different emission types: standard continuous wave (CW), pulsed, and mode-hop-free (MHF). Standard CW and pulsed operation give the largest spectral tuning ranges of up to approx. 500 cm^{-1}. EC-QCLs combined with a detector can then be used as miniature spectrometer. Some commercially available EC-QCL models combine several laser heads in order to achieve tuning ranges of over 1000 cm^{-1}. EC-QCLs have been demonstrated for many applications, such as spectroscopy of liquids [30] and infrared microspectroscopy [75, 76].

The use of an external cavity is not only an advantage, and limits EC-QCLs in several ways. The grating adds to the size of the laser. This is usually not an issue for most applications or sensor uses. However, for point-of-care measurements or personalised sensors, further miniaturisation will be needed before commercial products can be realised. Additionally, the laser must be kept stable because the cavity accuracy is sensitive to vibrations, which is a large constraint for many applications.

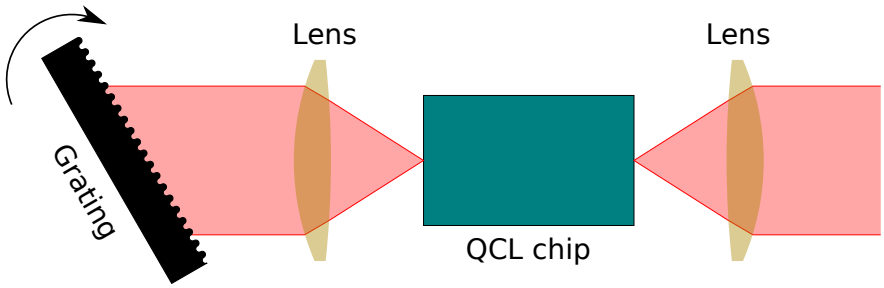

Figure 2.9: Schematic illustration of an external-cavity QCL in a quasi-Littrow configuration. A moving grating is used to choose the emission wavelength, and the laser can be scanned over a broad wavelength range by continuously tuning the grating.

The wavelength accuracy and repeatability of commercial EC-QCLs are typically lower than for DFB-QCLs, and multimode emission with fluctuations over time have been shown [77]. EC-QCLs are therefore less suitable for gas spectroscopy where the absorption features have narrow linewidths. EC-QCLs in CW-MHF operation have been used for gas spectroscopy [78,79], however MHF operation results in narrower spectral coverage and slower tuning rates. Pulsed EC-QCLs also experience variation in pulse intensity at up to 3% standard deviation, which is a detriment to quantitative measurements. This can be mitigated by averaging a set amount of pulses, which can reduce the energy variation to less than 0.1%. Averaging has the added effect of increasing measurement time, but the total measurement time can still be kept to less than a minute for e.g. liquid spectroscopy. Pulsed operation has lower energy consumption and reduces the need for water cooling, and pulsed operation may therefore be advantageous for portable devices.

2.4 Optical Components

2.4.1 Detectors

Several detector types are used for MIR spectroscopy. Photoconductive detectors are used if high sensitivity is required. These detectors are made from semiconductor alloys, such as mercury cadmium telluride (MCT), indium antimonide (InSb), or similar materials, and detect electrons that are excited from the valence band to the conduction band by incident photons. MCT detectors are widely used, and

require either liquid nitrogen cooling or multistage thermoelectric cooling. MCT detectors with thermoelectric cooling are available commercially with detectivity up to 3×10^9 cm $Hz^{1/2}$ W^{-1} at wavelengths up to 10.6 μm [80]. Pyroelectric or thermal detectors may be used instead if lower detectivity is acceptable. Incident light is absorbed onto a pyroelectric detector, which causes heating of a ferroelectric material in the detector, thus producing a pyroelectric voltage. Pyroelectric detectors have traditionally used deuterated triglycine sulfate (DTGS) as a sensing element, but today several variations exist. These detectors are cheaper than photoconductive detectors, and have higher potential for miniaturisation because they may be operated without cooling. Detectors with quantum well structures have also been shown to be suitable for photon detection [81]. These quantum hetereostructure detectors base their operation on subband or intersubband transitions, similar to QCLs, and may enable further integration into a MIR sensor system.

2.4.2 Other Optical Components

Other optical components are necessary for e.g. light guiding in free-space systems and for fibre-coupling. Metals such as aluminium, silver, and gold can be used to coat mirrors, as these are reflective over long wavelength ranges. Borosilicate glasses, which are used for lenses and beamsplitters in the visible and near-infrared ranges, become opaque in the mid-infrared. Instead, infrared-transparent inorganic compunds such as CaF_2, ZnSe, and KBr are used for components that transmit infrared light [23]. The specific material used for the components is chosen according to the wavelength region of interest, as the material should have a high transmission. For example, KBr can be used as a beamsplitter material for mid-infrared spectroscopy, and allows for measurements up to 25 μm before material absorption becomes an issue. Several infrared-transparent materials are sensitive to moisture, which must be taken into consideration if water is used as a solvent.

2.4.3 Optical Fibres in the Mid-Infrared

Optical technology in the mid-infrared range has not enjoyed the same widespread use as near-infrared technologies, which is especially evident when considering the available optical fibres. 1.55 μm has become the standard wavelength for the telecom industry [82], and the concomitant fibre development has resulted in silica fibres with approximately 0.2 dB/km loss at a price of less than 1 USD per metre. At

the same time, fibres suitable for mid-infrared wavelengths typically have losses of 0.3 dB/m at 8 μm with prices of more than 100 USD per metre. Silica has increased losses for wavelengths longer than 1.8 μm due to multiphonon absorption, which has necessitated production of speciality mid-infrared fibres. Finding appropriate materials has not been simple, and common mid-infrared fibres include exotic materials such as chalcogenide and tellurium-based glasses [83–86]. Chalcogenide glasses have been reported with losses down to 12 dB/km at 3 μm [87], however the absorption in most chalcogenide systems increases rapidly above 8 μm. Silver halide and hollow-core fibres have become the two most common fibre types for wavelengths longer than 8 μm.

Silver halide fibres are polycrystalline compounds of AgBrCl in various concentrations, and form soft and ductile materials [88]. These fibres are typically made with core sizes of at least 300 μm, and are encapsulated in plastic or metallic tubing to maintain structural integrity. As silver halide is very soft it can be looped with a small bend radius without significant increase in optical loss, and can be used for evanescent field sensing.

Hollow-core fibres consist of a hollow glass capillary coated on the inside with a silver layer for reflection and a dielectric layer for protection, see Fig. 2.10. These fibres can be fabricated with optical losses down to 0.1 dB/m. The loss in hollow-core waveguides (HWGs) is related to the inner radius as $1/R^3$, as well as the bending radius as $1/R$, and large inner diameters (∼1mm) are therefore not unusual [89, 90]. HWGs are rugged and have low insertion losses, but have increased losses with bending and can not be used directly for external evanescent field sensing.

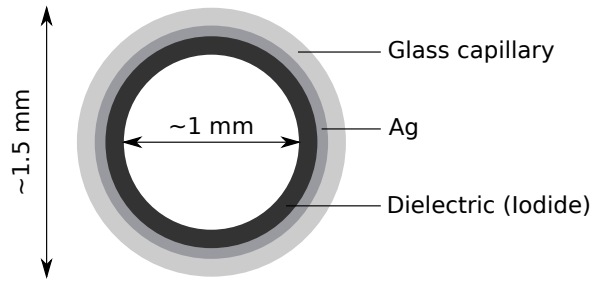

Figure 2.10: Cross section of a typical hollow-core waveguide.

2.5 Biomedical Mid-Infrared Spectroscopy

Optical spectroscopy techniques in combination with lab-on-a-chip technology, waveguides, or fibre-optic sensors are increasingly being studied for biochemical sensing. Such sensors may offer label-free sensing, possibilities for remote sensing, and high robustness in challenging environments. Mid-infrared (MIR) spectroscopy has an especially large potential for real-time sensing in complex environments in biomedical applications. As mentioned, MIR spectroscopy gives unique fingerprints of molecules, and has more intense absorption bands than near-infrared spectroscopy. The relatively recent commercial availability of QCLs also means that this field is less mature than visible/near-infrared spectroscopy, and as such there are many unrealised potential applications.

This chapter will discuss the current main biomedical application areas for MIR spectroscopy, with focus on glucose sensing for management of diabetes. The importance of glucose sensing, the principle behind commercial electrochemical sensors, and sensor placement considerations will be introduced. These sections are only meant to give required background for a more in-depth discussion of glucose sensing with MIR spectroscopy. More details can be found in Paper I and in the references.

2.5.1 Glucose Sensing

Personal glucose sensors are essential for patients with diabetes, who have lost the ability to control their own blood glucose level (BGL). Patients with type 1 diabetes no longer produce the glucose-regulating hormone insulin, while patients with type 2 diabetes have an increased resistance to the effects of insulin. Type 2 diabetes is often managed through diet and medications, while type 1 diabetes, which affects 10% of diabetic patients, must be managed with self-monitoring of blood glucose (SMBG) and insulin injections or infusions. The goal of this is to keep the BGL within normoglycaemic levels, typically defined as 72–180 mg/dL (4–10 mM) [91]. Too low BGL, known as hypoglycaemia ($<$70 mg/dL, or 3.9 mM), can lead to seizures, loss of consciousness, and even death as the brain becomes starved of glucose [92]. Too high BGL on the other hand, called hyperglycaemia ($>$180 mg/dL, or 10 mM), leads to serious long-term complications, including

kidney damage and nerve damage, which severely affects the quality of life for diabetic patients [93].

Electrochemical Glucose Sensors

Glucose sensors used today by diabetic patients are either invasive or minimally invasive. The most common sensor type uses a fingerprick method where the patient lances their finger to produce a blood drop, and then places this on a glucometer. The glucometer estimates the BGL from an enzymatic reaction within a few seconds. The basic principle of these electrochemical glucose sensors is to measure the current produced by oxidation of glucose molecules [94]. This can be written as a simplified reaction:

$$\text{glucose} + \text{O}_2 \xrightarrow{\text{glucose oxidase}} \text{gluconic acid} + \text{H}_2\text{O}_2 \tag{2.19}$$

An enzyme such as glucose oxidase (GOx) is used to facilitate this enzymatic reaction. In a second step the hydrogen peroxide dissociates:

$$\text{H}_2\text{O}_2 \rightarrow \text{O}_2 + 2\text{H}^+ + 2\text{e}^- \tag{2.20}$$

and the resulting current is used as an estimate for the glucose concentration. Current electrochemical glucose sensors are more advanced than what the above reactions indicate. For example, a mediator molecule is usually introduced as an alternative synthetic electron acceptor. This eliminates the dependence on available oxygen in the immediate area of the detector. These mediator molecules are also made to transport electrons from the enzyme to the electrode surface.

SMBG by fingerprick measurements gives information only at discrete points in time, and must be repeated several times per day for proper BGL control. Many patients find this painful and cumbersome, and often measure less than the recommended minimum of 4 times per day [95]. Continuous glucose monitoring (CGM) devices based on electrochemical sensing have been developed as an alternative to fingerprick measurements. These devices are worn on the body for several days, and provide regularly updated BGL values.

Sensor Placement

Glucose sensing in humans for out-patient care requires a sensor system that is portable and ideally even wearable. The placement of a wearable sensor is a

non-trivial and complex issue. Factors such as invasiveness, how cumbersome they are, and how user-friendly they are must all be considered. Glucose sensing in combination with insulin infusions and a control system could be used to make an artificial pancreas (AP), which would mimic the function of healthy pancreas with minimal patient involvement [96]. The sensor placement is also important in regard to development of an AP, as an AP needs to detect changes in glucose levels fast for optimal control.

Electrochemical CGM devices are increasingly used by diabetic patients. Most of these devices are placed in a patch on the skin with a small filament implanted subcutaneously (SC). An enzymatic reaction is then employed for glucose measurements, and the glucose levels are updated approximately every five minutes. These measurements are performed in the interstitial fluid (ISF), which is the fluid surrounding cells in the intercellular matrix. CGM devices must be replaced every 1-2 weeks due to decreased sensor performance, and the measured glucose levels in the ISF have been found to lag behind the actual BGL by approximately 5-15 minutes, which can be detrimental to diabetes management [7, 8]. The sensor lag is a combination of physiological lag as glucose has to diffuse into the ISF, as well as internal sensor lag (e.g. electrons being transported to the electrode). These sensor types require a lot of involvement from the patient, as the patient still has to manage their own insulin infusions/injections based on the sensor data. In addition, the sensor must typically be calibrated against fingerprick measurements twice per day, and because of this fingerprick measurements are not completely avoided. An AP with SC glucose measurements and SC insulin infusions improves glucose control, but still has limitations such as a significant amount of time spent in hyperglycaemia [97].

Non-invasive glucose sensing has for a long time been seen as the end goal for diabetes management. Non-invasive sensing includes any methods that do not penetrate the skin and should in theory be painless and less of a hassle than current methods. The main challenge for non-invasive methods is the lack of measureable glucose. It has been suggested that glucose levels can be measured in easily collectable fluids, such as sweat [98], tears [99], or saliva [100], but the correlation with the internal BGL has not been entirely convincing. Another option is to measure through the skin, which has proved difficult for most methods that have been investigated [101]. Methods such as reverse iontophoresis have been used to extract glucose molecules through the skin, with concentration measurements based on the glucose diffusion rate. However, these devices were not very accurate, and

had side effects such as skin irritation [102]. There has also been research on optical spectroscopy methods for non-invasive sensing, typically with light backreflected from skin. Mid-infrared spectroscopy is difficult to use non-invasively due to high water absorption, although some preliminary results of glucose measurements in non-diabetic subjects have been published [11, 103]. Near-infrared spectroscopy is less affected by water absorption, but has much lower selectivity. Thus far, there have been no commercially successful non-invasive glucose sensors.

Another possibly viable solution for glucose monitoring is to perform the sensing in the peritoneal space. The peritoneal cavity is the space between organs in the abdomen, and contains peritoneal fluid. The peritoneal fluid contains, among other things, white blood cells, proteins, lactate, as well as glucose. It has been suggested that measurements of glucose and injections of insulin in the peritoneum can more closely mimic the dynamics of a healthy pancreas, with both faster detection of rapid changes in BGL and faster uptake of insulin [13, 104]. However, sensing in the peritoneal cavity is more invasive than currently employed methods, and carries the risk of infection and pain. Short-term peritoneal glucose measurements with electrochemical sensors have been demonstrated in an animal model [105]. A long-term study has also been described, although the full results have not been published yet [106]. Sensing could be done with an optical fibre-based solution by inserting the fibre through an abdominal port. Such ports have already seen some limited clinical use for intraperitoneal (IP) infusion of insulin, and this type of insulin delivery has been shown to improve time spent in the normoglycaemic range compared to subcutaneous insulin infusions [107, 108]. Development of suitable IP glucose sensing technology, together with IP insulin infusions, may enable a safe and effective AP that requires minimal user input.

Glucose Sensing with Mid-Infrared Spectroscopy

Heise et al. showed one of the earliest studies of physiological glucose concentrations in whole blood using an ATR-FTIR spectrometer in 1989 [109]. The same group also demonstrated that multiple analyte concentrations, including glucose, could be determined in human blood plasma with FTIR spectroscopy in the same year [110]. Since then, FTIR spectroscopy has been used to measure glucose levels with transmission through dried serum samples [111], and recently in transmission configuration through otherwise untreated plasma samples [112].

Laser-based measurements of glucose in the MIR range were first demonstrated in the mid-2000's, both on synthetic solutions and on serum samples [113, 114].

These studies used either multiple single-wavelength lead-salt lasers or QCLs, due to a lack of tuneable lasers in the wavelength region. Vrančić et al. later showed preliminary measurements of glucose levels in the ISF of rat models using only one single-wavelength laser [115]. This study employed transmission measurements through a 20 μm gap between two fibres, and achieved quite accurate glucose measurements at 17.5% standard deviation. The authors acknowledged that accurate measurements over a longer timeframe would require measurements at multiple wavelengths in order to account for drift of the source and interference from multiple analytes.

QCL-based MIR spectroscopy for glucose measurements has taken great strides following the recent commercial availability of broadly tuneable EC-QCLs. In 2013, Brandstetter et al. demonstrated accurate measurements of glucose and other analytes in human blood serum with an automated tuneable QCL-based system [9]. More recently, the Heise group has shown a similar system for measurements of micro-dialysate samples from humans, using a QCL with four laser heads for a total tuning range of over 1000 cm^{-1} [10, 77]. In both cases these systems have aimed at rapid and reagent-free measurements for patients in an ICU setting.

As mentioned previously, Liakat et al. developed a sensor system based on detection of backscattered light from the hand, although measurements were only shown for a few subjects and a narrow glucose concentration range (75-160 mg/dL) [11]. Werth et al. improved the system by including an integrating sphere [116], but measurements in more subjects and over longer time spans are necessary to validate the sensitivity. Kino et al. have taken a different approach with ATR spectroscopy of the inner lip mucosa, so far with either an FTIR spectrometer or several single-wavelength QCLs [12]. Several groups have also developed variants of photoacoustic or photothermal spectroscopy system with EC-QCL sources for non-invasive measurements [117–119], and photothermal deflection spectroscopy in particular may enable non-invasive measurements in deeper skin layers compared to direct ATR measurements.

Isensee et al. showed transflection measurements of glucose based on an implant meant for minimally invasive measurements [120]. So far, this system has only been demonstrated for measurements of synthetic aqueous solutions. There are otherwise few studies on systems meant for invasive or minimally invasive measurements of glucose, and few studies with fibre-coupled EC-QCLs that have investigated the effect of fibre-coupled EC-QCL-based remote sensing.

Comparison of QCL-Based and FTIR Spectroscopy

The spectral power density of QCLs is several orders of magnitude higher than for FTIR spectrometers (10^4 is often reported). Higher spectral power density can be used to achieve shorter measurement times and/or longer optical pathlengths, which can be advantageous for many applications. However, the advantage from higher spectral power density is difficult to leverage completely in practical applications, especially for pulsed QCLs. In pulsed operation there is always some intensity variability between pulses. As the variability is a random distribution around an average value, the laser noise can be reduced by averaging a set amount of pulses. Averaging over pulses will add to the measurement time, but QCL measurements still tend to be faster than FTIR measurements.

FTIR spectrometers are able to cover much broader spectral ranges than single tuneable QCLs. QCLs should be chosen carefully in order to cover the correct spectral range for any analytes of interest, and the target application should therefore be clearly defined. FTIR spectrometers on the other hand are easier to use as standard laboratory equipment, as they cover the entire mid-infrared wavelength range. Several commercial products combine multiple EC-QCLs in order to cover a larger spectral area, but these are consequently more expensive and still cover less than 1/3 of the FTIR spectrum.

For miniaturised and portable sensor applications QCLs have a clear advantage over FTIR spectrometers regarding size. Traditional FTIR spectrometers use free-space optics, which makes them quite bulky. Miniaturised spectrometers based on micro-electro-mechanical systems (MEMS) have been demonstrated [121], but these typically have narrower tuning ranges, lower resolution, and lower sensitivity. EC-QCLs are compact compared to standard FTIR spectrometers. For applications where even EC-QCLs are too big and vibrations could influence measurements, it could be possible to instead use a few single-wavelength laser chips in an array. This has been investigated several times in relation to glucose sensing [77, 103, 113], and the results indicate that 5–10 wavenumbers may be sufficient to accurately predict glucose concentrations in ISF or blood micro-dialysate.

2.5.2 Other Application Areas

QCL-based spectroscopy has many other potential biomedical applications apart from glucose sensing, and a few other application areas will be outlined in order to

give a perspective of these possibilities. Breath analysis is one area where optical spectroscopy is a highly suitable measurement method. Standard methods for gas analysis include mass spectroscopy and gas chromatography that use expensive and large equipment, or low-cost semiconductor or electrochemical sensors, which have lower selectivity. QCL-based spectroscopy has been used to detect biomarkers in breath, which are low-concentration endogenous molecules that can be used to track disease progression. These biomarkers include acetone, ammonia, carbon monoxide, and nitric oxide, and studies have demonstrated both detection of singular gas species and multigas analysis [122–125]. Infrared spectroscopy has also been used to determine the $^{13}CO_2/^{12}CO_2$-ratio [126, 127], which is used in studies of liver function where exogenous isotopes are introduced into the body.

Infrared microspectroscopy with QCLs has increasingly been studied and employed for histopathology, i.e. tissue studies for disease diagnostics. Histopathology requires a tissue biopsy sample that is extensively prepared before investigation by an expert clinician. Diagnosis by eye is subjective and prone to error, and the entire process is very time-consuming. MIR microspectroscopy as a label-free method can potentially reduce the required preparatory steps, while multivariate data analysis can be used for accurate and objective identification of tissue changes. So far, QCL-based infrared microspectroscopy systems have been used to differentiate normal and cancerous tissues, classify tissues at different cancer stages, as well as identify other abnormal tissue changes [128–132]. FTIR-based microspectroscopy has previously been extensively studied for histopathology diagnosis and other tissue analysis, but has failed to translate to clinical use, partly due to low SNR and slow data acquisition [133]. The newer studies with QCL-based systems show that infrared microspectroscopy may finally be used outside of a research setting.

2.6 Multivariate Data Analysis

For spectroscopy geared towards biomedical applications, one can expect to measure complex samples with multiple analytes. Although single analytes have distinct and easily interpretable infrared spectra, samples such as bodily fluids have overlapping absorption bands and the resulting infrared spectra are typically very complex. As a result, spectral features can not easily be assigned to particular analytes, and simple methods such as measuring the height of an absorption band can not be used for quantitative measurements. In some cases, processing such as centrifuging can

be applied to the samples to remove unwanted interfering analytes, thus giving less complex spectra. However, for some applications, such as personalised sensors, it is necessary to measure samples without any physical pretreatment. Data processing in the form of multivariate analysis has therefore become an important procedure for quantitative analysis in mid-infrared spectroscopy.

The following sections will explain common regression models and classification methods for multivariate analysis, as well as methods for model validation and how to present model error. Pre-processing methods and feature selection methods commonly used for spectral data will also be described.

2.6.1 Regression Analysis

Regression analysis is a methodology used for estimating a set of dependent variables, e.g. analyte concentrations, based on independent variables, e.g. data points in an infrared spectrum. The simplest type of regression is linear regression, which fits a linear equation to the observed data, where the linear equation minimises the sum of squares distances between the measured data and the regression line. Simple linear regression is vulnerable to noisy independent variables and overfitting, and is therefore typically not used as a stand-alone method to analyse spectral data. In addition, simple linear regression does not work on data where there are more independent variables than observations, which is often the case for spectral data. Different learning methods are used to overcome these issues, either by modifying the data prior to regression or by modifying the linear regression method.

Principal Component Regression

Principal component regression (PCR) combines principal component analysis (PCA) with linear regression by using the components from PCA as regression coefficients in a linear regression model. PCA is effectively a dimensionality reduction method, where the data of interest is transformed into a new coordinate system according to the data variance [134]. Mathematically, this is done through a matrix transformation of the independent variables, $\mathbf{X}$:

$$\mathbf{X} = \mathbf{T}\mathbf{P}' + \mathbf{P} \tag{2.21}$$

$\mathbf{T}$ are the *scores* representing the original data in the transformed coordinate system, while $\mathbf{P}$ are the *weights* that the original data have to be multiplied with in order

to produce the component scores. A synthetic dataset with three independent variables has been plotted in Fig. 2.11 in order to demonstrate this. Two new axes have been drawn along the directions with the most variance in the data. These axes are properly called *latent variables*, but for PCA they are called principal components (PCs).

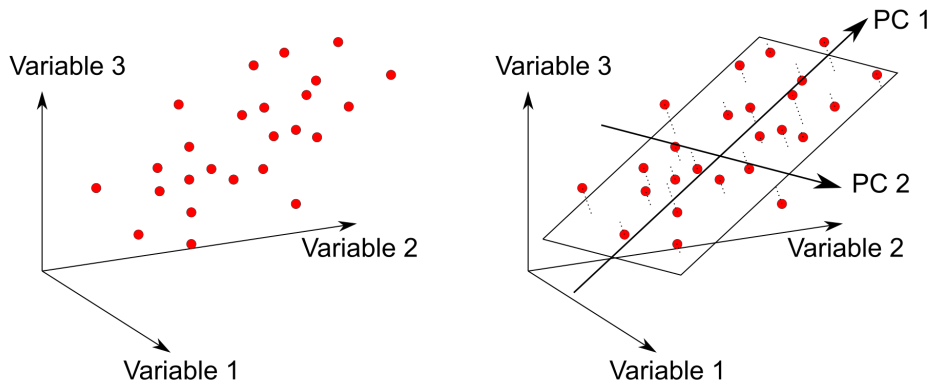

Figure 2.11: Example dataset with three independent variables. The first two principal components (PCs) are drawn along the directions where the data has the highest variance.

The number of possible PCs is equal to the number of variables that are measured. Optical spectra may have hundreds of measured wavenumbers, and PCA can therefore produce hundreds of components. However, only the first few components contain useful information, and only these need to be used in further modelling. PCs that mainly contain noise are discarded, and the remaining components are used to make simple and robust models. Regression analysis can be done with PCA by regressing the dependent variables on the PCs. This regression is done with ordinary least-squares (OLS). As mentioned, OLS tries to minimise the residual sum of squares between the predicted and the true dependent values, on the form:

$$\min_{\mathbf{w}} ||\mathbf{X}\mathbf{w} - \mathbf{Y}||_2^2 \tag{2.22}$$

where $\mathbf{w}$ is a vector describing the minimisation coefficients, and $\mathbf{Y}$ is a vector that contains the true dependent variables. $||\cdot||_2$ denotes the Euclidian norm. For PCR the two-dimensional $\mathbf{X}$ matrix is replaced by the transformed $\mathbf{T}$ matrix.

PCR can produce robust models with good prediction accuracy. However, the performance of PCR declines if the number of observations is much lower than the number of independent variables, which is often the case for optical spectroscopy.

In addition, PCR is very susceptible to data where variables with low variance also have high predictive power. Such low-variance components can easily be dropped, which is detrimental to the predictive power of the model.

Partial Least-Squares Regression

Partial least-squares regression (PLSR) performs dimensionality reduction on both the independent and dependent variables [135]. PLSR is therefore very similar to PCR, which unlike PLSR only transforms the independent variables. PLSR circumvents some of the issues with PCR, as the first latent variables are those that explain the most variance from both the independent and the dependent variables.

PLSR tends to have better prediction accuracy than PCR on data from vibrational spectroscopy, and generally uses fewer latent variables (LVs) to achieve this. Due to the simpler, more robust, and better models, PLSR has become a staple regression method for spectroscopy data. One drawback with both PLSR and PCR is that the LVs or PCs are less interpretable than the original independent variables.

Other Regression Methods

There are many other variants of linear regression methods that are variably used in machine learning and sometimes for spectral data. For example, regularisation methods (ridge, lasso, elastic net, etc.) add information to the data in order to decrease the modelling complexity, and this can subsequently be used in combination with regression. Compared to OLS, these regularisation methods add a penalty term to the minimisation problem. For ridge regression, the minimisation problem is then of the form [136]:

$$\min_{\mathbf{w}} ||\mathbf{X}\mathbf{w} - \mathbf{Y}||_2^2 + ||\alpha\mathbf{w}||_2^2 \tag{2.23}$$

where α is a penalty term that restricts the size of the coefficients. This is known as the $\mathbf{L}_2$ penalty term, while lasso regularisation uses the $\mathbf{L_1}$ penalty term [137] and the elastic net combines these two penalty terms [138]. This approach differs from the dimensionality reduction methods such as PCR and PLSR, and can be advantageous for certain types of data.

2.6.2 Classification Methods

The purpose of classification methods is to divide data into discrete groups based on a set of criteria, and various classification methods have different approaches to this problem [139]. k-nearest neighbours (kNN) is an example of a very simple model, which classifies data points based on their proximity to the k nearest neighbours in the training data. Support vector machines (SVMs) separate data points based on multidimensional hyperplanes, where the hyperplanes try to maximise the separation between data categories. Many classification methods can also be adapted for regression analysis, and vice versa.

2.6.3 Neural Networks

Artificial neural networks (ANNs) are a set of data mining methods that add a layer of abstraction in order to extract additional information from data. The structure of ANNs is inspired by biology, where *neurons* are connected by *weights* [140]. All ANNs are divided into three types of layers, the input, hidden, and output layers. Each data point in a measurement is assigned to a neuron in the input layer. The input from one layer is turned into the output of the next layer via a function in the neuron. ANNs can be used for both regression and classification of data. Deep ANNs, which use multiple hidden layers, have in recent years gained popularity [141].

Convolutional neural networks (CNNs) use a kernel function in order to convolve the output from neurons, see Fig. 2.12. This variant of ANNs is a method that is widely used for multidimensional data, e.g. two-dimensional data for image or video analysis [142]. CNNs have recently also been applied to one-dimensional spectroscopy data [143].

A neural network must first be trained on some known data in order to predict unknown data, as with all machine learning methods. The training process is done as follows:

- Weights are initialised for all the nodes. This can be done randomly, or with special initialisation methods that have been developed for faster convergence.

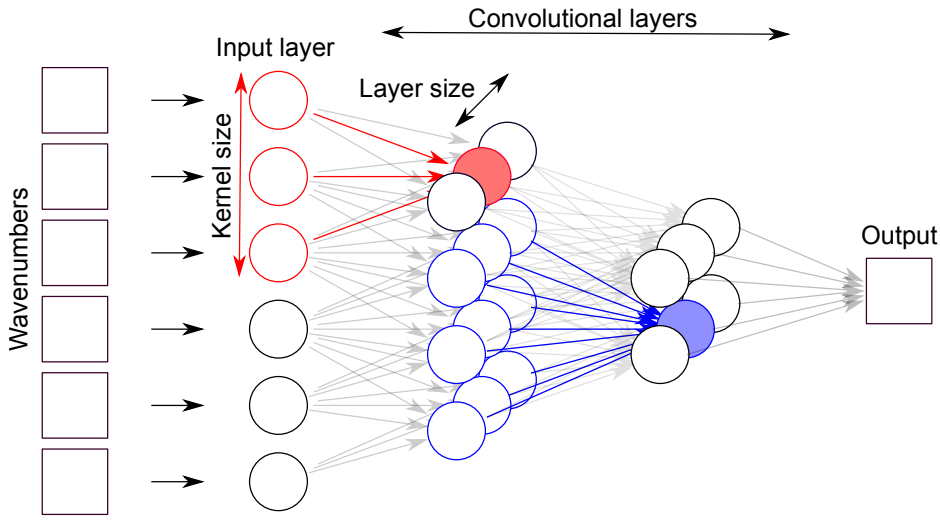

Figure 2.12: Example of a CNN with two convolutional layers. Kernel size and layer size are indicated. Each circle represents a neuron. Figure adapted from ref. [31].

- Every training sample is run through the neural network from the input layer to the output layer with the current weights. The output of each node is calculated, and the final output value is the value of the last node.
- The output value is compared to the true value, and the difference between the two, which is the measurement error, is described by a loss function.
- The error is propagated backwards in the neural network, and the weights are adjusted by the gradient descent method.

The above process is repeated until the loss function is minimised. Similarly to PCR and PLSR, the hidden layers in the ANN perform a matrix transformation of the input, although this transformation is non-linear.

2.6.4 Practical Modelling

Model Validation

Regression modelling is usually done in two steps. First, the model is trained on a subset of the available data, where both the independent and dependent variables are shown to the model. Secondly, the model is validated on unknown data,

where the model has to predict the dependent variables from only the independent variables. The error values for the prediction can then be used to evaluate how well the model performs.

Most regression models have one or several variable parameters, such as the latent variables in PLSR, and these can either be set by the user, or a search algorithm can be implemented in order to optimise the prediction accuracy. Optimising directly on the training set can give very good accuracy on the known data. However, this usually results in overfitting, which gives poor prediction on the validation data. Model parameters should not be adjusted after introducing the validation data, as this undermines the test of prediction accuracy and makes the results less universal.

Cross-validation (CV) is a common method used to validate the predictive ability of a model with only training data. CV is done in several rounds, see Fig. 2.13, and in each round the training data is divided into a training subset and a validation subset [134]. The model is then built on the training subset, and the predictive ability is tested on the validation subset. This is repeated several times with different training and validation subsets, and the average prediction accuracy is used to evaluate the performance of the model. CV can be done with e.g. leave-one-out CV, k-fold CV, or random permutations CV.

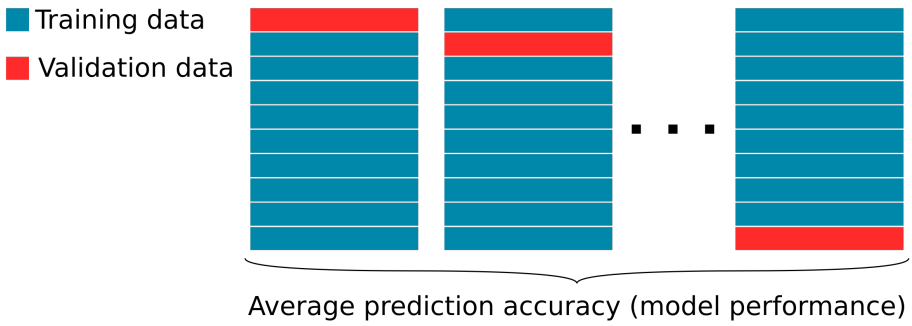

Figure 2.13: Illustration of k-fold cross-validation, where the training data is divided, and training and prediction is performed in several rounds. The model can then be evaluated based on an average prediction accuracy.

A common process for model validation is to perform CV on the training data, and then to validate the model with previously unused validation data, sometimes called test data. CV on training data often overestimates how well the model

performs, and it is therefore common to get somewhat better prediction accuracy in the CV phase than on the unknown validation data.

Measures of Error

The performance of regression and classification models must be validated with a measure of error [144]. The achieved prediction accuracy is usually used to measure the difference between the predicted values and the observed (reference) values. Different error measurements can be used, including root-mean-square errors (RMSE), standard error of prediction (SEP), and coefficient of determination (R^2). RMSE-values are commonly used, and are calculated as:

$$\text{RMSE} = \sqrt{\frac{\sum_n (\hat{y}_n - y_n)^2}{N}} \tag{2.24}$$

where $\hat{y}_n$ is the predicted value, y_n is the reference value, and N is the total number of measurements. RMSE is a positive value where a lower value indicates a better model, and for perfect prediction the RMSE is zero. RMSE is scale-dependent, which means that RMSE-values tend to increase if larger concentration ranges are used. One should therefore be careful when comparing RMSE between different datasets. RMSE is also sensitive to large deviations from the reference values, and is therefore disproportionally affected by outliers. SEP is similar to RMSE, but SEP does not include the bias, which is the average difference between $\hat{y}$ and y in the prediction set [145]. This term is usually small, and therefore SEP usually yields values similar to RMSE. The coefficient of determination is a measure of the proportion of variance in the dependent variable that can be predicted from the independent variable, and is defined as:

$$\text{R}^2 = 1 - \frac{\sum_n (y_n - \hat{y}_n)^2}{\sum_n (y_n - \bar{y})^2} \tag{2.25}$$

where $\bar{y}$ is the mean of the measured values. R^2=1 indicates that there is no unexplained variance, and for worse prediction accuracy R^2 decreases.

Another alternative method for error measurements is to use the mean absolute error (MAE), which gives the average of the absolute errors between the prediction and reference values:

$$\text{MAE} = \frac{\sum_n |\hat{y}_n - y_n|}{N} \tag{2.26}$$

MAE avoids squaring the values, but is still scale-dependent like RMSE. The mean absolute percentage error (MAPE) works around this by expressing MAE as a percentage error. MAE and MAPE are seen as more interpretable than RMSE-values, and as more informative since they are not weighted towards measurements with large deviations. However, it can be argued that RMSE-values are useful for sensor development, as measurements with large errors can have a disproportionate effect on the user or patient. From this viewpoint, the MAE can give an overly optimistic view of the performance of both the sensor and the learning algorithm. Several measure of errors may be reported for a dataset in order to more easily compare with other literature.

2.6.5 Spectral Pre-Processing

Spectral pre-processing encompasses all methods applied to data prior to the learning algorithm. The goal of pre-processing is to remove unwanted variations in the data that are not related to variations in analyte concentrations [146]. This includes environmental factors, drift in equipment, and so on. Such variations can affect model accuracy heavily. Pre-processing methods should ideally be applied so that the same procedure can be subsequently used on similar datasets. The two main approaches are filtering/smoothing methods, which try to reduce noise, and scatter correction methods, which try to remove e.g. baseline shifts.

Feature selection can be seen as a type of pre-processing. However, feature selection is performed quite differently to other pre-processing methods, and will therefore be described in a separate section below.

Pre-Processing Methods

Common methods for spectral filtering/smoothing include Savitzky-Golay (SG) filtering, Fourier filtering, and moving average. For SG filtering a segment size is defined, and a polynomial is fitted to each segment of the spectrum. SG filtering can be adapted to data with different noise features, as the segment size and polynomial order can be optimised. Fourier filtering is done by taking the Fourier transform of the spectra, cutting of the Fourier signal at a certain frequency, and then back-transforming the result. This method is very efficient, but there is a risk of removing informative features, or creating artefacts in the back-transformed spectrum. Moving average is a classical smoothing method where each data point

in a spectrum is replaced by the average of the adjacent data points. The number of adjacent data points used for averaging is set by the user.

Scatter effects in spectra can be divided into effects that create spectral offsets, or spectral amplification. These are not necessarily caused by scattering directly, for example spectral offsets can be a result of source drift, but the mathematical correction is the same in any case. The simplest way to correct for scatter effects is spectral differentiation by finite differences. The first derivative of the spectrum removes any offsets, and the second derivative also removes linear trends. The disadvantage is that differentiation by finite differences amplifies noise in the spectra, and this is very detrimental to the regression if the SNR is low. This can be ameliorated by filtering prior to differentiation, and SG filtering in particular is often used with differentiaton by taking the derivative of the fitted polynomial at each data point. Other methods have been designed to deal with scattering effects, including standard normal variate (SNV), multiplicative scatter correction (MSC) and extended MSC (EMSC). These methods are more commonly used in near-infrared spectroscopy, as scatter effects are more dominant due the longer pathlengths used. Simple baseline correction functions can also be used to remove offset effects.

Pre-processing methods can be used in combination, however the optimal order is not readily apparent. Various studies use different orders, and some studies have shown different orders can have positive or negative outcomes depending on the exact methods used [147]. Many studies have also found the optimal combination of pre-processing methods for one or a few datasets, but the "optimum" seems to vary between datasets, sample types, and measurement methods. The optimal combination is usually found through an exhaustive search of all possible combinations of methods, although this is very time-consuming. Other approaches such as experimental design or genetic algorithm searches have been used to search through fewer combinations with minimal loss of accuracy, but such methods are so far not extensively used [148,149]. The choice of pre-processing methods therefore remains very user-defined and to some degree subjective.

Feature Selection

As the name implies, feature selection methods are used to select a certain subset of spectral features, which are then used for further analysis [150]. Feature selection is a useful tool for analysis of spectral data for several reasons. Datasets from vibrational spectroscopy often have few samples/measurements, and many

variables (features). Many, or even most, of these variables may not have any relevant information. It has been argued that the addition of irrelevant features should not degrade a regression model. However, with enough irrelevant features, some of them will randomly correlate with other features, which complicates the model and can lead to overfitting. As experimental equipment is not perfect, some of these irrelevant features can also be noisy. Adding noisy features is also detrimental to a regression model. A high number of variables also makes the model less interpretable, and increases the computational demand for the data modelling. One goal of feature selection is therefore to remove irrelevant features, but feature selection should be used carefully, so as to not remove relevant features. As with other pre-processing methods, feature selection should also be validated with cross-validation on the training set. Feature selection methods can broadly be divided into three different categories, which are described below.

Filter methods: Features can be filtered by individually scoring them according to some requirement, e.g. how well they correlate with the response variable. This can be done directly prior to the regression model being run, and in that case the filter is independent from the model. One example of this is the Pearson correlation coefficient. Filter methods are very computationally efficient and quite robust to overfitting. However, one must set a threshold for the filter, and the initial choice is often arbitrary. Filters also tend to select redundant features, and any interactions between features are usually not taken into account.

Wrapper methods: In wrapper methods several subsets of features are generated and then searched through. The modelling accuracy is evaluated for each feature subset, and the best subset is selected. Wrapper methods are better for detecting possible interactions between variables, and can often find good subsets of features with fewer redundant variables. These methods are more computationally expensive, and with few measurements there is a bigger chance of overfitting to a suboptimal feature subset.

There are a number of ways to generate feature subsets. Forward selection starts with no features in the model, and iteratively adds the feature that reduces the model error the most. Forward selection then stops when a required number of features is obtained or a decided performance threshold is reached. Backward elimination, on the other hand, starts with all features and iteratively removes the least important ones. Sequential feature selection

combines these two, by reconsidering dropped and added variables at each step. Moving window selection looks for one or more continuous regions of features, and selects the window(s) that achieve the best modelling accuracy. Genetic algorithms start with a randomised population of feature subsets, which are then mixed and mutated over several *generations*. These different methods all have advantages and disadvantages. For example, forward selection and related methods can often get stuck in local maxima, while subsets found by genetic algorithms can be heavily affected by the initial population of feature subsets.

Embedded methods: These methods have the feature selection built into the regression model. One large class of embedded methods are the regularisation-based approaches, which includes lasso, ridge regression, and elastic net. All features in the data are included in the model, but a penalty is applied on the values of the regression coefficients. This penalty can shrink regression coefficients, and even reduce them to zero. Embedded methods perform the feature selection and regression modelling at the same time, and are less computationally expensive than wrapper methods. However, they are more difficult to interpret, as the feature selection performance can not be separated from the performance of the regression model. Embedded methods are also not applicable to all types of data, and are therefore less universal than other feature selection methods.

Chapter 3

Methods

3.1 Experimental QCL Setups

In this work, two main setup types were used based on either transmission spectroscopy or ATR spectroscopy. The main technical components were the same in these measurement configurations, including the QCL, the detector, an analog-to-digital converter card, and a control computer. The laser was a pulsed EC-QCL (Hedgehog-UT, Daylight Solutions Inc., USA) with a broad tuning range of 8.3–11 μm (1200–904 cm^{-1}) [151]. The laser had variable parameters for pulse frequency and pulse width, which were set to 100 kHz and 500 ns for most of the measurements done in this work, see Fig. 3.1. This gave a duty cycle of 5%, which was the maximum allowable before water cooling became necessary. The laser was operated with an internal temperature of 19°C for all measurements. The maximum average output power of the QCL was 22 mW at approximately 9.7 μm emission wavelength, which decreased to approximately 5–10 mW at the edges of the tuning range. The spectral linewidth of the laser was specified as <1 cm^{-1} by the manufacturer. The laser emitted linearly polarised light with a vertical orientation (100:1) according to specifications, and this was confirmed with a linear polariser.

The QCL could be run in three different measurement modes; single-wavelength, continuous wavelength sweep, or step-and-scan wavelength sweep. Measurements at single wavelengths were mainly used for initial testing and noise analysis. Full spectra were acquired with the continuous wavelength sweep, while step-and-scan sweep was not used in this work. Spectra were recorded in the range 1200–925 cm^{-1}, and the laser was tuned with a scanning speed of 275 cm^{-1}/s. Each laser scan therefore took 1 second to perform, and consisted of 100 000 laser pulses. The part of the tuning range below 925 cm^{-1} was not recorded as there

were few relevant absorption lines in that area, and the sensitivity of the detector and increased water absorption meant that the SNR was low.

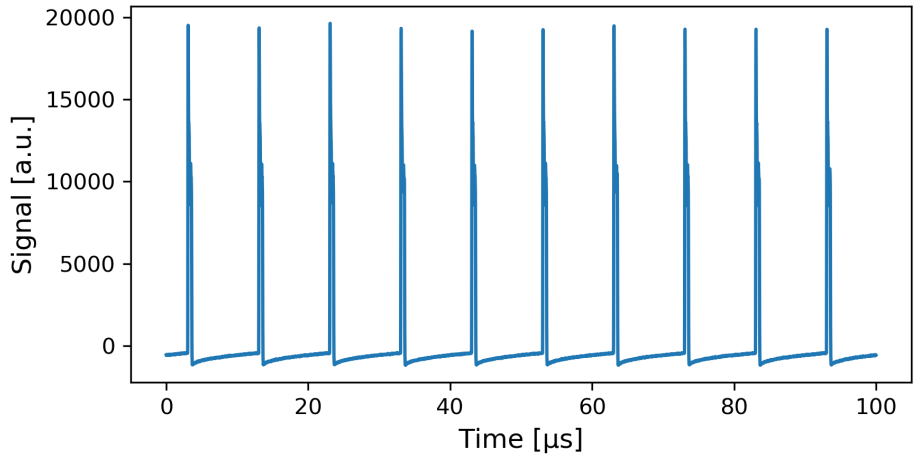

Figure 3.1: Example plot of 100 µs recorded laser pulses emitted from the EC-QCL, with a frequency of 100 kHz and a pulse width of 500 ns.

The infrared detector was a mercury cadmium telluride (MCT) detector (PCI-4TE, Vigo System S.A., Poland). MCT detectors are photoconductive detectors with a semiconductor band structure. This detector was cooled down to an internal temperature of -75.2°C with four-stage thermoelectric cooling. The detector element had an optical area of 2×2 mm, and the detectivity was 3×10^{9} cm $Hz^{1/2}$ W^{-1} at 10.6 µm.

Data Recording

The signal measured on the MCT detector was recorded with an analog-to-digital converter (ADC) card (M2p.5946-x4, Spectrum Instrumentation GmbH, Germany). This digitiser was installed on a PCIe bus on the control computer motherboard in order to enable fast data transfer. The ADC sampled data at a rate of up to 80 MS/s with a 16 bit resolution. A modified driver (C++) based on an example driver from Spectrum Instrumentation was used to control the ADC, and a GUI front-end (Python) written for this driver was used to perform measurements.

The ADC was connected to the detector via an SMB to SMA connector for the analog signal. In addition, the digitiser had input channels for digital signals, which were connected to the laser controller. The laser controller had a DB-15 connector

with 15 pins for digital I/O signals. Two of the pins connected to the ADC gave high signals when scanning from high to low wavenumbers, and for each individual laser pulse. The digital channels could be recorded simultaneously with the detector signal by lowering the resolution of the analog input. This functionality was tested, but was not used further for this work. Only the rising edge TTL at the start of each scan was used for the measurements presented, and it was used to trigger data acquisition. Each measurement consisted of 10 laser scans, which gave a total measurement time of 10 seconds. The scans were saved separately in binary files. Averaging over laser pulses and scans was done for noise reduction, as this type of pulsed QCL has significant variation in pulse intensity, specified as 3% by the manufacturer [151]. This variation was reduced to less than 0.1% by averaging, as characterised in Paper II.

The card had capability for sampling from up to four different channels at once, as long as the total sampling rate was 80 MS/s or less. The measurement setups in this work only used one channel at a time, and the sampling rate was set to the maximum of 80 MS/s as a default. Laser pulses were therefore recorded with 40 datapoints per pulse, as each pulse was 500 ns long. This sampling rate gives ample information for pulse integration, and a lower sampling rate could be sufficient for describing the pulse intensity. For future studies it will therefore be possible to sample from several measurement arms simultaneously, which will decrease the sampling rate in each arm, without infringing on the sampling quality.

Infrared Spectra

Recorded measurements from the QCL-based setups were converted into infrared spectra with a Python script. The script produced separate text files for each measured spectrum. Spectra were made by integrating each laser pulse and averaging over a set number, n, of laser pulses from the raw data. For the presented data $n = 255$, which resulted in spectra with 390 data points. The ten acquired scans were then averaged to produce a raw spectrum. These averaging processes were performed for noise reduction. Each final spectrum consisted of a background measurement (I_0) and a sample measurement (I), and absorbance spectra were calculated as $A = -\log(I/I_0)$. Demineralised water was used for the background measurements.

Optical Fibres

Two main fibre types were used in the experimental setups in this work, namely silver halide fibres and hollow-core fibres. The silver halide fibres were acquired from Art photonics GmbH (Germany), and had core diameters of 400 μm or 600 μm. These fibres had PEEK protective tubing, and were fitted with optical SMA connectors on one end. The optical loss in these fibres was approximately 0.3 dB/m, which meant a total loss of approximately 0.18 dB for the setups used here with two 30 cm long fibres. These fibres were step index and multimode, and the intensity profile of the laser after transport through the fibres was not investigated further in this work.

Some hollow-core fibres with an inner diameter of 300 μm were acquired (OKSI Fibers Inc., USA). These fibres were also fitted with SMA connectors, and had losses given as approximately 1 dB/m. Additional hollow-core fibres with 1 mm inner diameter were made at Tohoku University during a research exchange. The reflective silver layer in these fibres was made in a chemical silver-mirror reaction, where a silver solution was introduced into a capillary bundle together with a reducing agent, see Fig. 3.2. A vacuum pump was used to draw these solutions through the bundle for a set amount of time. A bundle with 7 capillaries was used in this process, so the maximum yield from each silver-mirror reaction was 7 1-metre long fibres. In total five different bundles were made with flow times of 2–12 minutes. A dielectric layer, iodide, was added as a protective inner layer to some of the fibres. These fibres were not fitted with connectors. The fabricated hollow-core fibres were more lossy than the commercially acquired fibres, with optical losses estimated as 5–6 dB/m from FTIR spectroscopy measurements. However, the large core size meant that these fibres could collect light more efficiently as out-coupling fibres. Large diameter hollow-core fibres can be acquired commercially for future studies if lower losses are necessary.

3.1.1 Transmission Setup

Measurements in the transmission setup were performed by introducing a sample in a gap between two silver halide fibres, see Fig. 3.3a. The light emitted from the source was coupled into a fibre with an optical assembly (OKSI Fibers Inc., USA). Initial measurements were done with 400 μm core diameter fibres for both in-coupling and out-coupling of light. However, this did not give optimal light

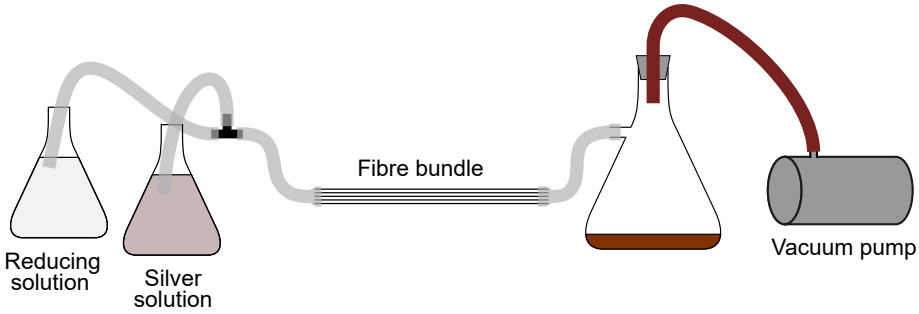

Figure 3.2: Process for silver-mirror reaction used to create hollow-core optical fibres. A silver solution and a reducing agent (glucose solution) are drawn through a capillary bundle using a vacuum pump. Silver atoms are deposited in the capillaries, forming a reflective layer.

collection, as the radiation diverged in the fibre gap. All presented measurements were therefore done with a 400 µm core fibre for in-coupling of light and a 600 µm core fibre for out-coupling. The fibres were mounted onto two 3-axis stages (Thorlabs Inc., USA), with the mounting points approximately 2 cm from the fibre gap.

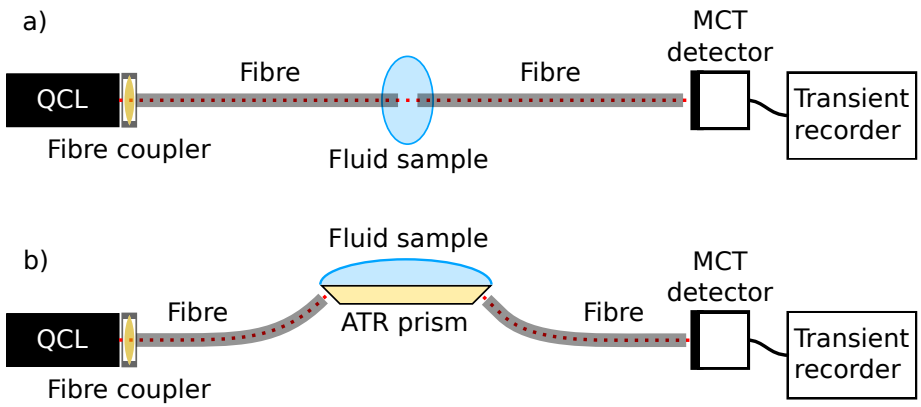

Figure 3.3: Schematic illustration of the two main measurement configurations used in this work, with a) transmission spectroscopy and b) ATR spectroscopy. Figure adapted from ref. [152].

3.1.2 ATR Setup

Silver halide fibres were used to guide light in the first ATR setup tested during this work, in Paper II [152]. A ZnSe lens was then placed directly after the ATR crystal in order to increase the light coupling efficiency. For later studies, hollow-core fibres with larger cores were used for light guiding, see Fig. 3.3b. In Paper VI the hollow-core fibres with large diameters were used for both in-coupling and out-coupling of light. The larger diameter meant that light was collected more efficiently from the prism, and the ZnSe lens was therefore not used. This simplified the alignment of the system, and the lack of a lens was not found to noticeably decrease the collected signal. Paper II and Paper VI used trapezoidal prisms as internal reflection elements (IREs), and for these studies the optical fibre ends proximal to the prisms were mounted at 45° angles. The fibres were mounted at 70° angles for the Si IREs that were used in Paper IV. The angled fibre mounts were attached to 3-axis stages for fine-adjustment of the fibre positions.

Internal Reflection Elements

The ZnS crystals used in Paper II and Paper VI were acquired commercially from Sinoptix (China). These IREs were multireflection trapezoidal prisms. Three additional crystals were made at Tohoku University, two ZnS prisms with trapezoidal dimensions and one rectangular CaF prism. These prisms were cut from larger elements with a low-speed saw (IsoMet, Buehler Ltd., USA) and the facets were polished by hand. Initial testing was done with these prisms.

Silicon (Si) wafer chips (IRUBIS GmbH, Germany) were also investigated as IREs in the QCL-based ATR setup. Hemispherical Si elements are more common as IREs, but due to the large size and the absorption properties of Si they become too opaque for spectroscopy measurements below 1400 cm^{-1}. Si wafers are typically 500 μm thick, and single-reflection measurements can therefore be performed at long wavelengths with acceptable optical loss. The Si wafers were etched on the underside with a KOH wet chemical etch, which produced V-shaped grooves. The resulting chips could be used as basic IREs. The Si IREs could be further modified on the top surface with reactive ion etching, which is a dry etching process. This created a structure with micropillars on the top surface, which functioned as a field enhancement layer. This field enhancement induced a signal enhancement in the measured spectra, which was investigated in Paper IV.

3.2 FTIR Spectroscopy

FTIR spectroscopy was used for initial measurements and comparison with the QCL-based measurements, as well as a separate study on data analysis. The photonics lab at the Department of Electronics, NTNU had an Alpha II spectrometer (Bruker Optics Inc., USA) available. This was a compact FTIR spectrometer that could be used with either a module for transmission spectroscopy, or a module for ATR spectroscopy. Only the ATR module was used for this work, and it had a single-reflection diamond IRE. This FTIR spectrometer was operated with the OPUS software (Bruker Optics Inc., USA) installed on a separate computer. The spectrometer saved data in the 4000-400 cm^{-1} spectral range. The acquired spectra were made by averaging 128 scans in the spectrometer, which gave a measurement time of about 3 minutes. An initial resolution of 2 cm^{-1} was set for the measurements, which was reduced to 1 cm^{-1} through a zero-filling factor of 2 in the Fourier transform algorithm. Background spectra were obtained approximately every 30 minutes. Spectra were saved in text files, and further analysis was done in a separate program.

A Tensor spectrometer (Tensor27, Bruker Optics Inc., USA) at Tohoku University was used for a study on data analysis of spectral data. This spectrometer had a custom-built ATR module, which has been described by Kino et al. [12]. Light emitted from the spectrometer was focussed into a hollow-core fibre, which guided the light to a ZnS prism. The light from this prism was focussed onto a liquid nitrogen-cooled infrared detector. The spectrometer was operated through the OPUS software. This spectrometer had a measurement range of 4000–500 cm^{-1}. The acquired spectra were measured with a resolution of 4 cm^{-1} and 32 spectrometer scans were averaged for each measurement. A zero-filling factor of 2 applied during the Fourier transformation brought the data point spacing down to 2 cm^{-1}.

3.3 Simulations

Light propagation was simulated in the ZnS prisms in order to ensure an integral number of reflections through the prisms. The main parameters that were investigated in these trapezoidal structures were prism height and length. Ray optics simulations were performed with Zemax OpticStudio.

Behaviour in the Si IREs was investigated with the finite element method using COMSOL Multiphysics (Sweden). The Si IREs were simplified to a two-dimensional (2D) cross section. The light source was modelled as a plane wave with an incidence angle of 41°, based on an estimation of the angle of incidence. The field strength of the evanescent field in the sample volume was integrated for both the basic and the signal-enhanced Si IREs. The enhancement factor was then calculated as the ratio of total field intensity between the two Si IRE types.

3.4 Data Analysis and Software Development

All multivariate analysis of spectral data for this thesis was done through Python programming. A software package, which we have called SpecAnalysis, was assembled to enable automation of various analysis methods. SpecAnalysis is capable of analysing data for both regression and classification, and contains many methods for spectral pre-processing and feature selection. This software has been made available on GitHub (`https://github.com/jernelv/SpecAnalysis`).

SpecAnalysis is in part based on scikit-learn [153], which is a Python tool package for machine learning. Several of the included methods were also developed in-house. The software has a graphic user interface and functionality that allows the user to test many different analysis parameters in sequence.

Chapter 4

Summary of Papers

The main application for this work was mid-infrared spectroscopy of glucose in biological fluids. The thesis itself spans across various methods for optimisation of the sensor system, measurements of synthetic aqueous solutions and biological fluids, as well as multivariate analysis of spectroscopy data. As a result, the thesis includes experimental work, simulations, as well as work on data analysis methods.

This chapter gives a brief overview and short discussion of each paper included in the thesis.

4.1 Evaluation of Optical Techniques

Paper I

A review of optical methods for continuous glucose monitoring
I.L. Jernelv, K. Milenko, S.S. Fuglerud, D.R. Hjelme, R. Ellingsen, A. Aksnes
Applied Spectroscopy Reviews, Vol. 54(7), pp. 543-572, 2019.

This work was a review of a selection of the available optical measurement methods that have been researched for continuous glucose monitoring (CGM). The idea was to evaluate several potential techniques for glucose sensing in order to make a more informed choice regarding the thesis subject. The paper first introduced background on BGL management required for diabetic patients, current electrochemical CGM systems, and some considerations such as the sensor placement. Six main optical techniques were evaluated, namely near-infrared, mid-infrared, Raman, and fluorescence spectroscopy, as well as photoacoustic sensing and optical coherence tomography. The basic principles of these methods were outlined, together with specific challenges for in vivo glucose measurements. An overview of the research status for each method was then given, and a comparative discussion was included at the end.

Prior to this publication, there were several other reviews of glucose sensor technologies suggested as alternatives to electrochemical glucose sensors. Many of these were focussed on non-invasive sensor systems, or on sensor concepts that were relatively close to realisation of a device. This review concentrated on only optical technologies regardless of intended sensor placement, and covered early-stage research in addition to more advanced sensor concepts. It was challenging to precisely compare different technologies, especially those with mainly early-stage research. Research groups were found to use different metrics to evaluate their sensor systems that were not necessarily directly comparable. Fluorescence spectroscopy had come furthest among the methods with several systems used in human trials and one system close to commercialisation.

MIR spectroscopy was seen as a measurement technique with low/medium maturity and a high development potential for biomedical applications. Tuneable laser sources with high spectral power density have only recently become available in the MIR range, and the research effort is still in the early stages. MIR spectroscopy therefore became the focus of this thesis.

4.2 Measurements of Synthetic Aqueous Solutions and System Benchmarking

Paper II

Infrared Spectroscopy with a Fiber-Coupled Quantum Cascade Laser for Attenuated Total Reflection Measurements Towards Biomedical Applications
I.L. Jernelv, K. Strøm, D.R. Hjelme, A. Aksnes
Sensors, Vol. 19(23), 5130, 2019.

In this work, we demonstrated QCL-based infrared spectroscopy with transmission and ATR sensing for synthetic aqueous solutions. The transmission configuration used a gap between optical fibres for sensing, while the ATR configuration used a multi-reflection ZnS prism as a sensing surface. Silver halide fibres were used to guide the laser radiation in both sensing configurations.

Laser noise was characterised based on averaging over laser pulses and laser scans. A low relative standard deviation of the signal was found (0.07%) for settings that resulted in a measurement time of only 10 seconds. The solutions that were measured contained glucose, as well as albumin, lactate, and urea as interfering analytes. Sets of the aqueous solutions were measured in both transmission and ATR configurations. A ZnS prism with 5 reflections on the top surface was used for the ATR measurements, and the prism dimensions were determined based on ray-tracing simulations. The measured spectra were investigated with multivariate analysis, and it was demonstrated that both glucose and albumin concentrations could be accurately determined in both measurement configurations. Glucose concentrations were determined with RMSECV$<$20 mg/dL for both transmission and ATR measurements.

This benchmarking and characterisation showed that our system was stable and that measurements with low noise level could be acquired. Simultaneous determination of several analytes in aqueous solutions was also promising for further studies.

Paper III

Mid-infrared spectroscopy with a fiber-coupled tuneable quantum cascade laser for glucose sensing

I.L. Jernelv, K. Strøm, D.R. Hjelme, A. Aksnes

Proceedings of SPIE 11233, Optical Fibers and Sensors for Medical Diagnostics and Treatment Applications XX, 1123311, 2020.

This paper is a continuation of the work in Paper II. A fibre-coupled QCL spectroscopy setup was used to investigate more complex aqueous solutions in transmission mode. Lower concentrations of glucose were used than in Paper I, and fructose was added as an additional interfering analyte. A thorough characterisation of the optimal transmission pathlength was demonstrated.

Similar to Brandstetter et al. [30], we showed that the optimal pathlength was longer than the theoretical optimum, as the theoretical calculation does not account for the source intensity. We also found a longer optimal pathlength than in ref. [30] at 200 μm, and this can be attributed to the higher power of the QCL used in our study. The SNR did not improve as much as expected, but this might be a consequence of the fibre-coupled sensing and an introduction of mode noise or interference. The relatively long pathlength is advantageous because of the increased absorbance signal, and because the transmission gap becomes less prone to clogging.

As in Paper II, the concentrations of glucose and the other analytes could be determined accurately at the same time with PLS regression. The prediction accuracies for glucose and albumin were improved by approximately 20% with the use of a CNN for multivariate analysis. For glucose, the RMSECV was 10.7 mg/dL with PLS regression and 8.3 mg/dL with CNN with a concentration range of 0–600 mg/dL. This study demonstrated a robust characterisation of our QCL setup in transmission mode, and an in-depth analysis of complex aqueous solutions.

4.3 Signal Enhancement

Paper IV

Signal enhancement in microstructured silicon attenuated total reflection elements with quantum cascade laser-based spectroscopy
I.L. Jernelv, J. Høvik, D.R. Hjelme, A. Aksnes
Proceedings of SPIE 11359, Biomedical Spectroscopy, Microscopy, and Imaging, 113590A, 2020.

In this study, internal reflection elements (IREs) based on silicon (Si) wafer chips were investigated for potential signal enhancement in ATR spectroscopy. The Si IREs either had a flat top surface for standard ATR spectroscopy, or a top surface with micropillars for signal enhancement. The micropillars act as an effective medium layer in the IRE, and the signal enhancement arises from an interference effect and an increased field strength between the pillars. A comparison was also done with an FTIR spectrometer using a single-reflection diamond IRE. Measurements of aqueous glucose solutions were used to evaluate the performance of the different IRE types.

The absorbance signal was enhanced by up to a factor of 3.8 in the micropillar IREs. The highest effective signal enhancement factor was a bit lower at 3.1, due to some simultaneous increase in the noise level. The behaviour of these two prototype microstructured IREs was modelled accurately through simulations using the finite element method (FEM). One signal-enhancement (SE) IRE gave a constant enhancement effect over the entire available wavelength region. The second SE IRE had no enhancement above 1060 cm^{-1}, and thus the micropillar geometry did not act as an effective enhancement layer for shorter wavelengths. The Si IREs, including the flat-topped versions, were all found to have lower limits of quantification than the diamond IRE in the FTIR spectrometer.

This study showed an effective signal enhancement in single-reflection IREs together with improved sensitivity in measurements of glucose solutions. Increased sensitivity in ATR spectroscopy is usually obtained with multi-reflection prisms, which are big, expensive, and difficult to integrate into miniaturised sensors. These single-reflection IREs could potentially be placed on a fibre tip for remote sensing in reflection mode. Large-scale fabrication could also make them cheap enough for single-use applications in biomedical sensing.

4.4 Data Analysis

Paper V

Convolutional neural networks for classification and regression analysis of one-dimensional spectral data
I.L. Jernelv, D.R. Hjelme, Y. Matsuura, A. Aksnes
Preprint published on arxiv.org, arXiv ID 2005.07530, 2020.

Improvements in data analysis processes for infrared spectroscopy is a large research subject. This work represented an in-depth study of the applicability of convolutional neural networks (CNNs) on vibrational spectroscopy data, and the effect of spectral pretreatment on spectral data prior to CNN compared to other machine learning methods. Both classification and regression methods were investigated. Various open datasets were included in the analysis, in addition to one dataset created for this study. These datasets used either MIR, NIR, or Raman spectroscopy for data acquisition and encompassed food items, pharmaceutical tablets, and synthetic aqueous solutions.

It was found that CNNs usually outperformed other methods when applied to raw data, although not in all cases. Prediction accuracy typically improved when pre-processing or feature selection methods were applied to the data, both for CNN and other methods. Use of pretreatment also decreased the advantage that CNN had over most other methods.

Finding the best spectral pretreatment is time-consuming, and there is no optimal process that is valid for every dataset. CNNs have been suggested as a method to achieve better prediction accuracy without use of other spectral pretreatment. However, this ignores the large parameter space available when training a CNN, including parameters such as the number of layers, layer size, kernel size, etc. As a result, finding the optimal CNN parameters can be as much work as finding the optimal pretreatment process. The effect of these CNN parameters may also be less intuitive than other pretreatment methods; e.g. it is not obvious why a certain kernel size would work better for one dataset than another, while the effect of a filter is more tangible.

This study demonstrated that CNNs can be used to analyse one-dimensional spectral data for both classification and regression purposes. However, the benefit of CNN decreases with proper use of pre-processing and feature selection methods.

4.5 Characterisation of Biological Fluids

Paper VI

Infrared measurements of glucose in peritoneal fluid with a tuneable quantum cascade laser

I.L. Jernelv, D.R. Hjelme, A. Aksnes

Biomedical Optics Express, Vol. 11(7), pp. 3818-3829, 2020.

In this work, fluid samples acquired from animal experiments were measured in QCL-based spectroscopy setups in order to test sensing performance on real-life samples. Peritoneal fluid and blood plasma samples from altogether six different pigs were measured in both ATR and transmission configurations. Highly accurate predictions of glucose levels were made for both measurement configurations, with mean absolute percentage error (MAPE) of 12.2% in the ATR configuration and 8.7% in the transmission configuration. Concentrations in the blood plasma samples were predicted with even better accuracy (MAPE$<$8%), which can partially be attributed to the smaller dataset.

Spectra from the peritoneal fluid samples were also compared to the blood plasma spectra. The general spectral shapes were found to be quite similar, although the blood plasma samples had an overall higher absorbance. The optical measurements, together with measurements of the albumin and total protein concentrations in a selection of the samples, supported the view that peritoneal fluid can be seen as ultrafiltered plasma with lower concentration levels of major constituents. Optical spectroscopy measurements may therefore be more straightforward in peritoneal fluid, compared to blood plasma or ISF. This was also in part suggested by the regression analysis, as PLS models with 6 LVs were used for blood plasma, while only 5 LVs were necessary for the peritoneal fluid data.

This study demonstrated optical glucose detection at physiological concentrations in peritoneal fluid for the first time. The QCL-based sensing approach is reagent-free with a measurement time of only 10 s, and there are several avenues for setup miniaturisation. The ATR configuration in particular lends itself well for point-of-care monitoring, as reflection-mode sensing can be realised with an IRE integrated on a fibre tip. A portable sensor will likely require smaller single-wavelength lasers that are less sensitive to vibrations.

Chapter 5
Conclusions

The papers included in this thesis cover several aspects of QCL-based mid-infrared spectroscopy. The main intended application was continuous glucose monitoring. A sensor concept was realised through experimental verification of QCL-based infrared spectroscopy setups in ATR and transmission configurations, with multivariate analysis of the resulting spectral data.

Current literature was reviewed in Paper I, which gave a perspective on various optical technologies that have been used for glucose measurements. Based on this review, MIR spectroscopy was evaluated as a technology with low/medium maturity for portable and miniaturised sensors, and high potential for sensor development. Laser-based spectroscopy in particular has the possibility for fast and accurate measurements in a POC sensor. We therefore developed and built a fibre-coupled QCL-based spectroscopy system, and characterised and benchmarked this system on aqueous solutions in Paper II and Paper III. In these studies, glucose concentrations were determined with RMSECV$<$20 mg/dL in the ATR configuration and RMSECV$<$10 mg/dL in transmission. Subsequently, peritoneal fluid from pigs used in animal trials was investigated in Paper VI. It was found that peritoneal fluid had lower absorbance than blood plasma, and thus may be a less complex fluid for optical measurements. Predictions of the glucose concentrations in peritoneal fluid were demonstrated with with 8.7% and 12.2% MAPE in transmission and ATR configurations, respectively. This is well within the requirement for glucose sensors, and is on par or better than commercially available electrochemical CGM devices. Electrochemical sensors have a typical measurement time of 5 minutes and lag behind the BGL by 5-15 minutes, while our results were achieved with a measurement time of only 10 seconds, and this fast measurement time can be leveraged to provide better glucose control. Further miniaturisation is needed for a practical POC sensor, and single-reflection IREs with signal enhancement based on an interference effect were investigated in Paper IV as a means to achieve

a smaller sensing area. An enhancement of the SNR up to a factor of 3.1 was demonstrated.

The implemented regression methods were found to be highly accurate for prediction of glucose concentrations in both synthetic aqueous solutions and biological fluids from animal experiments. The effects of spectral pre-processing and different methods for concentration prediction were shown on the datasets that were measured in the QCL-based setups. In addition, a separate study was performed in Paper V in order to investigate spectral pre-processing and feature selection methods on different publicly available datasets acquired with vibrational spectroscopy, both for regression and classification analysis. This work concentrated on convolutional neural networks (CNNs) as a way to reduce the need for pretreatment prior to analysis.

To summarise, this doctoral study has shown an in-depth investigation of spectroscopy-based measurements of glucose in peritoneal fluid, which has demonstrated the potential for optical glucose monitoring in the peritoneal cavity.

Outlook

The papers published have demonstrated an ATR sensing concept with a fibre-coupled QCL, which is an important step towards an in vivo glucose sensor based on mid-infrared spectroscopy. The work should be continued towards realisation of in vivo sensing in the peritoneal cavity of an animal model. Measurements in an animal model in transmission mode will also be possible, but is not necessarily conducive to a practical device. Transmission gaps are prone to clogging, and there are mechanical challenges involved in keeping the fibre ends aligned. Sensing in reflection mode is potentially more stable, and the input fibre can more easily be used simultaneously as an output fibre in an ATR probe. Further work on the data analysis methods should then be performed in order to confirm if a smaller subset of wavelengths can be used to accurately identify and measure the glucose concentration in a clinical setting.

The long-term goal of these developments is to facilitate rapid QCL-based spectroscopy of glucose in the peritoneal cavity. Once accurate glucose sensing is possible in humans with minimal delay, a combination with insulin infusions and a control system will enable a true artificial pancreas.

References

[1] K. E. Thorpe, L. Allen, and P. Joski. The Role of Chronic Disease, Obesity, and Improved Treatment and Detection in Accounting for the Rise in Healthcare Spending Between 1987 and 2011. *Applied Health Economics and Health Policy*, 13(4):381–387, 2015.

[2] D. Howdon and N. Rice. Health care expenditures, age, proximity to death and morbidity: Implications for an ageing population. *Journal of Health Economics*, 57:60–74, 2018.

[3] P. Thavendiranathan, A. Bagai, A. Ebidia, A. S. Detsky, and N. K. Choudhry. Do Blood Tests Cause Anemia in Hospitalized Patients? The Effect of Diagnostic Phlebotomy on Hemoglobin and Hematocrit Levels. *Journal of General Internal Medicine*, 20(6):520–524, 2005.

[4] C. G. Koch, L. Li, Z. Sun, E. D. Hixson, A. Tang, S. C. Phillips, E. H. Blackstone, and J. M. Henderson. Hospital-Acquired Anemia: Prevalence, Outcomes, and Healthcare Implications. *Journal of Hospital Medicine*, 8(9):506–512, 2013.

[5] A. P. F. Turner. Biosensors: sense and sensibility. *Chem. Soc. Rev.*, 42(8):3184–3196, 2013.

[6] I. D. B. Rennie, H. Keen, and A. Southon. A Rapid Enzyme-Strip Method for Estimating Blood-Sugar. *The Lancet*, 284(7365):884–886, 1964.

[7] L. Dye, M. Mansfield, N. Lasikiewicz, L. Mahawish, R. Schnell, D. Talbot, H. Chauhan, F. Croden, and C. Lawton. Correspondence of continuous interstitial glucose measurement against arterialised and capillary glucose following an oral glucose tolerance test in healthy volunteers. *British Journal of Nutrition*, 103(1):134–140, 2010.

[8] M. Sinha, K. M. McKeon, S. Parker, L. G. Goergen, H. Zheng, F. H. El-Khatib, and S. J. Russell. A Comparison of Time Delay in Three Continuous Glucose Monitors for Adolescents and Adults. *Journal of Diabetes Science and Technology*, 11(6):1132–1137, 2017.

[9] M. Brandstetter, T. Sumalowitsch, A. Genner, A. E. Posch, C. Herwig, A. Drolz, V. Fuhrmann, T. Perkmann, and B. Lendl. Reagent-free monitoring of multiple clinically relevant parameters in human blood plasma using a mid-infrared quantum cascade laser based sensor system. *Analyst*, 138(14):4022–4028, 2013.

[10] T. Vahlsing, S. Delbeck, J. Budde, D. Ihrig, S. Leonhardt, and H. M. Heise. Reliable glucose monitoring by ex-vivo blood micro-dialysis and infrared spectrometry for patients in critical care. In *Proc. SPIE, Optical Diagnostics and Sensing XVII: Toward Point-of-Care Diagnostics*, volume 10072, 2017.

[11] S. Liakat, K. A. Bors, L. Xu, C. M. Woods, J. Doyle, and C. F. Gmachl. Noninvasive in vivo glucose sensing on human subject using mid-infrared light. *Biomed. Opt. Express*, 5(7):2397–2404, 2014.

[12] S. Kino, S. Omori, T. Katagiri, and Y. Matsuura. Hollow optical-fiber based infrared spectroscopy for measurement of blood glucose level by using multi-reflection prism. *Biomedical Optics Express*, 7(2):701–708, 2016.

[13] D. R. Burnett, L. M. Huyett, H. C. Zisser, F. J. Doyle, and B. D. Mensh. Glucose sensing in the peritoneal space offers faster kinetics than sensing in the subcutaneous space. *Diabetes*, 63(7):2498–2505, 2014.

[14] O. Bibikova, J. Haas, Á. I. López-Lorente, A. Popov, M. Kinnunen, Y. Ryabchikov, A. Kabashin, I. Meglinski, and B. Mizaikoff. Surface enhanced infrared absorption spectroscopy based on gold nanostars and spherical nanoparticles. *Analytica Chimica Acta*, 990:141–149, 2017.

[15] L. Sykora, A. Müller, A. Kondratiev, A. Roth, V. Mozin, A. Fehr, and G. Zörnack. Silicon ATR crystal with subwavelength structures optimized for blood analysis. In *Proc. SPIE, Optical Fibers and Sensors for Medical Diagnostics and Treatment Applications XIX*, volume 10872, 2019.

[16] M. Quinten. *Optical Properties of Nanoparticle Systems: Mie and beyond*. John Wiley & Sons, Inc, Weinheim, Germany, 2010.

[17] R. W. Boyd. *Nonlinear Optics*. Academic Press, Burlington, MA, 2019.

[18] B. E. A. Saleh and M. C. Teich. *Fundamentals of Photonics*. John Wiley & Sons, Inc, 2007.

[19] C. Kittel. *Introduction to Solid State Physics (Eight Edition)*. John Wiley & Sons, Ltd, Danvers, MA, 2005.

[20] L. V. Wang and H. Wu. *Biomedical Optics: Principles and Imaging*. John Wiley & Sons, Ltd, Hoboken, New Jersey, 2007.

[21] F. K. Tittel, D. Richter, and A. Fried. Mid-infrared laser applications in spectroscopy. In *Solid-state mid-infrared laser sources*, pages 458–529. Springer, 2003.

[22] BS ISO 20473:2007. Optics and photonics. Spectral bands. Standard, International Organization for Standardization, Geneva, CH, 2007.

[23] B. H. Stuart. *Infrared Spectroscopy: Fundamentals and Applications*. John Wiley & Sons, 2004.

[24] J. E. Bertie and Z. Lan. Infrared Intensities of Liquids XX: The Intensity of the OH Stretching Band of Liquid Water Revisited, and the Best Current Values of the Optical Constants of $H_2O(1)$ at 25°C Between 15,000 and 1 cm^{-1}. *Applied Spectroscopy*, 50(8):1047–1057, 1996.

[25] J.-J. Max and C. Chapados. Glucose And Fructose Hydrates in Aqueous Solutions by IR Spectroscopy. *J. Phys. Chem.*, 111:2679–2689, 2007.

[26] H. Buiteveld, J. H. M. Hakvoort, and M. Donze. Optical properties of pure water. In *Proc. SPIE, Ocean Optics XII*, volume 2258, pages 174–183, 1994.

[27] R. Cole. Optimum optical density in spectrophotometry. *Journal of the Optical Society of America*, 41(1):38–40, 1951.

[28] H. L. Mark and P. R. Griffiths. Analysis of Noise in Fourier Transform Infrared Spectra. *Applied Spectroscopy*, 56(5):633–639, 2002.

[29] P. S. Jensen and J. Bak. Near-Infrared Transmission Spectroscopy of Aqueous Solutions: Influence of Optical Pathlength on Signal-to-Noise Ratio. *Applied Spectroscopy*, 56(12):1600–1606, 2002.

[30] M. Brandstetter, L. Volgger, A. Genner, C. Jungbauer, and B. Lendl. Direct determination of glucose, lactate and triglycerides in blood serum by a tunable quantum cascade laser-based mid-IR sensor. *Applied Physics B*, 110(2):233–239, 2013.

[31] I. L. Jernelv, K. Strøm, D. R. Hjelme, and A. Aksnes. Mid-infrared spectroscopy with a fiber-coupled tuneable quantum cascade laser for glucose sensing. In *Proc. SPIE, Optical Fibers and Sensors for Medical Diagnostics and Treatment Applications XX*, volume 11233, 2020.

[32] C. Vigano, J. M. Ruysschaert, and E. Goormaghtigh. Sensor applications of attenuated total reflection infrared spectroscopy. *Talanta*, 65(5):1132–1142, 2005.

[33] N. J. Harrick and F. K. du Pré. Effective Thickness of Bulk Materials and of Thin Films for Internal Reflection Spectroscopy. *Applied Optics*, 5(11):1739, 1966.

[34] L. A. Averett, P. R. Griffiths, and K. Nishikida. Effective path length in attenuated total reflection spectroscopy. *Analytical Chemistry*, 80(8):3045–3049, 2008.

[35] P. R. Griffiths and J. A. De Haseth. *Fourier Transform Infrared Spectrometry*. John Wiley & Sons, Inc, 2nd edition, 2007.

[36] N. Punjabi, J. Satija, and S. Mukherji. Evanescent Wave Absorption Based Fiber-Optic Sensor - Cascading of Bend and Tapered Geometry for Enhanced Sensitivity. In A. Mason, S. Mukhopadhyay, and K. Jayasundera, editors, *Sensing Technology: Current Status and Future Trends III. Smart Sensors, Measurement and Instrumentation*, pages 25–45. Springer International Publishing, 2015.

[37] S. Delbeck, L. Küpper, and H. M. Heise. Applications of tapered flat silver halide fiber elements for infrared biospectroscopy with aspects of optical stability and biocompatibility. In *Proc. SPIE, Optical Fibers and Sensors for Medical Diagnostics and Treatment Applications XVIII*, volume 10488, 2018.

[38] P. Wägli, Y. C. Chang, A. Homsy, L. Hvozdara, H. P. Herzig, and N. F. De Rooij. Microfluidic droplet-based liquid-liquid extraction and on-chip IR spectroscopy detection of cocaine in human saliva. *Analytical Chemistry*, 85(15):7558–7565, 2013.

[39] M. Sieger, J. Haas, M. Jetter, P. Michler, M. Godejohann, and B. Mizaikoff. Mid-Infrared Spectroscopy Platform Based on GaAs/AlGaAs Thin-Film Waveguides and Quantum Cascade Lasers. *Analytical Chemistry*, 88(5):2558–2562, 2016.

[40] M. Vlk, V. Mittal, G. S. Murugan, and J. Jágerská. Suspended Tantalum Pentoxide Rib Waveguides for Laser Absorption Spectroscopy. In *The European Conference on Lasers and Electro-Optics*, 2019.

[41] A. Wilk, J. C. Carter, M. Chrisp, A. M. Manuel, P. Mirkarimi, J. B. Alameda, and B. Mizaikoff. Substrate-integrated hollow waveguides: A new level of integration in mid-infrared gas sensing. *Analytical Chemistry*, 85(23):11205–11210, 2013.

[42] M Osawa. Surface-Enhanced Infrared Absorption. In S. Kawata, editor, *Near-Field Optics and Surface Plasmon Polaritons. Topics in Applied Physics*. Springer, Berlin, Heidelberg, 2001.

[43] Ó. Esteban, A. González-Cano, B. Mizaikoff, N. Díaz-Herrera, and M.-C. Navarrete. Generation of Surface Plasmons at Waveguide Surfaces in the Mid-Infrared Region. *Plasmonics*, 7(4):647–652, 2012.

[44] L. V. Brown, X. Yang, K. Zhao, B. Y. Zheng, P. Nordlander, and N. J. Halas. Fan-Shaped Gold Nanoantennas above Reflective Substrates for Surface-Enhanced Infrared Absorption (SEIRA). *Nano Letters*, 15(2):1272–1280, 2015.

[45] Y.-B. Chen. Development of mid-infrared surface plasmon resonance-based sensors with highly-doped silicon for biomedical and chemical applications. *Optics Express*, 17(5):3130–3140, 2009.

[46] Á. I. López-Lorente, J. Izquierdo, C. Kranz, and B. Mizaikoff. Boron-doped diamond modified with gold nanoparticles for the characterization of bovine serum albumin protein. *Vibrational Spectroscopy*, 91:147–156, 2017.

[47] J. Haas, A. Müller, L. Sykora, and B. Mizaikoff. Analytical performance of μ-groove silicon attenuated total reflection waveguides. *Analyst*, 144(10):3398–3404, 2019.

[48] F. Berz. On a quarter wave light condenser. *British Journal of Applied Physics*, 16(11):1733–1738, 1965.

[49] P. Huber-Wälchli and Hs. H. Günthard. Interference Enhanced Attenuated Total Reflection (IEATR). A new technique for i.r. matrix spectroscopy with high sensitivity. *Spectrochimica Acta Part A: Molecular Spectroscopy*, 34(12):1253–1262, 1978.

[50] S. Colburn, A. Zhan, and A. Majumdar. Tunable metasurfaces via subwavelength phase shifters with uniform amplitude. *Scientific Reports*, 7:40174, 2017.

[51] C. Buzea, I. I. Pacheco, and K. Robbie. Nanomaterials and nanoparticles: Sources and toxicity. *Biointerphases*, 2(4):MR17–MR71, 2007.

[52] P. V. Asharani, Y. L. Wu, Z. Gong, and S. Valiyaveettil. Toxicity of silver nanoparticles in zebrafish models. *Nanotechnology*, 19(25):255102, 2008.

[53] M. Razeghi. Semiconductor Lasers. In *Fundamentals of Solid State Engineering*. Springer, Boston, MA, 2006.

[54] P. Unger. *High-Power Diode Lasers*. Springer, Berlin, Heidelberg, 2007.

[55] J. Faist. *Quantum Cascade Lasers*. OUP Oxford, 2013.

[56] C. Gmachl, F. Capasso, D. L. Sivco, and A. Y. Cho. Recent progress in quantum cascade lasers and applications. *Reports on Progress in Physics*, 64(11):1533–1601, 2001.

[57] A. Lyakh, M. Suttinger, R. Go, P. Figueiredo, and A. Todi. 5.6 μm quantum cascade lasers based on a two-material active region composition with a room temperature wall-plug efficiency exceeding 28%. *Applied Physics Letters*, 109(12):121109, 2016.

[58] Y. Bai, N. Bandyopadhyay, S. Tsao, S. Slivken, and M. Razeghi. Room temperature quantum cascade lasers with 27% wall plug efficiency. *Applied Physics Letters*, 98(18), 2011.

[59] J. Faist, F. Capasso, D. L. Sivco, C. Sirtori, A. L. Hutchinson, and A. Y. Cho. Quantum Cascade Laser. *Science*, 264(5158):553–556, 1994.

[60] R. F. Kazarinov and R. A. Suris. Possibility of the amplification of electromagnetic waves in a semiconductor with a superlattices. *Sov. Phys. Semicond.*, 7:707–709, 1971.

[61] R. Q. Yang. Infrared laser based on intersubband transitions in quantum wells. *Superlattices and Microstructures*, 17(1):77–83, 1995.

[62] M. Kim, C. L. Canedy, W. W. Bewley, C. S. Kim, J. R. Lindle, J. Abell, I. Vurgaftman, and J. R. Meyer. Interband cascade laser emitting at λ=3.75 μm in continuous wave above room temperature. *Applied Physics Letters*, 92(19):191110, 2008.

[63] W. W. Bewley, C. L. Canedy, C. S. Kim, M. Kim, C. D. Merritt, J. Abell, I. Vurgaftman, and J. R. Meyer. Continuous-wave interband cascade lasers operating above room temperature at λ = 4.7-5.6 μm. *Optics Express*, 20(3):3235–3240, 2012.

[64] A. Schliesser, N. Picqué, and T. W. Hänsch. Mid-infrared frequency combs. *Nature Photonics*, 6(7):440–449, 2012.

[65] F. Adler, P. Masłowski, A. Foltynowicz, K. C. Cossel, T. C. Briles, I. Hartl, and J. Ye. Mid-infrared Fourier transform spectroscopy with a broadband frequency comb. *Optics Express*, 18(21):21861, 2010.

[66] A. V. Muraviev, V. O. Smolski, Z. E. Loparo, and K. L. Vodopyanov. Massively parallel sensing of trace molecules and their isotopologues with broadband subharmonic mid-infrared frequency combs. *Nature Photonics*, 12(4):209–214, 2018.

[67] J. Faist, G. Villares, G. Scalari, M. Rösch, C. Bonzon, A. Hugi, and M. Beck. Quantum Cascade Laser Frequency Combs. *Nanophotonics*, 5(2):272–291, 2016.

[68] G. Scalari, J. Faist, and N. Picqué. On-chip mid-infrared and THz frequency combs for spectroscopy. *Applied Physics Letters*, 114(15):150401, 2019.

[69] J. Kuligowski, G. Quintás, and B. Lendl. High performance liquid chromatography with on-line dual quantum cascade laser detection for the determination of carbohydrates, alcohols and organic acids in wine and grape juice. *Applied Physics B: Lasers and Optics*, 99(4):833–840, 2010.

[70] Y. Wang, M. G. Soskind, W. Wang, and G. Wysocki. High-resolution multi-heterodyne spectroscopy based on Fabry-Perot quantum cascade lasers. *Applied Physics Letters*, 104(3):031114, 2014.

[71] M. Jahjah, W. Ren, P. Stefański, R. Lewicki, J. Zhang, W. Jiang, J. Tarka, and F. K. Tittel. A compact QCL based methane and nitrous oxide sensor for environmental and medical applications. *Analyst*, 139(9):2065–2069, 2014.

[72] F. Kapsalidis, M. Shahmohammadi, M. J. Süess, J. M. Wolf, E. Gini, M. Beck, M. Hundt, B. Tuzson, L. Emmenegger, and J. Faist. Dual-wavelength DFB quantum cascade lasers: sources for multi-species trace gas spectroscopy. *Applied Physics B: Lasers and Optics*, 124(6):107, 2018.

[73] P. Rauter and F. Capasso. Multi-wavelength quantum cascade laser arrays. *Laser and Photonics Reviews*, 9(5):452–477, 2015.

[74] A. Hugi, R. Maulini, and J. Faist. External cavity quantum cascade laser. *Semiconductor Science and Technology*, 25(8):083001, 2010.

[75] G. Ramer, A. Balbekova, A. Schwaighofer, and B. Lendl. Method for Time-Resolved Monitoring of a Solid State Biological Film Using Photothermal Infrared Nanoscopy on the Example of Poly-L-lysine. *Analytical Chemistry*, 87(8):4415–4420, 2015.

[76] K. Yeh, S. Kenkel, J. N. Liu, and R. Bhargava. Fast Infrared Chemical Imaging with a Quantum Cascade Laser. *Analytical Chemistry*, 87(1):485–493, 2015.

[77] M. Grafen, K. Nalpantidis, A. Ostendorf, D. Ihrig, and H. M. Heise. Characterization of a multi-module tunable EC-QCL system for mid-infrared biofluid spectroscopy for hospital use and personalized diabetes technology. In *Proc. SPIE, Optical Diagnostics and Sensing XVI: Toward Point-of-Care Diagnostics*, volume 9715, 2016.

[78] G. Wysocki, R. Lewicki, R. F. Curl, F. K. Tittel, L. Diehl, F. Capasso, M. Troccoli, G. Hofler, D. Bour, S. Corzine, R. Maulini, M. Giovannini, and J. Faist. Widely tunable mode-hop free external cavity quantum cascade lasers for high resolution spectroscopy and chemical sensing. *Applied Physics B: Lasers and Optics*, 92(3):305–311, 2008.

[79] R. Ghorbani and F. M. Schmidt. Real-time breath gas analysis of CO and CO_2 using an EC-QCL. *Applied Physics B: Lasers and Optics*, 123(5):144, 2017.

[80] Vigo System S.A. PCI-4TE detector. `https://vigo.com.pl/produkty/pci-4te/`. Accessed: 2020-05-09.

[81] C. Downs and T. E. Vandervelde. Progress in infrared photodetectors since 2000. *Sensors*, 13(4):5054–5098, 2013.

[82] W. A. Gambling. The Rise and Rise of Optical Fibers. *IEEE Journal on Selected Topics in Quantum Electronics*, 6(6):1084–1093, 2000.

[83] M. F. Churbanov, G. E. Snopatin, V. S. Shiryaev, V. G. Plotnichenko, and E. M. Dianov. Recent advances in preparation of high-purity glasses based on arsenic chalcogenides for fiber optics. *Journal of Non-Crystalline Solids*, 357(11-13):2352–2357, 2011.

[84] P. Lucas, Z. Yang, M. K. Fah, T. Luo, S. Jiang, C. Boussard-Pledel, M.-L. Anne, and B. Bureau. Telluride glasses for far infrared photonic applications. *Optical Materials Express*, 3(8):1049–1058, 2013.

[85] B. Bureau, C. Boussard, S. Cui, R. Chahal, M. L. Anne, V. Nazabal, O. Sire, O. Loréal, P. Lucas, V. Monbet, J.-L. Doualan, P. Camy, H. Tariel, F. Charpentier, L. Quetel, J.-L. Adam, and J. Lucas. Chalcogenide optical fibers for mid-infrared sensing. *Optical Engineering*, 53(2):027101, 2014.

[86] Z. Tang, V. S. Shiryaev, D. Furniss, L. Sojka, S. Sujecki, T. M. Benson, A. B. Seddon, and M. F. Churbanov. Low loss Ge-As-Se chalcogenide glass fiber, fabricated using extruded preform, for mid-infrared photonics. *Optical Materials Express*, 5(8):1722–1737, 2015.

[87] G. E. Snopatin, M. F. Churbanov, A. A. Pushkin, V. V. Gerasimenko, E. M. Dianov, and V. G. Plotnichenko. High purity arsenic-sulfide glasses and fibers with minimum attenuation of 12 dB/km. *Optoelectronics and Advanced Materials - Rapid Communications*, 3(7):669–671, 2009.

[88] N. Barkay, A. Levite, F. Moser, and A. Katzir. Mechanical properties of mixed silver-halide crystals and polycrystalline optical fibers. *Journal of Applied Physics*, 64(10):5256–5258, 1988.

[89] J. A. Harrington. A Review of IR Transmitting, Hollow Waveguides. *Fiber and Integrated Optics*, 19(3):211–227, 2000.

[90] P. Patimisco, V. Spagnolo, M. S. Vitiello, G. Scamarcio, C. M. Bledt, and J. A. Harrington. Low-Loss Hollow Waveguide Fibers for Mid-Infrared Quantum Cascade Laser Sensing Applications. *Sensors*, 13(1):1329–1340, 2013.

[91] T. Battelino, I. Conget, B. Olsen, I. Schütz-Fuhrmann, E. Hommel, R. Hoogma, U. Schierloh, N. Sulli, and J. Bolinder. The use and efficacy of continuous glucose monitoring in type 1 diabetes treated with insulin pump therapy: a randomised controlled trial. *Diabetologia*, 55(12):3155–3162, 2012.

[92] B. M. Frier. Morbidity of hypoglycemia in type 1 diabetes. *Diabetes Research and Clinical Practice*, 65S:S47–S52, 2004.

[93] D. M. Nathan. Long-Term Complications of Diabetes Mellitus. *New England Journal of Medicine*, 328(23):1676–1685, 1993.

[94] J. Wang. Electrochemical glucose biosensors. *Chem. Rev.*, 108(2):814–825, 2008.

[95] A. E. Minder, D. Albrecht, J. Schäfer, and H. Zulewski. Frequency of blood glucose testing in well educated patients with diabetes mellitus type 1: How often is enough? *Diabetes Research and Clinical Practice*, 101(1):57–61, 2013.

[96] C. Cobelli, E. Renard, and B. Kovatchev. Artificial Pancreas: Past, Present, Future. *Diabetes*, 60(11):2672–2682, 2011.

[97] S. C. Christiansen, A. L. Fougner, Ø. Stavdahl, K. Kölle, R. Ellingsen, and S. M. Carlsen. A Review of the Current Challenges Associated with the Development of an Artificial Pancreas by a Double Subcutaneous Approach. *Diabetes Therapy*, 8(3):489–506, 2017.

[98] J. Moyer, D. Wilson, I. Finkelshtein, B. Wong, and R. Potts. Correlation Between Sweat Glucose and Blood Glucose in Subjects with Diabetes. *Diabetes Technology & Therapeutics*, 14(5):398–402, 2012.

[99] J. T. Baca, D. N. Finegold, and S. A. Asher. Tear Glucose Analysis for the Noninvasive Detection and Monitoring of Diabetes Mellitus. *The Ocular Surface*, 5(4):280–293, 2007.

[100] W. Zhang, Y. Du, and M. L. Wang. Noninvasive glucose monitoring using saliva nano-biosensor. *Sensing and Bio-Sensing Research*, 4:23–29, 2015.

[101] S. K. Vashist. Non-invasive glucose monitoring technology in diabetes management: A review. *Analytica Chimica Acta*, 750:16–27, 2012.

[102] The Diabetes Research in Children Network (DirectNet) Study Group. A Randomized Multicenter Trial Comparing the GlucoWatch Biographer with Standard Glucose Monitoring in Children with Type 1 Diabetes. *Diabetes care*, 28(5):1101–1106, 2005.

[103] R. Kasahara, S. Kino, S. Soyama, and Y. Matsuura. Noninvasive glucose monitoring using mid-infrared absorption spectroscopy based on a few wavenumbers. *Biomedical Optics Express*, 9(1):289–302, 2018.

[104] A. L. Fougner, K. Kölle, N. K. Skjærvold, N. A. L. Elvemo, D. R. Hjelme, R. Ellingsen, S. M. Carlsen, and Ø. Stavdahl. Intraperitoneal Glucose Sensing is Sometimes Surprisingly Rapid. *Modeling, Identification and Control*, 37(2):121–131, 2016.

[105] M. K. Åm, K. Kölle, A. L. Fougner, I. Dirnena-Fusini, P. C. Bösch, R. Ellingsen, D. R. Hjelme, Ø. Stavdahl, S. M. Carlsen, and S. C. Christiansen. Effect of sensor location on continuous intraperitoneal glucose sensing in an animal model. *PLoS ONE*, 13(10):1–21, 2018.

[106] L. M. Huyett, R. Mittal, H. C. Zisser, E. S. Luxon, A. Yee, E. Dassau, F. J. Doyle, and D. R. Burnett. Preliminary Evaluation of a Long-Term Intraperitoneal Glucose Sensor With Flushing Mechanism. *Journal of Diabetes Science and Technology*, 10(5):1192–1194, 2016.

[107] A. Liebl, R. Hoogma, E. Renard, P. Geelhoed-Duijvestijn, E. Klein, J. Diglas, L. Kessler, V. Melki, P. Diem, J. M. Brun, P. Schaepelynck-Bélicar, and T. Frei. A reduction in severe hypoglycaemia in type 1 diabetes in a randomized crossover study of continuous intraperitoneal compared with subcutaneous insulin infusion. *Diabetes, Obesity and Metabolism*, 11(11):1001–1008, 2009.

[108] E. Dassau, E. Renard, J. Place, A. Farret, M. J. Pelletier, J. Lee, L. M. Huyett, A. Chakrabarty, F. J. Doyle, and H. C. Zisser. Intraperitoneal insulin delivery provides superior glycaemic regulation to subcutaneous insulin delivery in model predictive control-based fully-automated artificial pancreas in patients with type 1 diabetes: a pilot study. *Diabetes, Obesity and Metabolism*, 19(12):1698–1705, 2017.

[109] H. M. Heise, R. Marbach, G. Janatsch, and J. D. Kruse-Jarres. Multivariate Determination of Glucose in Whole Blood by Attenuated Total Reflection Infrared Spectroscopy. *Anal. Chem.*, 61(18):2009–2015, 1989.

[110] G. Janatsch, J. D. Kruse-Jarres, R. Marbach, and H. M. Heise. Multivariate Calibration for Assays in Clinical Chemistry Using Attenuated Total Reflection Infrared Spectra of Human Blood Plasma. *Analytical Chemistry*, 61(18):2016–2023, 1989.

[111] R. A. Shaw, S. Kotowich, M. Leroux, and H. H. Mantsch. Multianalyte serum analysis using mid-infrared spectroscopy. *Ann. Clin. Biochem.*, 35(5):624–632, 1998.

[112] T. E. Jessen, A. T. Höskuldsson, P. J. Bjerrum, H. Verder, L. Sørensen, P. S. Bratholm, B. Christensen, L. S. Jensen, and M. A. B. Jensen. Simultaneous determination of glucose, triglycerides, urea, cholesterol, albumin and total protein in human plasma by Fourier transform infrared spectroscopy: Direct clinical biochemistry without reagents. *Clinical Biochemistry*, 47(13-14):1306–1312, 2014.

[113] W. B. Martin, S. Mirov, and R. Venugopalan. Middle Infrared, Quantum Cascade Laser Optoelectronic Absorption System for Monitoring Glucose in Serum. *Applied Spectroscopy*, 59(7):881–884, 2005.

[114] A. Lambrecht, T. Beyer, K. Hebestreit, R. Mischler, and W. Petrich. Continuous Glucose Monitoring by Means of Fiber-Based, Mid-Infrared Laser Spectroscopy. *Applied spectroscopy*, 60(7):729–736, jul 2006.

[115] C. Vrančić, N. Kröger, N. Gretz, S. Neudecker, A. Pucci, and W. Petrich. A Quantitative Look Inside the Body: Minimally Invasive Infrared Analysis in Vivo. *Analytical Chemistry*, 86(21):10511–10514, 2014.

[116] A. Werth, S. Liakat, A. Dong, C. M. Woods, and C. F. Gmachl. Implementation of an integrating sphere for the enhancement of noninvasive glucose

detection using quantum cascade laser spectroscopy. *Applied Physics B*, 124(5):75, 2018.

[117] J. Kottmann, J. M. Rey, and M. W. Sigrist. Mid-Infrared Photoacoustic Detection of Glucose in Human Skin: Towards Non-Invasive Diagnostics. *Sensors*, 16(10):1–14, 2016.

[118] O. Hertzberg, A. Bauer, A. Küderle, M. A. Pleitez, and W. Mäntele. Depth-selective photothermal IR spectroscopy of skin: potential application for non-invasive glucose measurement. *Analyst*, 142(3):495–502, 2017.

[119] J. Y. Sim, C.-G. Ahn, E. Jeong, and B. K. Kim. In vivo Microscopic Photoacoustic Spectroscopy for Non-Invasive Glucose Monitoring Invulnerable to Skin Secretion Products. *Scientific Reports*, 8(1):1–11, 2018.

[120] K. Isensee, N. Müller, A. Pucci, and W. Petrich. Towards a quantum cascade laser-based implant for the continuous monitoring of glucose. *The Analyst*, 143(24):6025–6036, 2018.

[121] M. Erfan, Y. M. Sabry, B. Mortada, K. Sharaf, and D. Khalil. Mid infrared MEMS FTIR spectrometer. In *Proc. SPIE, MOEMS and Miniaturized Systems XV*, volume 9760, 2016.

[122] A. Reyes-Reyes, R. C. Horsten, H. P. Urbach, and N. Bhattacharya. Study of the Exhaled Acetone in Type 1 Diabetes Using Quantum Cascade Laser Spectroscopy. *Analytical Chemistry*, 87(1):507–512, 2015.

[123] K. Owen and A. Farooq. A calibration-free ammonia breath sensor using a quantum cascade laser with WMS 2f/1f. *Applied Physics B: Lasers and Optics*, 116(2):371–383, 2014.

[124] A. De, G. Dutta Banik, A. Maity, M. Pal, and M. Pradhan. Continuous wave external-cavity quantum cascade laser-based high-resolution cavity ring-down spectrometer for ultrasensitive trace gas detection. *Optics Letters*, 41(9):1949–1952, 2016.

[125] A. Reyes-Reyes, Z. Hou, E. van Mastrigt, R. C. Horsten, J. C. de Jongste, M. W. Pijnenburg, H. P. Urbach, and N. Bhattacharya. Multicomponent gas analysis using broadband quantum cascade laser spectroscopy. *Optics Express*, 22(15):18299–18309, 2014.

[126] V. L. Kasyutich and P. A. Martin. $^{13}CO_2/^{12}CO_2$ isotopic ratio measurements with a continuous-wave quantum cascade laser in exhaled breath. *Infrared Physics and Technology*, 55(1):60–66, 2012.

[127] K. Wörle, F. Seichter, A. Wilk, C. Armacost, T. Day, M. Godejohann, U. Wachter, J. Vogt, P. Radermacher, and B. Mizaikoff. Breath analysis with broadly tunable quantum cascade lasers. *Analytical Chemistry*, 85(5):2697–2702, 2013.

[128] N. Kröger-Lui, N. Gretz, K. Haase, B. Kränzlin, S. Neudecker, A. Pucci, A. Regenscheit, A. Schönhals, and W. Petrich. Rapid identification of goblet cells in unstained colon thin sections by means of quantum cascade laser-based infrared microspectroscopy. *Analyst*, 140(7):2086–2092, 2015.

[129] M. J. Pilling, A. Henderson, B. Bird, M. D. Brown, N. W. Clarke, and P. Gardner. High-throughput quantum cascade laser (QCL) spectral histopathology: A practical approach towards clinical translation. *Faraday Discussions*, 187:135–154, 2016.

[130] H. Sreedhar, V. K. Varma, F. V. Gambacorta, G. Guzman, and M. J. Walsh. Infrared spectroscopic imaging detects chemical modifications in liver fibrosis due to diabetes and disease. *Biomedical Optics Express*, 7(6):2419–2424, 2016.

[131] B. Bird and J. Rowlette. High definition infrared chemical imaging of colorectal tissue using a Spero QCL microscope. *Analyst*, 142(8):1381–1386, 2017.

[132] C. Kuepper, A. Kallenbach-Thieltges, H. Juette, A. Tannapfel, F. Großerueschkamp, and K. Gerwert. Quantum Cascade Laser-Based Infrared Microscopy for Label-Free and Automated Cancer Classification in Tissue Sections. *Scientific Reports*, 8(1):1–10, 2018.

[133] A. Ogunleke, V. Bobroff, H. H. Chen, J. Rowlette, M. Delugin, B. Recur, Y. Hwu, and C. Petibois. Fourier-transform vs. quantum-cascade-laser infrared microscopes for histo-pathology: From lab to hospital? *TrAC - Trends in Analytical Chemistry*, 89:190–196, 2017.

[134] H. Martens and M. Martens. *Multivariate Analysis of Quality An Introduction*. John Wiley & Sons, Ltd, 2001.

[135] S. Wold, M. Sjöström, and L. Eriksson. PLS-regression: A basic tool of chemometrics. *Chemometrics and Intelligent Laboratory Systems*, 58(2):109–130, 2001.

[136] A. E. Hoerl. Application of Ridge Analysis to Regression Problems. *Chemical Engineering Progress*, 58(3):54–59, 1962.

[137] R. Tibshirani. Regression Shrinkage and Selection via the Lasso. *Journal of the Royal Statistical Society: Series B (Methodological)*, 58(1):267–288, 1996.

[138] H. Zou and T. Hastie. Regularization and variable selection via the elastic net. *Journal of the Royal Statistical Society. Series B: Statistical Methodology*, 67(2):301–320, 2005.

[139] T. Hastie, R. Tibshirani, and J. Friedman. *The Elements of Statistical Learning*. Springer, New York, NY, second edition, 2009.

[140] J. M. Zurada. *Introduction to artificial neural systems*. West, 1992.

[141] J. Schmidhuber. Deep Learning in neural networks: An overview. *Neural Networks*, 61:85–117, 2015.

[142] W. Rawat and Z. Wang. Deep Convolutional Neural Networks for Image Classification: A Comprehensive Review. *Neural Computation*, 29(9):2352–2449, 2017.

[143] J. Acquarelli, T. van Laarhoven, J. Gerretzen, T. N. Tran, L. M. C. Buydens, and E. Marchiori. Convolutional neural networks for vibrational spectroscopic data analysis. *Analytica Chimica Acta*, 954:22–31, 2017.

[144] R. J. Hyndman and A. B. Koehler. Another look at measures of forecast accuracy. *International Journal of Forecasting*, 22(4):679–688, 2006.

[145] T. Naes and T. Isaksson. SEP or RMSEP, Which is Best? *NIR news*, 2(4):16, 1991.

[146] Å. Rinnan, F. van den Berg, and S. B. Engelsen. Review of the most common pre-processing techniques for near-infrared spectra. *TrAC - Trends in Analytical Chemistry*, 28(10):1201–1222, 2009.

[147] H. J. Butler, B. R. Smith, R. Fritzsch, P. Radhakrishnan, D. S. Palmer, and M. J. Baker. Optimised spectral pre-processing for discrimination of biofluids via ATR-FTIR spectroscopy. *Analyst*, 143(24):6121–6134, 2018.

[148] O. Devos and L. Duponchel. Parallel genetic algorithm co-optimization of spectral pre-processing and wavelength selection for PLS regression. *Chemometrics and Intelligent Laboratory Systems*, 107(1):50–58, 2011.

[149] J. Gerretzen, E. Szymańska, J. J. Jansen, J. Bart, H. J. Van Manen, E. R. Van Den Heuvel, and L. M. C. Buydens. Simple and Effective Way for Data Preprocessing Selection Based on Design of Experiments. *Analytical Chemistry*, 87(24):12096–12103, 2015.

[150] G. Chandrashekar and F. Sahin. A survey on feature selection methods. *Computers and Electrical Engineering*, 40(1):16–28, 2014.

[151] DRS Daylight solutions, Hedgehog-UT. `https://www.daylightsolutions.com/product/hedgehog/`. Accessed: 2020-05-07.

[152] I. L. Jernelv, K. Strøm, D. R. Hjelme, and A. Aksnes. Infrared Spectroscopy with a Fiber-Coupled Quantum Cascade Laser for Attenuated Total Reflection Measurements Towards Biomedical Applications. *Sensors*, 19(23):5130, 2019.

[153] F. Pedregosa, G. Varoquaux, A. Gramfort, V. Michel, B. Thirion, O. Grisel, M. Blondel, P. Prettenhofer, R. Weiss, V. Dubourg, J. Vanderplas, A. Passos, D. Cournapeau, M. Brucher, M. Perrot, and É. Duchesnay. Scikit-learn: Machine Learning in Python. *Journal of Machine Learning Research*, 12:2825–2830, 2011.

Publications

Paper I

A review of optical methods for continuous glucose monitoring
I.L. Jernelv, K. Milenko, S.S. Fuglerud, D.R. Hjelme, R. Ellingsen, A. Aksnes
Applied Spectroscopy Reviews, Vol. 54(7), pp. 543-572, 2019.

Note: This is the Accepted Manuscript version of the article published in Applied Spectroscopy Reviews

A Review of Optical Methods for Continuous Glucose Monitoring

Ine L. Jernelv*, Karolina Milenko, Silje S. Fuglerud, Dag R. Hjelme, Reinold Ellingsen, Astrid Aksnes

Department of Electronic Systems, Norwegian University of Science and Technology, Trondheim, Norway

*ine.jernelv@ntnu.no

Abstract

Frequent glucose monitoring is a fundamental part of diabetes management, and good glucose control is important for long-term health outcomes. New types of electrochemical sensors that allow for continuous glucose monitoring (CGM) have become an important tool for diabetes management, although they still have drawbacks such as short lifetime and a need for frequent calibration. Other technologies are still being researched for CGM, in an attempt to replace the electrochemical sensors. Optical methods have several advantages for CGM, including potentially long sensor lifetimes and short measurement times, and many developments have been made over the last decades.

This paper will review optical measurement methods for CGM, their challenges, and the current research status. The different methods will be compared, and the future prospects for optical methods will be discussed.

Keywords: optical spectroscopy; quantitative optical methods, biomedical applications, continuous glucose monitoring, glucose sensors

Introduction

The demand for cheap and user-friendly biosensors is continually growing, and blood glucose monitoring, which is essential for diabetes management, contributes substantially to the world's biosensor market (1). Most current glucose sensors utilise an electrochemical reaction in order to measure glucose, and these sensors have been greatly improved since their invention in the 1960's (2). However, electrochemical sensors still have some issues in terms of longevity, ease of use, and accuracy. Many companies have tried to develop and commercialise alternatives to these sensors, with limited success so far. Optical measurement methods are already widely used in both medical

and industrial fields, and have several characteristics that can be advantageous for glucose sensors. Consequently, optical techniques have been of great interest in glucose sensor development.

The three market leaders that provide continuous glucose monitoring (CGM) devices today are Medtronic, Dexcom, and Abbott (3–6). The devices from these companies allow for continuous tracking of glucose levels, with measurements provided every 1-5 minutes. A small filament is placed subcutaneously, and glucose measurements are performed based on an enzymatic reaction. These CGM devices have to be replaced regularly due to the degradation of reagents and the immune response of the body (7–9). The sensors with the longest lifetimes are operational for approximately one week, and most of the devices need to be calibrated several times per day against finger-prick measurements. Both the short lifetime and the frequent calibrations increase the burden of use for patients.

Many earlier reviews of alternative glucose sensors have focussed on non-invasive glucose monitoring as the solution to current challenges with continuous glucose monitoring (10–12). However, the non-invasive CGM devices developed over the last decades have not attained any large-scale market, although several of them have been released commercially. The most prominent ones, the GlucoWatch and the Pendra, were based on reverse iontophoresis and impedance spectroscopy, respectively (13, 14). Both devices were found to be less accurate than what was portrayed in clinical trials, and the GlucoWatch caused skin irritation on the measurement site due to the electrical stimulation (15–17). The devices were discontinued not long after release, likely due to a combination of low accuracy, patient dissatisfaction, and high cost.

This review will focus on methods that employ optical measurement methods for glucose monitoring, as these technologies have many advantages for CGM. Monitoring with optical methods is reagent-free and measurements can potentially be performed in less than a minute. Cheap and miniaturised optical components have become available, which is a benefit for personalised sensor systems. Research into both invasive and non-invasive methods will be presented. Six different technologies will be described, together with the major challenges and the current research status. A discussion of optical measurement methods and a future outlook for these technologies are also included.

Continuous Monitoring of Glucose

Continuous glucose monitoring has developed as its own field over the last decades, and some background information is needed to compare different optical techniques. A short introduction to diabetes management is given below. The methods used to assess glucose monitoring devices will be also be presented, together with an overview of the different measurement sites used for CGM. Electrochemical glucose sensors will be briefly described.

Glucose concentrations are typically given in units of mg/dl or mmol/l (also written mM). Medical studies usually use mmol/l, while technical papers tend towards using mg/dl. This paper will report glucose concentrations in mg/dl, and if the referenced article uses mmol/l this number will be given in parentheses.

Management of Type 1 Diabetes

In people with diabetes mellitus type 1 (DM1) an autoimmune process has destroyed the insulin-producing beta cells in the pancreas. This makes patients with DM1 dependent on exogenous supplies of insulin to control their glucose level. Insulin can be delivered by multiple daily subcutaneous insulin injections, or by continuous subcutaneous (SC) delivery of insulin with an insulin pump controlled by the patient (18). Insulin doses are adjusted according to physical activity, meal size and composition, and the actual glucose level. Despite all efforts, most DM1 patients struggle to regulate their blood glucose level (BGL) in the desired range, and glucose can easily depart outside of the normal physiological range, typically defined as 72-180 mg/dl (4-10 mmol/l) (19, 20). Hypoglycaemia occurs when the BGL is too low (<70 mg/dl or 3.9 mmol/l), and can lead to seizures, loss of consciousness, and even death (21). Hyperglycaemia occurs when the BGL is higher than 180 mg/dl (10 mmol/l), and can lead to serious long-term complications, including kidney damage, diabetic retinopathy, heart disease and neuropathy (22).

Given the importance of keeping glucose in the desired range, management of DM1 includes frequent measurements of the BGL. Good control of the BGL reduces development of long-term complications (23, 24). Finger-prick measurements of capillary blood glucose is still the most prevalent form of daily self-monitoring of blood glucose (SMBG) in DM1 patients. These measurements are performed by pricking the skin with a lancet, and placing a drop of blood on a disposable test strip. A meter is used to measure the test strip and calculate the glucose level. Diabetic patients are recommended to measure their glucose values at least four times per day, and more often if they are at risk for large excursions from their target glucose level (25). However, SMBG by finger-prick measurements is inconvenient and painful, and many diabetic patients measure less frequently. Some even avoid glucose measurements for days or weeks. Another disadvantage of these measurements is that they only provide information about the BGL at a single point in time. Large excursions in the BGL during the day may be missed, no information on BGL trends is available, and there is a complete lack of information at night. Hence, much effort has been invested into making CGM devices. CGM devices are sensor systems that continually provide glucose measurements for patients. Several of these devices are commercially available, and researchers are still trying to develop more precise and robust methods for CGM. CGM has been

shown to improve glucose control in patients with DM1 as compared to SMBG with finger-prick measurements, especially in patients with otherwise poorly controlled glucose levels (26, 27). In addition, CGM is a prerequisite for making fully automated delivery of insulin in patients with DM1, also known as a closed-loop system or an artificial pancreas (28).

Assessing Glucose Monitoring

The precision of CGM devices is often measured by mean or median average relative difference (ARD), with most of the current commercial devices achieving median ARDs of 10-15 % and mean ARDs of 15-20%. ARD is sometimes known as absolute relative error (ARE). The ARD for each measurement is calculated as follows:

$$ARD_i = 100\% \times \frac{|Y_i - y_i|}{Y_i}$$

where Y_i is the reference glucose value and y_i is the measured glucose value. The mean and median ARDs are then calculated based on the individual ARDs. The reference glucose measurement is a measurement of the BGL performed at the same time, typically done either with a blood-gas analyser or another glucose monitoring device. ARDs are easy to calculate and interpret, but they do not indicate the direction of the error and ARDs are usually lower if a smaller glucose range is investigated.

Other common methods for evaluating glucose sensors are the Clarke error grid (CEG) and the Parkes error grid (also called the consensus error grid), shown in Fig. 1 (29, 30). The CEG plots the results from a glucose meter against a reference measurement method, and the plot is divided into five clinically relevant areas. Zone A contains the values that are within an ARD of 20% of the reference measurements, while zone B contains measurements with more than 20% error that would still lead to correct treatment. Zone C and D contain measurements that would lead to unnecessary treatment or a dangerous lack of treatment, respectively. Measurements in Zone E will indicate that the patient is in hypoglycaemia when they in reality are hyperglycaemic, and vice versa. The Parkes error grid uses the same regions as the CEG with similar definitions and improves upon some issues with the CEG, such as the discontinuous transitions between some regions (e.g. direct transitions between zone B and zone E for some glucose values).

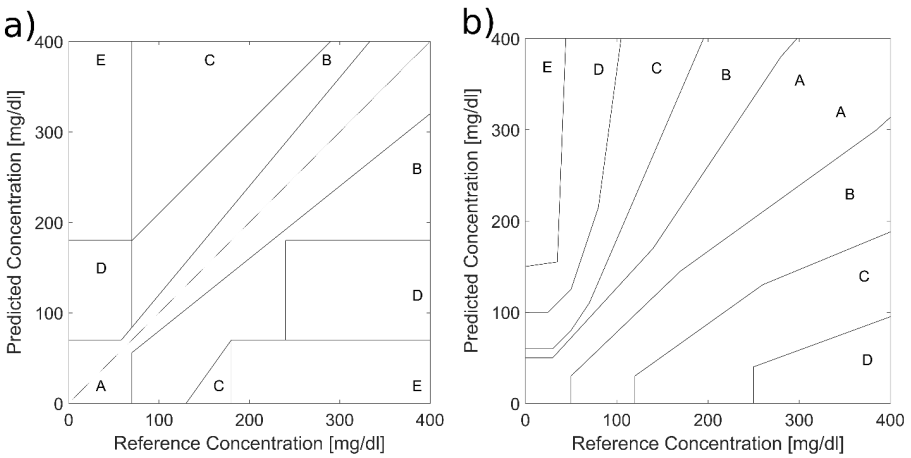

Figure 1: a) Clarke error grid and b) Parkes error grid for glucose monitoring. The y-axis indicates glucose values measured with the new device, while reference values are represented on the x-axis. See the text for an overview of the different zones.

Glucose measurements from a sensor that is under testing can also be compared to a reference method with Bland-Altman plots (31). Other standard statistical measures are frequently reported, especially in studies that are more preliminary. These include for example R, R^2, standard error of prediction (SEP), and root-mean-square error of prediction (RMSEP). This large variety of reported evaluation methods can make it challenging to compare different systems and technologies.

There has been an ongoing discussion about the best methods for quantifying the accuracy of CGM devices. For example, the CEG does not evaluate how CGM systems handle the rate of glucose change, and the continuous glucose-error grid analysis (CG-EGA) was developed in order to improve the evaluation of continuous glucose sensors (32). However, obtaining enough data for the CG-EGA is very time-consuming, and it has not been shown to be better than the CEG (33).

Measurement Sites

Many different measurement sites have been suggested for continuous glucose monitoring systems. The measurement sites can be divided into general categories based on how invasive the measurements sites are to the patients. Non-invasive methods use measurement sites where no instruments are inserted into the body. Measurements of easily available body fluids are non-invasive, and optical measurements of skin are considered non-invasive although light is sent into

the body. On the other hand, sensor systems that penetrate blood vessels or the abdominal cavity are considered invasive. Methods that introduce sensor parts subcutaneously are often called "minimally invasive", as no blood vessels are compromised.

Non-invasive CGM systems have been pursued for several decades, with the goals of improving the comfort and convenience of diabetic patients who have to monitor their glucose levels daily. Measurements in sweat (34), saliva (35), and breath (36) have all been investigated, but the concentration of glucose or other correlating analytes have generally been too low, have not correlated well with the BGL, or have had too slow dynamics. Measuring in tear fluid has also been suggested, where a sensor similar to a contact lens would have to be worn on the eye for continuous measurements. However, the glucose concentration is much lower in tear fluid than in blood, and the glucose levels in tear fluid and blood do not seem to correlate well throughout the day (37, 38). Systems that measure through skin have therefore received the most attention among the different non-invasive modalities. Many technologies have been investigated, including impedance spectroscopy, ultrasound, reverse iontophoresis, as well as many optical methods (12). Light penetrates from several micrometres to several millimetres into skin depending on wavelength, and can also be used to measure in the aqueous humour of the eye. Optical methods have therefore received a lot of attention for non-invasive CGM, and some of this research will be described below.

Minimally invasive glucose measurements are typically performed by placing sensor parts subcutaneously. The glucose measurements are then done in the interstitial fluid (ISF), which is the fluid between tissue cells, rather than in the blood. In the steady state, i.e. when blood glucose is stable, the glucose concentration in the ISF is quite similar to the BGL. However, glucose has to diffuse from blood capillaries into the ISF, which causes a time delay in ISF glucose measurements of approximately 5-10 minutes (39, 40). The commonly used electrochemical CGM systems, as mentioned, measure glucose concentration subcutaneously. Optical measurement methods can also be used to measure the ISF, with optical fibres and/or other sensor parts placed subcutaneously.

Recent research suggests that glucose measurements and insulin infusions directly in the peritoneum (abdominal cavity) will give better dynamics for controlling glucose levels (41, 42). Hence, investigations of sensing in peritoneal fluid may be an interesting avenue for CGM. The CGM system could either be implantable or have the light source placed outside the body, which would require a permanent port or fibre penetrating the abdominal wall to the measurement site. There are challenges with both approaches. An implantable sensor would have to be robust and durable without maintenance for a long time. An open port increases the danger of infection and may cause discomfort for the user. The technological challenges for a port solution will be limited, as similar port technology already exists for insulin administration (43). No matter which method is

used, sensing in the peritoneum will definitely be considered invasive. To our knowledge, no CGM devices intended for peritoneal measurements have been developed yet, although some existing devices have been modified and tested in animal models (44).

Electrochemical CGM Systems

Devices using an SC sensor and the glucose-oxidase reaction are the most common CGM systems used for daily management of diabetes. The sensors have a thin filament embedded subcutaneously, which measures the glucose concentration. A transmitter is attached to the sensor and transfers data to a device used for information display. A smartphone or an included receiver shows real-time data from the sensor, often with trend arrows and alerts for hypo- and hyperglycaemia.

These sensors measure the glucose concentration via an electrochemical reaction (2). In the basic reaction, glucose-oxidase facilitates the redox reaction of glucose with water, which produces gluconolactone and hydrogen peroxide (glucose + O_2 -> gluconolactone + H_2O_2). A small electrical current amplifies the dissociation of hydrogen peroxide, which produces free electrons. The glucose concentration in the immediate area is then determined from the electrical current resulting from these electrons. Mediator molecules other than oxygen can be used as electron donors in order to decrease the dependency on oxygen (45).

Due to the degradation of chemical reagents and biofouling the sensors have to be replaced approximately once per week, depending on the manufacturer. The user can insert the device without the help of medical personnel. The sensors also require a warm-up period after insertion, where the glucose measurements are inaccurate for up to several hours, depending on the model. This is possibly due to local trauma in the immediate area, which is caused by the sensor insertion. In addition, regular injection of an SC foreign body may induce local SC fibroses or other tissue changes over time (46). Most devices require calibrations twice per day, where the sensor is calibrated against finger-prick measurements. If the calibration process is done while glucose levels are rapidly changing, the measured glucose level on the device will not correlate well with the actual BGL. The sensor measures the glucose concentration in the ISF rather than measuring blood glucose directly, with the associated time delay as compared to the BGL. Additional delay is introduced because of the reaction process, and because glucose must diffuse to the sensor filament as the surrounding area becomes depleted (47). Consequently, alarms about low glucose levels can occur after the patient has already started experiencing hypoglycaemia, where a prompt reaction is often needed. However, many CGM systems use advanced algorithms to predict hypoglycaemia, and can reduce the perceived time delay.

Despite several limitations, these devices generally measure glucose concentrations quite well. Electrochemical CGM has become well established among physicians and patients, and has

been shown to improve glucose control in patients. Any new inventions that seek to replace today's CGMs will likely have to significantly improve upon either reliability, sensitivity, specificity, sensor lifetime, or perceived quality of life in order to succeed.

Optical Methods for Glucose Measurements

Six main optical technologies are included in this review. Near-infrared, mid-infrared, Raman, and photoacoustic spectroscopy are spectroscopic, meaning that they use the direct interaction between light and glucose to determine the glucose concentration. Systems using fluorescence spectroscopy do not measure glucose directly; rather, they typically measure the signal from molecules that can reversibly bind to glucose. The last technology, optical coherence tomography, measures the change in scattering properties in tissue as a function of glucose concentration. The following sections will give an overview of how these technologies are used in glucose sensing. A brief description of the technical aspects will be provided for each method, together with a discussion on challenges and a review of the research status in the area. The examples of in vivo research are limited to more recent and well-documented systems, with a focus on systems that are intended for personal use. The research stage and other relevant characteristics of most of these systems are summarised in Table 1.

Other optical techniques, such as measuring optical rotation (48), have been suggested for glucose monitoring. However, the studies on these methods are sparse and often several decades old. There are also studies that use variants of optical techniques, such as several recent studies using photothermal deflection spectroscopy (49, 50). As these methods have mostly been investigated by single research groups it is difficult to review how well they measure glucose. The review will therefore be limited to the above-mentioned six technologies for conciseness.

Near-Infrared (NIR) Spectroscopy

The near-infrared region extends from 700 to 2500 nm and contains absorption bands primarily caused by hydrogen vibrations (CH, NH, OH). The short wave band (780-1500 nm) is used for non-invasive measurements, while for aqueous measurements the first overtone (1500-1800 nm) and the combination band (2050-2100 nm) are mostly used (51). The absorption bands are broad and easily influenced by hydrogen bonding, temperature effects and molecules with similar absorption spectra. NIR sources and detectors are readily available and cheap. Common sources are LED arrays for non-invasive studies and tungsten-halogen lamps for benchtop measurements. Doped InGaAs detectors are common, and cooled InSb detectors are also used.

In general, transmission spectroscopy is commonly used for aqueous solutions, while reflectance spectroscopy is used for non-invasive measurements. The optimal path length through

Table 1 Summary of research results using optical measurement methods for glucose monitoring

Method and wavelength	**Research stage and type**	**Citations/Company**	**Measurement site/ solution**	**Glucose range**	**Accuracy**
Transmisison **near-infrared spectroscopy,** combinational band and first overtone	in vitro	Goodarzi et al. (70)	Aqueous solutions and serum solutions	36-540 mg/dl (1-30 mM)	RMSEP down to 10.1 mg/dl (0.56 mM)
Transmission **near-infrared spectroscopy,** 2-2.5 µm	in vivo, non-invasive	Olesberg et al. (72)	Skin fold, rat	90-630 mg/dl (5-35 mM)	SEP of 35.6 mg/dl (1.98 mM)
Diffuse reflectance n**ear-infrared spectroscopy,** first overtone	in vivo, non-invasive	Maruo et al. (73)	Skin, forearm	50-500	SEP of 28.7 mg/dl and 27.2 mg/dL
Transmission **near-infrared spectroscopy,** first overtone	Prototype in vitro, aimed at in vivo invasive	Ryckeboer et al. (75)	Aqueous solutions	18-684 mg/dl (1-36 mM)	RMSEP of 20.5 mg/dl (1.14 mM)
Transmission **near-infrared spectroscopy** combined with microdialysis, 1300, 1450, 1550 nm LEDs	Prototype, invasive	Mohammadi et al. (78)	Microdialysate from arm	60-350 mg/dl	Mean ARD 8.5%
Diffuse reflectance **Near-infrared LEDs** in short wave range	in vivo, non-invasive	Zanon et al., Biovotion AG (80)	Skin on the upper arm	30-400 mg/dl	Mean ARD 35.4%
ATR mid-infrared spectroscopy, FTIR source	in vitro	Heise et al. (86)	Blood plasma	36-482 mg/dl	RMSEP = 10.4 mg/dl
Transmission **mid-infrared spectroscopy**, 1230-1030 cm^{-1}	in vitro	Brandstetter et al. (87)	Blood serum	Approx. 20-140 mg/dl	RMSEP = 6.9 mg/dl
Back-scattered **mid-infrared spectroscopy**, 8-10 µm	in vivo, non-invasive	Liakat et al. (90)	Thenar skin fold of the hand	80-160 mg/dl	84% of measurements in zone A of CEG
Transmission **mid-infrared spectroscopy**, 9.7 µm	in vivo, minimally invasive	Vrančić et al. (93)	Transcutaneous, rats	Approx. 75-600 mg/dl	Median ARD 11.0%

ATR **mid-infrared spectroscopy**, 1155 cm^{-1}	in vivo, non-invasive	Kino et al. (94)	Inner lip, human	Approx. 75-175 mg/dl	Measurement errors less than 20%, R^2 = 0.75
Raman spectroscopy in reflection mode, 785 nm	in vitro	Pelletier et al. (104)	Aqueous humour of the eye, human	0-800 mg/dl	RMSEP = 22 mg/dl
Transmission **Raman spectroscopy,** 830 nm	in vivo, non-invasive	Kong et al. (106)	Thenar skin fold of the hand	75-320 mg/dl	R^2=0.81, RMSEP=16.8 mg/dl
Transmission **Raman spectroscopy**, same system as Kong et al. (106)	in vivo, non-invasive	Shih et al. (107)	Ear, dog	100-460mg/dl (5.6-25.6 mM)	RMSEP approx. 27-36 mg/dl (1.5-2 mM)
Surface-enhanced **Raman spectroscopy**, 785 nm	in vivo, minimally invasive	Ma et al. (109)	Subcutaneous, rats	31-600 mg/dl collectively from 5 rats	100% of measurements in zone A+B of CEG
Photoacoustic spectroscopy, dual-wavelength scheme around 1100 cm^{-1}	in vivo, non-invasive	Kottmann et al. (114)	Arm skin	90-170 mg/dl	R = 0.8
Photoacoustic spectroscopy, 1220-1000 cm^{-1}	in vivo, non-invasive	Pleitez et al. (116)	Arm skin	40-250 mg/dl, collectively from 3 subjects	100% of measurements in zone A+B of CEG
Fluorescence sensing	Prototype, minimally invasive	Dutt-Ballerstadt et al., Biotex Inc. (127)	Subscutaneous on arm	100-350 mg/dl	Mean ARE 13%
Fluorescence sensing	Prototype, minimally invasive	Müller et al., Eyesense GmbH (129)	Subcutaneous on arm and abdomen	60-370 mg/dl	Mean ARD 8.3% on arm, 11.4% on abdomen
Fluorescence sensing	Product, invasive	Mortellaro et al., Senseonics Inc. (131)	Implanted subcutaneously	40-400 mg/dl	Mean ARD 11.1%
Optical coherence tomography, 1300 nm	in vivo, non-invasive	Larin et al. (135)	Ear, rabbit	110-400 mg/dl	R = 0.88
Optical coherence tomography, 1310 nm	in vivo, non-invasive	Gabbay et al. GlucoLight (140)	Skin, human	98-442 mg/dl	mean ARD 11.5%

aqueous glucose samples in transmission mode is dependent on the wavelength and instrumentation, and is in the range 0.5-5 mm (52). The effective path length for non-invasive reflectance measurements is dependent on penetration depth and is heavily weighted towards the upper layer of the skin. It has been estimated to 0.4 to 10 mm, depending on the wavelength (53–55).

Challenges

Sensor placement is a great challenge for non-invasive measurements. The focus has mostly been on the skin (finger-tip, forearm (56), upper-arm), but the eye (57), lip (58), tongue (59), and mouth have also been suggested. Changes in the local environment such as a sunburn, fever, sweating, swelling, or areas with scarring, tattoos or moles can interfere with the spectra, making the results hard to reproduce in different physiological states and especially between patients. Zhang et al. further discuss this issue for spectral data obtained by non-invasive measurements through the skin (60). Although the results of calibration models look promising, there is a need for more validation and variations over humidity, pressure, skin type, age, and other factors.

For invasive measurements in the ISF or the peritoneum, the water absorption is very high around 1400 and 1900 nm, resulting in a weak signal and low signal-to-noise ratio (SNR). Invasive measurements would also require a sensor structure that does not trigger immune responses and does not cause discomfort to the user, which rules out materials such as uncoated glass (61).

Molecules with absorption spectra that are similar to glucose can cause interference in NIRS measurements. Examples of known molecules with absorbance similar to glucose in the NIR range are lactate, urea (62), and sugars such as fructose. Other molecules with similar spectra are glutamine, ammonia, and glutamate (63). Interfering molecules represent a challenge for NIR sensing if not included in the initial model, as the peaks are broad, overlapping, and the glucose signal is relatively weak compared to the water absorption bands.

Research Status

Several groups have researched in vitro transmission NIRS glucose measurements in plasma (64–66), whole blood (67), and other matrices designed to simulate bodily fluids (68). Depending on the complexity of the matrix, the equipment, the concentration range investigated (typically 18-540 mg/dl), and the pre-processing methods (see (69) for a review of techniques), the RMSEP is typically in the range 9 to 45 mg/dl. For example, glucose in the presence of urea and sodium D-lactate has been reliably measured in the physiological range by Goodarzi et al. down to 36 mg/dl (2 mM) with an RMSEP down to 10.1 mg/dl (0.56 mM) (70).

An application of NIR spectroscopy for non-invasive glucose sensing was patented by Rosenthal et al. in 1992 and spurred intensive research within this area in the 90's (71). Most of the focus within NIRS sensing has been directed at non-invasive efforts, but advances past initial trials have yet to be presented to the public. Arnold and Small have pointed out several parameters that must be investigated in non-invasive sensing for comparability with other studies: spectral range, degrees of freedom, path length, spectral variance and chemical basis of selectivity (54). Many studies do not consider these parameters, making it difficult for the reader to assess whether the correlation is due to glucose, some co-varying factor, or overfitting by the multivariate calibration model. A study considering this was performed by Olesberg et al., who measured glucose non-invasively on a skin fold on the back of one rat for approximately 7 hours (72). The glucose level was increased to above 540 mg/dl (30 mM) and held there for 2 hours, when it was allowed to return to normal. They used a fibre probe and found a SEP of 66.6 mg/dl (3.7 mM), which was improved to 35.6 mg/dl (1.98 mM) when accounting for the time delay (15 minutes). Only one animal was used, and the between-subject variation can therefore not be evaluated.

Maruo et al. demonstrated a non-invasive NIRS-based sensor with a SEP of less than 32.2 mg/dl in 2003 (56). One diabetic and five healthy human subjects were included in this study, and the BGL was varied between 50 and 350 mg/dl. In 2006 they followed up with a clinical study with five healthy and seven diabetic subjects, where glucose varied between 50 and 500 mg/dl, and they obtained a SEP of 27.2 mg/dl (73). After this, they have been working on data analysis and perturbations to the model to account for fat content. In 2015, they published a paper detailing how a non-invasive model can be built based on Beer-Lambert's law, without the use of chemometrics (74).

The authors are not aware of any current non-invasive CGMs for DM1 on the international market, although several companies have tried to develop non-invasive NIR-based sensors since the late 90's, such as Diasensor (Biocontrol Technology), SugarTrac (Lifetrac), and Dream Beam (Futrex Medical Instrumentation). This stands as a testament to the complexity of the problem.

A less traditional approach to aqueous glucose sensing was proposed by Ryckeboer et al., who suggested measuring glucose by waveguide-based absorption spectroscopy on a silicon chip in the range 1540-1610 nm (75). The results in vitro with glucose in range 18-684 mg/dl (1-36 mM) were promising, with an RMSEP of 20.5 mg/dl (1.14 mM). There have been no clinical trials, but a patent suggesting that the sensor can be miniaturised and implanted was granted in 2017 (76).

A minimally invasive chip-based NIR CGM sensor using microdialysis of ISF has been suggested by Mohammadi et al. The sensor has been used in two in vivo trials, the first on 10 DM1 patients for 30 hours (77), and the second one with six subjects for 12 hours (78). The glucose concentration range was approximately 60-350 mg/dl. The measurement accuracy was 13.8%

overall mean ARE in the first study, and a mean ARD of 8.5% was obtained in the second study. The device offers an improvement over the electrochemical CGMs in that there are no degradable enzymes and thus the device can be replaced less frequently. However, it suffers from the aforementioned time lag in the ISF as compared to the BGL. The authors also reported issues with air bubbles forming in the sensor.

Some groups have combined different technologies for improved glucose prediction. Most notable within NIR technology is the research from the team around Caduff and Zanon (affiliated with Biovotin AG), who have worked towards a non-invasive wearable multisensory system based on dielectric spectroscopy (DS), temperature, humidity, and sweat sensors combined with 3 NIR LEDs. In their latest study, the sensor was used by 20 DM1 subjects with BGL in the range 30-400 mg/dl, and a mean ARD of 35.4 % was obtained (79, 80). As the authors point out, they have some challenges to overcome before the sensor matches the accuracy of CGMs on the market today. They do not suggest to improve or add to the sensors, but rather to focus further efforts on development of more complex algorithms.

Mid-Infrared (MIR) Spectroscopy

Mid-infrared (MIR) spectroscopy uses light approximately in the 4000-400 cm^{-1} (2.5-25 µm) range, although many applications focus on the 4000-1000 cm^{-1} (2.5-10 µm) range (81). Wavenumbers (cm^{-1}) are commonly used in the literature on mid-infrared spectroscopy, and will also mainly be used in this article. Glucose has absorption peaks in several areas in the mid-infrared range, most notably around 3000 cm^{-1}, around 1400 cm^{-1}, and in the 1200-1000 cm^{-1} range. Glucose absorbance in the 1200-1000 cm^{-1} range has received the most attention for sensor studies, as the features around 3000 cm^{-1} and 1400 cm^{-1} overlap with strong water absorption peaks. This absorbance is related to the skeletal vibrations of glucose, i.e. vibrations that are characteristic for the entire molecule.

Fourier transform infrared (FTIR) spectrometers are commonly used for benchtop infrared spectroscopy. These spectrometers use radiation from infrared sources such as heated silicon carbide elements, which cover the entire wavelength range. However, current FTIR spectrometers are too large for personalised CGM devices, and the total light emitted is too weak for clinical measurements. Few other radiation sources have existed in the MIR, and one of the biggest limitations for MIR spectroscopy has therefore been the lack of high-energy sources. New avenues have opened for MIR spectroscopy with the invention and development of quantum cascade lasers (QCLs) (82, 83). A QCL is a type of semiconductor laser that can be tailored to specific single wavelengths, or it can be tuneable over a desired wavelength range. Several detector types can be used in the MIR range, including thermopile, pyroelectric, and photoconductive detectors.

Most available research relies on transmission MIR spectroscopy for subcutaneous glucose measurements, or reflectance spectroscopy for non-invasive measurements. CGM systems can also use attenuated total reflectance (ATR) spectroscopy, as illustrated in Fig. 2 (84). In ATR spectroscopy, light is guided by total internal reflection (TIR) in a crystal or fibre that is in contact with the sample, and the evanescent field from the light extends into the sample. The light is detected after exiting the crystal, and the absorbance spectrum is based on the evanescent light absorbed by the sample.

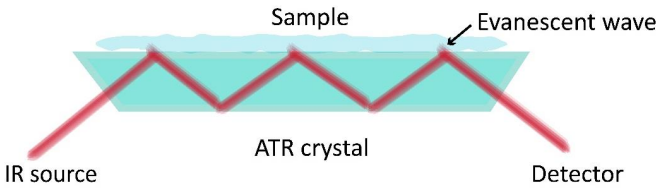

Figure 2: Attenuated total reflectance (ATR) is a common technique in infrared spectroscopy. Light can undergo multiple internal reflections in a crystal or fibre with high refractive index. The evanescent wave resulting from this can extend into a sample that is in contact with the crystal. Absorption of this evanescent wave is used to construct an infrared absorption spectrum.

One advantage that MIR spectroscopy may have over near-infrared spectroscopy is that absorption in the MIR range is defined by fundamental molecular vibrations. NIR absorption bands are typically overtones and combination bands, which are often weaker and broader. Consequently, MIR absorption bands are relatively sharp, more selective, and have a stronger signal compared to NIR absorption bands.

Challenges

Mid-infrared light penetrates only a few micrometres into skin, and MIR spectroscopy has therefore received little attention for non-invasive glucose measurements. The MIR spectrum of skin is also highly dependent on the skin water content, which acts as a major confounding factor. Any measurements through skin would therefore have to be calibrated individually due to individual differences in skin properties.

These challenges are minimised if MIR spectroscopy is used for measurements in the ISF or in peritoneal fluid. The largest limitation for MIR spectroscopy today is the prohibitive price of MIR lasers and other components. Tuneable lasers are necessary if a large wavelength range needs

to be investigated, and these lasers have so far been limited to research use due to high price and low production volume.

Water absorption is very strong in the MIR spectrum, and much stronger than glucose absorption, which means that a high SNR is needed for accurate measurements.

Research Status

MIR spectroscopy has been used to measure glucose accurately in different artificial solutions and in vitro bodily fluids. Several early studies were reported in the 90's by the Heise group, using FTIR spectrometers for the measurements (85, 86). Although both the data analysis and spectrometers have improved since then, these studies demonstrated that glucose concentrations could be predicted with adequate accuracy at physiological concentrations (RMSEP = 10.4 mg/dl). Glucose has also been measured with high accuracy in different aqueous solutions and in vitro fluids using QCLs. Brandstetter et al. reported a study which included in vitro human serum samples, and were able to measure glucose concentrations with an RMSEP of 6.9 mg/dl, where the glucose concentration range was approximately 20-140 mg/dl (87). Broad wavelength ranges have typically been investigated in these studies, with multivariate data analysis being used to extract the relevant information. This would necessitate the use of tuneable MIR lasers if the same principle is used in CGM sensors, and these lasers are currently too large and expensive for personal use. However, sufficiently accurate concentration predictions may also be performed with only a few wavelengths or a narrow wavelength range, which could be handled with smaller lasers (88, 89).

Several research groups have studied MIR spectroscopy for CGM. The Gmachl group performed non-invasive measurements of the back-scattered light from the skin between the thumb and forefinger (90). Measurements were performed in three human subjects, with 84% of the measured glucose values in zone A of the CEG. Glucose was measured in the range 75-160 mg/dl, and the accuracy of the system is therefore unknown for the hypoglycaemic and hyperglycaemic ranges. The group is now using an integrating sphere in the set-up in order to collect more light and improve signal stability (91).

Vrančić et al. developed a system using a QCL at a single wavelength (9.7 µm), and tested the system with transmission mode SC measurements in 3 rats (92, 93). They were able to measure with integration times down to 4 seconds, resulting in practically continuous measurements. The CGM measurements followed the reference measurements closely, and gave a median ARD of 11.0%. The measured glucose range was approximately 80-550 mg/dl. These measurements were performed for approximately 3 hours in each rat, and over a longer time period the one-laser set-up would likely suffer from signal drift. Drift could be ameliorated by either adding a laser at a different wavelength as a reference or using a tuneable laser, as commented by the authors.

Kino et al. have reported measurements of human lip mucosa with ATR-based sensing (94). They employed an FTIR source, hollow-core optical fibres for light transport, and a multi-reflection ATR prism to perform glucose measurements around 1100 cm^{-1}. They accomplished measurement errors of less than 20%. However, they did not measure hyperglycaemic or hypoglycaemic glucose concentrations, which limits the applicability of the results. This group has also reported early results using a single-wavelength QCL source at 9.7 µm (95).

Glucose monitoring devices using MIR spectroscopy that could be used in a critical care setting have been developed. The Optiscanner (96, 97) from Optiscan Biomedical has received the CE mark. In this system, blood samples are obtained via an intravenous connection to the patient, and glucose is measured in plasma after blood sample centrifugation. A spectrometer in the Optiscanner uses 25 fixed wavelengths to determine the glucose concentration. A prototype system with a QCL source has also been suggested by the Lendl group (98).

Raman Spectroscopy

Raman spectroscopy employs Raman scattering in order to observe vibrational modes in molecules (81). Raman scattering is an inelastic scattering process where a small amount of energy is transferred between a molecule and a photon. As the scattering process couples to vibrational modes in the molecule, the energy of the scattered photon is shifted by the energy of one vibrational state. The emitted photon can have lower or higher energy than the absorbed photon, as shown in Fig. 3. Raman scattering has a much smaller scattering cross section than elastic scattering, and standard Raman spectroscopy usually requires long acquisition times.

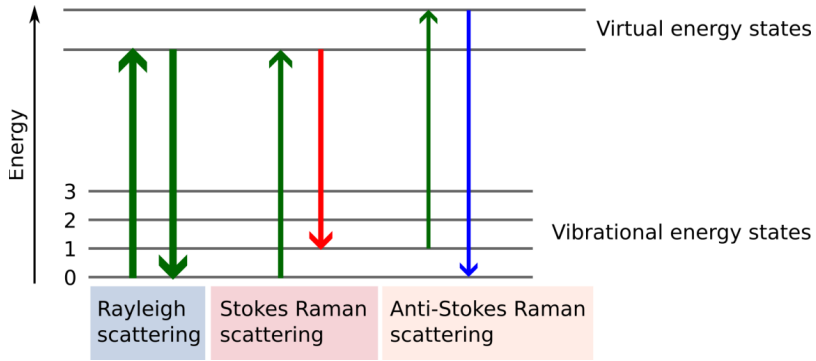

Fig. 3: Rayleigh scattering is elastic, and does not change the energy of the photon. The molecule absorbs energy in Stokes Raman scattering, where the photon is shifted to a longer wavelength, and vice versa for anti-Stokes scattering. Measurements of Raman scattering are used in Raman spectroscopy to detect and quantify molecules.

The resulting frequency shift is particular to the vibrational modes of the molecule and independent of excitation photon frequency, and therefore the Raman spectrum for glucose can be quite clearly distinguished from other biological compounds. A single-wavelength source is sufficient to produce the entire Raman spectrum, as only the frequency shift is measured. The use of visible or NIR light gives the advantage of employing widely available optical components.

The Raman signal can be increased by several orders of magnitude with the use of surface-enhanced Raman scattering (SERS) (99). In SERS the electromagnetic field is highly amplified in the presence of metal nanoparticles, because of local surface plasmon resonances. This is usually realised by incorporating a SERS substrate in the sensor system, which is covered by metal nanoparticles or a roughened metal surface. When using SERS one has to consider fabrication process, biocompatibility and the stability of the metal nanoparticles.

Challenges

Raman spectroscopy uses visible or NIR wavelengths for excitation, which can induce a background fluorescence signal. This can be minimised by using longer wavelengths, where biological compounds are typically less fluorescent. The application of visible or NIR light reduces the absorption by water, which allows for measurements of aqueous samples.

The main challenge of Raman spectroscopy is the small scattering cross section, which can be 10 orders of magnitude smaller than the fluorescence cross section. This may result in the Raman scattering signal being masked by interfering fluorescence signals (100). Additionally, long acquisition times are necessary in order to obtain good a SNR.

Using SERS will improve the Raman signal and shorten measurement times, which is very beneficial for sensor development. However, implanted SERS substrates will experience biofouling, and may degrade over time. The development of SERS sensors is therefore dependent on the biocompatibility and potential toxicity of SERS substrates. Studies have indicated that at least some types of nanoparticles can aggregate in tissues, with detrimental effects to the organism (101, 102).

Research Status

Over the last few decades, there has been a great interest in developing a non-invasive CGM system based on Raman spectroscopy. In vitro glucose measurements have been reported in aqueous humour from rabbits and humans (103, 104). The aqueous humour is not as complex as blood, as it has fewer Raman-sensitive molecules and is less absorptive, which is an advantage for Raman spectroscopy. Although initial studies showed a correlation between blood and humour glucose levels (RMSEP of 22 mg/dl), the development of a device for personal use has not been realised.

Another approach for non-invasive glucose is to measure through skin. Research from the MIT George R. Harrison Spectroscopy Laboratory on continuous transdermal measurements has led to the development of a portable Raman system in transmission mode (105, 106). The Raman spectra of the thenar skin fold from 18 human volunteers showed good correlation with finger-prick measurements during an oral glucose tolerance test. 100% of the measurements were in the A and B zone of the CEG, with an RMSEP of 16.8 mg/dl. This system was also used by Shih et al. to measure glucose levels in a dog model (107). They achieved RMSEPs of approximately 27-36 mg/dl (1.5-2 mM) when the BGL was stable. Glucose values in the hypoglycaemic range were not measured.

A minimally invasive approach for glucose monitoring has been proposed by the Van Duyne group, based on a SERS chip implanted subcutaneously in rats (108, 109). Measurements have been demonstrated 17 days after sensor implantation, where only one calibration was performed. In their largest study, 100% of measurements from all rats were in zone A and zone B of the CEG. Moreover, the RMSEP was 13.7 mg/dL for low glucose concentrations (<80 mg/dl). An acquisition time of 2 minutes was reported. The SERS substrate must be evaluated with respect to its biocompatibility, as it is implanted under the skin.

To the best of the authors' knowledge, no commercialised CGM device based on Raman spectroscopy exists to date, although at least one company was able to CE mark a system. The US-based company C8 Medisensors developed the HG1-c, which was a non-invasive device that could provide glucose measurements every 5 minutes (110). The device had issues with accuracy, and although 92% of measurements were in the A+B zones of the CEG, only 52% of measurements were in the A zone. C8 Medisensors closed down in 2013.

Photoacoustic Spectroscopy

Photoacoustic spectroscopy measures light that is absorbed in matter via acoustic detection(111). Light is introduced into tissue, which absorbs and scatters according to the wavelength and tissue components. The absorbed energy induces local heating, which generates a sound wave through thermal expansion. The sound wave is then detected in a photoacoustic cell by a piezoelectric transducer (microphone). Photoacoustic (PA) cells are usually open-ended, and the open end is placed in contact with the sample. A simple schematic is shown in Fig. 4.

Selective detection of glucose is achieved by using specific wavelengths that target glucose absorption bands. QCLs or FTIR sources are most commonly used for photoacoustic spectroscopy of glucose, as the MIR absorption bands are typically targeted. NIR light sources can be used if the NIR absorption bands of glucose are targeted. Acquisition times with PA spectroscopy can be as low as a few seconds, as the main limitation is the scan time of the light source.

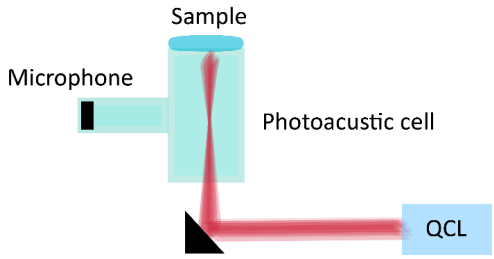

Figure 4: Schematic of a photoacoustic spectroscopy set-up. The source can be a QCL or another infrared source. A sample is illuminated and heated, and the resulting sound waves propagating in the photoacoustic cell are detected by a microphone.

Challenges

The challenges in PA spectroscopy for glucose monitoring are partially determined by the glucose absorption bands targeted. For MIR absorption bands it is necessary to use weak FTIR sources or expensive QCLs, while for NIR absorption bands the signal becomes much weaker.

The photoacoustic cell can be very sensitive to environmental variation, such as changes in temperature, humidity, and pressure. This has major effects on the measured glucose signal, and the accuracy seems to be limited for measurements of hypoglycaemic concentrations.

Research Status

Several groups have worked on creating a CGM device based on photoacoustic spectroscopy. The research has been focussed on non-invasive systems.

Kottmann et al. have reported the development of a small photoacoustic cell used for human in vivo measurements of glucose concentrations (112–114). Their measurements were quite accurate for glucose concentrations in the range 90-180 mg/dl ($R^2 = 0.8$). This was done using a set-up with two QCLs at fixed wavelengths, where the lasers alternated between being directed at the PA cell and a power meter. This allowed for improving issues with long-term drift. However, their best results were obtained while ventilating the PA cell with a constant flow of N_2. An N_2 flow will stabilise the humidity conditions inside the cell, but is not a feasible solution for a personalised device.

A similar sensor system based on photoacoustic spectroscopy has been reported by Pleitez et al. (115–117) They used a tuneable QCL with a range between 1220 and 1000 cm^{-1} as a source, and an open-ended PA cell was used as a cavity. Preliminary measurements were performed on volunteers who underwent oral glucose tolerance tests, and 100% of the measured glucose values were in zone A+B of the CEG.

A study of the Aprise sensor from Glucon Inc. was reported in 2007, which was a non-invasive sensor based on photoacoustic spectroscopy (118). 62 subjects were included in the study, and they underwent oral glucose tolerance, mixed meal, or glucose infusion tests. The study achieved a mean ARD of 19.9% for the sensor, and 94.6% of the paired measurements were within the A and B zones of the Clarke error grid. Although these preliminary results were quite good, the device was never commercialised. The sensor has not been described further in peer-reviewed literature, and the company website does not seem to be functional (glucon.com).

Fluorescence Sensing

Many molecules in the body are fluorescent, meaning that they can emit light at specific wavelengths after being excited by some incident radiation. Fluorescent molecules (fluorophores) can also be fabricated with specific desired properties, such as binding affinities and emission wavelengths, so that they are more useful in applications. Fluorescence sensing allows for very sensitive measurements, which has made it an interesting technology for clinical applications.

Studies have shown that glucose emits fluorescent light, and that glucose concentration affects fluorescence intensity. However, the direct fluorescent properties of glucose have not been a large focus in CGM research due to the low signal produced and issues with interfering signals. Instead, many research groups have tried to measure glucose via fluorescent labelling (119, 120). In this case, a fluorescence signal is produced from an exogenous fluorophore, i.e. a fluorophore that is introduced into the body. These fluorophores are engineered to form a complex with glucose molecules and should only fluoresce in the presence of glucose, as illustrated in Fig. 5. The fluorescent light intensity will depend on the glucose concentration, as more fluorophores are active when there is more glucose nearby. Several fluorescent systems have been investigated for glucose sensing, including boronic acid derivatives and concanavalin A (ConA). The chosen system should have a high selectivity for glucose over similar molecules, and has to be biocompatible.

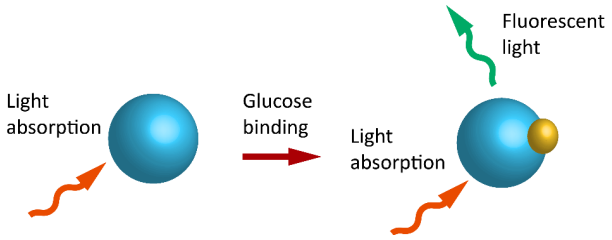

Figure 5: Sensing through fluorescent labelling. Fluorescence is suppressed when glucose is not present. When glucose binds to the fluorophore, fluorescence can occur.

Light in the UV or visible light range is typically used in fluorescence spectroscopy; cheap LEDs and photodiodes can therefore generally be used for measurements. These components can also be made very small, which is beneficial for wearable sensor systems. The light source that is used should not excite other endogenous fluorophores. Additionally, it is advantageous to create a fluorescent system where the fluorescence does not overlap with the fluorescence of other molecules, or with fluorescence absorption bands of other molecules, as this will be an interfering factor.

Challenges

There are several limitations for non-invasive measurements using fluorescence spectroscopy, as light scattered from skin would also be dependent on the amount of pigmentation and other differences in skin properties.

For minimally invasive and invasive measurements, fluorescence spectroscopy would still need calibration against finger-prick measurements. Drift of the fluorescence signal will occur both due to drift of the source, as well as gradual loss of fluorophores due to photobleaching.

There have been issues with achieving a linear fluorescent signal over the entire physiological range of glucose concentrations (119). Many fluorophores also bind other sugars such as galactose and fructose. Issues with saturation and the presence of interferents therefore limits the number of useful fluorophores.

Research Status

Several studies were conducted in the early 2000's into different possible fluorophores for glucose measurements, but many of these struggled with challenges such as low solubility and narrow measurement ranges. Several groups have tried to develop contact lens glucose sensors using fluorescence spectroscopy over the last decades (121–123). As mentioned, the glucose level in tear fluid does not seem to correlate well with the BGL, which has been a challenge for this research.

A subcutaneous glucose sensor based on fluorescence spectroscopy was first suggested in 1979 by Schultz et al. (124) This sensor concept has been further researched by the same group (125, 126), and is now under development by BioTex Inc. under the name Fluorescence Affinity Sensor (FAS). This sensor utilises a fluorophore inside a hollow dialysis fibre that is connected to an optical fibre, where fluorescence-labelled ConA is used as the fluorophore. Glucose displaces the dextran bound to the ConA, which induces a fluorescent signal proportional to the glucose concentration. The sensor has been tested in several pilot studies in humans and pigs (127, 128). For the human pilot study, a mean ARE between the sensor and the reference measurement of 13% was

achieved. The delay between the sensor measurement and the reference BGL was on average 4 minutes.

A clinical trial was reported by Müller et al., where they presented a similar fluorescence-based CGM system called FiberSense (129). Their measurement method was also based on labelled ConA. The sensor was implanted in two sites in six subjects for 14 days. The overall mean ARD was 8.3% for sensors used on the upper arm, and 11.4% for sensors used on the abdomen. The photometer with the source and detector was worn only during measurement sessions, while the sensor head was worn continuously for the entire study. The measurement sessions lasted for approximately 3 hours, and few data points were collected in the hypoglycaemic range. The sensor was calibrated once per day against finger-prick measurements.

The American company Senseonics has released the Eversense CGM system in Europe after receiving the CE mark in 2016. The Eversense has a mean ARD of 11.1% (130). This system consists of an implantable sensor that is placed under the skin, a removable transmitter that is worn over the sensor, and a smartphone app that receives the signal from the transmitter (131). The sensor is cylindrical with dimensions 3.3 mm x 15 mm, and can be inserted subcutaneously through a small incision. The sensor is approved for 90 days of continuous use before a replacement is necessary.

The sensor itself consists of a small polymer case. A light-emitting diode (LED) in the case excites the fluorophore and two photodiodes measure the fluorescent signal. The outside of the case is covered in a glucose-indicating hydrogel. Glucose reversibly binds to a boronic-acid derivative, which serves as the fluorescent indicator in the hydrogel.

To date, this is the only commercially available wearable CGM device that is based on an optical method. The sensor has a long lifetime relative to other commercially available glucose sensors, but must be placed through a small surgical incision in the arm by a physician. This may give some discomfort and risk of infection, although questionnaires answered by users indicate that the implantation is acceptable (132). Similar to other devices, the Eversense sensor also needs to be calibrated with finger-prick measurements twice per day.

Optical Coherence Tomography

Optical coherence tomography (OCT) is a measurement method that uses an interferometer with low coherence light (133). OCT requires one reference and one sample arm for the light, a moving window to vary the path length, and a photodetector for the signal. The light scattered back from tissue is combined with light from the reference arm, and the interference signal is sent to the photodetector. An interferogram is created if light from both arms has travelled the same optical distance, i.e. within the coherence length. The refractive index of the ISF will change as the glucose

concentration changes, which in turn changes the scattering coefficient. This change in scattering coefficient and concomitant variation in the interferogram is used to determine the glucose concentration.

OCT typically employs light in the NIR range, and as in NIR spectroscopy relatively cheap and small components are available. This method is used in several applications for 3D imaging with micrometre resolution, such as imaging of biological tissues.

Challenges

OCT is sensitive to motion artefacts, as any changes to the reference or sample arm lengths will interfere with the output signal. Non-invasive OCT is also sensitive to changes in the local environment of the skin, such as variations in skin temperature, pH, and humidity.

The measured change in scattering coefficient is relatively small, which is a major challenge for OCT in glucose sensing. The scattering coefficient can be affected by variations of other physiological compounds, and corrections must be made for individual differences in skin properties.

Research Status

There has been some research on OCT for non-invasive glucose measurements.
Larin et al. reported several studies that purported to show that OCT could be used to measure blood glucose non-invasively (134, 135). In vivo measurements in their OCT system correlated quite well with the BGL ($R = 0.88$), but both motion artefacts and skin temperature could significantly affect the OCT signal.

Several other research groups have been able to attain similar results with OCT and related systems, but it has not seemed to move past preliminary in vivo studies (136, 137). The company GlucoLight apparently worked on a glucose monitoring device based on OCT, and filed several patents in the late 2000's (138, 139). A small pilot study based on this device was also published in 2008, where 12 subjects with DM1 and 15 subject with type 2 diabetes participated (140). Measurements were conducted for 2 hours in each subject, and the device achieved a mean ARD of 11.5%. Hypoglycaemic glucose concentrations were not measured, and no further results from this system have been reported.

Discussion

The development of most optical methods for glucose monitoring is still progressing quite slowly, with few systems reaching even the prototype stage. These optical methods share many of the same challenges, such as a need for miniaturisation and high price of suitable components. There is also

the inherent challenge of measurements based on intensity, as such measurements are prone to signal drift. Many preliminary studies of new CGM methods also have problems with study size and duration. In vivo studies will often have results for measurements in only one or a few subjects, and for measurements performed over a few hours. This gives us some information on how a system performs under optimal conditions, but tells us very little about the between-subject variation and how the system performs for the entire lifetime of the device.

Additionally, there are separate issues for systems that attempt to measure non-invasively and invasively. The main challenges for non-invasive measurements are improving the SNR, correlation between measured glucose and the actual BGL, and the possible issues of calibrating the device to individual differences in skin properties. As mentioned, many non-invasive methods struggle with calibrating across individuals due to e.g. differences in skin water content and pigmentation. The model may work well on the person that the calibration is built on, but is often not transferable. Individual calibration can be implemented to improve device accuracy, although this is time-consuming. The main challenges for invasive measurements include minimising biofouling, extending sensor lifetime, correcting for signal drift, and ensuring patient acceptability.

Optical methods have several general advantages for CGM. Most optical techniques are generally not dependent on any reagents, which means that the lifetime can be much longer than for electrochemical sensors. This is especially important for minimally invasive and invasive measurements. Even systems based on fluorescence spectroscopy, which are dependent on fluorophores, seem to have much longer lifetimes than current electrochemical sensors. Optical sensing does not consume glucose, and the glucose concentration is therefore unchanged in the area surrounding the sensor. Non-invasive optical measurements would also have potential for pain-free CGM that affects the body minimally, given that a high measurement accuracy can be achieved. Smaller and cheaper components are continually being developed, which is an advantage for personalised devices.

The different optical technologies all have advantages and disadvantages. Interesting in vivo results have been shown using photoacoustic spectroscopy, but the sensitivity is too low for accurate measurements at physiological concentrations. Raman spectroscopy suffers from a very low signal that can be improved using SERS, but the challenge then becomes achieving stable surface-enhancement. The SERS substrate may degrade over time in the body, which limits the device lifetime and creates a risk for biotoxicity. NIRS has been explored extensively for non-invasive CGM, but no devices have yet been successfully commercialised. There are relatively few studies on MIRS for glucose measurements, as non-invasive measurements are less feasible than for NIRS and the price of components is generally high. Studies have shown that both NIRS and MIRS can measure glucose accurately in ISF and similar fluids, and these methods have high potential for

use in minimally invasive or invasive CGM systems. CGM systems that use fluorescent labelling have progressed the furthest of all the optical methods. Several devices are in a prototype stage, and the Eversense system is currently being commercialised. Glucose can be measured accurately with good fluorescence labelling, and the sensors have long lifetimes.

Of course, it is difficult to predict how the other optical methods will fare in the future, and if any of them are more likely to succeed due to technological advantages. There seems to be a trend, especially in non-invasive glucose measurements, of increased focus on developing data processing methods. This suggests that the instrumentation has reached a state where new advances only provide incremental improvements in sensitivity and that smart enough algorithms may account for the variable factors. Unless there is a large leap in technology or data processing techniques, this may be a fundamental limit for non-invasive CGM with optical methods. Indeed, with the implantable system from Eversense and many other groups working on invasive or minimally invasive systems, it seems that we might be moving away from the idea of non-invasive methods as the optimal solution. Minimally invasive sensors are already accepted by many patients in the form electrochemical CGM devices. Utilising sensing systems developed for the peritoneum is also a possibility, and may give faster sensor dynamics. This can lead to closed-loop systems that more closely mimic the functions of a healthy pancreas.

Conclusions

Current electrochemical CGM devices are an improvement for diabetes management as compared to intermittent finger-prick measurements, but they have short sensor lifetimes and must be calibrated against finger-prick measurements daily. Much effort has been spent on research into glucose measurement methods that could potentially replace these devices. Optical methods have many beneficial properties for CGM, but few devices have been commercialised despite decades of research.

Electrochemical devices are now the gold standard for CGM, and new devices will likely have to improve upon some aspects of these sensors in order to be accepted by patients and physicians. Several studies have shown progress for sensor systems based on spectroscopy, with some of the most promising results for MIR, NIR and Raman spectroscopy. Systems based on fluorescent labelling sensors have been the most successful so far, with several prototypes in development and one system being commercialised. The Eversense is a promising alternative to current electrochemical methods; its main advantage seems to be the comparably long lifetime. As long as patients tolerate the sensor insertion and removal, it may be the first optical CGM device to enjoy success.

Funding

This work was supported by the Research Council of Norway through the Double Intraperitoneal Artificial Pancreas project, grant number 248872.

List of Abbreviations

ARD – Absolute relative difference

ARE – Absolute relative error

ATR – Attenuated total reflectance

BGL – Blood glucose level

CEG – Clarke error grid

CG-EGA – Continuous glucose-error grid analysis

CGM – Continuous glucose monitoring

ConA – Concanavalin A

DM1 – Diabetes mellitus type 1

ISF – Interstitial fluid

FTIR – Fourier transform infrared

MIR – Mid-infrared

NIR – Near-infrared

OCT – Optical coherence tomography

PA - Photoacoustic

QCL – Quantum cascade laser

RMSEP – Root-mean-square error of prediction

SC – Subcutaneous

SEP – Standard error of prediction

SERS – Surface-enhanced Raman spectroscopy

SMBG – Self-monitoring of blood glucose

SNR – Signal-to-noise ratio

UV – Ultraviolet

1. Turner, A. P. F. (2013) Biosensors - Sense and sensitivity. *Chem. Soc. Rev.* 42 (8): 3184–3196.

2. Wang, J. (2008) Electrochemical glucose biosensors. *Chem. Rev.* 108 (2): 814–825.

3. Keenan, D. B., Mastrototaro, J. J., Zisser, H., Cooper, K. A., Raghavendhar, G., Lee, S. W., Yusi, J., Bailey, T. S., Brazg, R. L., and Shah, R. V. (2012) Accuracy of the Enlite 6-Day Glucose Sensor with Guardian and Veo Calibration Algorithms. *Diabetes Technol. Ther.* 14 (3): 225–231.

4. Bailey, T. S., Chang, A., and Christiansen, M. (2015) Clinical Accuracy of a Continuous Glucose Monitoring System With an Advanced Algorithm. *J. Diabetes Sci. Technol.* 9 (2): 209–214.

5. Thabit, H., Leelarathna, L., Wilinska, M. E., Elleri, D., Allen, J. M., Lubina-Solomon, A., Walkinshaw, E., Stadler, M., Choudhary, P., Mader, J. K., Dellweg, S., Benesch, C., Pieber, T. R., Arnolds, S., Heller, S. R., Amiel, S. A., Dunger, D., Evans, M. L., and Hovorka, R. (2015) Accuracy of Continuous Glucose Monitoring During Three Closed-Loop Home Studies Under Free-Living Conditions. *Diabetes Technol. Ther.* 17 (11): 801–807.

6. Weinstein, R. L., Schwartz, S. L., Brazg, R. L., Bugler, J. R., Peyser, T. A., and McGarraugh, G. V. (2007) Accuracy of the 5-Day FreeStyle Navigator Continuous Glucose Monitoring System. *Diabetes Care* 30 (5): 1125–30.

7. Valdes, T. I., and Moussy, F. (2000) *In Vitro* and *In Vivo* Degradation of Glucose Oxidase Enzyme Used for an Implantable Glucose Biosensor. *Diabetes Technol. Ther.* 2 (3): 367–376.

8. Scholten, K., and Meng, E. (2018) A review of implantable biosensors for closed-loop glucose control and other drug delivery applications. *Int. J. Pharm.*

9. Novak, M. T., Yuan, F., and Reichert, W. M. (2010) Modeling the relative impact of capsular tissue effects on implanted glucose sensor time lag and signal attenuation. *Anal. Bioanal. Chem.* 398 (4): 1695–1705.

10. Tura, A., Maran, A., and Pacini, G. (2007) Non-invasive glucose monitoring: Assessment of technologies and devices according to quantitative criteria. *Diabetes Res. Clin. Pract.* 77 (1): 16–40.

11. Girardin, C. M., Huot, C., Gonthier, M., and Delvin, E. (2009) Continuous glucose monitoring: A review of biochemical perspectives and clinical use in type 1 diabetes. *Clin. Biochem.* 42 (3): 136–142.

12. Vashist, S. K. (2012) Non-invasive glucose monitoring technology in diabetes management: A review. *Anal. Chim. Acta* 750: 16–27.

13. Potts, R. O., Tamada, J. A., and Tierney, M. J. (2002) Glucose monitoring by reverse iontophoresis. *Diabetes. Metab. Res. Rev.* 18 (Suppl. 1): S49–S53.

14. Caduff, A., Hirt, E., Feldman, Y., Ali, Z., and Heinemann, L. (2003) First human experiments with a novel non-invasive, non-optical continuous glucose monitoring system. *Biosens. Bioelectron.* 19 (3): 209–217.

15. The Diabetes Research in Children Network (DirectNet) Study Group. (2004) Accuracy of the GlucoWatch G2 Biographer and the Continuous Glucose Monitoring System During Hypoglycemia. *Diabetes Care* 27 (3): 722–726.

16. The Diabetes Research in Children Network (DirectNet) Study Group. (2005) Youth and Parent Satisfaction With Clinical Use of the GlucoWatch G2 Biographer in the Management of Pediatric Type 1 Diabetes. *Diabetes Care* 28 (8): 1929–1935.

17. Wentholt, I. M. E., Hoekstra, J. B. L., Zwart, A., and DeVries, J. H. (2005) Pendra goes Dutch: lessons for the CE mark in Europe. *Diabetologia* 48 (6): 1055–1058.

18. Retnakaran, R., Hochman, J., DeVries, J. H., Hanaire-Broutin, H., Heine, R. J., Melki, V., and Zinman, B. (2004) Continuous Subcutaneous Insulin Infusion Versus Multiple Daily Injections: The impact of baseline A1c. *Diabetes Care* 27 (11): 2590–2596.

19. Battelino, T., Conget, I., Olsen, B., Schütz-Fuhrmann, I., Hommel, E., Hoogma, R., Schierloh, U., Sulli, N., and Bolinder, J. (2012) The use and efficacy of continuous glucose monitoring in type 1 diabetes treated with insulin pump therapy: A randomised controlled trial. *Diabetologia* 55 (12): 3155–3162.

20. Breton, M., Farret, A., Bruttomesso, D., Anderson, S., Magni, L., Patek, S., Man, C. D., Place, J., Demartini, S., Del Favero, S., Toffanin, C., Hughes-Karvetski, C., Dassau, E., Zisser, H., Doyle, F. J., De Nicolao, G., Avogaro, A., Cobelli, C., Renard, E., and Kovatchev, B. (2012) Fully Integrated Artificial Pancreas in Type 1 Diabetes: Modular Closed-Loop Glucose Control Maintains Near Normoglycemia. *Diabetes* 61 (9): 2230–2237.

21. Frier, B. M. (2004) Morbidity of hypoglycemia in type 1 diabetes. *Diabetes Res. Clin. Pract.* 65S: S47–S52.

22. Nathan, D. M. (1993) Long-Term Complications of Diabetes Mellitus. *N. Engl. J. Med.* 328: 1676–1685.

23. Wang, P. H., Lau, J., and Chalmers, T. C. (1993) Meta-analysis of effects of intensive blood-glucose control on late complications of type I diabetes. *Lancet* 341 (8856): 1306–1309.

24. The Diabetes Control and Complications Trial Research Group. (1993) The Effect of Intensive Treatment of Diabetes on the Development and Progression of Long-Term Complications in Insulin-Dependent Diabetes Mellitus. *N. Engl. J. Med.* 329 (14): 977–986.

25. Minder, A. E., Albrecht, D., Schäfer, J., and Zulewski, H. (2013) Frequency of blood glucose testing in well educated patients with diabetes mellitus type 1: How often is enough? *Diabetes Res. Clin. Pract.* 101 (1): 57–61.

26. Deiss, D., Bolinder, J., Riveline, J. P., Battelino, T., Bosi, E., Tubiana-Rufi, N., Kerr, D., and Phillip, M. (2006) Improved Glycemic Control in Poorly Controlled Patients with Type 1 Diabetes Using Real-Time Continuous Glucose Monitoring. *Diabetes Care* 29 (12): 2730–2732.

27. Pickup, J. C., Freeman, S. C., and Sutton, A. J. (2011) Glycaemic control in type 1 diabetes during real time continuous glucose monitoring compared with self monitoring of blood glucose: meta-analysis of randomised controlled trials using individual patient data. *BMJ* 343: d3805.

28. Cobelli, C., Renard, E., and Kovatchev, B. (2011) Artificial Pancreas: Past, Present, Future. *Diabetes* 60 (11): 2672–2682.

29. Clarke, W. L., Cox, D., Gonder-Frederick, L. A., Carter, W., and Pohl, S. L. (1987) Evaluating Clinical Accuracy of Systems for Self-Monitoring of Blood Glucose. *Diabetes Care* 10 (5): 622–628.

30. Parkes, J. L., Slatin, S. L., Pardo, S., and Ginsberg, B. H. (2000) A New Consensus Error Grid to Evaluate the Clinical Significance of Inaccuracies in the Measurement of Blood Glucose. *Diabetes Care* 23 (8): 1143–1148.

31. Bland, J. M., and Altman, D. G. (1986) Statistical Methods for Assessing Agreement Between Two Methods of Clinical Measurement. *Lancet* 327: 307–310.

32. Kovatchev, B. P., Gonder-Frederick, L. A., Cox, D. J., and Clarke, W. L. (2004) Evaluating the Accuracy of Continuous Glucose-Monitoring Sensors: Continuous glucose-error grid

analysis illustrated by TheraSense Freestyle Navigator data. *Diabetes Care* 27 (8): 1922–1928.

33. Wentholt, I. M., Hoekstra, J. B., and DeVries, J. H. (2006) A Critical Appraisal of the Continuous Glucose-Error Grid Analysis. *Diabetes Care* 29 (8): 1805–1811.

34. Moyer, J., Wilson, D., Finkelshtein, I., Wong, B., and Potts, R. (2012) Correlation Between Sweat Glucose and Blood Glucose in Subjects with Diabetes. *Diabetes Technol. Ther.* 14 (5): 398–402.

35. Sener, A., Jurysta, C., Bulur, N., Oguzhan, B., Satman, I., Yilmaz, T. M., and Malaisse, W. J. (2009) Salivary Glucose Concentration and Excretion in Normal and Diabetic Subjects. *J. Biomed. Biotechnol.* 2009.

36. Wang, C., Mbi, A., and Shepherd, M. (2010) A Study on Breath Acetone in Diabetic Patients Using a Cavity Ringdown Breath Analyzer: Exploring Correlations of Breath Acetone with Blood Glucose and Glycohemoglobin A1C. *IEEE Sens. J.* 10 (1): 54–63.

37. Baca, J. T., Taormina, C. R., Feingold, E., Finegold, D. N., Grabowski, J. J., and Asher, S. A. (2007) Mass Spectral Determination of Fasting Tear Glucose Concentrations in Nondiabetic Volunteers. *Clin. Chem.* 53 (7): 1370–1372.

38. Baca, J. T., Finegold, D. N., and Asher, S. A. (2007) Tear Glucose Analysis for the Noninvasive Detection and Monitoring of Diabetes Mellitus. *Ocul. Surf.* 5 (4): 280–293.

39. Wentholt, I. M., Vollebregt, M. A., Hart, A. A., Hoekstra, J. B., and DeVries, J. H. (2005) Comparison of a Needle-Type and a Microdialysis Continuous Glucose Monitor in Type 1 Diabetic Patients. *Diabetes Care* 28 (12): 2871–2876.

40. Basu, A., Dube, S., Veettil, S., Slama, M., Kudva, Y. C., Peyser, T., Carter, R. E., Cobelli, C., and Basu, R. (2015) Time Lag of Glucose From Intravascular to Interstitial Compartment in Type 1 Diabetes. *J. Diabetes Sci. Technol.* 9 (1): 63–68.

41. Burnett, D. R., Huyett, L. M., Zisser, H. C., Doyle, F. J., and Mensh, B. D. (2014) Glucose Sensing in the Peritoneal Space Offers Faster Kinetics Than Sensing in the Subcutaneous Space. *Diabetes* 63 (7): 2498–2505.

42. Fougner, A. L., Kölle, K., Skjærvold, N. K., Elvemo, N. A. L., Hjelme, D. R., Ellingsen, R., Carlsen, S. M., and Stavdahl, Ø. (2016) Intraperitoneal Glucose Sensing is Sometimes Surprisingly Rapid. *Model. Identif. Control* 37 (2): 121–131.

43. Renard, E. (2008) Insulin Delivery Route for the Artificial Pancreas: Subcutaneous, Intraperitoneal, or Intravenous? Pros and Cons. *J. Diabetes Sci. Technol.* 2 (4): 735–738.

44. Huyett, L. M., Mittal, R., Zisser, H. C., Luxon, E. S., Yee, A., Dassau, E., Doyle, F. J., and Burnett, D. R. (2016) Preliminary Evaluation of a Long-Term Intraperitoneal Glucose Sensor With Flushing Mechanism. *J. Diabetes Sci. Technol.* 10 (5): 1192–1194.

45. Heller, A., and Feldman, B. (2008) Electrochemical Glucose Sensors and Their Applications in Diabetes Management. *Chem. Rev.* 108 (7): 2482–2505.

46. Ward, W. K. (2008) A Review of the Foreign-Body Response to Subcutaneously-Implanted Devices: The Role of Macrophages and Cytokines in Biofouling and Fibrosis. *J. Diabetes Sci. Technol.* 2 (5): 768–777.

47. Keenan, D. B., Mastrototaro, J. J., Voskanyan, G., and Steil, G. M. (2009) Delays in Minimally Invasive Continuous Glucose Monitoring Devices: A Review of Current Technology. *J. Diabetes Sci. Technol.* 3 (5): 1207–14.

48. Purvinis, G., Cameron, B. D., and Altrogge, D. M. (2011) Noninvasive Polarimetric-Based Glucose Monitoring: An in Vivo Study. *J. Diabetes Sci. Technol.* 5 (2): 380–387.

49. Pleitez, M. A., Hertzberg, O., Bauer, A., Seeger, M., Lieblein, T., Von Lilienfeld-Toal, H., and Mäntele, W. (2015) Photothermal deflectometry enhanced by total internal reflection enables non-invasive glucose monitoring in human epidermis. *Analyst* 140: 483–488.

50. Hertzberg, O., Bauer, A., Küderle, A., Pleitez, M. A., and Mäntele, W. (2017) Depth-selective photothermal IR spectroscopy of skin: potential application for non-invasive glucose measurement. *Analyst* 142: 495–502.

51. Yang, W., Liao, N., Cheng, H., Li, Y., Bai, X., and Deng, C. (2018) Determination of NIR informative wavebands for transmission non-invasive blood glucose measurement using a Fourier transform spectrometer. *AIP Adv.* 8 (3): 35216.

52. Jensen, P. S., and Bak, J. (2002) Near-Infrared Transmission Spectroscopy of Aqueous Solutions: Influence of Optical Pathlength on Signal-to-Noise Ratio. *Appl. Spectrosc.* 56 (12): 1600–1606.

53. Heise, H. M., Marbach, R., Koschinsky, T., and Gries, F. A. (1994) Noninvasive Blood Glucose Sensors Based on Near-Infrared Spectroscopy. *Artif. Organs* 18 (6): 439–447.

54. Arnold, M. A., and Small, G. W. (2005) Noninvasive Glucose Sensing. *Anal. Chem.* 77 (17): 5429–5439.

55. Liu, J., Liu, R., and Xu, K. (2015) Accuracy of Noninvasive Glucose Sensing Based on Near-Infrared Spectroscopy. *Appl. Spectrosc.* 69 (11): 1313–1318.

56. Maruo, K., Tsurugi, M., Tamura, M., and Ozaki, Y. (2003) In Vivo Noninvasive Measurement of Blood Glucose by Near-Infrared Diffuse-Reflectance Spectroscopy. *Appl. Spectrosc.* 57 (10): 1236–1244.

57. Schrader, W., Meuer, P., Popp, J., Kiefer, W., Menzebach, J. U., and Schrader, B. (2005) Non-invasive glucose determination in the human eye. *J. Mol. Struct.* 735–736 (Spec. Iss.): 299–306.

58. Marbach, R., Koschinsky, T. H., Gries, F. A., and Heise, H. M. (1993) Noninvasive Blood Glucose Assay by Near-Infrared Diffuse Reflectance Spectroscopy of the Human Inner Lip. *Appl. Spectrosc.* 47 (7): 875–881.

59. Burmeister, J. J., Arnold, M. A., and Small, G. W. (2000) Noninvasive Blood Glucose Measurements by Near-Infrared Transmission Spectroscopy Across Human Tongues. *Diabetes Technol. Ther.* 2 (1): 5–16.

60. Zhang, W., Liu, R., Zhang, W., Jia, H., and Xu, K. (2013) Discussion on the validity of NIR spectral data in non-invasive blood glucose sensing. *Biomed. Opt. Express* 4 (6): 789–802.

61. van der Kamp, K. W. H. J., Hauch, K. D., Feijen, J., and Horbett, T. A. (1995) Contact activation during incubation of five different polyurethanes or glass in plasma. *J. Biomed. Mater. Res.* 29: 1303–1306.

62. Ren, M., and Arnold, M. A. (2007) Comparison of multivariate calibration models for glucose, urea, and lactate from near-infrared and Raman spectra. *Anal. Bioanal. Chem.* 387 (3): 879–888.

63. Chung, H., Arnold, M. A., Rhiel, M., and Murhammer, D. W. (1996) Simultaneous Measurements of Glucose , Glutamine , Ammonia , Lactate , and Glutamate in Aqueous Solutions by Near-Infrared Spectroscopy. *Appl. Spectrosc.* 50 (2): 270–276.

64. Heise, H. M., Marbach, R., Bittner, A., and Koschinsky, T. (1998) Clinical chemistry and near infrared spectroscopy: Multicomponent assay for human plasma and its evaluation for the determination of blood substrates. *J. Near Infrared Spectrosc.* 6 (1): 361–374.

65. Turza, S., Mitsunori, K., and Kawano, S. (2006) Near infrared analysis of whole blood and

plasma in blood-collecting tubes. *J. Near Infrared Spectrosc.* 14: 147–153.

66. Sharma, S., Goodarzi, M., Delanghe, J., Ramon, H., and Saeys, W. (2014) Using Experimental Data Designs and Multivariate Modeling to Assess the Effect of Glycated Serum Protein Concentration on Glucose Prediction from Near-Infrared Spectra of Human Serum. *Appl. Spectrosc.* 68 (4): 398–405.

67. Amerov, A. K., Chen, J., Small, G. W., and Arnold, M. A. (2005) Scattering and Absorption Effects in the Determination of Glucose in Whole Blood by Near-Infrared Spectroscopy. *Anal. Chem.* 77 (14): 4587–4594.

68. Kramer, K. E., and Small, G. W. (2009) Digital Filtering and Model Updating Methods for Improving the Robustness of Near-Infrared Multivariate Calibrations. *Appl. Spectrosc.* 63 (2): 246–255.

69. Goodarzi, M., Sharma, S., Ramon, H., and Saeys, W. (2015) Multivariate calibration of NIR spectroscopic sensors for continuous glucose monitoring. *TrAC - Trends Anal. Chem.* 67: 147–158.

70. Goodarzi, M., and Saeys, W. (2016) Selection of the most informative near infrared spectroscopy wavebands for continuous glucose monitoring in human serum. *Talanta* 146: 155–165.

71. Rosenthal, R. D., Paynter, L. N., and Mackie, L. H. (1992) Non-Invasive Measurement of Blood Glucose. *U.S. Pat. No. 5,086,229*.

72. Olesberg, J. T., Liu, L., Van Zee, V., and Arnold, M. A. (2006) In Vivo Near-Infrared Spectroscopy of Rat Skin Tissue with Varying Blood Glucose Levels. *Anal. Chem.* 78 (1): 215–223.

73. Maruo, K., Oota, T., Tsurugi, M., Nakagawa, T., Arimoto, H., Hayakawa, M., Tamura, M., Ozaki, Y., and Yamada, Y. (2006) Noninvasive Near-Infrared Blood Glucose Monitoring Using a Calibration Model Built by a Numerical Simulation Method : Trial Application to Patients in an Intensive Care Unit. *Appl. Spectrosc.* 60 (12): 1423–1431.

74. Maruo, K., and Yamada, Y. (2015) Near-infrared noninvasive blood glucose prediction without using multivariate analyses: introduction of imaginary spectra due to scattering change in the skin. *J. Biomed. Opt.* 20 (4): 47003.

75. Ryckeboer, E., Bockstaele, R., Vanslembrouck, M., and Baets, R. (2014) Glucose sensing by waveguide-based absorption spectroscopy on a silicon chip. *Biomed. Opt. Express* 5 (5): 1636–1648.

76. Delbeke, D., Baets, R., Bogaerts, W., and Ryckeboer, E. M. P. (2017) Implantable sensor. *U.S. Pat. No. 9,532,738*.

77. Ben Mohammadi, L., Klotzbuecher, T., Sigloch, S., Welzel, K., Göddel, M., Pieber, T. R., and Schaupp, L. (2014) In vivo evaluation of a chip based near infrared sensor for continuous glucose monitoring. *Biosens. Bioelectron.* 53: 99–104.

78. Ben Mohammadi, L., Klotzbuecher, T., Sigloch, S., Welzel, K., Goeddel, M., Pieber, T. R., and Schaupp, L. (2015) Clinical performance of a low cost near infrared sensor for continuous glucose monitoring applied with subcutaneous microdialysis. *Biomed. Microdevices* 17 (4): 73.

79. Caduff, A., Zanon, M., Zakharov, P., Mueller, M., Talary, M., Krebs, A., Stahel, W. A., and Donath, M. (2018) First Experiences With a Wearable Multisensor in an Outpatient Glucose Monitoring Study, Part I: The Users' View. *J. Diabetes Sci. Technol.* 12 (3): 562–568.

80. Zanon, M., Mueller, M., Zakharov, P., Talary, M. S., Donath, M., Stahel, W. A., and Caduff, A. (2017) First Experiences With a Wearable Multisensor Device in a Noninvasive

Continuous Glucose Monitoring Study at Home, Part II: The Investigators' View. *J. Diabetes Sci. Technol.* 12 (3): 554–561.

81. Ellis, D. I., and Goodacre, R. (2006) Metabolic fingerprinting in disease diagnosis : biomedical applications of infrared and Raman spectroscopy. *Analyst* 131: 875–885.

82. Faist, J., Capasso, F., Sivco, D. L., Sirtori, C., Hutchinson, A. L., and Cho, A. Y. (1994) Quantum cascade laser. *Science* 264 (5158): 553–6.

83. Schwaighofer, A., Brandstetter, M., and Lendl, B. (2017) Quantum cascade lasers (QCLs) in biomedical spectroscopy. *Chem. Soc. Rev.* 46: 5903–5924.

84. Heise, H. M., Ku, L., and Butvina, L. N. (1998) Attenuated total reflection mid-infrared spectroscopy for clinical chemistry applications using silver halide fibers. *Sensors Actuators B* 51: 84–91.

85. Bhandare, P., Mendelson, Y., Peura, R. A., Janatsch, G., Kruse-Jarres, J. D., Marbach, R., and Heise, H. M. (1993) Multivariate Determination of Glucose in Whole Blood Using Partial Least-Squares and Artificial Neural Networks Based on Mid-Infrared Spectroscopy. *Appl. Spectrosc.* 47 (8): 1214–1221.

86. Heise, H. M., Marbach, R., Koschinsky, T., and Gries, F. A. (1994) Multicomponent Assay for Blood Substrates in Human Plasma by Mid-Infrared Spectroscopy and its Evaluation for Clinical Analysis. *Appl. Spectrosc.* 48 (1): 85–95.

87. Brandstetter, M., Volgger, L., Genner, A., Jungbauer, C., and Lendl, B. (2013) Direct determination of glucose, lactate and triglycerides in blood serum by a tunable quantum cascade laser-based mid-IR sensor. *Appl. Phys. B* 110 (2): 233–239.

88. Martin, W. B., Mirov, S., and Venugopalan, R. (2002) Using two discrete frequencies within the middle infrared to quantitatively determine glucose in serum. *J. Biomed. Opt.* 7 (4): 613–617.

89. Kasahara, R., Kino, S., Soyama, S., and Matsuura, Y. (2018) Noninvasive glucose monitoring using mid-infrared absorption spectroscopy based on a few wavenumbers. *Biomed. Opt. Express* 9 (1): 289–302.

90. Liakat, S., Bors, K. A., Xu, L., Woods, C. M., Doyle, J., and Gmachl, C. F. (2014) Noninvasive in vivo glucose sensing on human subject using mid-infrared light. *Biomed. Opt. Express* 5 (7): 2397–2404.

91. Werth, A., Liakat, S., Dong, A., Woods, C. M., and Gmachl, C. F. (2018) Implementation of an integrating sphere for the enhancement of noninvasive glucose detection using quantum cascade laser spectroscopy. *Appl. Phys. B* 124: 75.

92. Vrančić, C., Fomichova, A., Gretz, N., Herrmann, C., Neudecker, S., Pucci, A., and Petrich, W. (2011) Continuous glucose monitoring by means of mid-infrared transmission laser spectroscopy in vitro. *Analyst* 136 (6): 1192–1198.

93. Vrančić, C., Kruger, N., Gretz, N., Neudecker, S., Pucci, A., and Petrich, W. (2014) A quantitative look inside the body: Minimally invasive infrared analysis in vivo. *Anal. Chem.* 86 (21): 10511–10514.

94. Kino, S., Omori, S., Katagiri, T., and Matsuura, Y. (2016) Hollow optical-fiber based infrared spectroscopy for measurement of blood glucose level by using multi-reflection prism. *Biomed. Opt. Express* 7 (2): 701–708.

95. Yoshioka, K., Kino, S., and Matsuura, Y. (2017) Noninvasive measurement of blood glucose level using mid-infrared quantum cascade lasers. *Biomed. Imaging Sens. Conf.* 10251.

96. Magarian, P., and Sterling, B. (2009) Plasma-Generating Glucose Monitor Accuracy

Demonstrated in an Animal Model. *J. Diabetes Sci. Technol.* 3 (6): 1411–1418.

97. Barassi, A., Umbrello, M., Ghilardi, F., Damele, C. A. L., Massaccesi, L., Iapichino, G., and Melzi d'Eril, G. V. (2015) Evaluation of the performance of a new OptiScanner™ 5000 system for an intermittent glucose monitoring. *Clin. Chim. Acta* 438: 252–254.

98. Brandstetter, M., Sumalowitsch, T., Genner, A., Posch, A. E., Herwig, C., Drolz, A., Fuhrmann, V., Perkmann, T., and Lendl, B. (2013) Reagent-free monitoring of multiple clinically relevant parameters in human blood plasma using a mid-infrared quantum cascade laser based sensor system. *Analyst* 138: 4022–4028.

99. Xu, H., Wang, X.-H., Persson, M. P., Xu, H. Q., Käll, M., and Johansson, P. (2004) Unified Treatment of Fluorescence and Raman Scattering Processes near Metal Surfaces. *Phys. Rev. Lett.* 93 (24): 243002.

100. Schrader, B. (1996) Raman spectroscopy in the near infrared - a most capable method of vibrational spectroscopy. *Fresenius. J. Anal. Chem.* 355 (3–4): 233–239.

101. Asharani, P. V., Lian Wu, Y., Gong, Z., and Valiyaveettil, S. (2008) Toxicity of silver nanoparticles in zebrafish models. *Nanotechnology* 19 (25): 255102.

102. Dykman, L. A., and Khlebtsov, N. G. (2014) Uptake of engineered gold nanoparticles into mammalian cells. *Chem. Rev.* 114 (2): 1258–1288.

103. Borchert, M. S., Storrie-Lombardi, M. C., and Lambert, J. L. (1999) A noninvasive glucose monitor: preliminary results in rabbits. *Diabetes Technol. Ther.* 1 (2): 145–151.

104. Pelletier, C. C., Lambert, J. L., and Borchert, M. (2005) Determination of glucose in human aqueous humor using Raman spectroscopy and designed-solution calibration. *Appl. Spectrosc.* 59 (8): 1024–1031.

105. Dingari, N. C., Barman, I., Kang, J. W., Kong, C.-R., Dasari, R. R., and Feld, M. S. (2011) Wavelength selection-based nonlinear calibration for transcutaneous blood glucose sensing using Raman spectroscopy. *J. Biomed. Opt.* 16 (8): 87009.

106. Kong, C. R., Barman, I., Dingari, N. C., Kang, J. W., Galindo, L., Dasari, R. R., and Feld, M. S. (2011) A novel non-imaging optics based Raman spectroscopy device for transdermal blood analyte measurement. *AIP Adv.* 1 (3): 32175.

107. Shih, W.-C., Bechtel, K. L., and Rebec, M. V. (2015) Noninvasive glucose sensing by transcutaneous Raman spectroscopy. *J. Biomed. Opt.* 20 (5): 51036.

108. Yuen, J. M., Shah, N. C., Walsh, J. T., Glucksberg, M. R., and Van Duyne, R. P. (2010) Transcutaneous Glucose Sensing by Surface-Enhanced Spatially Offset Raman Spectroscopy in a Rat Model. *Anal. Chem.* 82 (20): 8382–8385.

109. Ma, K., Yuen, J. M., Shah, N. C., Walsh, J. T., Glucksberg, M. R., and Van Duyne, R. P. (2011) In Vivo, Transcutaneous Glucose Sensing Using Surface-Enhanced Spatially Offset Raman Spectroscopy: Multiple Rats, Improved Hypoglycemic Accuracy, Low Incident Power, and Continuous Monitoring for Greater than 17 Days. *Anal. Chem.* 83 (23): 9146–9152.

110. Lipson, J., Bernhardt, J., Block, U., Freeman, W. R., Hofmeister, R., Hristakeva, M., Lenosky, T., McNamara, R., Petrasek, D., Veltkamp, D., and Waydo, S. (2009) Requirements for Calibration in Noninvasive Glucose Monitoring by Raman Spectroscopy. *J. Diabetes Sci. Technol.* 3 (2): 233–241.

111. West, G. A., Barrett, J. J., Siebert, D. R., and Reddy, K. V. (1983) Photoacoustic spectroscopy. *Rev. Sci. Instrum.* 54 (7): 797–817.

112. Kottmann, J., Rey, J. M., and Sigrist, M. W. (2011) New photoacoustic cell design for

studying aqueous solutions and gels. *Rev. Sci. Instrum.* 82 (8): 84903.

113. Kottmann, J., Rey, J. M., Reichmann, E., and Sigrist, M. W. (2012) Glucose sensing in human epidermis using mid-infrared photoacoustic detection. *Biomed. Opt. Express* 3 (4): 667–680.

114. Kottmann, J., Rey, J. M., and Sigrist, M. W. (2016) Mid-Infrared Photoacoustic Detection of Glucose in Human Skin: Towards Non-Invasive Diagnostics. *Sensors* 16 (10): 1–14.

115. Pleitez, M., Von Lilienfeld-Toal, H., and Mäntele, W. (2012) Infrared spectroscopic analysis of human interstitial fluid in vitro and in vivo using FT-IR spectroscopy and pulsed quantum cascade lasers (QCL): Establishing a new approach to non invasive glucose measurement. *Spectrochim. Acta - Part A Mol. Biomol. Spectrosc.* 85 (1): 61–65.

116. Pleitez, M. A., Lieblein, T., Bauer, A., Hertzberg, O., Von Lilienfeld-Toal, H., and Mäntele, W. (2013) In Vivo Noninvasive Monitoring of Glucose Concentration in Human Epidermis by Mid-Infrared Pulsed Photoacoustic Spectroscopy. *Anal. Chem.* 85 (2): 1013–1020.

117. Pleitez, M. A., Lieblein, T., Bauer, A., Hertzberg, O., Von Lilienfeld-Toal, H., and Mäntele, W. (2013) Windowless ultrasound photoacoustic cell for in vivo mid-IR spectroscopy of human epidermis: Low interference by changes of air pressure, temperature, and humidity caused by skin contact opens the possibility for a non-invasive monitoring of glucose in th. *Rev. Sci. Instrum.* 84 (8): 84901.

118. Weiss, R., Yegorchikov, Y., Shusterman, A., and Raz, I. (2007) Noninvasive Continuous Glucose Monitoring Using Photoacoustic Technology—Results from the First 62 Subjects. *Diabetes Technol. Ther.* 9 (1): 68–74.

119. Moschou, E. A., Sharma, B. V., Deo, S. K., and Daunert, S. (2004) Fluorescence Glucose Detection: Advances Toward the Ideal In Vivo Biosensor. *J. Fluoresc.* 14 (5): 535–547.

120. Pickup, J. C., Hussain, F., Evans, N. D., Rolinski, O. J., and Birch, D. J. S. (2005) Fluorescence-based glucose sensors. *Biosens. Bioelectron.* 20 (12): 2555–2565.

121. Badugu, R., Lakowicz, J. R., and Geddes, C. D. (2004) Ophthalmic glucose sensing: a novel monosaccharide sensing disposable and colorless lens. *Analyst* 129 (6): 516–521.

122. Badugu, R., Lakowicz, J. R., and Geddes, C. D. (2005) A glucose-sensing contact lens : from bench top to patient. *Curr. Opin. Biotechnol.* 16: 100–107.

123. Yao, H., Shum, A. J., Cowan, M., Lähdesmäki, I., and Parviz, B. A. (2011) A contact lens with embedded sensor for monitoring tear glucose level. *Biosens. Bioelectron.* 26 (7): 3290–3296.

124. Schultz, J. S., and Sims, G. (1979) Affinity sensors for individual metabolites. *Biotechnol. Bioeng. Symp.* (9): 65–71.

125. Schultz, J. S., Mansouri, S., and Goldstein, I. J. (1982) Affinity Sensor: A New Technique for Developing Implantable Sensors for Glucose and Other Metabolites. *Diabetes Care* 5 (3): 245–53.

126. Ballerstadt, R., and Schultz, J. S. (2000) A Fluorescence Affinity Hollow Fiber Sensor for Continuous Transdermal Glucose Monitoring. *Anal. Chem.* 72 (17): 4185–4192.

127. Dutt-Ballerstadt, R., Evans, C., Pillai, A. P., Orzeck, E., Drabek, R., Gowda, A., and McNichols, R. (2012) A Human Pilot Study of the Fluorescence Affinity Sensor for Continuous Glucose Monitoring in Diabetes. *J. Diabetes Sci. Technol.* 6 (2): 362–370.

128. Dutt-ballerstadt, R., Evans, C., Pillai, A. P., Gowda, A., Mcnichols, R., Rios, J., and Cohn, W. (2013) Acute In Vivo Performance Evaluation of the Fluorescence Affinity Sensor in the Intravascular and Interstitial Space in Swine. *J. Diabetes Sci. Technol.* 7 (1): 35–44.

129. Muller, A. J., Knuth, M., Nikolaus, K. S., Krivanek, R., Kuster, F., and Hasslacher, C. (2013) First clinical evaluation of a new percutaneous optical fiber glucose sensor for continuous glucose monitoring in diabetes. *J. Diabetes Sci. Technol.* 7 (1): 13–23.

130. Kropff, J., Choudhary, P., Neupane, S., Barnard, K., Bain, S. C., Kapitza, C., Forst, T., Link, M., Dehennis, A., and De Vries, J. H. (2017) Accuracy and Longevity of an Implantable Continuous Glucose Sensor in the PRECISE study: A 180-day, Prospective, Multicenter, Pivotal Trial. *Diabetes Care* 40 (1): 63–68.

131. Mortellaro, M., and DeHennis, A. (2014) Performance characterization of an abiotic and fluorescent-based continuous glucose monitoring system in patients with type 1 diabetes. *Biosens. Bioelectron.* 61: 227–231.

132. Barnard, K. D., Kropff, J., Choudhary, P., Neupane, S., Bain, S. C., Kapitza, C., Forst, T., Link, M., Mdingi, C., and DeVries, J. H. (2017) Acceptability of Implantable Continuous Glucose Monitoring Sensor. *J. Diabetes Sci. Technol.* 12 (3): 634–638.

133. Fercher, A. F., Drexler, W., Hitzenberger, C. K., and Lasser, T. (2003) Optical coherence tomography - principles and applications. *Reports Prog. Phys.* 66: 239–303.

134. Larin, K. V., Eledrisi, M. S., Motamedi, M., and Esenaliev, R. O. (2002) Noninvasive blood glucose monitoring with optical coherence tomography: A pilot study in human subjects. *Diabetes Care* 25 (12): 2263–2267.

135. Larin, K. V, Motamedi, M., Ashitkov, T. V, and Esenaliev, R. O. (2003) Specificity of noninvasive blood glucose sensing using optical coherence tomography technique: a pilot study. *Phys. Med. Biol* 48: 1371–1390.

136. Kinnunen, M., Myllylä, R., and Vainio, S. (2008) Detecting glucose-induced changes in in vitro and in vivo experiments with optical coherence tomography. *J. Biomed. Opt.* 13 (2): 21111.

137. John, P., Vasa, N. J., Unni, S. N., and Rao, S. R. (2017) Glucose sensing in oral mucosa simulating phantom using differential absorption based frequency domain low-coherence interferometry. *Appl. Opt.* 56 (29): 8257.

138. Schurman, M. J., and Shakespeare, W. J. (2007) Method and apparatus for monitoring glucose levels in a biological tissue. *U.S Pat. No. 7,254,429*.

139. Schurman, M. J., and Shakespeare, W. J. (2009) OCT based method for diagnosis and therapy. *U.S. Pat. No. 7,510,849*.

140. Gabbay, R. A., and Sivarajah, S. (2008) Optical Coherence Tomography-Based Continuous Noninvasive Glucose Monitoring in Patients with Diabetes. *Diabetes Technol. Ther.* 10 (3): 188–193.

Paper II

Infrared Spectroscopy with a Fiber-Coupled Quantum Cascade Laser for Attenuated Total Reflection Measurements Towards Biomedical Applications
I.L. Jernelv, K. Strøm, D.R. Hjelme, A. Aksnes
Sensors, Vol. 19(23), 5130, 2019.

sensors

MDPI

Article

Infrared Spectroscopy with a Fiber-Coupled Quantum Cascade Laser for Attenuated Total Reflection Measurements Towards Biomedical Applications

Ine L. Jernelv *, Karina Strøm, Dag Roar Hjelme and Astrid Aksnes

Department of Electronic Systems, Norwegian University of Science and Technology (NTNU), O.S. Bragstads plass 2A, 7491 Trondheim, Norway; strmkarina@gmail.com (K.S.); dag.hjelme@ntnu.no (D.R.H.); astrid.aksnes@ntnu.no (A.A.)

* Correspondence: ine.jernelv@ntnu.no

Received: 15 October 2019; Accepted: 20 November 2019; Published: 23 November 2019

Abstract: The development of rapid and accurate biomedical laser spectroscopy systems in the mid-infrared has been enabled by the commercial availability of external-cavity quantum cascade lasers (EC-QCLs). EC-QCLs are a preferable alternative to benchtop instruments such as Fourier transform infrared spectrometers for sensor development as they are small and have high spectral power density. They also allow for the investigation of multiple analytes due to their broad tuneability and through the use of multivariate analysis. This article presents an in vitro investigation with two fiber-coupled measurement setups based on attenuated total reflection spectroscopy and direct transmission spectroscopy for sensing. A pulsed EC-QCL (1200–900 cm^{-1}) was used for measurements of glucose and albumin in aqueous solutions, with lactate and urea as interferents. This analyte composition was chosen as an example of a complex aqueous solution with relevance for biomedical sensors. Glucose concentrations were determined in both setup types with root-mean-square error of cross-validation (RMSECV) of less than 20 mg/dL using partial least-squares (PLS) regression. These results demonstrate accurate analyte measurements, and are promising for further development of fiber-coupled, miniaturised in vivo sensors based on mid-infrared spectroscopy.

Keywords: biomedical spectroscopy; quantum cascade lasers; mid-infrared; glucose

1. Introduction

Sensor development in the mid-infrared (MIR) region is interesting for many applications, with research ranging from sensor chips for gas detection to biomedical applications [1,2]. Biomedical applications are particularly important due to rising costs associated with healthcare, and a need for rapid, reagent-free, and non-destructive measurement techniques. Sensing in the MIR wavelength range, typically defined as 2.5–25 µm (4000–400 cm^{-1}), has advantages over several other optical measurement methods [3]. For example, MIR spectroscopy measures the absorption of fundamental molecular vibrations, which gives relatively sharp and strong absorption bands.

MIR spectroscopy has been a standard laboratory technique for decades through the use of e.g., Fourier-transform interferometer (FTIR) spectrometers, but these benchtop instruments have several limitations regarding on-demand and portable sensing. FTIR spectrometers are traditionally bulky instruments with free-space optics and require relatively large sampling volumes. Additionally, FTIR spectrometers commonly use thermal emitters such as SiC globars, which provide a low overall spectral power density in the MIR wavelength range. Consequently, these spectrometers have had limited sensitivity for measurements of biomedical samples, as they usually contain water which

strongly absorbs in the MIR range. Other alternatives, such as CO_2 lasers or lead–salt lasers, can provide higher spectral power density. However, these lasers have seen limited use for biomedical applications due to narrow wavelength ranges, and a need for cryogenic operating temperatures in the case of lead–salt lasers [4,5].

The introduction of broadly tuneable quantum cascade lasers (QCLs) has sparked new research interest within this field. The main advantage of QCLs is their high spectral emission power, which can reach a factor of 10^4 higher than that of the thermal sources used in FTIR spectrometers. Additionally, QCLs are small, can be made tuneable over several hundred wavenumbers, and can be operated with thermoelectric cooling [6]. This makes QCLs well-suited for sensor development. Several resonator designs are routinely used in QCLs [2]. The simplest design is the Fabry-Pérot (FP) resonator, which is made by cleaving the ends of the gain chip. FP-QCLs have multimode emission, and can be tuned a few wavenumbers by changing the temperature or current over the chip. Singlemode emission from a QCL can be achieved by making a Bragg grating on the laser chip, commonly referred to as distributed feedback (DFB) technology. The tuning range of a DFB-QCL is approximately 5 cm^{-1}, which makes this resonator design more suitable for gas spectroscopy, although multiple DFB-QCLs can be combined for a wider spectral range. The use of an external cavity (EC) provides a broader tuning range up to several hundred cm^{-1}, with emission in either continuous wave or pulsed mode. EC-QCLs can therefore be used for detection of several analytes through multivariate analysis.

QCLs are particularly advantageous for biomedical applications. For benchtop uses the QCLs are compact, they have high spectral power density which gives a high signal-to-noise ratio (SNR) even in aqueous samples, and can reach measurement times down to a few seconds. For personal and portable uses, QCLs have a large potential for miniaturised sensors, especially with single-wavelength laser chips. Some miniaturised MIR sensors with thermal sources have been made, many with MOEMS-based (micro-opto-electromechanical systems) technology [7,8], but these are still most suited for gas sensing. Today, portable sensors that are used clinically instead typically rely on enzymatic reactions. As an example, glucose sensors for monitoring diabetes are the most common type of portable biomedical sensor [9]. Monitoring the glucose level is essential for diabetic patients, and is done either with fingerprick measurements of blood or with continuous glucose monitoring (CGM) devices worn on the body [10]. In both cases the measurements are facilitated by an enzymatic reaction, which for the CGM devices limits the sensor lifetime to less than two weeks due to sensor and reagent degradation [11,12]. Optical methods such as MIR spectroscopy can circumvent some of these difficulties as the measurements are reagent-free. However, other complications exist for optical methods, including differentiation of overlapping spectral bands and obtaining accurate measurements of low analyte concentrations [13].

QCLs have been employed by several research groups in setups for glucose measurements, aimed at use in portable sensors or larger sensors for intensive care, mainly using variations of transmission or attenuated total reflection (ATR) spectroscopy [14–20]. Promising initial results were also shown for in vivo glucose monitoring in interstitial fluid with a QCL, albeit with short-term measurements using a single-wavelength laser [21]. Other variants such as measurements of the photoacoustic signal or backreflected light from skin have also been investigated [22–26], but non-invasive sensing through skin is challenging in the MIR range due to strong water absorption.

Transmission and ATR measurements are both done through absorption spectroscopy, but ATR spectrocopy uses the evanescent field decaying out from waveguides or prisms where radiation has undergone total internal reflection (TIR). Different materials are used to enable evanescent sensing in ATR spectroscopy. ZnS offers a good compromise as a prism material in biomedical applications as it is cheap, has a high refractive index (approx. 2.2 at 10 μm), and is non-toxic. The Matsuura group has several publications on fiber-coupled ATR spectroscopy aimed toward non-invasive measurements of the inner lip mucosa [16,27,28]. They have used either an FTIR spectrometer as a source, which has a low power density, or 2–3 single-wavelength QCLs, which suffers from drift between the lasers. Another recent study showed detection of glucose in saliva in an EC-QCL ATR setup,

but the water matrix was evaporated from the sample before measurements and the setup was in free-space [18]. Using a fiber-coupled system would have several advantages, as it simplifies further sensor development in regard to reducing sensor dimensions and portable sensing. A combination of ATR spectroscopy and fiber-coupling could be used in a probe design suitable for a portable sensor. This configuration could potentially be employed for minimally invasive sensing right under the skin. So far, studies of fiber-coupled ATR setups with EC-QCL sources have not been reported in detail, and a robust study of the achievable sensitivity in aqueous solutions is required.

In this article, we report on a fiber-coupled EC-QCL setup with sensing based on ATR spectroscopy with a ZnS prism. The ATR measurements are compared to transmission measurements, with transmission directly through a gap between two optical fibers. Comparing the ATR setup with a transmission setup will serve to validate the findings in the ATR setup. The sensing capabilities of these setups are tested by measuring aqueous solutions with glucose and albumin, as well as lactate and urea as interfering species. These analytes were chosen as an example system as they are present in biofluids, and glucose and proteins are especially relevant for biomedical sensors.

2. Materials and Methods

2.1. Experimental Setup

The setup (Figure 1) employed an external-cavity quantum cascade laser (EC-QCL, Hedgehog-UT, Daylight Solutions, San Diego, CA, USA) with a maximum tuning range between 1200 cm^{-1} and 900 cm^{-1} (8.33–11.1 µm). The EC-QCL was operated in pulsed mode with a pulse width of 500 ns and a repetition rate of 100 kHz, giving a duty cycle of 5%. The maximum average power for these settings was 22 mW. The laser head was thermoelectrically cooled to 19 °C for all measurements. The laser head emitted radiation in a collimated beam which was 100:1 vertically polarised according to the specifications. A mercury-cadmium-telluride (MCT) detector (Vigo System, Ozarow Mazowiecki, Poland) with a 2 × 2 mm detector element was used to detect the mid-infrared radiation. This detector used a four-stage thermoelectric cooling system in order to operate at −75.2 °C, and had a detectivity of 3×10^9 cm $Hz^{0.5}$ W^{-1}.

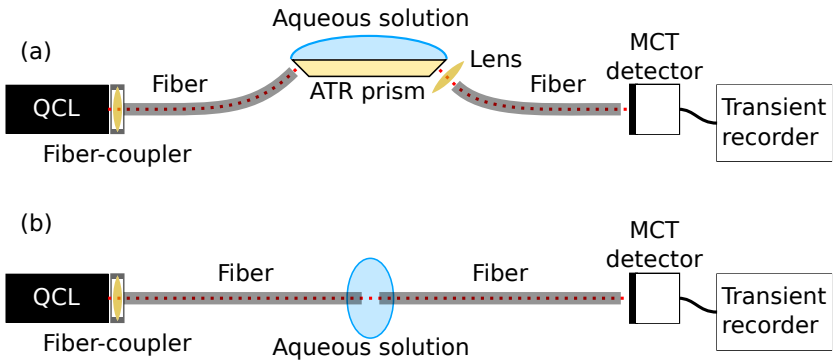

Figure 1. Overview of the two experimental setups, with sensing through (**a**) ATR spectroscopy and (**b**) transmission spectroscopy. For simplicity, the laser controller, the trigger line going from the laser controller to the transient recorder, and the control computer are not shown.

The emitted beam was coupled into a silver halide fiber with an optical assembly (OptoKnowledge Systems, Los Angeles, CA, USA). This optical assembly was designed to minimise the coupling loss in the wavelength range for the laser, with a loss of <5%. In the ATR setup, these fibers were used to couple the radiation into and out of a ZnS prism (Sinoptix, Shanghai, China). The ZnS

prism was a trapezoid with 45 degree facets for in- and out-coupling of radiation. The top facet of the prism was 24 × 6 mm^2, and the prism height was 2.4 mm. The silver halide fiber (Art photonics, Berlin, Germany) used for in-coupling had a core size of 400 μm, while the out-coupling fiber had a core size of 600 μm, both with optical losses of 0.2–0.3 dB/m. Radiation exiting from the ZnS prism was focussed onto the out-coupling fiber using a ZnSe lens (Thorlabs, Newton, NJ, USA). In the transmission measurements, the fibers were aligned and a 165 μm gap between the fibers was used for sensing. The transmission pathlength was chosen based on a trade-off between analyte absorbance signal and the noise level, and was similar to the optimal pathlength found in other work [15].

Data acquisition was done with an analogue-to-digital converter card (M2p.5946-X4, 80 MS/s, 16 bit, Spectrum Instrumentation, Großhansdorf, Germany). The digitiser was controlled with a modified driver written in C++, and operated via a GUI front-end written in Python. A trigger signal between the laser controller and the digitiser card was used to start the data acquisition for each measurement. Spectra were acquired by operating the laser in scan-mode, where the laser was continuously tuned over a chosen wavelength range.

2.2. Data Processing

For each spectrum, a background measurement (I_0) and a sample measurement (I) were recorded for the 1200–925 cm^{-1} tuning range. Demineralised water was used for the background measurements. Each background and sample measurement consisted of ten scans over the tuning range. Spectra were made by averaging over 255 laser pulses from the raw data, and then averaging over the 10 acquired scans from each measurement, for the purpose of noise reduction. Each scan took 1 s to acquire with a tuning speed of 275 cm^{-1}/s, and consisted of approximately 100,000 pulses. Each spectrum was reduced to 390 data points after the spectral binning. From this, the absorbance spectra of the samples were calculated as $A = -\log(I/I_0)$.

An alignment procedure was also performed on the spectra in order to correct for offset between scans and measurements. The scans were aligned to the first scan of each measurement by a chi-squared minimisation algorithm. Subsequently, each sample measurement was aligned to a background measurement.

Data analysis for prediction of analyte concentrations was done using a program developed in-house (Python). Partial least-squares (PLS) regression was used for prediction of glucose concentrations [29]. The data sets were standardised prior to PLSR by subtracting the mean and scaling to unit variance. Smoothing with a Savitzky–Golay filter was also applied as a pre-processing method [30]. The root-mean-square error of cross-validation (RMSECV) and the coefficient of determination (R^2) were used to evaluate the prediction accuracy of the regression. RMSECV was calculated from either a leave-one-out cross-validation (LOOCV), leave-5-out cross-validation (L5OCV), or leave-one-dataset-out cross-validation (LDOCV).

We would like to note that RMSE-values are scale-dependent, which means that the RMSE will vary if different concentration ranges are used. As a result, RMSE-values are difficult to compare between studies if different concentration ranges are used. R^2 has therefore been included as an alternative evaluation metric.

2.3. Sample Overview

Aqueous solutions were made by dissolving the analytes in a phosphate-buffered saline (PBS) solution. PBS is a buffer solution that has ion concentrations matching the human body and helps maintain pH, and can be made by dissolving PBS tablets (VWR) in water. Glucose (D-(+)-glucose, Sigma Aldrich), albumin (bovine serum albumin, VWR), lactate (sodium L-lactate, Sigma Aldrich), and urea (Sigma Aldrich) were added to solutions in varying concentrations. 25 unique solutions were made, with concentration ranges as shown in Table 1.

Table 1. Concentration ranges of analytes used in the setups to test the measurement sensitivity for analytes with overlapping absorption bands.

Analytes	Concentration Range [mg/dL]
Glucose	0–800
Albumin	0–6000
Urea	0–200
Lactate	0–90

Analyte concentrations were designated to cover the entire design space, and were determined by a quadratic Scheffe model with A-optimality design. Optimal design allows for using fewer samples in the analysis while still maintaining robust concentration predictions [31]. Ten additional samples with glucose in demineralised water were also made for initial system characterisation, with glucose concentrations in the range 0–810 mg/dL.

ATR measurements were performed by placing the sample on the ZnS crystal, and the crystal was wiped clean with ethanol between each measurement. Transmission measurements were done by putting the sample in a gap between two fibers, and the gap was emptied and rinsed with ethanol between each measurement. For the two setup configurations, all samples were measured in four different series, with two series each on two different days.

3. Results and Analysis

3.1. Optical Propagation in ZnS Prism

Propagation of light in the ZnS ATR prism was simulated in Zemax OpticStudio using ray tracing, see Figure 2. The radiation source was modelled as a beam with an initial diameter of 400 µm, as this was the core size of the fiber. The divergence angle of this beam was set according to the numerical aperture (NA = 0.30) of the silver halide fiber. This created nine reflections in total as the beam propagated through the crystal, with five reflections on the top facet. The propagation length inside the prism is calculated to approximately 30.5 mm.

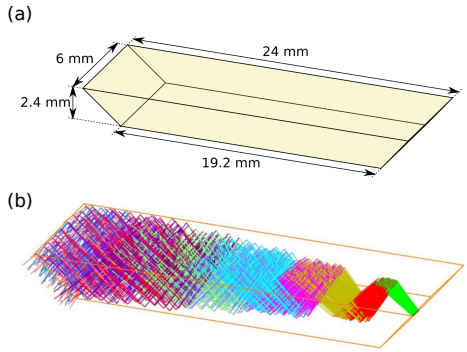

Figure 2. (**a**) Geometry of ZnS prism, and (**b**) ray-tracing simulation (Zemax OpticStudio) of trajectories of IR radiation in the prism.

The beam diverges rapidly inside the prism due to the large initial size and the divergence angle from the optical fiber. Due to this divergence, the more radial parts of the beam will have a somewhat longer pathlength than the center, and will therefore reach the detector at a different time. For most of the radial parts of the beam, the largest pathlength difference is calculated to 0.25 mm.

The penetration depth for the evanescent field extending from the prism is between approximately 4 µm and 5.4 µm depending on the wavelength [32]. With 5 reflections this gives in a total interaction length of 20–27 µm.

3.2. Laser Intensity Variation

The pulsed operation of the QCL means that there is inherently some intensity variation between laser pulses. It is therefore common to average, or bin, over several laser pulses in order to reduce this variation.

In order to characterise pulse-to-pulse variation 100,000 laser pulses at 1190 cm^{-1} (8.4 µm) were recorded. Additionally, to investigate scan-to-scan variation 50 separate scans in the range 1200–925 cm^{-1} were recorded. Example results of averaging over pulses and scans are shown in Figure 3. These measurements were recorded in the fiber-coupled transmission setup, after transmitting the beam through a 165 µm layer of water.

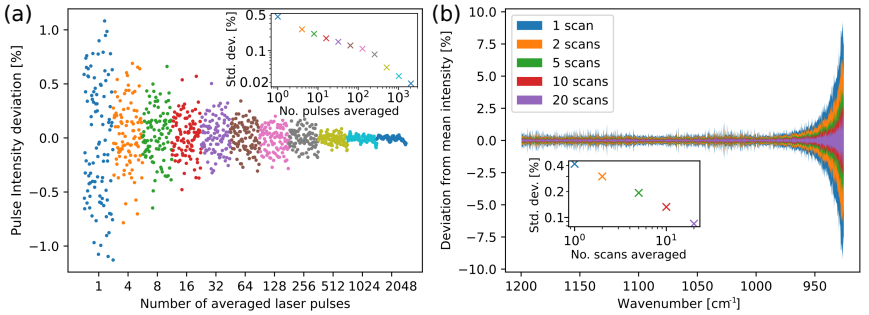

Figure 3. (**a**) Characterisation of the pulse-to-pulse intensity variation from the laser with averaging over pulses at a single wavelength, where the inset shows how the relative standard deviation decreases with pulse averaging. (**b**) Characterisation of scan-to-scan variation with averaging over multiple scans, where the inset shows the average relative standard deviation using the 1200–1000 cm^{-1} range.

Pulse averaging was tested from one to 2560 pulses, while scan averaging was tested from one to 20 scans. The relative standard deviation (RSD) decreases when averaging over more pulses, and when averaging over several scans. Averaging over scans in the transmission setup also reveals that the standard deviation becomes much larger for wavenumbers below approximately 970 cm^{-1} (longer than 10.3 µm), see Figure 3b. The increase in noise can be attributed to the stronger water absorption in this wavelength area. The result is not unexpected, and the water absorption should be taken into account when choosing pathlength. In our case, we maintained the long pathlength in the transmission setup in order to increase sensitivity, as none of the analytes were expected to have crucial information below 970 cm^{-1}. This effect on the RSD is much smaller in the ATR setup, as the interaction length is much shorter.

Averaging over pulses is a trade-off between the reduction in noise, and measurement time or wavelength resolution. In this system, averaging over 10 scans and 255 pulses in each measurement gave an RSD of approx. 0.07%, which is equivalent to 0.0003 absorbance units. For the transmission measurements, this RSD was calculated for 1200–1000 cm^{-1}, where the laser noise was dominant. Each scan takes 1 s to perform and contains 100,000 pulses, which gives a total measurement time of 10 s and a nominal resolution of 0.7 cm^{-1}.

3.3. Glucose Spectra

Ten glucose solutions were measured in the ATR and transmission configurations in order to characterise the setups. Typical spectra from these measurements are shown in Figure 4, after being subjected to a Savitzky–Golay filter (width 9). These measurements were also repeated within the same day and on separate days, for a total of four measurement series in each setup.

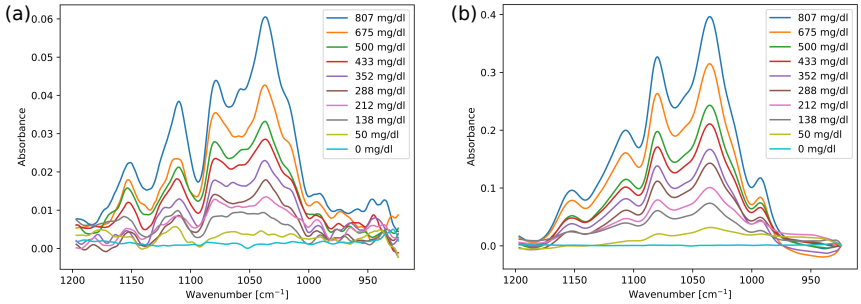

Figure 4. Absorbance spectra of different glucose concentrations for (**a**) measurements acquired in the ATR setup and (**b**) measurements acquired in the transmission setup.

As the setups are based on absorption spectroscopy, there are no major structural differences between the spectra, and the same glucose absorption peaks are present. There are some distortions in the ATR spectra, such as the lower dip around 1090 cm^{-1}. Band distortions are known to occur in ATR spectroscopy, and are typically explained by anomalous dispersion (AD) in the refractive index of the measured sample [33]. Distortions caused by AD usually involve both intensity variations and frequency shifts, while the spectra in Figure 4a mainly display intensity variations. In addition, the spectral distortions are almost independent of glucose concentration, contrary to the concentration-dependent distortion expected from AD effects. This is in agreement with previous results, as e.g., Rowe et al. [34] found a change in refractive index of <0.01 in whole blood as compared to water. Band distortions are also found in other spectroscopy techniques that involve reflections, e.g., transflection spectroscopy [35]. It has been suggested that band variations in transflection measurements can be caused by reflections and interferences at interfaces [36], and a similar effect could also apply to ATR configurations. We therefore find it likely that the distortions occur due to reflections in optical components in the setup. The distortions in the ATR spectra did not affect the linearity of the glucose absorbance. However, the absorbance intensity in the ATR measurements is approximately 7 times lower than for the transmission measurements, which results in a lower overall SNR.

The main cause of the lower absorbance in the ATR measurements is the relatively shorter interaction length between the radiation and the sample in the ATR setup versus the transmission setup. The estimated interaction length of 20–27 µm in the prism agrees well with the seven-factor difference in absorbance. This also indicates that other causes for signal loss are relatively unimportant in our configuration, for example through material scattering in the prism and losses at the out-coupling facet of the prism.

Glucose concentrations can easily be predicted in these simple aqueous solutions. The prediction errors are summarised in Table 2. Using PLS regression and LOOCV, the RMSECV for glucose was found to be 8.5 mg/dL for the transmission measurements, and 10.2 mg/dL for the ATR measurements. These RMSECV values were found using 3 latent variables (LVs). For LDOCV, where datasets from four different measurements series were used in the cross-validation, the RMSECV values were slightly higher at 12.8 mg/dL for the ATR setup and 9.7 mg/dL for the transmission setup.

Table 2. Prediction errors for glucose in aqueous solutions obtained with PLS regression.

ATR Measurements			
Cross-Validation	**RMSECV [mg/dL]**	**R^2**	**LVs**
LOOCV	10.2	0.998	3
LDOCV	12.8	0.997	4
Transmission Measurements			
Cross-Validation	**RMSECV [mg/dL]**	**R^2**	**LVs**
LOOCV	7.5	0.999	3
LDOCV	9.7	0.998	4

3.4. Sample Analysis

In more realistic sensing scenarios, it is important that the sensor is selective. It is also advantageous if the sensor can be used for more than one analyte, e.g., for management and tracking progression of several disease markers simultaneously. Therefore, more complex solutions with glucose, albumin, lactate, and urea were measured in the ATR and transmission setups. A total of 25 samples were used for training a regression model and cross-validation. The samples were measured in four series on two different days. As with the pure glucose spectra, the analysis was done on spectra with averaging over 255 pulses and ten spectra. Binning up to 510 pulses was also tested, but this did not yield significantly different RMSE-values in the regression analysis.

Figure 5 shows pure analyte spectra of the four species used in the samples, acquired in the transmission setup. Lactate has two absorption bands at 1040 cm^{-1} and 1124 cm^{-1} that overlap with glucose. Urea has only one small absorption band at approx. 1160 cm^{-1}, but even this can interfere with glucose prediction depending on the latent variables found in the PLS model training. Albumin also has several absorption bands in the EC-QCL emission range. The concentration of albumin and other proteins is usually determined using the spectral region around 1600 cm^{-1}, but it has been shown that the 1200–1000 cm^{-1} range is sufficient to determine total protein and albumin content in human blood plasma [37,38].

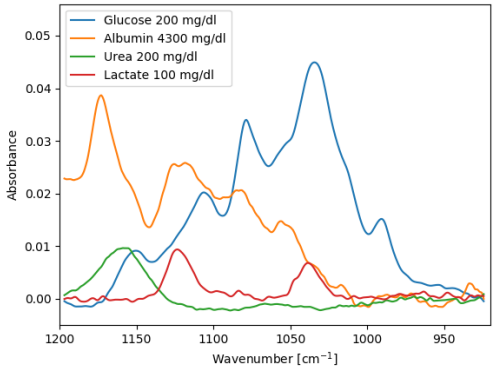

Figure 5. Absorbance spectra of pure analytes in demineralised water acquired in the transmission setup.

The normal physiological glucose concentration range for a healthy person is between 70 and 110 mg/dL. A blood glucose level (BGL) lower than 70 mg/dL is called hypoglycaemic, while a BGL above 180 mg/dL is called hyperglycaemic [39,40]. For people with diabetes the BGL can go up towards 400 mg/dL before hyperglycaemia symptoms become severe if the BGL goes unchecked.

However, a broader glucose concentration range (0–800 mg/dL) has been used in these aqueous solutions in order to test the robustness of the measurement setups and the regression analysis. Similarly, concentration ranges of albumin, lactate, and urea (see Table 1) encompass human serum concentrations, but the highest concentrations used here are unlikely in physiological situations [38,41].

The prediction accuracies obtained for glucose and albumin are summarised in Table 3. In the ATR setup, an RMSECV of 16.3 mg/dL was achieved for glucose with L5OCV, while the RMSECV was 15.4 mg/dL in the transmission setup. The best prediction results were obtained using four or five latent variables. For cross-validation where one dataset was left out, the RMSECV for glucose was found to be 15.5 mg/dL for transmission measurements and 18.4 mg/dL for ATR measurements. This demonstrates that the setups were stable over time, as the prediction errors did not change significantly when datasets acquired at different times and on different days were used for cross-validation. The same trends were found for the analysis of albumin concentrations. For transmission spectroscopy, comparable prediction errors for glucose have been found in a previous study with a fiber-based EC-QCL setup [17], but this study used narrower concentration ranges, which can affect RMSE-values, and employed a reference arm for stability.

Table 3. Concentration predictions for glucose and albumin in aqueous solutions measured in the ATR and transmission setups, using PLS regression.

ATR Measurements						
Cross-Validation	**Glucose**			**Albumin**		
	RMSECV [mg/dL]	**R^2**	**LVs**	**RMSECV [mg/dL]**	**R^2**	**LVs**
L5OCV	16.3	0.996	5	174.5	0.988	6
LDOCV	18.4	0.994	5	178.1	0.988	5
Transmission Measurements						
Cross-Validation	**Glucose**			**Albumin**		
	RMSECV [mg/dL]	**R^2**	**LVs**	**RMSECV [mg/dL]**	**R^2**	**LVs**
L5OCV	15.4	0.996	4	157.9	0.991	4
LDOCV	15.5	0.996	5	162.4	0.990	4

Figure 6 shows the predicted glucose concentrations for L5OCV plotted against the reference concentrations for the measurements in the ATR and transmission setups. Glucose prediction is linear over the entire range, also at low physiological concentrations (<100 mg/dL). This, together with the RMSECV levels, indicates that our findings are significant for physiologically relevant glucose concentrations.

It was also found that the measurements in the transmission setup could be used to predict the concentrations of urea and lactate in the complex solutions. The RMSECV values for L5OCV were found to be 8.1 mg/dL for lactate and 9.9 mg/dL for urea. Accurate predictions could not be made for these analytes in the ATR setup ($R^2 < 0.5$). This is likely due to a combination of a lower SNR in the ATR measurements and the overlap between lactate and urea absorption bands with the other analytes.

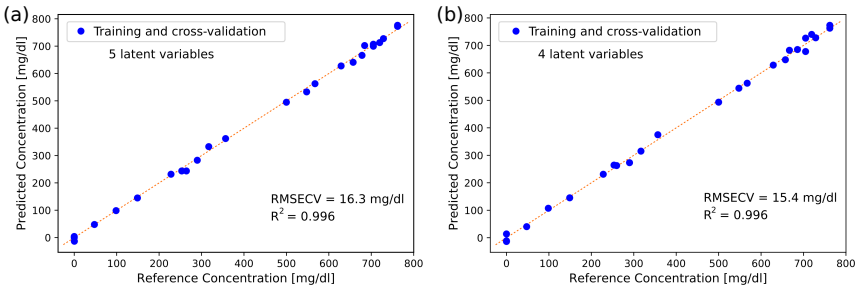

Figure 6. Glucose concentration levels in 25 aqueous samples plotted against reference concentrations with (**a**) the ATR setup for measurements and (**b**) the transmission setup for measurements. PLS regression with 5 or 4 latent variables and leave-5-out cross-validation was used for prediction.

4. Discussion

An important feature of this system is the use of fiber-coupling, as fiber-coupling is very advantageous for further development of a practical glucose measurement system. Fiber-coupling enables simpler light guiding as compared to free-space, and light reflections from e.g., liquid cells are avoided. A fiber-based setup can also more easily be incorporated in miniaturised and portable sensors. Mid-infrared fibers have acceptable optical loss (approx. 0.3 dB/m) for these applications, although they are still quite expensive. The large-core fibers used in mid-infrared sensing are stiff and can be challenging to manipulate and align. Fiber-coupling also has the potential for more sources of loss, e.g., at the fiber-coupler. However, in our system the optical loss was <5% in the coupler and approximately 0.3 dB/m in the fibers, which was not significant for the results.

As expected when comparing measurements in ATR and transmission setups, the absorbance intensity was significantly lower in the ATR measurements due to the shorter interaction length. However, the RMSECV values for glucose and albumin measured in the ATR setup were still comparable to those from the transmission setup. This indicates that ATR measurements are sensitive enough for biomedical measurements despite the shorter interaction length. The geometry of an ATR fiber probe may also have several practical advantages over a transmission configuration. For example, a small transmission gap is prone to clogging and ensuring alignment of the fiber ends can be mechanically challenging. An ATR fiber probe is potentially more mechanically stable, since the measurand is on the surface of the prism rather than being in a gap between fibers. In addition, the input fiber can more easily also serve as an output fiber using an ATR probe.

The ZnS prism used for the ATR measurements was a suitable sensing interface, as the crystal surface was stable and easy to clean. ZnS is also well-suited in any potential in vivo applications, as it is non-toxic to humans. The main challenge with ATR spectroscopy and concentration predictions seemed to be the lower SNR as compared to the transmission measurements, which gave somewhat higher prediction errors. The primary cause behind this was the reduced interaction length. This effect may be ameliorated by further optimising the prism dimensions. For example, a prism with half the height (1.2 mm) would have twice as many internal reflections with approximately the same optical pathlength through the prism. Thus the interaction length with the sample could be increased, without increasing pathlength and material absorption.

The dimensions of the sensor should be reduced for portable sensing applications, and this can be achieved in several ways. One alternative is to create a fiber-coupled probe design with an ATR prism or looped bare optical fibers at the end of a fiber [5,42]. A fiber probe with an ATR prism necessitates a smaller crystal, down to single-reflection, with concomitant signal reduction. This signal reduction can be counteracted with the use of e.g., surface-enhanced infrared absorption spectroscopy (SEIRAS) [43]. SEIRAS can be achieved by coating the ATR prism with metal nanoparticles, but these substrates

often have difficulties with stability and reproducibility. Another option is to fabricate micrometer structures onto the sampling facet of the ATR crystal. Such structures on ATR crystals have been shown to enhance the absorption signal up to a factor of 10–100 [44]. On the other hand, evanescent sensing with looped fibers can be used to maintain a long interaction length, while avoiding the need for surface engineering. However, looped optical fibers are fragile and would likely need to be encased in a flow-through chamber for stability.

For a portable sensor another avenue of size reduction is to use a smaller QCL source. As EC-QCLs are a recent commercial product, they will likely become somewhat smaller in the future. However, for personal and wearable sensors such as glucose sensors the dimensions must be reduced even further. One option is to use a few single-wavelength laser chips in order to target the most informative wavenumbers. It has been suggested several times that only a few wavenumbers are needed for an adequately accurate prediction of glucose concentrations, also for non-invasive measurements [27,41]. Robust measurements using a few wavenumbers must be tested thoroughly in realistic conditions in order to confirm this.

This study has demonstrated the use of an EC-QCL on samples with glucose and albumin as an example. However, we would like to emphasise that measurements with QCLs in applications for biomedicine and biotechnology have many additional potential uses where MIR spectroscopy with high sensitivity could replace other benchtop and portable measurement methods. In research, QCLs have so far also been used for breath analysis in order to detect disease markers, and in histopathology to e.g., detect cancer [2,45,46]. EC-QCLs also have many potential uses where they can outperform methods that today require labelling or reagents, such as protein analysis, cell studies and pharmaceutical and food analysis [47].

5. Conclusions

A fiber-coupled EC-QCL was used for multianalyte sensing in both ATR and transmission measurement configurations. Glucose and albumin concentrations were determined in solutions that also contained urea and lactate, with promising results. The RMSECV values for glucose were well under 20 mg/dL, even though a broad concentration range was used. The low cross-validation errors were also very promising considering the addition of other analytes with overlapping absorption bands. The simultaneous determination of several biomarkers is relevant for further sensor development, and the use of optimal design for analyte concentrations allowed for investigating the entire design space for four analytes with relatively few samples, while still obtaining robust analyte predictions. This is advantageous for testing and characterisation of sensor setups, as fewer total measurements are needed while precision is still maintained.

The intensity variation in the laser pulses was evaluated, and was decreased to an acceptable level with averaging while the measurement time did not exceed 10 s. Both setups were mechanically stable over time, and it was shown that measurements from different days could be used for concentration predictions. This concept study should be further assessed by measuring and analysing larger datasets, including samples of bodily fluids. As the ATR setup is fiber-coupled, it lends itself well to further developments towards a miniaturised and portable sensor.

Future developments include improving the SNR in the ATR measurements through optimisations of the prism dimensions. We will also investigate the feasibility of using a thin silicon crystal with micrometer surface structures for signal enhancement as an ATR element. This could be a viable alternative for minimally invasive or non-invasive fiber-probe sensors for on-demand sensing.

Author Contributions: I.L.J. and K.S. conceptualised and designed the experiments; I.L.J and K.S. performed the experiments; I.L.J. implemented the code for the analysis and analysed the results; I.L.J. prepared the original draft; A.A. and D.R.H. supervised and reviewed the paper; A.A. and D.R.H. acquired funding for the project.

Funding: This work was supported by the Research Council of Norway through the Double Intraperitoneal Artificial Pancreas project, grant number 248872. The project is part of Center for Digital Life Norway and is also supported by the Research Council of Norway's grant 248810.

Conflicts of Interest: The authors declare no conflict of interest.

References

1. Kosterev, A.; Wysocki, G.; Bakhirkin, Y.; So, S.; Lewicki, R.; Fraser, M.; Tittel, F.; Curl, R.F. Application of quantum cascade lasers to trace gas analysis. *Appl. Phys. B Lasers Opt.* **2008**, *90*, 165–176. s00340-007-2846-9. [CrossRef]
2. Schwaighofer, A.; Brandstetter, M.; Lendl, B. Quantum cascade lasers (QCLs) in biomedical spectroscopy. *Chem. Soc. Rev.* **2017**, *46*, 5903–5924. [CrossRef]
3. De Bruyne, S.; Speeckaert, M.M.; Delanghe, J.R. Applications of mid-infrared spectroscopy in the clinical laboratory setting. *Crit. Rev. Clin. Lab. Sci.* **2018**, *55*, 1–20. [CrossRef]
4. Lambrecht, A.; Beyer, T.; Hebestreit, K.; Mischler, R.; Petrich, W. Continuous Glucose Monitoring by Means of Fiber-Based, Mid-Infrared Laser Spectroscopy. *Appl. Spectrosc.* **2006**, *60*, 729–736. [CrossRef]
5. Yu, S.; Li, D.; Chong, H.; Sun, C.; Yu, H.; Xu, K. In vitro glucose measurement using tunable mid-infrared laser spectroscopy combined with fiber-optic sensor. *Biomed. Opt. Express* **2013**, *5*, 275–286. [CrossRef]
6. Yao, Y.; Hoffman, A.J.; Gmachl, C.F. Mid-infrared quantum cascade lasers. *Nat. Photonics* **2012**, *6*, 432–439. [CrossRef]
7. Sandner, T.; Kenda, A.; Drabe, C.; Schenk, H.; Scherf, W. Miniaturized FTIR-spectrometer based on optical MEMS translatory actuator. In *MOEMS and Miniaturized Systems VI*; Dickensheets, D.L., Gogoi, B.P., Schenk, H., Eds.; International Society for Optics and Photonics: Bellingham, WA, USA, 2007; Volume 6466, pp. 1–12. [CrossRef]
8. Khalil, D.; Sabry, Y.; Omran, H.; Medhat, M.; Hafez, A.; Saadany, B. Characterization of MEMS FTIR spectrometer. In *MOEMS and Miniaturized Systems X*; Schenk, H., Piyawattanametha, W., Eds.; International Society for Optics and Photonics: Bellingham, WA, USA, 2011; Volume 7930, pp. 1–10. [CrossRef]
9. Turner, A.P.F. Biosensors—Sense and sensibility. *Chem. Soc. Rev.* **2013**, *42*, 3184–3196. [CrossRef]
10. Heller, A.; Feldman, B. Electrochemical Glucose Sensors and Their Applications in Diabetes Management. *Chem. Rev.* **2008**, *108*, 2482–2505. [CrossRef] [PubMed]
11. Valdes, T.I.; Moussy, F. In Vitro and In Vivo Degradation of Glucose Oxidase Enzyme Used for an Implantable Glucose Biosensor. *Diabetes Technol. Ther.* **2000**, *2*, 367–376. [CrossRef] [PubMed]
12. Scholten, K.; Meng, E. A review of implantable biosensors for closed-loop glucose control and other drug delivery applications. *Int. J. Pharm.* **2018**, *544*, 319–344. [CrossRef] [PubMed]
13. Jernelv, I.L.; Milenko, K.; Fuglerud, S.S.; Hjelme, D.R.; Ellingsen, R.; Aksnes, A. A review of optical methods for continuous glucose monitoring. *Appl. Spectrosc. Rev.* **2018**, *54*, 1–30. [CrossRef]
14. Martin, W.B.; Mirov, S.; Venugopalan, R. Middle Infrared, Quantum Cascade Laser Optoelectronic Absorption System for Monitoring Glucose in Serum. *Appl. Spectrosc.* **2005**, *59*, 881–884. 0003702054411580. [CrossRef] [PubMed]
15. Brandstetter, M.; Volgger, L.; Genner, A.; Jungbauer, C.; Lendl, B. Direct determination of glucose, lactate and triglycerides in blood serum by a tunable quantum cascade laser-based mid-IR sensor. *Appl. Phys. B* **2013**, *110*, 233–239. [CrossRef]
16. Kino, S.; Omori, S.; Katagiri, T.; Matsuura, Y. Hollow optical-fiber based infrared spectroscopy for measurement of blood glucose level by using multi-reflection prism. *Biomed. Opt. Express* **2016**, *7*, 701–708. [CrossRef] [PubMed]
17. Haase, K.; Müller, N.; Petrich, W. Towards a continuous glucose monitoring system using tunable quantum cascade lasers. In *Biomedical Vibrational Spectroscopy 2018: Advances in Research and Industry*; Mahadevan-Jansen, A., Petrich, W., Eds.; International Society for Optics and Photonics: Bellingham, WA, USA, 2018; Volume 1049008, pp. 1–8. [CrossRef]
18. Haas, J.; Catalán, E.V.; Piron, P.; Karlsson, M.; Mizaikoff, B. Infrared spectroscopy based on broadly tunable quantum cascade lasers and polycrystalline diamond waveguides. *Analyst* **2018**, *143*, 5112–5119. [CrossRef]
19. Isensee, K.; Müller, N.; Pucci, A.; Petrich, W. Towards a quantum cascade laser-based implant for the continuous monitoring of glucose. *Analyst* **2018**, *143*, 6025–6036. [CrossRef]

20. Grafen, M.; Delbeck, S.; Busch, H.; Heise, H.M.; Ostendorf, A. Evaluation and benchmarking of an EC-QCL-based mid-infrared spectrometer for monitoring metabolic blood parameters in critical care units. In *Optical Diagnostics and Sensing XVIII: Toward Point-of-Care Diagnostics*; Coté, G.L., Ed.; International Society for Optics and Photonics: Bellingham, WA, USA, 2018; Volume 10501, pp. 1–9. [CrossRef]
21. Vrančić, C.; Kröger, N.; Gretz, N.; Neudecker, S.; Pucci, A.; Petrich, W. A Quantitative Look Inside the Body: Minimally Invasive Infrared Analysis in Vivo. *Anal. Chem.* **2014**, *86*, 10511–10514. [CrossRef]
22. Pleitez, M.A.; Lieblein, T.; Bauer, A.; Hertzberg, O.; von Lilienfeld-Toal, H.; Mäntele, W. In Vivo Noninvasive Monitoring of Glucose Concentation in Human Epidermis by Mid-Infrared Pulsed Photoacoustic Spectroscopy. *Anal. Chem.* **2013**, *85*, 1013–1020. [CrossRef]
23. Liakat, S.; Bors, K.A.; Xu, L.; Woods, C.M.; Doyle, J.; Gmachl, C.F. Noninvasive in vivo glucose sensing on human subjects using mid-infrared light. *Biomed. Opt. Express* **2014**, *5*, 2397–2404. [CrossRef]
24. Kottmann, J.; Rey, J.M.; Sigrist, M.W. Mid-Infrared Photoacoustic Detection of Glucose in Human Skin: Towards Non-Invasive Diagnostics. *Sensors* **2016**, *16*, 1663. [CrossRef]
25. Hertzberg, O.; Bauer, A.; Küderle, A.; Pleitez, M.A.; Mäntele, W. Depth-selective photothermal IR spectroscopy of skin: Potential application for non-invasive glucose measurement. *Analyst* **2017**, *142*, 495–502. [CrossRef] [PubMed]
26. Sim, J.Y.; Ahn, C.G.; Jeong, E.J.; Kim, B.K. In vivo Microscopic Photoacoustic Spectroscopy for Non-Invasive Glucose Monitoring Invulnerable to Skin Secretion Products. *Sci. Rep.* **2018**, *8*, 1–11. s41598-018-19340-y. [CrossRef] [PubMed]
27. Kasahara, R.; Kino, S.; Soyama, S.; Matsuura, Y. Noninvasive glucose monitoring using mid-infrared absorption spectroscopy based on a few wavenumbers. *Biomed. Opt. Express* **2018**, *9*, 289–302. [CrossRef] [PubMed]
28. Matsuura, Y.; Koyama, T. Non-invasive blood glucose measurement using quantum cascade lasers. In *Quantum Sensing and Nano Electronics and Photonics XVI*; Razeghi, M., Lewis, J.S., Tournié, E., Khodaparast, G.A., Eds.; International Society for Optics and Photonics: Bellingham, WA, USA, 2019; Volume 1092606, pp. 1–7. [CrossRef]
29. Martens, H.; Martens, M. *Multivariate Analysis of Quality An Introduction*; John Wiley & Sons: Hoboken, NJ, USA, 2001.
30. Rinnan, Å.; Van den Berg, F.; Engelsen, S.B. Review of the most common pre-processing techniques for near-infrared spectra. *Trends Anal. Chem.* **2009**, *28*, 1201–1222. [CrossRef]
31. Sinha, B.K.; Mandal, N.K.; Pal, M.; Das, P. *Optimal Mixture Experiments*; Springer: Connaught Place, India, 2014. [CrossRef]
32. Averett, L.A.; Griffiths, P.R.; Nishikida, K. Effective path length in attenuated total reflection spectroscopy. *Anal. Chem.* **2008**, *80*, 3045–3049. [CrossRef]
33. Boulet-Audet, M.; Buffeteau, T.; Boudreault, S.; Daugey, N.; Pézolet, M. Quantitative Determination of Band Distortions in Diamond Attenuated Total Reflectance Infrared Spectra. *J. Phys. Chem. B* **2010**, *114*, 8255–8261. [CrossRef]
34. Rowe, D.J.; Smith, D.; Wilkinson, J.S. Complex refractive index spectra of whole blood and aqueous solutions of anticoagulants, analgesics and buffers in the mid-infrared. *Sci. Rep.* **2017**, *7*, 7356. s41598-017-07842-0. [CrossRef]
35. Miljković, M.; Bird, B.; Diem, M. Line shape distortion effects in infrared spectroscopy. *Analyst* **2012**, *137*, 3954–3964. [CrossRef]
36. Lee, J. On the non-existence of the so-called "electric field standing wave effect" in transflection FTIR spectra. *Vib. Spectrosc.* **2017**, *90*, 104–111. [CrossRef]
37. Schwaighofer, A.; Montemurro, M.; Freitag, S.; Kristament, C.; Culzoni, M.J.; Lendl, B. Beyond Fourier Transform Infrared Spectroscopy: External Cavity Quantum Cascade Laser-Based Mid-infrared Transmission Spectroscopy of Proteins in the Amide I and Amide II Region. *Anal. Chem.* **2018**, *90*, 7072–7079. acs.analchem.8b01632. [CrossRef]
38. Brandstetter, M.; Sumalowitsch, T.; Genner, A.; Posch, A.E.; Herwig, C.; Drolz, A.; Fuhrmann, V.; Perkmann, T.; Lendl, B. Reagent-free monitoring of multiple clinically relevant parameters in human blood plasma using a mid-infrared quantum cascade laser based sensor system. *Analyst* **2013**, *138*, 4022–4028. [CrossRef] [PubMed]

39. Battelino, T.; Conget, I.; Olsen, B.; Schütz-Fuhrmann, I.; Hommel, E.; Hoogma, R.; Schierloh, U.; Sulli, N.; Bolinder, J. The use and efficacy of continuous glucose monitoring in type 1 diabetes treated with insulin pump therapy: A randomised controlled trial. *Diabetologia* **2012**, *55*, 3155–3162. [CrossRef] [PubMed]
40. Breton, M.; Farret, A.; Bruttomesso, D.; Anderson, S.; Magni, L.; Patek, S.; Man, C.D.; Place, J.; Demartini, S.; Del Favero, S.; et al. Fully Integrated Artificial Pancreas in Type 1 Diabetes: Modular Closed-Loop Glucose Control Maintains Near Normoglycemia. *Diabetes* **2012**, *61*, 2230–2237. [CrossRef] [PubMed]
41. Martin, W.B.; Mirov, S.; Venugopalan, R. Using two discrete frequencies within the middle infrared to quantitatively determine glucose in serum. *J. Biomed. Opt.* **2002**, *7*, 613–617. [CrossRef]
42. Matsuura, Y.; Kino, S.; Katagiri, T. Hollow-fiber-based flexible probe for remote measurement of infrared attenuated total reflection. *Appl. Opt.* **2009**, *48*, 5396–5400. [CrossRef]
43. Andvaag, I.R.; Morhart, T.A.; Clarke, O.J.R.; Burgess, I.J. Hybrid Gold—Conductive Metal Oxide Films for Attenuated Total Reflectance Surface Enhanced Infrared Absorption Spectroscopy. *ACS Appl. Nano Mater.* **2019**, *2*, 1274–1284. [CrossRef]
44. Sykora, L.; Müller, A.; Kondratiev, A.; Roth, A.; Mozin, V.; Fehr, A.; Zörnack, G. Silicon ATR crystal with subwavelength structures optimized for blood analysis. In *Optical Fibers and Sensors for Medical Diagnostics and Treatment Applications XIX*; Gannot, I., Ed.; International Society for Optics and Photonics: Bellingham, WA, USA, 2019; Volume 10872F, pp. 1–8. [CrossRef]
45. Henderson, B.; Khodabakhsh, A.; Metsälä, M.; Ventrillard, I.; Schmidt, F.M.; Romanini, D.; Ritchie, G.A.; te Lintel Hekkert, S.; Briot, R.; Risby, T.; et al. Laser spectroscopy for breath analysis: Towards clinical implementation. *Appl. Phys. B Lasers Opt.* **2018**, *124*, 1–21. [CrossRef]
46. Kuepper, C.; Kallenbach-Thieltges, A.; Juette, H.; Tannapfel, A.; Großerueschkamp, F.; Gerwert, K. Quantum Cascade Laser-Based Infrared Microscopy for Label-Free and Automated Cancer Classification in Tissue Sections. *Sci. Rep.* **2018**, *8*, 7717. [CrossRef]
47. Lambrecht, A.; Pfeifer, M.; Konz, W.; Herbst, J.; Axtmann, F. Broadband spectroscopy with external cavity quantum cascade lasers beyond conventional absorption measurements. *Analyst* **2014**, *139*, 2070–2078. [CrossRef]

Paper III

Mid-infrared spectroscopy with a fiber-coupled tuneable quantum cascade laser for glucose sensing

I.L. Jernelv, K. Strøm, D.R. Hjelme, A. Aksnes

Proceedings of SPIE 11233, Optical Fibers and Sensors for Medical Diagnostics and Treatment Applications XX, 1123311, 2020.

Mid-infrared spectroscopy with a fiber-coupled tuneable quantum cascade laser for glucose sensing

Ine L. Jernelv*, Karina Strøm, Dag Roar Hjelme, and Astrid Aksnes

Department of Electronic Systems, Norwegian University of Science and Technology (NTNU), O.S. Bragstads plass 2A, 7491 Trondheim, Norway

ABSTRACT

A fiber-coupled transmission spectroscopy setup using a pulsed external-cavity quantum cascade laser (EC-QCL, 1200-900 cm^{-1}) has been developed and demonstrated for measurements of aqueous solutions. The system has been characterised with regard to the laser noise and optimal optical pathlength. Solutions with glucose were used to further test the setup, and glucose concentrations down to physiologically relevant levels (0-600 mg/dL) were investigated. Albumin, lactate, urea, and fructose in various concentrations were added as interfering substances as their absorption bands overlap with those of glucose, and because they may be of interest in a clinical setting. Analyte concentrations were predicted using partial least-squares (PLS) regression, and the root-mean-square error of cross-validation for glucose was 10.7 mg/dL. The advantages of using a convolutional neural network (CNN) for regression analysis in comparison to the PLS regression were also shown. The application of a CNN gave an improved prediction error (8.3 mg/dL), and was used to identify important spectral regions. These results are comparable to state-of-the-art enzymatic glucose sensors, and are encouraging for further research on optics-based glucose sensors.

Keywords: Quantum cascade laser, mid-infrared spectroscopy, biomedical sensing, laser spectroscopy, glucose

1. INTRODUCTION

The research effort on biomedical sensors is growing and rapidly developing, with blood glucose monitoring dominating the market for biomedical sensors.[1] Glucose sensors are vital for diabetic patients, as these patients have to monitor their blood glucose level in order to prevent long- and short-term complications. Most commercial glucose sensors today base their measurements on enzymatic reactions, and can be used either for finger-prick tests, or for minimally invasive continuous glucose monitoring (CGM). These sensors suffer a loss of accuracy and reliability over time due to sensor and enzyme degradation, and must typically be changed every 1-2 weeks. Optical spectroscopy may be a better alternative for CGM, as it is reagent-free and non-destructive.

Several research groups have worked with systems for biomedical laser spectroscopy in the mid-infrared following the commerical availability of EC-QCLs. These systems have mainly used either free-space configurations with liquid samples in transmission cells,[2,3] or fiber-coupled setups with either transmission, reflectance, or attenuated total reflection (ATR) sensing modalities.[4–7] Fiber-coupled setups are more practical for portable sensor development, while free-space setups can potentially be used for larger systems in e.g. intensive care. However, there have been few detailed studies using EC-QCLs as sources in fiber-coupled configurations.

In this study we present a fiber-coupled spectroscopy setup aimed at continuous glucose monitoring, with a broadly tuneable EC-QCL as a source. The system noise as a function of pathlength is characterised. The performance of the system is tested using aqueous solutions with glucose and several analytes with overlapping absorption bands. We also show an application of a convolutional neural network as a method for regression analysis, and compare its performance to standard partial least-squares regression.

* ine.jernelv@ntnu.no; phone +47 73594400

Optical Fibers and Sensors for Medical Diagnostics and Treatment Applications XX, edited by Israel Gannot
Proc. of SPIE Vol. 11233, 1123311 · © 2020 SPIE · CCC code: 1605-7422/20/$21 · doi: 10.1117/12.2543984

2. METHODS

2.1 Experimental setup

The experimental setup (see Fig. 1) in this study consisted of a mid-infrared laser with a controller, a photodetector, an analog-to-digital converter card (ADC), a control computer, and a transmission sensing interface between two optical fibers. A pulsed external-cavity quantum cascade laser (EC-QCL, Hedgehog-UT, Daylight Solutions Inc., USA) was used as the light source. The laser was tuneable in the range 1200-900 cm^{-1} (8.33-11.1 µm), and was operated with a pulse length of 500 ns and a repetition rate of 100 kHz, for a 5% duty cycle. This wavelength range covers the main vibrational bands of glucose in the mid-infrared fingerprint region. An MCT detector (PCI-4TE, Vigo System S.A., Poland) with a 2x2 mm detector element was used to detect the infrared signal. This detector had a 4-stage thermoelectric cooling system, and operated at -75.2°C with a detectivity of $3{\times}10^9$ $cmHz^{1/2}W^{-1}$ at 10.6 µm. The laser beam was focussed into a fiber with an optical assembly mounted on the laser (OKSI Fibers Inc., USA). Silver halide fibers (Art photonics GmbH, Germany) were used to guide the light and sensing was done in a 200 µm gap between two fibers. The in-coupling fiber had a core diameter of 400 µm, while the out-coupling fiber had a core diameter of 600 µm.

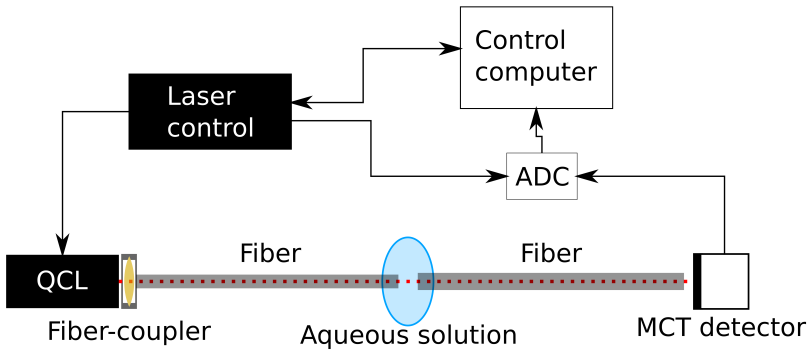

Figure 1: Sketch of the transmission setup. The arrows indicate the direction of data or information transfer.

2.2 Data recording

The analog signal from the MCT detector was recorded and digitised by an M2p.5946-x4 analog-to-digital converter card (Spectrum-Instrumentation GmbH, Germany). This board could digitise the signal at 80 MS/s with 16 bit resolution. The laser controller had a DB-15 connector with 15 pins for I/O signals. One of these pins generated a rising edge TTL at the start of each laser scan. This signal was used to trigger data acquisition. A scan speed of 275 cm^{-1}/s was used, and data recording was active for 1 second after the trigger. Spectra were recorded in the wavenumber range 1200-925 cm^{-1}.

Spectra were produced from the detected signal by integrating each laser pulse, and then creating data points by averaging n pulses, with $n = 255$ for these measurements. Additionally, for each measurement 10 laser scans were averaged to produce a raw spectrum, for a total measurement time of 10 s. This averaging was found to yield low measurement noise in a previous study.[7] Final measurement spectra were then made by subtracting a background spectrum of demineralised water.

2.3 Sample preparation

25 samples were prepared containing glucose, albumin, lactate, urea, and fructose, see Table 1 for an overview of analyte concentrations. Analyte concentrations in the samples were randomised according to an optimal design

model, in order to maintain experimental robustness with relatively few samples. A quadratic Scheffe model with A-optimality design was used for this sample set.

Analytes were dissolved in a phosphate-buffered saline (PBS) solution, which was made from PBS tablets and demineralised water. PBS is a solution with ion concentrations similar to the concentrations in the human body, and works as a buffer to maintain a constant pH. A separate set of seven samples with only glucose in demineralised water was prepared, with a concentration range of 0-500 mg/dL.

Table 1: Concentration ranges for analytes in the complex aqueous solutions.

Analyte	Concentration range
Glucose	0-600 mg/dL
Albumin	0-40 g/L
Lactate	0-250 mg/dL
Urea	0-250 mg/dL
Fructose	0-250 mg/dL

The additional analytes in the complex solutions were included based on their physiological relevance, as they are present in blood plasma and interstitial fluid in humans. The concentrations of lactate, urea, and fructose are exaggerated compared to physiological concentrations in order to increase the interference with the glucose levels.

2.4 Data analysis

All data analysis in this study was done with the freely available software SpecAnalysis, which is available on Github (https://github.com/jernelv/SpecAnalysis). This software is written in the Python programming language, and provides a system for pre-processing, feature selection, and multivariate analysis of spectral data.

2.4.1 Standard regression analysis

The absorbance spectra acquired from the different solutions were first analysed with partial least-squares (PLS) regression. All samples were measured five times over a period of two weeks, giving five separate datasets. Analyte prediction was evaluated with root-mean-square error of cross-validation (RMSECV), and additionally with the coefficient of determination (R^2), as RMSE-values are scale-dependent. Cross-validation (CV) was done with either leave-one-out (LOOCV) within datasets, or leave-one-dataset-out (LDOCV) between datasets.

The samples containing only glucose were analysed with PLS regression using 1 latent variable. PLS regression with 6 latent variables was used for the complex solutions. The data was mean centered and scaled prior to the regression analysis, and no other pre-processing was used.

2.4.2 Convolutional neural network

For further investigation of the acquired spectra we used a convolutional neural network (CNN) for concentration prediction. CNNs are a type of data mining model commonly used for e.g. image analysis, and have recently been applied to one-dimensional vibrational spectra.[8] CNNs are a variant of artificial neural networks (ANNs), which have previously been used for e.g. concentration prediction of glucose data from FTIR spectroscopy.[9] These ANNs used fully connected layers instead of convolutional layers, and had issues with overfitting on spectral data.

Neural networks are based on connected artificial neurons, where each neuron has an activation function that transforms an input into an output. These neurons are arranged in layers (see Fig. 2), which can be divided into input, output, and hidden layers. In standard ANNs the output of a neuron is used as input in every neuron in the next layer, giving fully connected layers. In a CNN the input is convolved using one or more kernel functions, which effectively reduces the number of times the output is used as an input in the next layer. This gives fewer connections and hidden variables in total, and CNNs are therefore computationally faster and are less prone to overfitting than equivalent fully-connected models. Neurons are connected together with weighted connections, which are set to a random initial value. The weights are then adjusted during the training phase.

For this study, we used a CNN with 2 hidden layers, and other CNN parameters were varied in order to find the optimal model. We searched through different ranges of layer size (5-35), kernel size (5-35), dropout rate (0-0.2) and stride (1-5). The stride is the step size of the kernel, while the dropout rate indicates the amount of randomly dropped neurons in the model, which is a method used to prevent overfitting.

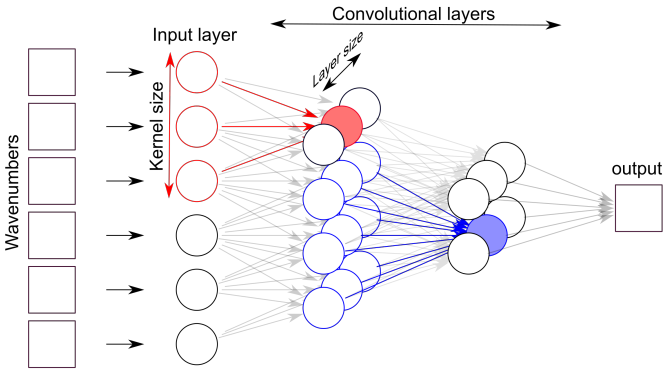

Figure 2: Example of a CNN with two convolutional (hidden) layers, where kernel and layer sizes are indicated. Each circle represents a neuron. A few neurons and connections have been highlighted in order to show the flow of input and output to and from neurons.

Neural networks are often seen as "black boxes" where the relation between the input data and the output regression is treated as an unknown. However, it is possible to look into this black box by operating directly on the output from neurons. The output of a neuron in a CNN is a product of a kernel used on a specific region of the spectrum. A feature selection method applied on these outputs can therefore be used to find regions of interest. In order to do this, we implemented a method for stability feature selection (SFS).[10] SFS is done by randomly selecting subsets of the data, and then retraining the last layer of the CNN. Features can then be scored according to the change in weights.

3. RESULTS AND DISCUSSION

3.1 Pathlength

Pathlength is an important parameter for transmission spectroscopy, as a trade-off between signal strength and noise level. For mid-infrared spectroscopy of aqueous media, such as in biomedical spectroscopy, pathlength is particularly significant because of the strong water absorption. Transmission FTIR spectroscopy has been limited to a few tens of micrometers, as FTIR sources have low spectral power density. A longer optimal pathlength can be expected for QCL systems, as they have several orders of magnitude higher spectral power density. Brandstetter et al.[2] demonstrated that a pathlength of approximately 140 µm was optimal for their QCL transmission setup, which was longer than the theoretical optimum.

System noise as a function of pathlength was investigated by recording transmission spectra through demineralised water with pathlengths in the range 130-260 µm. Full spectra were acquired at each position, as well as 100 000 pulses at 1190.5 cm^{-1} (8.4 µm). The relative standard deviation (RSD) when averaging over 255 pulses from the single-wavelength measurements is shown in Fig. 3a. The RSD is relatively constant at approximately 0.07% at shorter pathlengths, and then rapidly increases for pathlengths >210 µm. Figure 3b shows the measured intensities of single laser scans at different pathlengths. The shape of these spectra is a convolution of the laser emission profile and the water absorption.

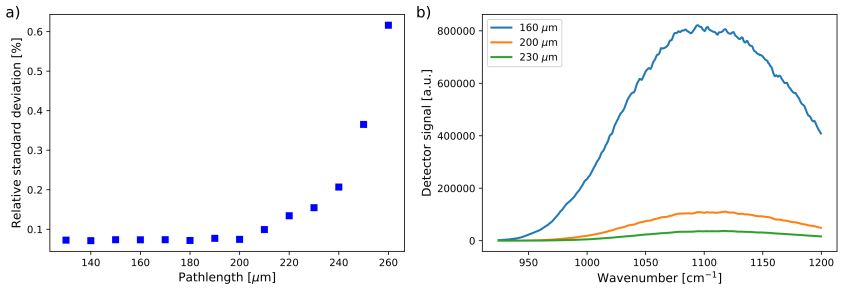

Figure 3: a) Relative standard deviation of laser pulse intensity at 8.4 µm for different transmission pathlengths. b) Signal intensity of single laser scans for different pathlengths. In both cases measurements were done with demineralised water between the fibers.

These results indicate that the laser noise dominates up to a pathlength of 210 µm. At longer pathlengths, the signal strength through the water decreases, until a point where detector noise becomes a significant part of the system noise. On the other hand, the absorbance signal from analytes increases linearly with an increase in pathlength. One should therefore use long pathlengths, as long as the system noise is not increased.

This was further validated by calculating the signal-to-noise ratio (SNR) as a function of pathlength based on full measurements. Standard samples of 100 mg/dL glucose in demineralised water were used for these measurements. We then used the same procedure as Brandstetter et al[2] to estimate SNR. The absorbance signal from the glucose peak at approximately 1080 cm^{-1} was used as the signal, while the RMS noise in the range 1040-1120 cm^{-1} was used as noise. The resulting plot of SNR as a function of pathlength is shown in Fig. 4c, and a pathlength of 200 µm was used for all further measurements.

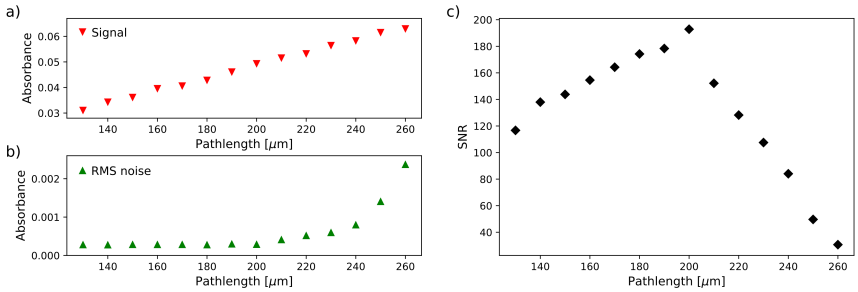

Figure 4: a) Absorbance signal as a function of pathlength, b) RMS noise as a function of pathlength, and c) SNR at 1080 cm^{-1} for a standard 100 mg/dL glucose solution in demineralised water.

With the sensing configuration in this setup, it was anticipated that some light could be lost in the gap between the two fibers, as light diverges when exiting a fiber. A fiber with a larger core was therefore used for the output in order to mitigate this effect. Based on the NA of the fiber (0.3), it was then expected that the output fiber would capture the entire beam. This was also indicated in the absorbance measurements, as the measured signal followed a linear trend as a function of pathlength (see Fig. 4a).

3.2 Glucose spectra

A preliminary characterisation of glucose absorbance spectra was done by measuring different glucose concentrations in water. Absorbance spectra are shown in Fig.5a, with the reference spectrum subtracted. Wavenumbers in the range 969-925 cm^{-1} were not included in the plot, as no absorption features were present.

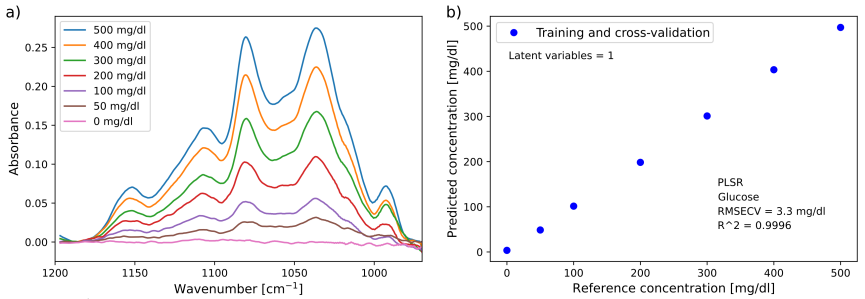

Figure 5: a) Absorbance spectra of aqueous glucose solutions with different glucose concentrations, and b) prediction of glucose concentrations in pure glucose solutions.

A prediction plot with leave-one-out cross-validation (LOOCV) of the pure glucose solutions is shown in Fig. 5b. This analysis was done using PLS regression with one latent variable, and gave an RMSECV of 3.3 mg/dL. For leave-one-dataset-out cross-validation the total RMSECV increased slightly to 4.3 mg/dL, with a coefficient of determination of R^2=0.9994.

3.3 Concentration measurements

For clinical applications, it is necessary to investigate if glucose concentrations can be predicted in the presence of other analytes with interfering absorption bands. Albumin, lactate, urea, and fructose were therefore added to a set of glucose solutions. These analytes were dissolved together with glucose in PBS solutions, to a total of 25 samples. Spectra of the individual analytes are shown in Fig. 6a. All the additional analytes have absorption bands that overlap with those from glucose. PBS also has two absorption bands in this wavelength range, and is scaled down to 1/3 for improved readability. As PBS has the same concentration in all samples it acts as a constant interference in the spectra.

Figure 6b shows a prediction plot for glucose in the complex solutions, with one case of leave-one-dataset-out cross-validation (LDOCV). The total RMSECV for LDOCV was 10.7 mg/dL. The RMSECV for leave-one-out cross-validation (LOOCV) within datasets was 9.4 mg/dL. The other analytes followed the same trend, with somewhat lower prediction errors for LOOCV than for LDOCV. This is as expected, since LOOCV does not capture e.g. between-day variations in the data. The prediction errors for all analytes are summarised in Table 2, and for conciseness only LDOCV is reported.

Table 2: Prediction errors with PLS regression for leave-one-dataset-out cross-validation (LDOCV) of all analytes used in the complex samples.

Analyte	RMSECV	R^2
Glucose	10.7 mg/dL	0.9972
Albumin	1.03 g/L	0.9922
Lactate	7.8 mg/dL	0.9917
Urea	11 mg/dL	0.9874
Fructose	8.7 mg/dL	0.9916

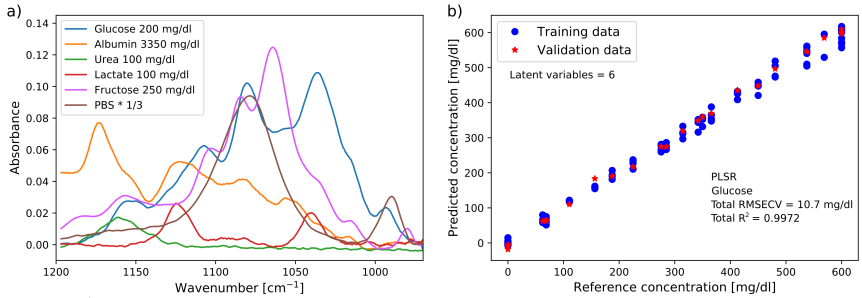

Figure 6: a) Absorbance spectra of different analytes and PBS dissolved in demineralised water with the background spectrum subtracted, and b) prediction of glucose concentrations in the complex solutions with PLSR and leave-one-dataset-out cross-validation, showing one case of the cross-validation.

This performance is comparable to the standard enzymatic glucose sensors used by diabetic patients, and has been found for solutions with analytes that are physiologically relevant for humans. The concentrations used here for lactate, urea, and fructose are higher than what is normally found in e.g. blood plasma or interstitial fluid, and the measurement error achieved for glucose should therefore be sufficient also for in vivo fluids. Measuring with a broadly tuneable laser also allows for simultaneous determination of other analytes which may have clinical significance.

3.4 Prediction with convolutional neural network

For the CNN, the total RMSECV for leave-one-dataset-out cross-validation was 8.3 mg/dL (see Fig. 7a), and for LOOCV the RMSECV was 8.1 mg/dL. Prediction results for all analytes are summarised in Table 3.

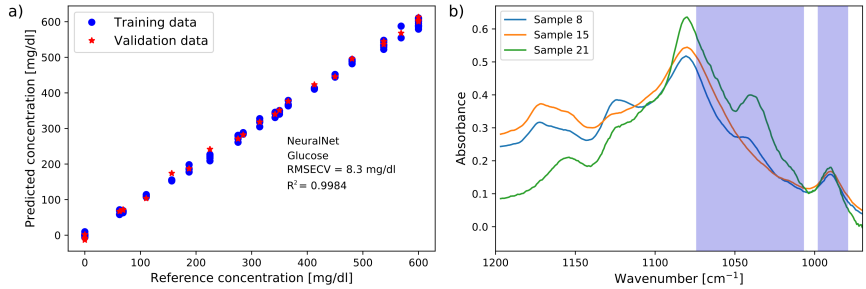

Figure 7: a) Prediction of glucose concentrations with CNN using leave-one-dataset-out cross-validation, showing one case of the cross-validation. b) Example spectra from the complex solutions, where important regions found with CNN and feature extraction have been marked. Glucose concentrations were 63 mg/dL, 0 mg/dL, and 422 mg/dL for Sample 8, 15, and 21 respectively. The other analytes were present in various concentrations.

Prediction errors were consistently lower for all analytes when using CNN as compared to PLS regression. The improvement was largest for glucose and albumin (approx. 20%). The difference was marginal for lactate and urea, which could be related to the lower intensity of their absorption features.

Table 3: Prediction errors with CNN regression for leave-one-dataset-out cross-validation of all analytes used in the complex samples.

Analyte	RMSECV	R^2
Glucose	8.3 mg/dL	0.9984
Albumin	0.89 g/L	0.9946
Lactate	7.5 mg/dL	0.9923
Urea	10.5 mg/dL	0.9885
Fructose	7.2 mg/dL	0.9945

Figure 7b shows the important spectral regions for glucose prediction as determined by CNN and stability feature selection. The important regions are overlayed on three example spectra from the complex solutions. This feature extraction has identified regions that overlap with glucose absorption features, which is not unexpected. It has also marked regions with relatively little interference from other analytes, which can be seen from Fig. 6. This indicates that feature extraction can be used as a tool to find out where the CNN is most sensitive to an analyte of interest. This can be used to e.g. narrow down the region of interest for further sensor development.

4. CONCLUSIONS

Glucose concentrations were predicted with high accuracy in solutions with other analytes with interfering absorption bands. An RMSECV of 10.7 mg/dL was shown with PLS regression, and this was further improved to 8.3 mg/dL with regression based on CNN. Several analytes found in e.g. interstitial fluid were used in these complex solutions, and the low prediction error achieved indicates that accurate in vivo measurements should be possible. Simultaneous determination of several analytes was also demonstrated. This is promising for future development of miniaturised sensors using optical fibers in the mid-infrared.

The high accuracy was in part achieved after a thorough analysis of the system noise. We showed that a pathlength of 200 µm in aqueous solutions could be used without detriment to the noise level. At the same time, this pathlength gave a higher absorbance signal, which resulted in a higher SNR as compared to longer or shorter pathlengths.

We also used a neural network in order to predict glucose concentration, and achieved better prediction errors than those in the PLS regression. The CNN results demonstrate that improved data modelling can be an important tool to achieve better prediction accuracies. Additional information could also be extracted from the CNN, such as the spectral regions where the model was most sensitive.

ACKNOWLEDGMENTS

This work was supported by the Research Council of Norway through the Double Intraperitoneal Artificial Pancreas project, grant number 248872. The project is part of Center for Digital Life Norway and is also supported by the Research Council of Norway's grant 248810.

REFERENCES

[1] Turner, A. P. F., "Biosensors - Sense and sensibility," *Chem. Soc. Rev.* **42**(8), 3184–3196 (2013).

[2] Brandstetter, M., Volgger, L., Genner, A., Jungbauer, C., and Lendl, B., "Direct determination of glucose, lactate and triglycerides in blood serum by a tunable quantum cascade laser-based mid-IR sensor," *Applied Physics B* **110**(2), 233–239 (2013).

[3] Vahlsing, T., Delbeck, S., Budde, J., Ihrig, D., Leonhardt, S., and Michael Heise, H., "Reliable glucose monitoring by ex-vivo blood microdialysis and infrared spectrometry for patients in critical care," *Optical Diagnostics and Sensing XVII: Toward Point-of-Care Diagnostics, Proc. SPIE* **10072** (2017).

[4] Isensee, K., Müller, N., Pucci, A., and Petrich, W., "Towards a quantum cascade laser-based implant for the continuous monitoring of glucose," *The Analyst* **143**(24) (2018).

[5] Liakat, S., Bors, K. a., Huang, T.-Y., Michel, A. P. M., Zanghi, E., and Gmachl, C. F., "In vitro measurements of physiological glucose concentrations in biological fluids using mid-infrared light.," *Biomedical Optics Express* **4**(7), 1083–90 (2013).
[6] Kasahara, R., Kino, S., Soyama, S., and Matsuura, Y., "Noninvasive glucose monitoring using mid-infrared absorption spectroscopy based on a few wavenumbers," *Biomedical Optics Express* **9**(1), 289–302 (2018).
[7] Jernelv, I. L., Strøm, K., Hjelme, D. R., and Aksnes, A., "Infrared spectroscopy with a fiber-coupled quantum cascade laser for attenuated total reflection measurements towards biomedical applications," *Sensors* **19**(23) (2019).
[8] Yang, J., Xu, J., Zhang, X., Wu, C., Lin, T., and Ying, Y., "Deep learning for vibrational spectral analysis: Recent progress and a practical guide," *Analytica Chimica Acta* **1081**, 6–17 (2019).
[9] Bhandare, P., Mendelson, Y., Peura, R. A., Janatsch, G., Kruse-Jarres, J. D., Marbach, R., and Heise, H. M., "Multivariate Determination of Glucose in Whole Blood Using Partial Least-Squares and Artificial Neural Networks Based on Mid-Infrared Spectroscopy," *Applied Spectroscopy* **47**(8), 1214–1221 (1993).
[10] Meinshausen, N. and Bühlmann, P., "Stability selection," *Journal of the Royal Statistical Society. Series B: Statistical Methodology* **72**(4), 417–473 (2010).

Paper IV

Signal enhancement in microstructured silicon attenuated total reflection elements with quantum cascade laser-based spectroscopy

I.L. Jernelv, J. Høvik, D.R. Hjelme, A. Aksnes

Proceedings of SPIE 11359, Biomedical Spectroscopy, Microscopy, and Imaging, 113590A, 2020.

Signal enhancement in microstructured silicon attenuated total reflection elements with quantum cascade laser-based spectroscopy

Ine L. Jernelv*, Jens Høvik, Dag Roar Hjelme, and Astrid Aksnes

Department of Electronic Systems, Norwegian University of Science and Technology (NTNU), O.S. Bragstads plass 2b, 7491 Trondheim, Norway

ABSTRACT

Sensors in mid-infrared spectroscopy based on attenuated total reflection (ATR) sensing with internal reflection elements (IREs) facilitate easier measurements of aqueous solutions or other opaque analytes. Micromachined silicon (Si) elements are an attractive alternative to conventional IREs, as they can be produced cheaply with silicon processing. Techniques for surface modifications are also easily integrated into the wafer process, and surface structures such as micropillars or nanoparticles can thereby be used for signal enhancement. Replacing the classic Fourier transform infrared (FTIR) spectrometers with tuneable quantum cascade lasers (QCLs) also opens up new avenues for sensing. In this study, the performance of basic and signal-enhanced Si IREs has been compared for measurements in a spectroscopy setup with a fibre-coupled tuneable QCL source. These IREs had V-shaped microgrooves etched on the underside for more efficient in-coupling of light, while the signal-enhanced IREs also had micropillars on the top surface. The results are also contrasted with measurements done in a standard ATR-FTIR spectrometer, using an Alpha II spectrometer with a single-reflection diamond ATR crystal. Various concentrations of glucose (75–5000 mg/dL) in aqueous solutions were used to characterise the system performance. The quality of the signal enhancement was evaluated with regard to sensitivity and noise level in the acquired spectra. The microstructured Si IREs gave a signal enhancement of up to a factor of 3.8 compared to a basic Si element, with some concomitant increase in noise. The absorbance was higher for both types of Si IREs as compared to the diamond ATR crystal. The effective enhancement and the the limit of quantification improved by a factor up to 3.1 in the signal-enhanced IREs compared to the basic Si element.

Keywords: Quantum cascade laser, attenuated total reflection, laser spectroscopy, mid-infrared, glucose

1. INTRODUCTION

Mid-infrared spectroscopy is a routinely used analytical technique, with recent promising developments towards new biomedical applications and miniaturised sensors. Sensors based on attenuated total reflection (ATR) spectroscopy facilitate easier measurements of aqueous solutions or other opaque analytes. Traditionally, relatively large and expensive crystals have been used as internal reflection elements (IREs).[1] Micromachined silicon wafers are an attractive alternative to conventional IREs, as they can be produced cheaply with silicon processing.[2] Additionally, techniques for surface modifications are easily integrated into the wafer process, and surface structures such as micropillars or nanoparticles can thereby be used for signal enhancement. Surface-enhanced infrared absorption spectroscopy (SEIRAS) has been used to achieve enhancement through excitation of localised surface plasmon resonances (LSPRs).[3] LSPRs can be generated at surfaces with rough metal layers or nanoparticles, and are resonant at specific wavelengths depending on the particle sizes. One drawback with this method is that the nanoparticle layer tends to degrade over time, and the substrate has low reproducibility. Another option is to introduce surface modifications through microstructuring, which has been demonstrated on silicon wafer chips.[4–6] Enhancement in different three-layer IRE systems has been demonstrated previously,[7] but the use of silicon is a step forward as it allows for utilisation of semiconductor device manufacturing.

Use of these signal-enhanced IREs enables sensor minaturisation, as they can achieve an increased absorbance signal through evanescent field sensing while maintaining small dimensions. Sensing in reflection mode is an

* ine.jernelv@ntnu.no; phone +47 73594400

Biomedical Spectroscopy, Microscopy, and Imaging, edited by Jürgen Popp, Csilla Gergely, Proc. of SPIE Vol. 11359, 113590A · © 2020 SPIE
CCC code: 0277-786X/20/$21 · doi: 10.1117/12.2554528

advantage for fibre-based applications, and this IRE geometry can potentially be contained on a fibre tip. Conventional silicon IREs are hemispherical, and the larger dimensions limit their use at long wavelengths as silicon has decreased transparency below ∼1400 cm^{-1}. Use of IREs based on silicon wafers makes it possible to measure at longer wavelengths as the typical 500 µm wafer thickness means that optical loss is limited. Replacing classic Fourier transform infrared (FTIR) spectrometers with tuneable quantum cascade lasers (QCLs) also opens up new avenues for sensors. For example, the smaller size of QCLs can contribute to a smaller device footprint. The high spectral power density compared to FTIR spectrometers also means that QCLs can outperform FTIR spectrometers in several applications.

Schumacher et al.[2] demonstrated utilisation of a silicon wafer with V-shaped grooves on the underside in the long wavelength region 1500–300 cm^{-1}. More recently, Sykora et. al.[5] showed that substantial signal enhancement could be achieved by microstructuring the top surface of a wafer. The analytical performance of this microstructured wafer was further studied in an FTIR spectrometer (1800–600 cm^{-1}) by Haas et al.[6] While Haas et al. also showed some spectra from QCL measurements, no results regarding analytical performance were shown. In the present study we quantify the signal enhancement achievable in commercially available microstructured silicon (Si) IREs in a QCL-based spectroscopy setup. The focus of this study is the 1200–925 cm^{-1} spectral range as it is relevant for many biomedical applications, such as glucose sensing.[8] The Si IREs were either basic chips with a flat sensing surface, or surface-enhanced chips with a microstructured sensing surface. The Si IREs were also simulated in order to examine the enhancement effect. A cursory comparison was done with measurements in an ATR-FTIR spectrometer with a diamond IRE.

2. METHODS

2.1 Experimental setup

Measurements in this study were done in a QCL-based ATR spectroscopy setup, see Fig. 1. The experimental equipment for this setup was a QCL source, a photoconductive detector, hollow-core fibres for guiding laser radiation, and internal reflection elements (IREs) for sensing. The laser source was a pulsed external-cavity (EC) QCL (Hedgehog-UT, Daylight Solutions, USA) with a tuning range of 1200–900 cm^{-1} (8.33–11.1 µm). The maximum average output power of the laser was 22 mW with a 5% duty cycle. The laser was cooled thermoelectrically and set to a temperature of 19°C for all measurements. This laser emitted radiation with linear vertical polarisation (100:1, according to specifications). The IR detector was a mercury-cadmium-telluride (MCT) detector (PCI-4TE, Vigo System SA, Poland) with a 2×2 mm element size. The laser beam was focussed into a fibre with an optical assembly mounted on the laser (OKSI fibers, USA). A 300 µm diameter hollow-core fibre (OKSI Fibers, USA) was used to couple light into the IREs, while a 1 mm diameter hollow-core fibre was used to guide light from the IREs to the detector. The laser radiation was found to be elliptical or nearly circularly polarised after transport through the fibres.

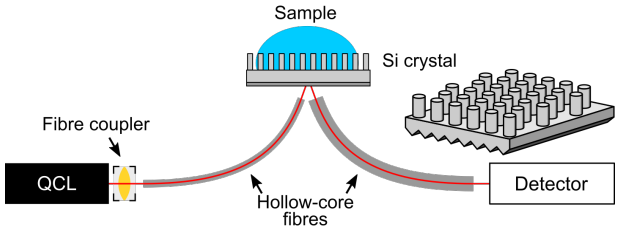

Figure 1: Illustration of experimental setup for the ATR spectroscopy measurements with a QCL source, fibre coupler, hollow-core fibres, Si IRE, and MCT detector. The inset shows a 3D view of an IRE with an optional micropillar enhancement layer. The micropillars are arranged in a hexagonal pattern, and the V-grooves under the wafer are oriented parallel to the laser beam path.

Two types of silicon wafer chips were acquired from IRUBIS GmbH (Germany). These Si IREs had V-shaped grooves etched on the underside for more efficient in-coupling of light. The V-grooves were oriented parallel to the laser beam path. Chips without any further processing had flat top surfaces and were used as standard single-reflection ATR crystals, and will be referred to as "basic" Si IREs. The elements could be further modified on the top surface with a reactive ion etch (RIE) step to create micropillar structures. These micropillar structures facilitate signal enhancement (SE) through an interference effect and field enhancement between the pillars.[9] This effect occurs when the micropillars and the sample form an effective medium layer due to the sub-wavelength sizes of the micropillars. Two IREs with micropillars were investigated for this study, and will be referred to as "SE element #1" and "SE element #2".

Measurements were acquired in an FTIR spectrometer (Alpha II, Bruker Optics Inc., USA) for comparison. This spectrometer was equipped with an ATR module using a single-reflection diamond IRE and had a measurement range of 4000–400 cm^{-1}.

2.2 Data recording

For the QCL setup, measurement spectra were acquired by tuning the laser over a wavelength range and recording the signal on the MCT detector. This analog signal was digitised by an analog-to-digital converter (ADC) card (M2p.5946-x4, Spectrum-Instrumentation GmbH, Germany). The signal was digitised at 80 MS/s with 16 bit resolution. A trigger from the laser controller was used to start data acquisition. The data presented here was recorded in the range 1200–925 cm^{-1}, with a scan speed of 275 cm^{-1}/s.

Averaging, or binning, was used to minimise laser noise. Spectral data points were made by integrating each laser pulse and then averaging a certain number of pulses ($n = 255$ for these measurements). In addition, 10 scans were averaged for each measurement. One spectrum took 10 seconds to record with these settings. Final absorbance spectra were then made by subtracting a background (water) measurement.

For the FTIR measurements, data recording was done with the OPUS software (Bruker Optics Inc., USA). Measurements were recorded in the 4000–400 cm^{-1} spectral range, and 128 scans were averaged for each measurement. The initial spectral resolution was set to 2 cm^{-1}. A zero-filling factor of 2 was used in the OPUS software for the fast Fourier transform (FFT), which gave an interpolation between data points so that the final data point spacing was 1 cm^{-1}. Each measurement in the FTIR spectrometer took approximately 3 minutes.

2.3 Simulations

The Si IREs were simulated in order to investigate the enhancement effect. The simulations were performed using the finite element method (COMSOL Multiphysics v.5.2, COMSOL AB, Stockholm, Sweden.). The simulation geometry was a cross section of the Si IREs in a two-dimensional (2D) environment. The light source was modelled as a plane-wave with an incidence angle of 41° and with in-plane polarisation (i.e. p-polarisation). The boundary conditions between the micropillars and the sample medium relative to the polarisation of the incident light is an important contribution to the increase in field strength. This contribution would disappear if s-polarised light was used, as this periodicity disappears for out-of-plane polarisation in a 2D simulation. The geometry was discretised such that the largest element size was 0.9 µm, roughly 1/10th of the free-space wavelength of the light source. A wavelength sweep was conducted for the wavelength range 1250–893 cm^{-1} (8.2–11 µm) where a surface integration was performed after each simulation to find the total electromagnetic field intensity in the sensing medium (i.e. the medium surrounding the micropillars). Finally the relation between the total field intensity in the sensing area with and without micropillars was calculated to give an indication of the total enhancement of the system.

2.4 Glucose solutions

Measurements were done on glucose solutions, where glucose (D-(+)-glucose, Sigma-Aldrich, USA) was dissolved in demineralised water. A total of 9 samples were made with glucose concentrations in the range 75-5000 mg/dL. A stock solution of 5000 mg glucose in 100 mL water was used to prepare the other samples by dilution.

2.5 Analysis

Calibration curves were made based on the height of the largest glucose absorption band, at approximately 1035 cm^{-1}. The performance of the IREs was then evaluated based on absorbance signal, noise level, limit of quantification (LoQ) and effective enhancement for the signal-enhanced IREs. The enhancement factor was calculated as signal-enhanced/basic absorption peak. Noise was calculated as the RMS-noise of blank spectra in the spectral region 1055–1015 cm^{-1}. Limit of quantification (LoQ) was then estimated based on a signal-to-noise (SNR) ratio of 10:1, where the signal was the height of the most intense absorption band and the RMS noise was the noise level. The effectivity of the signal enhancement was then calculated as the ratio of SNR between the signal-enhanced chips and the basic Si chips.

3. RESULTS AND DISCUSSION

3.1 IRE dimensions

The micropillar structures in the signal-enhanced Si IREs were imaged in a scanning electron microscope (Apreo SEM, FEI Company, USA), see Fig. 2.

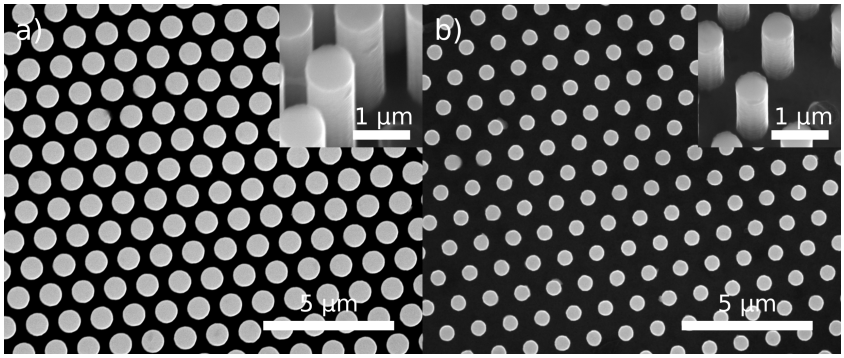

Figure 2: SEM pictographs of Si chips with patterned micropillars, a) SE element #1 and b) SE element #2. The insets show side views at an angle of approximately 25 degrees.

Dimensions of the micropillars are summarised in Table 1. Micropillar dimensions were evaluated with ImageJ, which is an open-source software for scientific image analysis. The pillar periodicity was essentially the same, so the main differences between the IREs were the pillar diameter and height.

Table 1: Geometrical parameters for the Si IREs with micropillar structures.

Dimension	SE element #1	SE element #2
Height	3.5 µm	1.66 µm
Pillar diameter	0.86 µm	0.57 µm
Period	1.25 µm	1.23 µm

3.2 Simulations

Simulations of the field enhancement effect were set up in COMSOL Multiphysics. The flat-topped and the two signal-enhanced elements were all simulated, and the micropillar dimensions from SEM were used for the signal-enhanced elements, see Fig. 3a) for a simulation snapshot.

Enhancement was estimated based on the field intensity in the area above the Si substrate, which was found by a field integration in the sensing medium. The total field intensity in the signal-enhanced IREs was then divided by the field intensity in the basic Si IRE. The resulting enhancement factors are plotted in Fig. 3b) as a function of wavelength. Based on this, SE element #1 had a high enhancement factor that tapered off sharply for wavelengths shorter than 10 µm, while SE element #2 had a more constant enhancement over the available wavelength range.

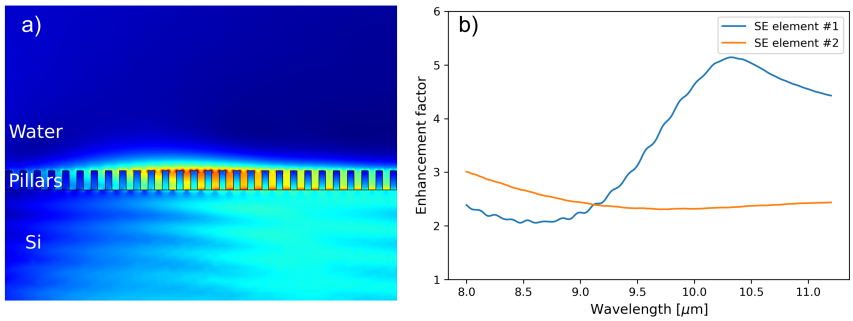

Figure 3: a) 2D structure based on SE element #2 used in the simulations, with evanescent field. b) Enhancement factor in the signal-enhanced Si IREs as a function of wavelength.

These 2D simulations have some limitations with regards to the real micropillar structures. Since the simulations are performed in a 2D environment the model closely resembles a linear array of pillars, even though the IREs themselves utilise a triangular honeycomb lattice. This 2D approximation might therefore lack certain intricacies which might deviate the simulated result from the experimentally verified data. For example, the distance between the pillars will vary between 1.2 µm and 2.1 µm depending on the cross section used for the simulations. We therefore used the pillar radius from SEM, and an average value for the pillar distances. Additionally the light source is not a perfect plane wave but includes field components which are incident on the chip surface with sharper angles than 41°. This leads to some radiation which is caught by the surface integration and thus slightly lowers the calculated amplification of the simulations.

3.3 Comparison between IRE types

Glucose measurements from the FTIR spectrometer with a diamond IRE and the basic Si IRE in the QCL setup are shown in Fig. 4. All glucose absorption bands were found by both methods, but there were some minor structural differences between the measurement sets. For example, the dip at 1000 cm^{-1} was lower for the basic Si element, and the height difference between the absorption bands at 1035 cm^{-1} and 1080 cm^{-1} was larger compared to the diamond IRE. This was likely due to alignment issues in the QCL setup. It was observed that fibre alignment relative to the chip and alignment of in- and out-coupling fibres relative to each other could influence the shape of the absorption spectrum. Overall the absorbance was ∼4.5 times higher in the QCL-based setup with an basic Si element compared to the ATR-FTIR spectrometer.

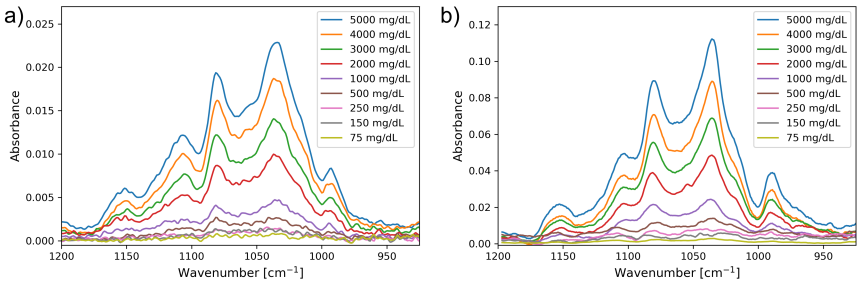

Figure 4: Example spectra from glucose solutions with water background subtracted using a) FTIR spectrometer with a single-reflection diamond IRE, and b) QCL setup with a single-reflection basic Si IRE.

One possible drawback with Si IREs is the formation of a silicon dioxide (SiO_2) layer on the sensing surface, which has been remarked in previous studies.[2,6] Absorption in thick layers of SiO_2 will affect measurements, but thicker layers are mainly formed under high temperature conditions. We expected the layer to be a few nanometers thick, and no clear absorption features could be seen for these IREs.

Measurements from the two signal-enhanced elements are shown in Fig. 5. Both IREs clearly displayed increased absorption compared to the basic Si IRE. The signal in SE element #1 appeared to gradually drop off above approximately 1045 cm^{-1}. This was as expected from the simulations, and the micropillar geometry in this element likely meant that the micropillar layer did not act as an effective medium layer for shorter wavelengths.

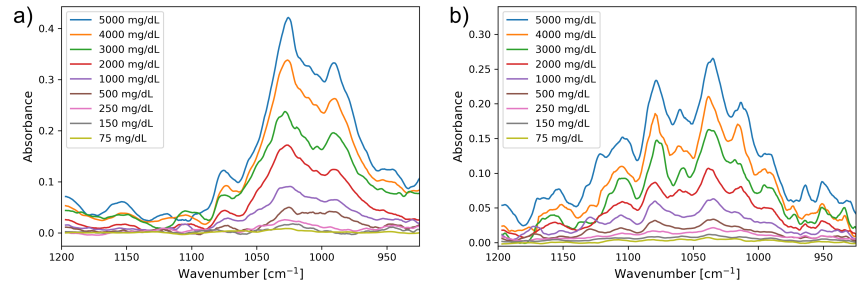

Figure 5: Example spectra from glucose solutions with water background subtracted in the QCL setup using a) SE element #1, and b) SE element #2.

For SE element #2, the signal enhancement was more uniform over the entire wavelength range. However, these spectra had some additional features, such as a splitting of the glucose absorption peak at 1020 cm^{-1}. Fibre alignment was again seen to have a large influence on the appearance of the absorption bands, which was the same behaviour as for the basic Si IRE.

Calibration curves for the measured IREs are shown in Fig. 6. This shows a direct comparison of the highest glucose absorption peaks for the different IREs and setup types. A linear correlation between the absorption peak and the concentration was observed for all IRE types.

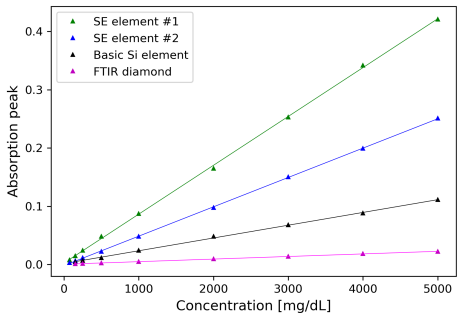

Figure 6: Calibration curves from measurements of glucose concentrations in the four IREs. Signal was measured as the height of the strongest absorption peak, at approximately 1035 cm^{-1}.

The performance of the different IREs is summarised in Table 2. LoQ improved in both signal-enhanced IREs compared to the basic Si IRE. However, the signal enhancement was accompanied by an increase in noise, and the effective enhancement was therefore somewhat lower than what the increase in absorbance signal would indicate. The effective enhancement was a factor of 3.1 and 1.9 in SE element #1 and SE element #2, respectively. The enhancement factors were a bit lower than expected from the COMSOL simulations, but were otherwise consistent. The achieved LoQ of 35 mg/dL indicates that these SE IREs could potentially be used in applications such as glucose sensing, as the range of physiological glucose concentrations in diabetic patients is 30–400 mg/dL.

Table 2: Performance comparison of the basic and signal-enhanced IREs in the QCL-based spectroscopy setup, as well as the diamond IRE in the ATR-FTIR spectrometer. The absorption peak was measured at approx. 1035 cm^{-1} for 5000 mg/dL glucose concentration, and the RMS noise was measured from blank spectra. Effective enhancement in the SE elements was based on the sensitivity improvement compared to the basic Si IRE.

IRE	Absorption peak	RMS noise	LoQ (mg/dL)	Enhancement	Effectivity
SE element #1	0.42	0.00027	35	3.8	3.1
SE element #2	0.25	0.00027	55	2.3	1.9
Basic Si	0.11	0.00022	100	-	-
Diamond (FTIR)	0.023	0.00009	195	-	-

The LoQ was worse in the FTIR spectrometer than the QCL-based setup with even the basic Si IRE, which can be attributed to the lower absorbance signal. The RMS noise was however lower in the spectrometer due to lower relative intensity noise (RIN) in the FTIR source, as well as the longer averaging in the spectrometer. The spectrometer SNR is proportional to $\sqrt{n}$ where n is the number of averaged scans. Noise could therefore have been improved in the FTIR by increasing measurement time and averaging more scans, however the measurement time was already over 3 minutes. This shows some of the advantages that QCLs can have over standard FTIR spectrometers with regards to measurement time and sensitivity.

The main challenges in the QCL-based setup were related to alignment and stability. As mentioned, fibre alignment was seen to influence the shape of absorption bands. However, measurements were repeatable after the setup was stabilised. The noise level was also influenced by vibrations in the fibres, and hence stability was also important for noise minimisation.

4. CONCLUSIONS

This study evaluated the performance of microstructured Si elements with and without a signal enhancement layer as IREs in a QCL-based ATR spectroscopy setup. The signal-enhanced chips were found to improve the absorbance signal up to a factor of 3.8, while due to simultaneous increase in noise the LoQ improved by up to a factor of 3.1. Very different behaviours were seen in the two IREs with micropillars for signal enhancement, which shows that it is important to consider pillar geometry in relation to the wavelength region used. The COMSOL simulations agreed well with the experimental results. 3D simulations should be done in the future to further investigate the effect of the micropillar lattice structure, and the effect of polarisation.

These micromachined Si IREs can be mass-produced and may potentially be integrated in single-use applications for e.g. biomedical measurements. The signal enhancement also gave good LoQs, considering the single-reflection geometries, and another possible application is to use these IREs as sensing surfaces for fibre-optic sensors in reflection mode. This work also demonstrated measurements with Si IREs below 1200 cm^{-1}, which is usually considered opaque for Si components.

ACKNOWLEDGMENTS

The Research Council of Norway is acknowledged for the support to the Norwegian Micro- and Nano-Fabrication Facility, NorFab, grant number 245963/F50, as well as the Double Intraperitoneal Artificial Pancreas project, grant number 248872. The project is part of Center for Digital Life Norway and is also supported by the Research Council of Norway's grant 248810. The authors would like to thank Lorenz Sykora at IRUBIS GmbH for a helpful discussion on the silicon internal reflection elements.

REFERENCES

[1] Jernelv, I. L., Strøm, K., Hjelme, D. R., and Aksnes, A., "Infrared spectroscopy with a fiber-coupled quantum cascade laser for attenuated total reflection measurements towards biomedical applications," *Sensors* **19**(23), 5130 (2019).

[2] Schumacher, H., Künzelmann, U., Vasilev, B., Eichhorn, K. J., and Bartha, J. W., "Applications of microstructured silicon wafers as internal reflection elements in attenuated total reflection Fourier transform infrared spectroscopy," *Applied Spectroscopy* **64**(9), 1022–1027 (2010).

[3] Bibikova, O., Haas, J., López-Lorente, Á. I., Popov, A., Kinnunen, M., Ryabchikov, Y., Kabashin, A., Meglinski, I., and Mizaikoff, B., "Surface enhanced infrared absorption spectroscopy based on gold nanostars and spherical nanoparticles," *Analytica Chimica Acta* **990**, 141–149 (2017).

[4] Morhart, T. A., Unni, B., Lardner, M. J., and Burgess, I. J., "Electrochemical ATR-SEIRAS Using Low-Cost, Micromachined Si Wafers," *Analytical Chemistry* **89**(21), 11818–11824 (2017).

[5] Sykora, L., Müller, A., Kondratiev, A., Roth, A., Mozin, V., Fehr, A., and Zörnack, G., "Silicon ATR crystal with subwavelength structures optimized for blood analysis," *Optical Fibers and Sensors for Medical Diagnostics and Treatment Applications XIX* **10872**, 14 (2019).

[6] Haas, J., Müller, A., Sykora, L., and Mizaikoff, B., "Analytical performance of μ-groove silicon attenuated total reflection waveguides," *Analyst* **144**(10), 3398–3404 (2019).

[7] Huber-Wälchli, P. and Günthard, H. H., "Interference Enhanced Attenuated Total Reflection (IEATR). A new technique for i.r. matrix spectroscopy with high sensitivity," *Spectrochimica Acta Part A: Molecular Spectroscopy* **34**(12), 1253–1262 (1978).

[8] Jernelv, I. L., Milenko, K., Fuglerud, S. S., Hjelme, D. R., Ellingsen, R., and Aksnes, A., "A review of optical methods for continuous glucose monitoring," *Applied Spectroscopy Reviews* **54**(7), 543–572 (2019).

[9] Berz, F., "On a quarter wave light condenser," *British Journal of Applied Physics* **16**(11), 1733–1738 (1965).

Paper V

Convolutional neural networks for classification and regression analysis of one-dimensional spectral data

I.L. Jernelv, D.R. Hjelme, Y. Matsuura, A. Aksnes

Preprint published on `arxiv.org`*, arXiv ID 2005.07530, 2020.*

Convolutional neural networks for classification and regression analysis of one-dimensional spectral data

Ine L. Jernelv,* Dag Roar Hjelme, and Astrid Aksnes
Department of Electronics, Norwegian University of Science and Technology (NTNU), O.S. Bragstads plass 2A, 7491 Trondheim, Norway

Yuji Matsuura
Graduate School of Biomedical Engineering, Tohoku University, Sendai, 980-8579, Japan
(Dated: May 15, 2020)

Convolutional neural networks (CNNs) are widely used for image recognition and text analysis, and have been suggested for application on one-dimensional data as a way to reduce the need for pre-processing steps. Pre-processing is an integral part of multivariate analysis, but determination of the optimal pre-processing methods can be time-consuming due to the large number of available methods. In this work, the performance of a CNN was investigated for classification and regression analysis of spectral data. The CNN was compared with various other chemometric methods, including support vector machines (SVMs) for classification and partial least squares regression (PLSR) for regression analysis. The comparisons were made both on raw data, and on data that had gone through pre-processing and/or feature selection methods. The models were used on spectral data acquired with methods based on near-infrared, mid-infrared, and Raman spectroscopy. For the classification datasets the models were evaluated based on the percentage of correctly classified observations, while for regression analysis the models were assessed based on the coefficient of determination (R^2). Our results show that CNNs can outperform standard chemometric methods, especially for classification tasks where no pre-processing is used. However, both CNN and the standard chemometric methods see improved performance when proper pre-processing and feature selection methods are used. These results demonstrate some of the capabilities and limitations of CNNs used on one-dimensional data.

I. INTRODUCTION

Chemometric methods are an essential part of understanding and interpreting vibrational spectral data. Vibrational spectroscopy uses variants of near-infrared (NIR), mid-infrared (MIR), or Raman spectroscopy techniques, and produce one-dimensional spectral data. Models for spectroscopy data usually try to either map the spectra to distinct classes (classification), or try to extract quantitative information (regression). Designing optimal models is challenging for both classification and regression analysis. Most samples have several constituents with overlapping bands, which makes simple considerations based on e.g. peak heights insufficient for any data interpretation or accurate analysis. Additionally, spectroscopy is used for applications in many different fields, including arts, forensics, food science, environment, and medicine [1–5].

For classification, common chemometric methods include linear discriminant classifiers, support vector machines, *k*-nearest neighbours, and logistic regression methods. For quantitative analysis, regression methods such as principal component regression, partial least-squares regression, and random forest regression are commonly used. Prior to the actual analysis, pre-processing methods and feature selection are often applied to the datasets.

* ine.jernelv@ntnu.no

Pre-processing methods are commonly applied to spectral data for several purposes, including noise removal and removal of unwanted physical phenomena that affect the data. The end goal of the applied pre-processing steps is to improve the interpretability of the data, and thereby achieve higher accuracy in the following classification or quantitative multivariate analysis. There are many methods for pre-processing, and the optimal choice of pre-processing methods usually depends on the measurement method used (NIR, MIR, Raman, etc.) and the aim of the analysis [6, 7]. In addition, factors such as sample matrix, equipment settings, and environmental influences can affect the data, so that previously applied pre-processing methods may not work well on a new dataset. Practically, the selection of methods is frequently based on previous experiences, or alternatively an exhaustive search of all possible methods that the researcher has available. Exhaustive searches should give the best results, but are computationally expensive and time-consuming. It has been shown that optimal - or at least close to optimal - pre-processing methods can be selected based on design of experiments [8], which could make the selection much faster.

Spectral data typically has relatively few samples (10s to a few 100s), each with many features (up to 1000s). This can be detrimental to multivariate analysis, as random correlations and noisy features may lead to a deterioration of the model, and a tendency to overfit can give low predictive ability. Feature selection is performed in order to remove irrelevant or redundant features, preferentially leaving only features that are relevant to the

analysis [9]. The objective of feature selection is the same as for pre-processing, namely increased interpretability of the data and better outcomes in multivariate analysis. Feature selection can be very computationally expensive and a plethora of feature selection methods exist, while some learning algorithms have built-in feature selection.

One alternative to optimisation of pre-processing and feature selection is to use learning models that are capable of extracting fundamental information from data, for example convolutional neural netoworks (CNNs). Artificial neural networks (ANNs) are computational models inspired by the biological neural connections in brains. One-layer ANNs have been used for classification and regression of spectral data for almost three decades, for example in combination with PLS [10]. ANNs are particularly useful for non-linear problems and can be used on almost any type of data. However, models such as PLS-ANN have not superseded standard chemometric methods, largely due to issues with overfitting and low interpretability [11]. CNNs can improve upon this, as the convolutional layers of the network are not fully connected, and are therefore in theory less prone to overfitting. Additionally, the convolution leads to fewer free parameters, and each layer becomes related to specific parts of the input data, which increases ease of operation and interpretability.

CNNs are widely used for data mining of two-dimensional data, including areas such as image recognition and text analysis. Neural networks have several interesting characteristics for data modelling, such as the capability to model nonlinear responses and to accentuate relevant features. CNNs can therefore be expected to perform well on learning tasks also for one-dimensional data, even without pre-processing or feature extraction methods. Thus far, only a few studies have used CNNs for classification or quantitative analysis on vibrational spectroscopic data. Acquarelli et al. [12] demonstrated that CNNs could outperform several standard chemometric methods for classification, both using raw and pre-processed spectral data. CNNs have also been shown to efficiently classify Raman spectra of mineral data without spectral preprocessing [13]. For quantitative analysis CNNs have been used both for feature selection for regression methods [14], and directly for regression analysis [15]. Outside of standard vibrational spectroscopy, some recent studies have also used CNNs for analysis of other spectral data, such as classification of hyperspectral data [16], functional near-infrared spectroscopy signals [17], and electrocardiogram (ECG) signals [18].

This study will investigate the performance of a CNN as compared to standard chemometric methods for classification and quantitative analysis on several datasets acquired with different spectroscopic methods. For classification the CNN will be compared to PLS-DA, kNN, SVM, and logistic regression, while for quantitative analysis the CNN will be compared to PCR, PLSR, random forest regression, and elastic net. The comparison will be made on models both with and without the use of pre-processing methods, as well as with and without feature selection methods. All methods used in this study were assembled in a software package, named SpecAnalysis, which has been made available online. In our view, there are two main original contributions in this work: Use of CNNs for both classification and regression analysis, with a comparison to several standard chemometric methods, and comparison of models with additional use of pre-processing and/or feature selection, to further assess the performance of CNNs.

II. MATERIALS AND METHODS

A. Data analysis

The analysis was done with a software package made in Python, called SpecAnalysis, which can be found on GitHub (`https://github.com/jernelv/SpecAnalysis`). Python is an open-source programming language, and can be used on all common operating systems. SpecAnalysis has a graphic user interface, and is therefore user-friendly even for spectroscopists who are not experienced programmers.

SpecAnalysis has functionality for spectral pre-processing, feature selection, various chemometric and machine learning methods, and can be employed for both regression analysis and classification tasks. Some methods in SpecAnalysis were based on tools from scikit-learn [19], while others were made in-house.

The methods used in this study for classification, regression analysis, and feature selection are briefly described below, and an overview of the pre-processing methods is given. More information on the methods can be found in the references or in the SpecAnalysis documentation.

1. Convolutional neural network

The basic structure of artificial neural networks (ANNs) consists of connected artificial neurons. Each neuron is characterised by an activation function, which is a function that acts on the input. Neural networks have three types of layers: input, hidden, and output layers. For the input and output layers, which are the first and last layers respectively, the activation functions are generally linear. Neural networks have one or more hidden layers, where the activation functions are normally non-linear. The output at each layer is used as the input of the next layer. In a fully-connected feed-forward ANN, all neurons in each layer are connected to all neurons in the next layer, with no connections going backward to previous layers. The connections between the layers are weighted, and these weights are learned in the training phase after a random initialisation.

In convolutional neural networks (CNNs) the hidden layers convolve the input and then give the result to the

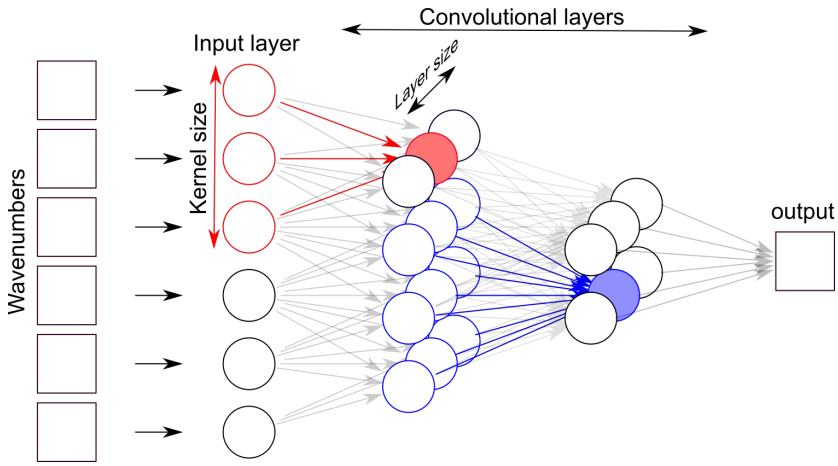

FIG. 1. Example of a CNN, where kernel and layer sizes are marked. A few neurons have been highlighted in order to show the flow of input and output. Figure reprinted from ref. [20].

next layer, see Fig. 1. Consequently, the layers are not fully connected. For image analysis this makes the neural network less computationally expensive, and a deeper network can be used. For one-dimensional data computational power is a lesser concern, but it has been suggested that CNNs may avoid issues with overfitting previously seen in ANNs. The relatively few samples in spectroscopy datasets and large amounts of features makes ANNs very prone to overfitting.

In a CNN, data is divided into one or several kernels, which will be associated with different sections of the input data [21]. The convolutional layer works by convolving, or shifting, the kernel from the first to the last variable. The kernel thereby acts as a filter, and can be shifted by different lengths called *strides*.

We tested both the Adam optimiser and the stochastic gradient descent (SGD) optimiser to train the neural network. These optimisers have a *learning rate* parameter, which indicates how much the weights are changed during training. SGD has the additional *momentum* parameter, which takes into account previous weight updates in order to converge faster. We also tested a *dropout* rate, which is another method used to handle overfitting by setting the output of some randomly selected neurons to zero.

The model parameters used for the CNN in this work are summarised in Table I, with the tested parameter ranges and the step sizes. The Keras framework was used to implement the CNNs in this study [22].

TABLE I. Model parameters in the CNN, with the parameter ranges investigated in this study and the step sizes used

Parameter	Range	Step
Kernel size	5–90	1
Layer size	5–50	1
Strides	1–25	1
SGD momentum	0.2–0.9	0.1
Learning rate	10^{-6}–10^{-2}	factor of 10
Dropout rate	0–0.3	0.1

2. *Regression methods for comparison*

Principal component regression: Principal component regression (PCR) is based on principal component analysis (PCA), where the original data is projected onto a smaller variable subspace with linearly uncorrelated variables, which are called principal components (PCs) [23]. The number of PCs used in each model was chosen through cross-validation, from the range 3–25 PCs.

Partial least-squares regression: Partial least-squares regression (PLSR) is one of the most commonly used multivariate analysis methods in spectroscopy [24]. PLSR finds a regression model by projecting both the dependent and independent variables to a new space defined by a set of latent variables. The number of PLSR latent variables (LVs) was chosen through cross-validation on training data, from the range 3–20 LVs.

Random forest regression: Random forest (RF) is an ensemble learning method that can be used for several purposes, and has been used successfully for regression of spectral data [25]. Random forest regression works by creating multiple decision trees, and combining these for regression analysis. RF regression was evaluated with maximum tree depth for each dataset and 200–600 decision trees.

Elastic net: Elastic net (Net) is another ensemble learning method that combines the penalty variables from lasso and ridge regression ($\mathbf{L}_1$ and $\mathbf{L}_2$, respectively) [26]. Elastic net was evaluated with an $\mathbf{L}_1/\mathbf{L}_2$ ratio of 0–1 in increments of 0.1.

3. Classification methods for comparison

Partials least-squares discriminant analysis: PLS discriminant analysis (PLS-DA) uses classical PLSR on categorical variables, which is enabled by dividing the categorical variable into dummy variables that describe the categories (also called one hot encoding) [27]. Optimal PLS-DA models were chosen based on LVs in the range 3–20.

k-nearest neighbours: k-nearest neighbours (kNN) is a simple learning method that classifies predicted data points based on their distance from the k nearest neighbours in the training set [28]. The distance between test data and training data can be calculated in different ways, e.g. Euclidean, Chebyshev, or cosine. This study used the Euclidean distance method as it is most common, and the models have been optimised for k in the range 3–10.

Support vector machines: Support vector machines (SVMs) are a class of learning methods that try to find hyperplanes in a multidimensional space in order to divide data points into separate classes [29]. A support vector classifier with a linear kernel was used for this study.

Logistic regression: Logistic regression (LogReg) is a categorical method used to fit data with a special logistic function [30]. LogReg models can be considered simplified ANNs with no hidden layers. We used a LogReg model with an $\mathbf{L}_2$ penalty.

4. Pre-processing methods

Various methods can be used on spectroscopic data to correct for scattering effects, including standard normal variate (SNV) and multiplicative scattering correction (MSC). Spectral derivatives can also widely used to remove unwanted spectral effects.

Filtering or smoothing methods can be used alone on data to reduce noise. In addition, filtering methods are used to improve the noise in spectral derivatives. Savitzky-Golay (SG) differentiation is by far the most common method used. In the smoothing step for SG filtering a polynomial is fitted to the data points in the window using linear least-squares.

The pre-processing methods used in this study can be divided into five separate steps, where some have different possible methods and associated variable parameters:

- *Data binning:* Binning together 1–16 data points
- *Scatter correction:*
  - Normalisation
  - Standard normal variate (SNV)
  - Multiplicative scattering correction (MSC)
- *Smoothing/filtering:*
  - Savitzky-Golay filter (order 1–3, width 5–21)
  - Fourier filter
  - Finite/infinite impulse response filters (Butterworth, Hamming, moving average)
- *Baseline corrections:*
  - Subtract constant value
  - Subtract linear background
  - Spectral derivative (1st or 2nd derivative)
- *Scaling:*
  - Mean centering
  - Scaling

Note that this is a small subset of all possible pre-processing methods that exist, and we chose some general methods that are often applied to spectroscopy data [6, 7]. There is a lack of consensus regarding the best order of different pre-processing steps, and recent studies have shown that there is no clear optimal order [31], although the order can influence the prediction accuracy.

5. Feature selection

Spectral data can contain many hundreds or thousands of spectral features. For most types of data, the spectra contain features that are either irrelevant or redundant. Many types of feature selection methods have been developed, see refs. [9, 32] for extensive reviews. We tested three different wrapper methods for the datasets in this study, which are briefly described below. Wrapper methods generally work by searching through several subsets of features and choosing a feature subset based on prediction accuracy, see Fig. 2 for a schematic.

Sequential selection: In forward selection, one starts by choosing the wavenumber which has the highest correlation with the Y-variable. The wavenumbers that give the highest model improvements are then added iteratively, until no improvements occur when more features

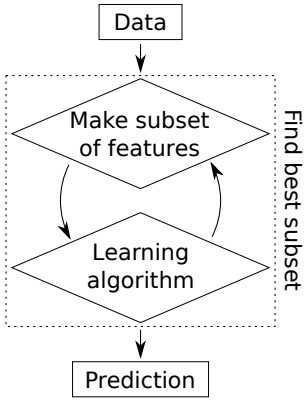

FIG. 2. General work flow of wrapper methods for feature selection.

are added. Backward elimination, on the other hand, starts with all the features, and tries to eliminate features that worsen the prediction. Sequential, or stepwise, selection combines these two methods by reconsidering variables for re-introduction or removal at each step.

Moving Window: A window is moved over the spectrum, and regression models are built using the data in the window position [33]. The window size can be varied over a set range. Optimal spectral intervals can then be chosen, based on the prediction error and number of regression components used in the model. Some moving window algorithms also try to optimise the selection of multiple windows [34].

Genetic Algorithm: Genetic algorithms (GA) for wavelength selection exist in many variants [35]. Generally, a population consisting of K vectors with length n are initialised. Two vectors are then selected from the population as parent vectors, and these are subjected to crossover and/or mutation, resulting in offspring vectors. The offspring are then evaluated based on their fitness, where they are either rejected or they replace the worst member of the population. Regression models are then built using the resulting vectors after a set amount of iterations.

B. Example datasets

Datasets of different sample types acquired with different measurement methods have been analysed. A dataset with aqueous solutions was measured in a custom-built ATR-FTIR setup for this study. Other openly available datasets of food items or pharmaceutical tablets measured with FTIR, NIR or Raman spectroscopy have also been investigated. An overview of the dataset properties is provided in Table II. For datasets with no preset test set, such as the Tablets data, we separated the data randomly into training and test sets based on a 67%/33% split. These datasets were chosen in order to represent different measurement methods and wavelength ranges within vibrational spectroscopy.

The following spectral datasets are investigated in this study:

- Solutions dataset, with aqueous solutions containing glucose, albumin, lactate, and urea, measured with ATR-FTIR. This dataset was acquired by the authors, see the next section for further details (dataset available from https://github.com/jernelv/SpecAnalysis)
- Tablets dataset, where the samples are categorised into four different tablet types with different relative amounts of active materiel, measured with both NIR and Raman spectroscopy [36]. Both datasets were used for classification, while the Tablets NIR dataset was also used for regression analysis since relative weight percentage was also available (dataset available from http://www.models.life.ku.dk/Tablets)
- Wines dataset, where the samples are categorised into wines with different origin countries, measured with FTIR spectroscopy [37] (dataset available from http://www.models.life.ku.dk/Wine_GCMS_FTIR)
- Fruit purées datasets measured with FTIR, where the samples are categorised into either strawberry or other purées [38] (dataset available from https://csr.quadram.ac.uk/example-datasets-for-download/)

The Solutions dataset was used in the regression analysis for prediction of glucose and albumin concentrations, and the Tablets NIR dataset was used for prediction of the relative weight percentage of the active material. The Tablets NIR, Tablets Raman, Fruits, and Wines datasets were employed for classification tasks of the categories described above.

1. *Solutions dataset*

In total, 90 unique aqueous solutions were made with four analytes, with the concentration ranges shown in Table III. Samples were made by dissolving the analytes in a phosphate-buffered saline solution (PBS). PBS is a buffer solution that helps maintain the pH in the solutions, and was made by dissolving PBS powder (Wako) in demineralised water. Glucose, albumin, urea, and lactate were then added to the solutions in varying concentrations.

The sample concentrations were determined with an optimal design model in order to randomise the concentrations while still filling the entire design space. The

TABLE II. Characteristics of the datasets used for classification and regression analysis

Data	Method	Wavelength range	Calibration samples	Validation samples	Features	Classes
Tablets	NIR	10507–7400 cm^{-1}	211	99	404	4
Tablets	Raman	3600-200 cm^{-1}	82	38	3402	4
Fruits	FTIR	1802–899 cm^{-1}	666	317	235	2
Wines	FTIR	5011–929 cm^{-1}	30	14	842	4
Solutions	FTIR	4000–500 cm^{-1}	60	30	1814	NA

TABLE III. Concentration ranges for the sample analytes used in the Solutions dataset

Analyte	Concentration ranges [mg/dl]
Glucose	0–800
Lactate	0–90
Albumin	0–6000
Urea	0–200

experimental design was made using a quadratic Scheffe model with A-optimality design.

60 samples were used for the training set and 30 samples for the prediction set. Samples were assigned randomly to the different sets.

Spectra were recorded using an FTIR spectrometer (Tensor27, Bruker, Germany). This spectrometer was modified in a custom setup for ATR measurements with multi-reflection prisms. Guiding optics and a hollow-core fiber was used to couple the light into a ZnS ATR crystal. This experimental setup has previously been used by the Matsuura group, see e.g. Kasahara et al. [39] for more details.

Data acquisition and initial spectral processing was performed using the OPUS software package (ver 6.0, Bruker Optics, Germany). 32 interferograms were co-added for each measurement, and scans were performed with a nominal resolution of 4 cm^{-1}. A zero-filling factor of 2 was used before the Fourier transform, which reduced the datapoint spacing to approximately 2 cm^{-1}, together with a 3-term Blackman-Harris apodisation.

Plots of the acquired spectra are shown in Fig. 3 for the range 4000-900 cm^{-1}. The inset shows the range 1500-900 cm^{-1}, which has the most informative spectral bands for the analytes in this dataset. This data was cut down to the 3000–800 cm^{-1} range for the analysis, due to large amounts of noise in the high absorption water bands.

The samples were placed manually on the ATR crystal (approx. 0.25 mL) for measurements. Each sample was measured 5 times in order to test measurement repeatability, with at least 2 repeat measurement done on the same day to check within-day variation. Background measurements of the ambient background were done every 30 minutes. The measurement series were performed over a period of two months.

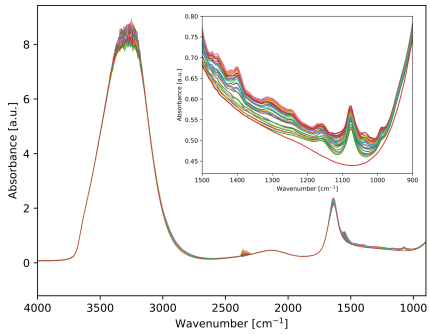

FIG. 3. Plot of the solutions spectra acquired in FTIR. The inset shows the fingerprint region.

C. Model evaluation

CNN was compared to other regression and classification models by applying the methods to the datasets in four different cases: raw data (i.e. no pre-processing), pre-processing prior to modelling, feature selection prior to modelling, and finally both pre-processing and feature selection prior to modelling. For CNN we mainly looked at raw data and pre-processing methods, which was in part due to the long processing time required for CNN compared to the other methods. Important spectral regions can be identified with neural networks through for example stability feature selection or network pruning, and some examples of this are included in the Supplementary Information.

The best combination of pre-processing methods is not necessarily the same for different classification or regression models. To ensure that the best methods were used for each model, we therefore tested all possible combinations of the pre-processing methods men-

tioned above. The method combination with the highest accuracy was then chosen based on leave-one-out cross-validation (LOOCV) on the training set.

Similarly, the optimal feature subset might not be the same for all models. We therefore did feature selection separately all methods and all datasets, and the best features selection was chosen based on LOOCV on the training dataset. All three wrapper methods described above were tested.

For the classification datasets, the models were evaluated based on the percentage of correctly classified samples in the test sets. For the regression analysis, the models were evaluated based on the coefficient of determination (R^2). The coefficient of determination indicates how close the predicted data correlate with the regression line. The root-mean-square error of prediction (RMSEP), which is a scale-dependent error value, was also calculated and is reported in the Supplementary Information. The best model parameters were chosen based on LOOCV on the training data in all cases, and prediction accuracy presented later was then calculated from the validation data.

III. RESULTS

A. Regression

The results of the regression analysis are summarised in Fig. 4, with the coefficient of determination (R^2) of the regression methods. Results are shown for regression on raw data, regression after pre-processing, and regression after pre-processing and feature selection. Full tables including the results for regression with only feature selection are included in the Supplementary Information.

For the raw data (no pre-processing) our CNN model outperformed all the other regression methods for all datasets. PLSR and PCR, which are commonly used chemometric methods, generally performed well (R^2>0.92) with PLSR being somewhat better than PCR. Random forest and elastic net had much worse prediction accuracy than the other methods for raw data, but had comparable performance after pre-processing or feature selection.

The CNN model also improved with application of pre-processing methods. After use of both pre-processing and feature selection on the other regression models, the CNN no longer had the singularly best performance on any of the datasets. However, the prediction accuracy was good for all the models tested here, with R^2>0.98 and R^2>0.99 for glucose and albumin in the Solutions dataset, respectively, and R^2>0.95 in the Tablets NIR dataset.

B. Classification

The results of the classification study are summarised in Fig. 5, with the percentage accuracy of each classification method. Results are shown for the same cases as in Fig. 4, namely raw data, pre-processing, and pre-processing together with feature selection. For the case where only feature selection was applied to the data the results can be found in the Supplementary Information.

For the raw data (no pre-processing), the CNN outperformed PLS-DA and *k*NN for all datasets. However, the percentage point difference between CNN and PLS-DA was not very large (<10%). The difference between CNN and *k*NN was also generally small, but for the Tablets Raman dataset kNN performed much worse than all other methods. The performance of SVM and LogReg were generally comparable to CNN.

For data with either pre-processing or feature selection, there was improvement for nearly all the methods. CNN also experienced improvement with pre-processing. The improvement was most significant for the Wines dataset, with an increase of more than 20 percentage points for all methods, as the classification accuracy was lowest for the raw data from this dataset.

Using both pre-processing and feature selection on the datasets gave the largest improvement for many methods. This also made the performance of CNN, SVM, and LogReg more similar. In some cases, especially for the *k*NN, feature selection in addition to other pre-processing methods did not lead to an increase in the prediction accuracy.

C. CNN parameters

Parameters for the CNN model were fine-tuned for each dataset, and the chosen parameters are summarised in the Supplementary Information. Some parameters, such as optimal kernel size, varied a lot between different datasets.

Two common methods for weight adjustment were used for this study, the Adam and the SGD optimisers. The SGD optimiser converged faster than the Adam optimiser, but did not always find an equally good prediction.

We also tested the number of layers used for the CNN model, up to 4 layers. The performance declined when using more than 2 layers for all datasets. This demonstrates that the CNN is prone to overfitting with the use of more layers.

Important spectral regions may be identified with CNNs using for example stability feature selection or network pruning. We performed a preliminary investigation of identification of important spectral regions in the datasets used for regression analysis. One example is shown in Fig. 6, where regions relevant to glucose levels in the Solutions dataset have been identified. Note that only the fingerprint region 1800–900 cm^{-1} is shown here,

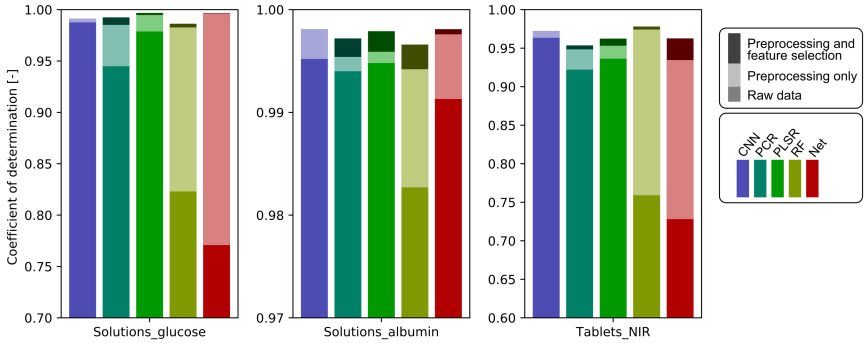

FIG. 4. Plot of coefficient of determination for the regression analysis. This is shown for raw data, pre-processed data, and use of both pre-processing and feature selection. Note the different scales for each subplot. Results for feature selection alone can also be found in the Supplementary Information.

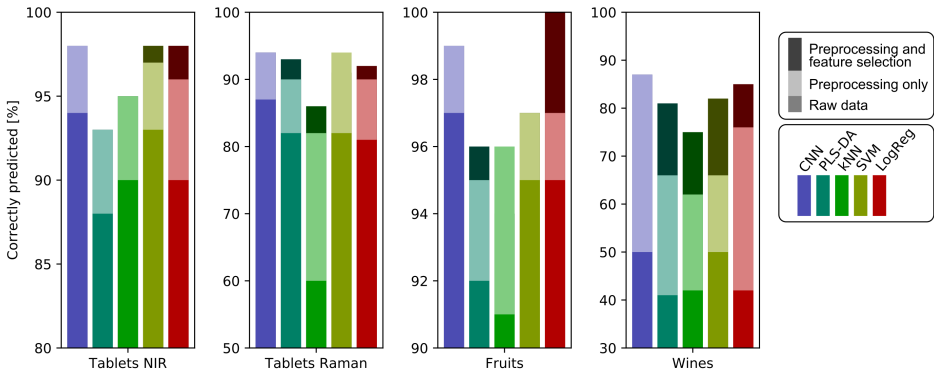

FIG. 5. Plot of percentage correctly classified samples in the classification datasets. This is shown for raw data, pre-processed data, and use of both pre-processing and feature selection. Note the different scales for each subplot. Results for feature selection alone can also be found in the Supplementary Information.

as no important spectral regions were identified outside of this area. The stability feature selection recognised the spectral regions at approximately 1180-970 cm^{-1} and 1500-1430 cm^{-1}, which corresponds well with glucose absorption bands. There was minimal change in identification of spectral regions between raw data and pre-processed data, which demonstrates that the CNN model is able to consistently identify relevant regions. More examples of the stability feature selection are shown in the Supplementary Information.

D. Use of pre-processing and feature selection

Pre-processing improved the model accuracy for all models, both for the classification and regression analysis. The specific pre-processing methods applied to each dataset and each model are summarised in the Supplementary Information. For most classification models, at least noise filtering and some type of scaling were used in the best pre-processing strategy. CNN and logistic regression were particularly sensitive to scaling, as ex-

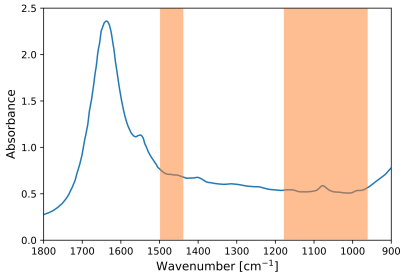

FIG. 6. Important spectral regions in the analysis of glucose concentrations in the Solutions dataset, plotted for the 1800–900 cm^{-1} region. The spectral regions were determined by stability feature selection based on the CNN model.

pected. For the Wines, Fruits, and Solutions datasets, spectral differentiation and filtering were also useful. Spectral differentiation has the benefit of removing baseline effects, as well as linear trends for the second derivative. Filtering prior to spectral differentiation also avoids the large amplification in noise that can otherwise occur. A small binning factor of 2 or 4 was also found to improve outcomes in several cases. Binning can improve SNR and leads to a dimension reduction; two factors that may both be beneficial for several machine learning methods. However, larger binning factors were mostly not positive, and may have obscured spectral information. Within each dataset, similar pre-processing steps were found to be optimal for the different modelling methods, indicating that pre-processing was mainly dataset-dependent.

Feature selection, either alone or together with pre-processing methods, often improved the prediction accuracy for both regression analysis and classification. Of the three wrapper methods that were tested, genetic algorithm resulted in the best performance, and generally selected similar relevant areas as in the stability feature selection for the CNN. Sequential forward selection and moving window did not always lead to improved accuracy, and particularly sequential forward selection seemed to get stuck in local maxima. Feature selection also improved the performance of the embedded methods with built-in feature selection, such as elastic net. Although elastic net is an embedded method, it is known to perform worse if there are many more features than observations, and often started off with low prediction accuracy on the raw data.

E. Discussion

CNN models can outperform standard chemometric methods, both for classification and regression analysis. CNN generally has a somewhat better performance than other methods when raw data is analysed directly. However, this advantage becomes much smaller when pre-processing and/or feature selection methods are applied to the datasets.

CNN has been suggested as a classification method that would depend less on pre-processing as compared to standard chemometric methods, e.g. by Acquarelli et al. [12]. In theory, CNN could therefore be used directly without the need for a time-consuming search of the optimal pre-processing steps and methods. However, this ignores the need for parameter tuning inherent in the CNN. A CNN includes several parameters such as layer size, kernel size, stride, etc., and the parameter choice can vary significantly between datasets. Hence, using CNN to avoid a choice of pre-processing methods may ultimately not save any computational time. Methods such as SVM and PLSR generally have fewer parameters, and are therefore easier to tune to optimal conditions, with only a small loss in accuracy as compared to CNN.

IV. CONCLUSION

In this study, a convolutional neural network (CNN) was applied for classification and regression analysis of various datasets acquired with spectroscopic methods. We compared the CNN to several standard methods used for classification and regression in chemometrics. The CNN generally performed better on raw data compared to both the classification and regression models. This was also the case when either pre-processing or feature selection were applied to the datasets, although the advantage of CNN decreased. In general, application of appropriate pre-processing and feature selection significantly improves the accuracy of most models.

CONFLICTS OF INTEREST

There are no conflicts of interest to declare.

ACKNOWLEDGMENTS

This work was supported by the Research Council of Norway through the Double Intraperitoneal Artificial Pancreas project, grant number 248872. The project is part of Centre for Digital Life Norway and is also supported by the Research Council of Norway's grant 248810.

The authors would like to thank Dr. Saiko Kino for training on the FTIR spectrometer setup at Tohoku University.

[1] L. G. Thygesen, M. M. Løkke, E. Micklander and S. B. Engelsen, *Trends in Food Science and Technology*, 2003, **14**, 50–57.

[2] C. Kendall, M. Isabelle, F. Bazant-Hegemark, J. Hutchings, L. Orr, J. Babrah, R. Baker and N. Stone, *Analyst*, 2009, **134**, 1029–1045.

[3] R. S. Das and Y. K. Agrawal, *Vibrational Spectroscopy*, 2011, **57**, 163–176.

[4] C. K. Muro, K. C. Doty, J. Bueno, L. Halámková and I. K. Lednev, *Analytical Chemistry*, 2015, **87**, 306–327.

[5] F. Pozzi and M. Leona, *Journal of Raman Spectroscopy*, 2016, **47**, 67–77.

[6] Å. Rinnan, F. van den Berg and S. B. Engelsen, *TrAC - Trends in Analytical Chemistry*, 2009, **28**, 1201–1222.

[7] J. Engel, J. Gerretzen, E. Szymańska, J. J. Jansen, G. Downey, L. Blanchet and L. M. Buydens, *TrAC - Trends in Analytical Chemistry*, 2013, **50**, 96–106.

[8] J. Gerretzen, E. Szymańska, J. J. Jansen, J. Bart, H. J. Van Manen, E. R. Van Den Heuvel and L. M. Buydens, *Analytical Chemistry*, 2015, **87**, 12096–12103.

[9] T. Mehmood, K. H. Liland, L. Snipen and S. Sæbø, *Chemometrics and Intelligent Laboratory Systems*, 2012, **118**, 62–69.

[10] P. Bhandare, Y. Mendelson, R. A. Peura, G. Janatsch, J. D. Kruse-Jarres, R. Marbach and H. M. Heise, *Applied Spectroscopy*, 1993, **47**, 1214–1221.

[11] F. Marini, R. Bucci, A. L. Magrì and A. D. Magrì, *Microchemical Journal*, 2008, **88**, 178–185.

[12] J. Acquarelli, T. van Laarhoven, J. Gerretzen, T. N. Tran, L. M. Buydens and E. Marchiori, *Analytica Chimica Acta*, 2017, **954**, 22–31.

[13] J. Liu, M. Osadchy, L. Ashton, M. Foster, C. J. Solomon and S. J. Gibson, *Analyst*, 2017, **142**, 4067–4074.

[14] S. Malek, F. Melgani and Y. Bazi, *Journal of Chemometrics*, 2018, **32**, 1–17.

[15] C. Cui and T. Fearn, *Chemometrics and Intelligent Laboratory Systems*, 2018, **182**, 9–20.

[16] Y. Chen, H. Jiang, C. Li, X. Jia and P. Ghamisi, *IEEE Transactions on Geoscience and Remote Sensing*, 2016, **54**, 6232–6251.

[17] R. Rosas-Romero, E. Guevara, K. Peng, D. K. Nguyen, F. Lesage, P. Pouliot and W. E. Lima-Saad, *Computers in Biology and Medicine*, 2019, **111**, 103355.

[18] S. Kiranyaz, T. Ince and M. Gabbouj, *IEEE Transactions on Biomedical Engineering*, 2015, **63**, 664–675.

[19] F. Pedregosa, G. Varoquaux, A. Gramfort, V. Michel, B. Thirion, O. Grisel, M. Blondel, P. Prettenhofer, R. Weiss, V. Dubourg, J. Vanderplas, A. Passos, D. Cournapeau, M. Brucher and É. Duchesnay, *Journal of Machine Learning Research*, 2011, **12**, 2825–2830.

[20] I. L. Jernelv, K. Strøm, D. R. Hjelme and A. Aksnes, *Proc. SPIE 11233, Optical Fibers and Sensors for Medical Diagnostics and Treatment Applications XX*, 2020, **1123311**, 1–9.

[21] I. Goodfellow, Y. Bengio and A. Courville, *Deep learning*, MIT press, 2016.

[22] N. Ketkar, *Deep Learning with Python*, Apress, Berkeley, CA., 2017.

[23] T. Næs and H. Martens, *Journal of Chemometrics*, 1988, **2**, 155–167.

[24] S. Wold, M. Sjöström and L. Eriksson, *Chemometrics and Intelligent Laboratory Systems*, 2001, **58**, 109–130.

[25] A. Liaw and M. Wiener, *R news*, 2002, **2**, 18–22.

[26] H. Zou and T. Hastie, *Journal of the Royal Statistical Society. Series B: Statistical Methodology*, 2005, **67**, 301–320.

[27] R. G. Brereton and G. R. Lloyd, *Journal of Chemometrics*, 2014, **28**, 213–225.

[28] N. S. Altman, *American Statistician*, 1992, **46**, 175–185.

[29] C. Cortes and V. Vapnik, *Machine Learning*, 1995, **20**, 273–297.

[30] T. Hastie and R. Tibshirani, *Journal of the American Statistical Association*, 1987, **82**, 371–386.

[31] H. J. Butler, B. R. Smith, R. Fritzsch, P. Radhakrishnan, D. S. Palmer and M. J. Baker, *Analyst*, 2018, **143**, 6121–6134.

[32] Y. Saeys, I. Inza and P. Larrañaga, *Bioinformatics*, 2007, **23**, 2507–2517.

[33] J.-h. Jiang, R. J. Berry, H. W. Siesler and Y. Ozaki, *Analytical Chemistry*, 2002, **74**, 3555–3565.

[34] S. Kasemsumran, Y. P. Du, K. Murayama, M. Huehne and Y. Ozaki, *Analytica Chimica Acta*, 2004, **512**, 223–230.

[35] D. Jouan-Rimbaud, D. L. Massart, R. Leardi and O. E. De Noord, *Analytical Chemistry*, 1995, **67**, 4295–4301.

[36] M. Dyrby, S. B. Engelsen, L. Nørgaard, M. Bruhn and L. Lundsberg-Nielsen, *Applied Spectroscopy*, 2002, **56**, 579–585.

[37] T. Skov, D. Ballabio and R. Bro, *Analytica Chimica Acta*, 2008, **615**, 18–29.

[38] J. K. Holland, E. K. Kemsley and R. H. Wilson, *Journal of the Science of Food and Agriculture*, 1998, **76**, 263–269.

[39] R. Kasahara, S. Kino, S. Soyama and Y. Matsuura, *Biomedical Optics Express*, 2018, **9**, 289–302.

Supplementary Information for "Convolutional neural networks for classification and regression analysis of one-dimensional spectral data"

Ine L. Jernelv,* Dag Roar Hjelme, and Astrid Aksnes
Department of Electronics, Norwegian University of Science and Technology (NTNU), O.S. Bragstads plass 2A, 7491 Trondheim, Norway

Yuji Matsuura
Graduate School of Biomedical Engineering, Tohoku University, Sendai, 980-8579, Japan
(Dated: May 15, 2020)

This supplemental information contains results and figures that were not included in the main article for conciseness, or due to a lack of space.

All analysis performed in this work was done in the software package SpecAnalysis, which has been made available online (https://github.com/jernelv/SpecAnalysis).

I. CNN PARAMETERS

The parameters used for our CNN for the regression and classification datasets are shown in Table I and Table II, respectively. Both the Adam and the SGD optimisers were tested, and the momentum parameter is given for the cases were the SGD optimiser had the best performance.

TABLE I. CNN parameters used for the regression datasets.

Dataset	Layer size	Kernel size	Learning rate	Stride	Momentum	Dropout
Solutions glucose	10	10	10^{-3}	4	0.9	0
Solutions albumin	19	16	10^{-3}	5	–	0
Tablets NIR	25	45	10^{-3}	3	0.8	0.1

TABLE II. CNN parameters used for the classification datasets.

Dataset	Layer size	Kernel size	Learning rate	Stride	Momentum	Dropout
Tablets NIR	6	5	10^{-3}	26	–	0
Tablets Raman	12	37	10^{-3}	6	0.9	0
Fruits	8	52	10^{-3}	12	–	0
Wines	4	46	10^{-3}	6	0.8	0

* ine.jernelv@ntnu.no

II. PREDICTION ACCURACY FOR CLASSIFICATION METHODS

Table III shows the prediction accuracy for the classification methods in four different experiments: classification on raw data, classification on pre-processed data, classification on data after feature selection, and classification after both pre-processing and feature selection. Note that feature selection was not done on CNN.

TABLE III. Classification accuracy [%] on data, with and without pre-processing and feature selection. The best accuracy for each model type and dataset is marked in bold.

	No feature selection									
	Raw data					Pre-processed data				
Dataset	CNN	PLS-DA	kNN	SVM	LogReg	CNN	PLS-DA	kNN	SVM	LogReg
Tablets NIR	**94**	88	90	93	90	**98**	93	95	97	96
Tablets Raman	**87**	82	60	82	81	**94**	90	82	**94**	90
Fruits	**97**	92	91	95	95	**99**	95	96	97	**99**
Wines	**50**	41	42	**50**	42	**87**	66	62	66	76

	Feature selection									
	Raw data					Pre-processed data				
Tablets NIR	–	90	90	**95**	92	–	93	95	**98**	**98**
Tablets Raman	–	**88**	61	85	84	–	93	86	91	**92**
Fruits	–	92	91	96	95	–	96	94	97	**100**
Wines	–	58	45	60	62	–	81	75	82	85

III. PREDICTION ACCURACY FOR REGRESSION METHODS

Table IV shows the prediction accuracy for the regression in four different experiments: regression analysis on raw data, regression on pre-processed data, regression on data after feature selection, and regression after both pre-processing and feature selection.

TABLE IV. Prediction accuracy with coefficient of determination (R^2), with and without pre-processing and feature selection. The best accuracy for each model type and dataset is marked in bold.

	No feature selection									
	Raw data					Pre-processed data				
Dataset	CNN	PCR	PLSR	RF	Net	CNN	PCR	PLSR	RF	Net
Glucose	**0.9876**	0.9449	0.9787	0.823	0.7708	0.9912	0.9852	0.9948	0.9827	**0.996**
Albumin	**0.9952**	0.994	0.9948	0.9827	0.9913	**0.9981**	0.9954	0.9959	0.9942	0.9972
Tablets NIR	**0.9635**	0.9221	0.9363	0.7591	0.7281	0.9723	0.9485	0.9532	**0.9742**	0.9364
	Feature selection									
	Raw data					Pre-processed data				
Glucose	–	0.9771	0.9833	0.9792	0.9811	–	0.9925	**0.9968**	0.9863	0.9965
Albumin	–	0.9965	0.9979	0.9864	0.9957	–	0.9972	0.9979	0.9966	**0.9981**
Tablets NIR	–	0.9318	0.9422	0.8826	0.8115	–	0.9536	0.9624	0.9781	0.9627

TABLE V. Prediction accuracy with root-mean-square error of prediction (RMSEP), with and without pre-processing and feature selection. The best accuracy for each model type and dataset is marked in bold.

	No feature selection									
	Raw data					Pre-processed data				
Dataset	CNN	PCR	PLSR	RF	Net	CNN	PCR	PLSR	RF	Net
Glucose	**26.58**	57	35.4	102.1	116.2	20.4	29.5	17.5	31.9	**15.3**
Albumin	**120**	135.6	126.6	230.7	163.8	**75.4**	119.5	111.5	133.5	92.3
Tablets NIR	**0.2653**	0.3684	0.3331	0.6478	0.6733	0.2196	0.2994	0.2856	**0.2132**	0.333
	Feature selection									
	Raw data					Pre-processed data				
Glucose	–	38.9	27.7	33.2	29	–	19.4	**15.1**	26.5	15.2
Albumin	–	113.8	105.8	111.2	121.9	–	95.8	85.3	0.110	77
Tablets NIR	–	0.3368	0.3173	0.4519	0.4806	–	0.2859	0.2656	**0.2118**	0.2628

IV. PRE-PROCESSING METHODS

Several pre-processing methods were evaluated for this study, and an overview can be found in Table VI. These pre-processing methods were divided into five separate steps, and all possible combinations were tested for each dataset and each model. A more in-depth description of the various methods can be found in the Readme for the SpecAnalysis software package (https://github.com/jernelv/SpecAnalysis) or in the references in the main article.

TABLE VI. Alternatives for pre-processing methods used in this study.

1. Binning	
- Binning together 1, 2, 4, 8, or 16 datapoints	
2. Scatter correction	
- Normalisation	
- Standard normal variate (SNV)	
- Multiple scatter correction (MSC)	
3. Smoothing/filtering	
- SG filter	Polynomial order: 1, 2, or 3
	Filter width: 3, 5, ..., 21 data points
- Fourier filter	Window function: none, Blackman-Harris, Hamming, Hann
	Filter cutoff: 20, 21, ... 50 points in Fourier space
	Filter window size: 1.1, 1.2, 1.3
- Finite/infinite impulse response filters:	Butterworth, Hamming, moving average (MA)
4. Baseline correction	
- Subtract constant value	
- Subtract linear background	
- Spectral differentiation: 1st or 2nd derivative	
5. Scaling	
- Mean centering	
- Scaling	

V. OPTIMAL PRE-PROCESSING METHODS FOR CLASSIFICATION

The following tables show the optimal pre-processing methods applied to each dataset for the classification analysis.

TABLE VII. Pre-processing methods applied to the Tablets NIR dataset.

Classification	Pre-processing
CNN	Baseline correction, scaling
PLS-DA	Baseline correction
kNN	Baseline correction and scaling
SVM	Scaling
LogReg	Binning, Butterworth filter, baseline correction, scaling

TABLE VIII. Pre-processing methods applied to the Tablets Raman dataset.

Classification	Pre-processing
CNN	Binning, baseline correction, scaling
PLS-DA	Binning, Fourier filter
kNN	Binning, normalisation, SG filter, baseline correction, scaling
SVM	Binning, SG filter, first derivative, scaling
LogReg	Binning, MA filter, scaling

TABLE IX. Pre-processing methods applied to the Wines dataset.

Classification	Pre-processing
CNN	Binning, SG filter, second derivative, scaling
PLS-DA	Binning, SG filter, second derivative
kNN	Binning, MA filter, second derivative, scaling
SVM	Binning, SG filter, second derivative, scaling
LogReg	Binning, SG filter, second derivative, scaling

TABLE X. Pre-processing methods applied to the Purées dataset.

Classification	Pre-processing
CNN	Binning, SG filter, second derivative, scaling
PLS-DA	Normalisation, first derivative, scaling
kNN	First derivative, scaling
SVM	Normalisation, scaling
LogReg	Normalisation, subtract linear baseline, scaling

VI. OPTIMAL PRE-PROCESSING METHODS FOR REGRESSION

The following tables show the sequency of the optimal pre-processing methods applied to each dataset for the regression analysis.

TABLE XI. Pre-processing methods applied to the Solutions dataset with glucose as the target analyte.

Regression	Pre-processing
CNN	Binning, MA filter, first derivative, scaling
PCR	First derivative, scaling
PLSR	SG filter, first derivative, scaling
RF	Binning, SG filter, second derivative
Net	SG filter, first derivative, scaling

TABLE XII. Pre-processing methods applied to the Solutions dataset with albumin as the target analyte.

Regression	Pre-processing
CNN	Binning, Butterworth filter, second derivative, scaling
PCR	Normalisation, SG filter, second derivative, scaling
PLSR	Binning, SG filter, first derivative, scaling
RF	Binning, SG filter, first derivative, scaling
Net	SG filter, scaling

TABLE XIII. Pre-processing methods applied to the Tablets NIR dataset for regression analysis.

Regression	Pre-processing
CNN	Binning, MSC, MA filter, scaling
PCR	Binning, MSC, SG filter, subtracted linear baseline, scaling
PLSR	Binning, MSC, SG filter
RF	Binning, SNV, Butterworth filter, second derivative
Net	MSC, SG filter, first derivative, scaling

VII. FEATURE SELECTION WITH CNN

In a preliminary analysis, stability feature selection was used on the regression data in order to identify the most important spectral regions. For the Solutions dataset, only the fingerprint region 1800–900 cm^{-1} has been plotted for clarity, as this was the area in the dataset where important information was identified by the CNN. Only minimal differences were seen in the important regions on the raw vs. the pre-processed data.

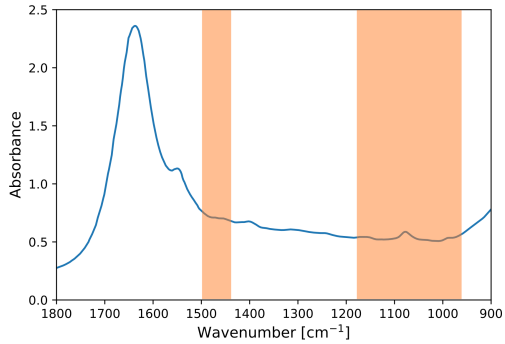

FIG. 1. Important regions identified for CNN regression analysis of glucose in the Solutions dataset.

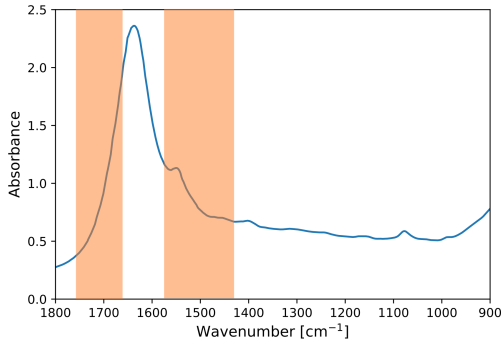

FIG. 2. Important regions identified for CNN regression analysis of albumin in the Solutions dataset.

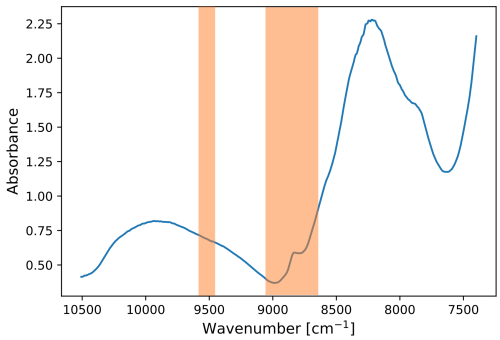

FIG. 3. Important regions identified for CNN regression analysis of weight percent in the Tablets NIR dataset.

Paper VI

Infrared measurements of glucose in peritoneal fluid with a tuneable quantum cascade laser

I.L. Jernelv, D.R. Hjelme, A. Aksnes

Biomedical Optics Express, Vol. 11(7), pp. 3818-3829, 2020.

Research Article | Vol. 11, No. 7 / 1 July 2020 / Biomedical Optics Express 3818
Biomedical Optics EXPRESS

Infrared measurements of glucose in peritoneal fluid with a tuneable quantum cascade laser

INE L. JERNELV,* DAG ROAR HJELME, AND ASTRID AKSNES

Department of Electronic Systems, Norwegian University of Science and Technology (NTNU), O.S. Bragstads plass 2A, 7491 Trondheim, Norway
ine.jernelv@ntnu.no

Abstract: Fast and accurate continuous glucose monitoring is needed in future systems for control of blood glucose levels in type 1 diabetes patients. Direct spectroscopic measurement of glucose in the peritoneal cavity is an attractive alternative to conventional electrochemical sensors placed subcutaneously. We demonstrate the feasibility of fast glucose measurements in peritoneal fluid using a fibre-coupled tuneable mid-infrared quantum cascade laser. Mid-infrared spectra (1200–925 cm^{-1}) of peritoneal fluid samples from pigs with physiological glucose levels (32–426 mg/dL, or 1.8–23.7 mmol/L) were acquired with a tuneable quantum cascade laser employing both transmission and attenuated total reflection (ATR) spectroscopy. Using partial least-squares regression, glucose concentrations were predicted with mean absolute percentage errors (MAPEs) of 8.7% and 12.2% in the transmission and ATR configurations, respectively. These results show that highly accurate concentration predictions are possible with mid-infrared spectroscopy of peritoneal fluid, and represent a first step towards a miniaturised optical sensor for intraperitoneal continuous glucose monitoring.

1. Introduction

Challenges related to chronic illnesses, an ageing population, and increased healthcare costs have led to great interest in development of sensor solutions that enable real-time or point-of-care (POC) monitoring, such as glucose sensors for diabetic patients. Monitoring of blood glucose levels (BGLs) is crucial for treatment of diabetes in order to avoid short- and long-term effects related to low (hypoglycaemia) and high (hyperglycaemia) glucose levels for patients treated with insulin [1–3]. Most commercially available glucose sensors are electrochemical and estimate glucose concentrations based on an enzymatic reaction, either with fingerprick measurements or with a continuous glucose monitoring (CGM) device worn on the body [4].

Optical measurement methods have a large potential for CGM, as they may be fast and reagent-free [5]. Mid-infrared (MIR) spectroscopy has several characteristics that are advantageous for POC monitoring. The MIR range, 2.5-25 µm, covers the fundamental vibrational and rotational absorption bands of organic and inorganic molecules. MIR spectroscopy can thereby produce relatively strong absorption bands with uniquely identifiable features. The commercial availability of tuneable quantum cascade lasers (QCLs) has also opened up more avenues for MIR spectroscopy applications [6]. QCLs are small, with high spectral power density, and can be engineered to cover a wanted wavelength region [7]. Tuneable QCLs have been used for in vitro measurements of e.g. human blood serum [8], and promising preliminary investigation of subcutaneous glucose measurements in rats has been shown with a single-wavelength QCL [9]. For non-invasive approaches, Werth et al [10]. showed glucose measurements based on backreflected light from the hand, while Kino et al [11]. determined glucose concentrations from measurements of the inner lip mucosa.

#393617 https://doi.org/10.1364/BOE.393617
Journal © 2020 Received 25 Mar 2020; revised 29 Apr 2020; accepted 1 May 2020; published 18 Jun 2020

Biomedical Optics EXPRESS

CGM devices used today are placed with a patch on for example the arm or the abdomen, with a small filament positioned under the skin. Through this, the glucose concentration is measured in the interstitial fluid (ISF) between cells. This approach often improves control over the BGL compared to fingerprick measurements as the user typically gets glucose measurements every 5 minutes [12]. However, measuring glucose in the ISF is not without disadvantages. Glucose molecules have to diffuse from capillaries to the ISF, in addition to the time constant between the tissue and the sensing site. Further uncertainties are introduced with changes in tissue dynamics, such as temperature and pressure in the region, as well as biofouling and encapsulation of the sensor due to an inflammatory response [13]. Subcutaneous (SC) glucose levels have been reported to lag behind the BGL by 5-15 minutes, which can be detrimental to glucose control [14–16]. Similar delays have also been found for various non-invasive approaches. This might be a real limit to further advancement of diabetes treatment. An artificial pancreas (AP), which would be a fully automated system with glucose measurements and insulin infusions, would depend heavily on detecting rapid changes in the BGL [17,18].

The abdominal cavity, or the peritoneal space, has been suggested as a potential site for glucose measurements and insulin infusions [19–21]. Peritoneal fluid, which lubricates the organ surfaces in the peritoneal space, contains glucose in similar concentrations to the BGL. Promising short-term studies with intraperitoneal (IP) glucose sensing using electrochemical sensors have been reported [22], and some preliminary data from recent long-term studies have been demonstrated [23]. These studies have shown faster glucose sensing dynamics in the peritoneal space compared to SC sites, indicating that the intraperitoneal space may be a better site for a fully automated AP. Peritoneal fluid may be considered an ultrafiltered plasma, with lower cellularity and lower total protein content than e.g. serum or ISF. We therefore expect the peritoneal cavity to be an attractive site for mid-infrared spectroscopic CGM. Glucose sensing in peritoneal fluid with mid-infrared spectroscopy has so far not been investigated.

In this study we demonstrate the feasibility of fast and accurate glucose measurements in peritoneal fluid from pigs using a fibre-coupled mid-infrared quantum cascade laser. The compositions of pig blood and human blood are similar [24,25], and the optical properties are expected to be similar. Due to this, and the general use of pigs as research animals, the results presented here should be transferable to humans. Highly accurate predictions of glucose levels in unknown fluid samples were achieved using regresssion methods on the MIR spectra. Comparable results were achieved both in transmission and attenuated total reflection (ATR) configurations using two fibre-coupled setups developed with the aim of future in vivo applications. This demonstrates the potential of mid-infrared spectroscopy as an optical measurement method for glucose monitoring in the peritoneal space.

2. Materials and methods

2.1. Biological samples

Peritoneal fluid and blood samples were collected from anaesthetised pigs that were used in animal trials from November to December 2019 at the Department of Clinical and Molecular Medicine, NTNU, Trondheim. The animal experiments were approved by the Norwegian Food Safety Authority (FOTS number 12948), and were in accordance with "The Norwegian Regulation on Animal Experimentation" and "Directive 2010/63/EU on the protection of animals used for scientific purposes". Samples were acquired from a total of six pigs. The animals were a mixture of male and female, and weighed 40-60 kg. No additional animals were sacrificed for these fluid measurements.

In total, 79 centrifuged peritoneal fluid samples from five different pigs, and 21 blood samples from two different pigs were obtained. Sample details are summarised in Table 1. In addition, five non-centrifuged peritoneal samples were acquired from one pig for comparison with the centrifuged peritoneal samples. Samples were kept in Eppendorf tubes with 1.5 mL volume

Biomedical Optics EXPRESS

and stored at -18°C. Most of the peritoneal samples were centrifuged to remove excess blood residue and coagulate material, but were otherwise untreated. The non-centrifuged peritoneal samples were heparinised in order to prevent coagulation. The blood samples were heparinised and centrifuged, and the resulting blood plasma samples were used for measurements.

Table 1. Overview of fluid samples from pigs.

Sample type	Pig #	No. samples	Initial glucose levels	Spiked glucose levels
Peritoneal (centrifuged)	1-3, 5, 6	79	33–140 mg/dL	32–426 mg/dL
Peritoneal (not centrifuged)	4	5	72–90 mg/dL	75–200 mg/dL
Blood plasma	4,5	21	65–105 mg/dL	65–346 mg/dL

The acquired samples were measured in a blood gas analyser (ABL 725, Radiometer ApS, Brønshøj, Denmark) to get accurate reference measurements for the glucose concentrations. The samples had an initial glucose concentration range of 33–140 mg/dL (1.8–7.8 mmol/L) for the peritoneal samples, and 65–105 mg/dL (3.6–5.8 mmol/L) for the blood plasma samples. A subset of samples were spiked in order to investigate the entire range of physiological concentrations found in humans. Spiking was performed by making a highly concentrated glucose solution in demineralised water, and adding an appropriate amount to each sample with a micropipette. This added less than 5% extra volume to each sample, and the calculated spiked concentrations were adjusted according to the additional volume. The final concentration ranges after spiking were 32–426 mg/dL (1.8–23.7 mmol/L) for the peritoneal fluid samples and 65–346 mg/dL (3.6–19.2 mmol/L) for the blood plasma samples. Lactate and electrolyte levels were also measured in the blood gas analyser, while total protein and albumin levels were measured in a selection of the samples at an external laboratory. The levels of these other analytes are summarised in the Appendix.

2.2. Data analysis

Multivariate data analysis for concentration prediction was done with the SpecAnalysis software, which can be found on GitHub (https://github.com/jernelv/SpecAnalysis). For the centrifuged peritoneal samples, the data was divided into a training set with 48 samples and a validation set with 31 samples. Samples from pig 1, 3, and 5 were used for training, and samples from pig 2 and 6 were used for the validation set. An optimal regression model was found by performing cross-validation (CV) on the training set. CV was done with random subsets (10 splits, 20 iterations). The best model from the training data was then applied to the validation data. A similar approach was used to analyse the subset of peritoneal samples that were not spiked. This subset consisted of 26 samples, with 14 samples used as a training set and 12 samples used as a validation set. The blood plasma dataset was not divided into training and validation sets, as the total dataset was 21 samples and the samples were obtained from only two pigs. Instead, leave-one-out cross-validation (LOOCV) was used to evaluate the prediction accuracy.

Modelling was done with partial least-squares (PLS) regression, a method for multivariate analysis that combines dimensionality reduction and linear regression. PLS regression with 3–12 latent variables (LVs) was evaluated with cross-validation.

Different pre-processing methods were used on the datasets. Data is always mean-centered prior to PLS regression, so this method was applied to all data. Different filter/smoothing methods (Savitzky-Golay filter, Fourier filter), spectral derivatives (first and second derivatives), background correction, and normalisation were tested on the data. All possible combinations of the included methods were tested in order to find the optimal pre-processing steps, and further details can be found in the Appendix.

Biomedical Optics EXPRESS

The regression models were evaluated with the mean absolute percentage error (MAPE), which is defined as:

$$\text{MAPE} = \frac{1}{n}\sum_{t=1}^{n} \left| \frac{y_t - \hat{y}_t}{y_t} \right| \quad (1)$$

where y_t are the real concentration levels and $\hat{y}_t$ are the predicted concentration levels, with n observations. MAPE is a common method used to evaluate regression models, and is independent of scale. MAPE is also referred to as mean absolute relative difference (MARD), especially for CGM systems. However, many other measures for prediction accuracy are also used, so for completeness the root-mean-square error (RMSE), the coefficient of determination (R^2), and the standard error of prediction (SEP) are reported in the Appendix.

2.3. Experimental setup

In this study we performed measurements in two experimental setups based on transmission spectroscopy and attenuated total reflection (ATR) spectroscopy, see Fig. 1. An external-cavity quantum cascade laser (EC-QCL, Hedgehog-UT, Daylight Solutions Inc., USA) was used as a light source in both setups. These setups were similar to those we previously characterised and used for measurements of aqueous solutions, see Ref. [26] for further details. The full tuning range of this laser was 1200–900 cm^{-1}, which corresponds to 8.3–11.1 μm. The EC-QCL ran in pulsed mode at a frequency of 100 kHz with 500 ns long pulses. An MCT detector (PCI-4TE, VIGO System S.A.) with thermoelectric cooling was used to collect the infrared radiation. Spectra were acquired in the 1200–925 cm^{-1} range, and the total measurement time for one raw spectrum was 10 s. The acquired measurements were calculated as absorbance ($A = -\log I/I_0$), based on the intensity measured with a sample (I) and the intensity measured with a reference (I_0). Deionised water was used for the reference spectra.

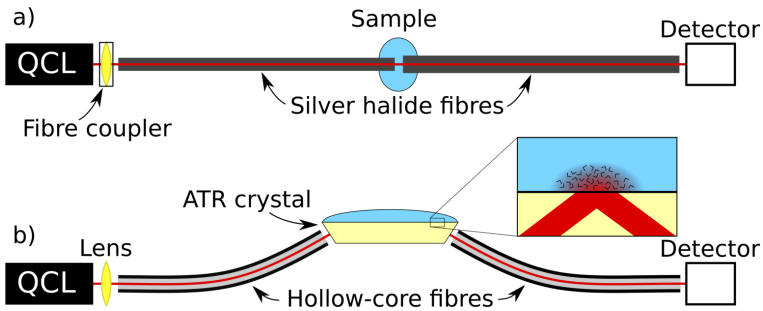

Fig. 1. Schematic illustration of the two experimental setups used for this study. a) Transmission spectroscopy setup. b) ATR spectroscopy setup. The inset illustrates light propagation and total internal reflection in an internal reflection element (IRE), which is the principle for evanescent field sensing.

Silver halide fibres (ART photonics GmbH, Germany) were used to guide light in the transmission setup, and a gap between the fibres was used for sensing. The gap between the fibres was 200 μm, in accordance with the optimal pathlength found previously for our setup [27]. 150 μL fluid was used for each measurement.

A trapezoidal ZnS prism was used as an internal reflection element (IRE) in the ATR setup. This prism had a surface area of 24 mm x 2.4 mm, and a height of 1.2 mm. The thickness of this prism was half of that used in our previous ATR experiments [26], and it had 11 reflections on

Biomedical Optics EXPRESS

the top surface. Hollow-core optical fibres with an inner diameter of 1 mm were used for in- and out-coupling of light. These fibres had an inner silver coating, which was made in a chemical silver-mirror reaction [28,29]. The larger hollow-core fibre could efficiently collect radiation from the end facet of the IRE without the need for additional focussing optics. 100 µL fluid was necessary for each measurement.

ATR spectroscopy is based on absorption of the evanescent field that arises in total internal reflection (TIR) between media with high and low refractive indices, see the inset in Fig. 1(b) for an illustration of the concept. The evanescent field is non-propagating, but can still interact resonantly with absorbing analytes. The absorbance signal correlates with the proportion of the field emanating from the crystal, and the absorbance increases approximately linearly with the number of reflections [30].

3. Results

3.1. Transmission setup

Spectra acquired from the three sample types that were measured (centrifuged and non-centrifuged peritoneal fluid, and blood plasma) are shown in Fig. 2 for comparison. These spectra were background-corrected, but otherwise untreated. The displayed spectra have similar glucose concentrations and are from unspiked samples from different individuals. The spectra are plotted for the range 1200–970 cm^{-1} for clarity, as the lower wavenumbers did not contain any visible spectral features. The non-centrifuged peritoneal fluid samples were acquired mainly for this comparison. These samples were not used further for regression analysis, as there were only five non-centrifuged samples in total.

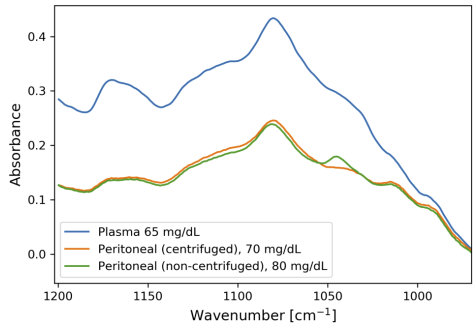

Fig. 2. Transmission spectra of peritoneal fluid (centrifuged and non-centrifuged) and plasma samples with similar glucose concentrations for comparison. The samples are all from different individuals.

The two types of peritoneal fluid samples had very similar spectra, with a difference in the absorption feature at approximately 1045 cm^{-1}. The non-centrifuged peritoneal fluid samples contained blood residue, and were found to have coagulate material that formed over time despite treatment with heparin as an anticoagulant. Spectra from the plasma samples had the same general shape as the peritoneal fluid spectra, but with a higher total absorbance. The non-centrifuged peritoneal fluid and blood plasma samples were heparinised, which could potentially also have affected the spectra. However, heparin does not have any notable absorption features in the wavelength range of the laser at the concentrations used [8], so this was not expected to affect the measurements.

Biomedical Optics EXPRESS

The predicted glucose concentrations in peritoneal fluid and blood plasma measured in the transmission setup are shown in Fig. 3, analysed with PLS regression using 5 and 6 LVs, respectively. For the peritoneal samples, the training data had an internal MAPE of 8.3% with cross-validation. For the 31 samples that were used as validation data, the MAPE was 8.7%. As a comparison, the MAPE for only the unspiked samples with concentration range 33-140 mg/dL was 6.1%. The blood plasma dataset was smaller at 21 samples in total, and therefore only cross-validation was done on this data. The MAPE for plasma was 7.7%. These results were achieved with a Savitzky-Golay filter for pre-processing (width 9, order 1). No additional pre-processing was used for this data.

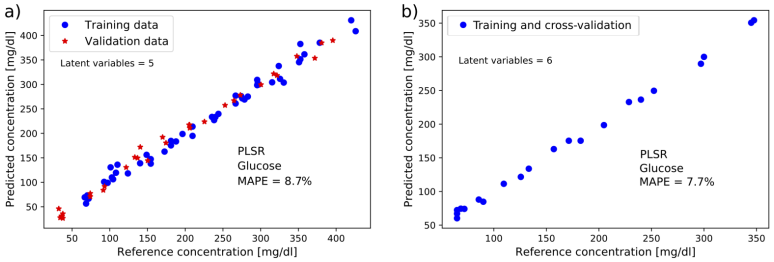

Fig. 3. Results from multivariate analysis of the transmission spectroscopy data. a) Prediction of glucose concentrations in spiked and unspiked samples of peritoneal fluid from pigs (48 samples for training, 31 samples for validation). b) Result from cross-validation of glucose prediction in spiked and unspiked samples of pig blood plasma (21 samples).

3.2. ATR setup

The acquired ATR spectra were affected by a high frequency noisy structure, most likely due to reflections/interferences in the setup. The intensity of these features was minimised through alignment, but was difficult to eliminate completely. However, as the effect on the spectra was constant between measurements, the concentration prediction was only minimally affected. The high frequency features could also be removed with filtering methods, and the example in Fig. 4(a) shows the result of applying a Fourier filter with a Blackman-Harris window function (cutoff at 28 datapoints in Fourier space, window size multiplier at 1.3).

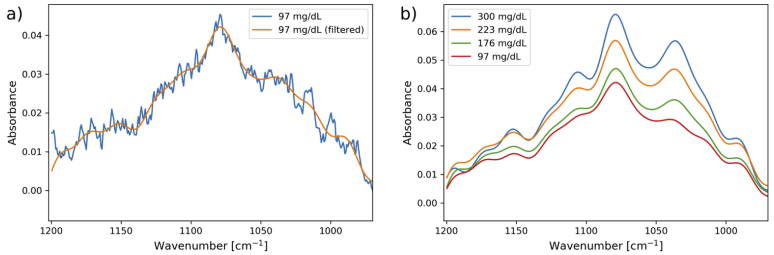

Fig. 4. a) Spectrum from ATR spectroscopy of a peritoneal fluid sample before and after Fourier filtering, and b) Filtered ATR spectra of peritoneal fluid samples with different glucose concentration levels.

Biomedical Optics EXPRESS

Example spectra of peritoneal samples with glucose concentrations ranging from 97-300 mg/dL are plotted in Fig. 4(b). The spectra have noticeable changes in absorption features with increasing glucose concentrations, in particular around the 1035 cm^{-1} glucose absorption peak.

For the ATR measurements, the predicted glucose concentrations for peritoneal fluid and plasma samples are shown in Fig. 5. The achieved MAPE for glucose in peritoneal fluid was 12.2%, and for blood plasma samples the MAPE for cross-validation was 7.8%. As in the transmission measurements, the optimal models were found using 5 LVs for the peritoneal fluid measurements and 6 LVs for the blood plasma measurements. Application of a Fourier filter with the same parameters as in Fig. 4 gave the lowest prediction errors. For the smaller dataset of unspiked peritoneal fluid samples, the achieved MAPE was 10.5%.

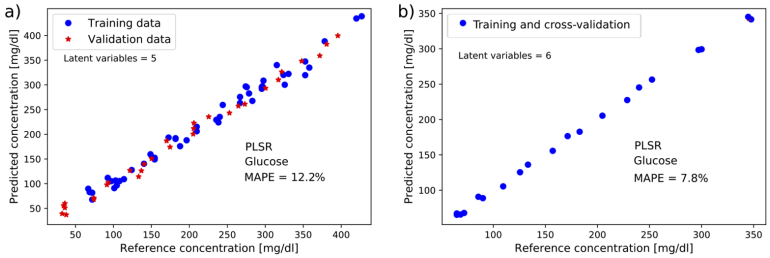

Fig. 5. Results from multivariate analysis of the ATR spectroscopy data. a) Prediction of glucose concentrations in spiked and unspiked samples of peritoneal fluid from pigs (48 samples for training, 31 samples for validation). b) Result from cross-validation of glucose prediction in spiked and unspiked samples of pig blood plasma (21 samples).

4. Discussion

Highly accurate prediction of glucose concentrations in peritoneal fluid was achieved with QCL-based spectroscopy with 8.7% and 12.2% MAPE in the transmission and ATR configurations, respectively. This is an encouraging preliminary result, as the accuracies of commercial electrochemical CGM systems are in the range 9–20% [31,32]. The results are very promising for fast and accurate glucose prediction as the measurement time was only 10 seconds, compared to electrochemical sensors that usually average over 5 minutes. Rapid measurements can potentially contribute to improvements in the health outcomes of diabetes patients, as long-term complications can be reduced if the BGL is measured continuously with high accuracy and short response time. Concentration prediction was also accurate for low glucose concentrations (<100 mg/dL), which is a critical concentration range for management of hypoglycaemia in diabetic patients. This is especially notable because the lowest concentration in the training set was 72 mg/dL, while the lowest concentration was 32 mg/dL in the validation set. Hence, the features in the measured spectra were still interpretable at very low concentrations, and the regression model could be extended to unknown concentrations. All measurements used for the validation set were from different pigs than the data in the training set, which also showed that accurate predictions could be made with samples from different individuals. Accurate predictions through cross-validation were also found for the blood plasma samples. The separate analysis of the unspiked peritoneal samples also demonstrated that glucose concentrations could be accurately determined in natural peritoneal fluid. The lower prediction errors compared to the full analysis, at 6.1% and 10.5% for transmission and ATR spectroscopy, respectively, can be attributed to the smaller dataset and narrower concentration range.

Biomedical Optics EXPRESS

The prediction error was somewhat worse in the ATR setup. This was likely due to a decrease in SNR due to a lower absorbance signal, and the presence of a high-frequeny noisy structure over the absorbance spectrum. The exact origin of this signal interference was not determined, but was probably related to reflections/interferences in the setup. Spectra with the same shape as in the transmission measurements could be recovered through Fourier filtering. With in vivo applications in mind, the multireflection prism used as an IRE will likely be too large and bulky for a practical implantable sensor. One option is to use a smaller single-reflection IRE with signal-enhancement, which has given good preliminary results in the same setup as used here [33]. As discussed in our earlier study [26], a commercialised QCL-based sensor will also likely require the use of a few fixed-wavelength lasers for cost and size reduction instead of a tuneable laser. Some previous QCL studies on glucose measurements have explored concentration predictions with only a few wavenumbers [34,35], which has demonstrated that this is a possible avenue for sensor development. These fibre-coupled setups are otherwise highly suitable for further development towards in vivo measurements.

The peritoneal fluid acquired directly from the pig trials was contaminated with blood residue, which was introduced by the abdominal incisions for placement of sampling tubes and a bladder catheter. Blood is not naturally found in peritoneal fluid, and was deemed as unwanted for further measurements. Most of the peritoneal samples were therefore centrifuged prior to measurements. This removes the blood cells, but also potentially white blood cells and larger proteins that are found naturally in the peritoneum. A few non-centrifuged peritoneal samples were therefore measured in order to investigate the difference between these sample types. The spectra of centrifuged and non-centrifuged samples were very similar, with the main difference being a stronger absorption feature in the non-centrifuged samples at 1045 cm^{-1} (Fig. 2). Absorption around 1035 cm^{-1} is an important feature of glucose, and the additional feature in non-centrifuged peritoneal fluid could potentially influence glucose concentration prediction. However, other fluids with larger interferences around 1035 cm^{-1}, such as blood serum, have previously been investigated with accurate glucose prediction [8], and the prediction of glucose concentration should therefore not have been unduly affected by using centrifuged samples. The origin of this absorption feature was also uncertain, as it could be a product of either blood residue or other analytes that were removed by centrifugation. The non-centrifuged samples were more difficult to work with due to formation of coagulate material, despite the addition of an anticoagulant, and the exact spiking concentration was more uncertain. It was therefore determined that centrifuged peritoneal samples were acceptable for this initial study.

Peritoneal fluid spectra had the same general shape as the blood plasma spectra, but the total absorbance signal was higher for the blood plasma spectra. This indicates a higher concentration of absorbing analytes in plasma compared to peritoneal fluid. This is in agreement with previous research, which has shown lower concentrations of e.g. albumin and lactate in bovine peritoneal fluid compared to bovine plasma [36]. This was also shown from the measurements of total protein and albumin in a subset of the samples, which was done at an external facility (see Table 2 in the Appendix). Total protein concentrations were more than twice as high in the blood plasma samples compared to the peritoneal samples, and the albumin concentrations were also found to be higher in blood plasma. Total protein and albumin concentrations in the non-centrifuged peritoneal samples did not differ considerably from the centrifuged samples. This indicates that protein concentrations were not meaningfully affected by centrifugation, although this is not a definitive conclusion as the non-centrifuged samples were from only one animal.

Although a total of 79 centrifuged peritoneal fluid samples were measured, these were obtained from only 5 individual pigs, and the initial glucose levels were in a relatively narrow range. The amount of peritoneal fluid in the body is limited (<50 mL), which restricts how much and how often peritoneal fluid can be sampled. A broader concentration range was achieved by spiking a subset of samples. Spiking is an efficient way to get a more varied sample set, however it does

Biomedical Optics EXPRESS

not necessarily reflect real-life variations. Peritoneal fluid is a complex matrix where several components are in equilibrium to some degree, and a change in glucose concentrations will usually occur together with a change in e.g. electrolyte levels. This could not be recreated with concentration spiking. Some between-individual and within-individual variation in the samples might therefore have been missed. However, the validation results were very good considering the large range of glucose concentrations. In addition, the samples used for validation were from different pigs than the ones that were used for training the regression model, which shows that concentration predictions with high accuracy can be achieved across individuals.

5. Conclusion

QCL-based spectroscopy setups were used for direct and reagent-free measurements of glucose levels in peritoneal fluid. Both direct transmission spectroscopy and evanescent field sensing were accurate for glucose level prediction, with achieved MAPEs of 8.7% and 12.2%, respectively. Spectra acquired from peritoneal fluid were found to be similar to those from blood plasma, but with less total overall absorbance.

This study demonstrates that glucose concentrations can be measured accurately in peritoneal fluid, with similar results to previous studies using mid-infrared spectroscopy for measurements of human blood serum [8]. Intraperitoneal sensing has been suggested as a faster and more accurate way of controlling glucose levels in diabetic patients. Future work should include in vivo measurements in an animal model to confirm the functionality of this sensor system in realistic sensing scenarios.

Appendix

Analyte overview

Table 2 summarises the fluid components that were measured in the peritoneal fluid samples and the blood plasma samples. Glucose, lactate, and electrolyte (Na^+, K^+, Ca^{2+}, Cl^-) levels were measured in in an ABL 725 blood gas analyser (ABL 725, Radiometer ApS, Brønshøj, Denmark). These measurements were done directly after each pig trial was finished, and the samples were subsequently frozen at -18°C. In addition, a selection of samples were sent to Sentrallaboratoriet, Faculty of Veterinary Medicine, Norwegian University of Life Sciences (NMBU) for measurements of total protein and albumin. Total protein concentration was measured with the Biuret method in an Advia 1800 Chemistry System (Siemens Healthineers AG, Germany). Albumin concentration was measured by capillary electrophoresis in a Sebia Capillarys 2 (Sebia GL, France). As total protein and albumin were measured in only a subset of the samples, it is likely that the concentrations ranges found were not completely representative of the actual variance in the samples.

Pre-processing methods

The measured mid-infrared spectra consisted of 390 datapoints in the 1200-925 cm^{-1} range and had a resolution of 0.7 cm^{-1}. Pre-processing methods were tested on the raw spectra as a part of the data analysis, and the variants tested are detailed in Table 3.

Prediction accuracy

Various measures of prediction accuracy are used in multivariate analysis. Table 4 summarises four different measurement errors from the analysis of peritoneal fluid and blood plasma in the QCL-based transmission and ATR spectroscopy setups. These are mean absolute percentage error (MAPE), root-mean-square error of prediction or cross-validation (RMSEP/RMSECV), coefficient of determination (R^2), and standard error of prediction (SEP). Training and validation sets were used for the peritoneal fluid samples, and the prediction accuracies are based on the

Biomedical Optics EXPRESS

Table 2. Overview of analyte concentrations in the different fluid types obtained from pig trials.

	Fluid type		
Analyte	Peritoneal (centrifuged)	Peritoneal (non-centrifuged)[a]	Blood plasma
Glucose	33–140 mg/dL	72–90 mg/dL	65–105 mg/dL
	(1.8–7.8 mmol/L)	(4–5 mmol/L)	(3.5–4.9 mmol/L)
Lactate	1.1–2.4 mmol/L	1.4–1.8 mmol/L	0.4–1.8 mmol/L
Na^+	134–138 mmol/L	132–135 mmol/L	131–138 mmol/L
K^+	3.9–5.2 mmol/L	5.3–5.5 mmol/L	4–4.7 mmol/L
Ca^{2+}	1.1–1.3 mmol/L	1.2 mmol/L	1.2–1.35 mmol/L
Cl^-	98–104 mmol/L	99–102 mmol/L	97–103 mmol/L
Total protein[b]	15–21 g/L	16–17 g/L	42–46 g/L
Albumin[b]	7–11 g/L	7–8 g/L	16–18 g/L

[a]Measured from only one individual
[b]Concentration ranges for total protein and albumin were obtained from a subset of samples, and are therefore likely not representative of the full variance in all the samples measured.

Table 3. The following variants of pre-processing methods were tested in this study, and all possible combinations were evaluated.

Method	Variants
Baseline correction	None, constant, linear
Savitzky-Golay filter	Filter width: 3, 5,. . . , 21 data points
	Polynomial order: 1st, 2nd, or 3rd
Fourier filter	Window function: none, Blackman-Harris, Hamming, Hann
	Filter cutoff: 20, 21,. . . , 50 data points in Fourier space
	Filter window size: 1.1, 1.2, 1.3
Spectral derivative	No derivative, 1st, or 2nd derivative
Normalisation	Scaling, standard normal variate, multiple scatter correction

results on the validation data. Analysis of the unspiked peritoneal fluid samples used a subset of the total datasets, with 14 samples in the training set and 12 samples in the validation set. As the plasma dataset was smaller, it was evaluated as a training set with leave-one-out cross-validation (LOOCV).

Table 4. Overview of various prediction errors obtained for multivariate analysis of glucose levels in peritoneal fluid and blood plasma from pigs.

Measurement	MAPE	RMSE	R^2	SEP
Peritoneal, transmission	8.7%	9.9 mg/dL	0.9926	10 mg/dL
Peritoneal, ATR	12.2%	12.8 mg/dL	0.989	11.8 mg/dL
Unspiked peritoneal, transmission	6.1%	5.5 mg/dL	0.9845	5.3 mg/dL
Unspiked peritoneal, ATR	10.5%	9.6 mg/dL	0.9621	9.4 mg/dL
Plasma, transmission	7.7%	9.2 mg/dL	0.9915	9.1 mg/dL
Plasma, ATR	7.8%	9.4 mg/dL	0.9899	9.3 mg/dL

Funding

Norges Forskningsråd (248810, 248872).

Biomedical Optics EXPRESS

Acknowledgments

This work was supported by the Research Council of Norway through the Double Intraperitoneal Artificial Pancreas project, grant number 248872. The project is part of Centre for Digital Life Norway and is also supported by the Research Council of Norway's grant 248810.

The authors would like to thank Marte Kierulf Åm and Patrick Christian Bösch for collecting and preparing the fluid samples used in this study.

Disclosures

The authors declare no conflicts of interest.

References

1. T. Battelino, I. Conget, B. Olsen, I. Schütz-Fuhrmann, E. Hommel, R. Hoogma, U. Schierloh, N. Sulli, and J. Bolinder, "The use and efficacy of continuous glucose monitoring in type 1 diabetes treated with insulin pump therapy: A randomised controlled trial," Diabetologia **55**(12), 3155–3162 (2012).
2. B. M. Frier, "Morbidity of hypoglycemia in type 1 diabetes," Diabetes Res. Clin. Pract. **65**, S47–S52 (2004).
3. D. M. Nathan, "Long-Term Complications of Diabetes Mellitus," N. Engl. J. Med. **328**(23), 1676–1685 (1993).
4. J. Wang, "Electrochemical glucose biosensors," Chem. Rev. **108**(2), 814–825 (2008).
5. I. L. Jernelv, K. Milenko, S. S. Fuglerud, D. R. Hjelme, R. Ellingsen, and A. Aksnes, "A review of optical methods for continuous glucose monitoring," Appl. Spectrosc. Rev. **54**(7), 543–572 (2019).
6. A. Schwaighofer, M. Brandstetter, and B. Lendl, "Quantum cascade lasers (QCLs) in biomedical spectroscopy," Chem. Soc. Rev. **46**(19), 5903–5924 (2017).
7. A. Hugi, R. Maulini, and J. Faist, "External cavity quantum cascade laser," Semicond. Sci. Technol. **25**(8), 083001 (2010).
8. M. Brandstetter, T. Sumalowitsch, A. Genner, A. E. Posch, C. Herwig, A. Drolz, V. Fuhrmann, T. Perkmann, and B. Lendl, "Reagent-free monitoring of multiple clinically relevant parameters in human blood plasma using a mid-infrared quantum cascade laser based sensor system," Analyst **138**(14), 4022–4028 (2013).
9. C. Vrančić, N. Kruger, N. Gretz, S. Neudecker, A. Pucci, and W. Petrich, "A quantitative look inside the body: Minimally invasive infrared analysis in vivo," Anal. Chem. **86**(21), 10511–10514 (2014).
10. A. Werth, S. Liakat, A. Dong, C. M. Woods, and C. F. Gmachl, "Implementation of an integrating sphere for the enhancement of noninvasive glucose detection using quantum cascade laser spectroscopy," Appl. Phys. B **124**(5), 75 (2018).
11. S. Kino, S. Omori, T. Katagiri, and Y. Matsuura, "Hollow optical-fiber based infrared spectroscopy for measurement of blood glucose level by using multi-reflection prism," Biomed. Opt. Express **7**(2), 701–708 (2016).
12. J. C. Pickup, S. C. Freeman, and A. J. Sutton, "Glycaemic control in type 1 diabetes during real time continuous glucose monitoring compared with self monitoring of blood glucose: meta-analysis of randomised controlled trials using individual patient data," BMJ **343**(jul07 1), d3805 (2011).
13. K. L. Helton, B. D. Ratner, and N. A. Wisniewski, "Biomechanics of the sensor-tissue interface - Effects of motion, pressure, and design on sensor performance and foreign body response - Part II: Examples and application," J. Diabetes Sci. Technol. **5**(3), 647–656 (2011).
14. M. S. Boyne, D. M. Silver, J. Kaplan, and C. D. Saudek, "Timing of Changes in Interstitial and Venous Blood Glucose Measured with a Continuous Subcutaneous Glucose Sensor," Diabetes **52**(11), 2790–2794 (2003).
15. L. Dye, M. Mansfield, N. Lasikiewicz, L. Mahawish, R. Schnell, D. Talbot, H. Chauhan, F. Croden, and C. Lawton, "Correspondence of continuous interstitial glucose measurement against arterialised and capillary glucose following an oral glucose tolerance test in healthy volunteers," Br. J. Nutr. **103**(1), 134–140 (2010).
16. M. Sinha, K. M. McKeon, S. Parker, L. G. Goergen, H. Zheng, F. H. El-Khatib, and S. J. Russell, "A Comparison of Time Delay in Three Continuous Glucose Monitors for Adolescents and Adults," J. Diabetes Sci. Technol. **11**(6), 1132–1137 (2017).
17. Ø. Stavdahl, A. L. Fougner, K. Kölle, S. C. Christiansen, R. Ellingsen, and S. M. Carlsen, "The Artificial Pancreas: A Dynamic Challenge," IFAC-PapersOnLine **49**(7), 765–772 (2016).
18. L. Huyett, E. Dassau, H. Zisser, and F. Iii, "Glucose Sensor Dynamics and the Artificial Pancreas," IEEE Control. Syst. Mag. **38**(1), 30–46 (2018).
19. D. R. Burnett, L. M. Huyett, H. C. Zisser, F. J. Doyle, and B. D. Mensh, "Glucose sensing in the peritoneal space offers faster kinetics than sensing in the subcutaneous space," Diabetes **63**(7), 2498–2505 (2014).
20. A. L. Fougner, K. Kölle, N. K. Skjærvold, N. A. Elvemo, D. R. Hjelme, R. Ellingsen, S. M. Carlsen, and Ø. Stavdahl, "Intraperitoneal Glucose Sensing is Sometimes Surprisingly Rapid," Model. Identif. Control. **37**(2), 121–131 (2016).
21. M. K. Åm, A. L. Fougner, R. Ellingsen, D. R. Hjelme, P. C. Bösch, O. Stavdahl, S. M. Carlsen, and S. C. Christiansen, "Why intraperitoneal glucose sensing is sometimes surprisingly rapid and sometimes slow: A hypothesis," Med. Hypotheses **132**, 109318 (2019).

Biomedical Optics EXPRESS

22. M. K. Åm, K. Kölle, A. L. Fougner, I. Dirnena-Fusini, P. C. Bösch, R. Ellingsen, D. R. Hjelme, O. Stavdahl, S. M. Carlsen, and S. C. Christiansen, "Effect of sensor location on continuous intraperitoneal glucose sensing in an animal model," PLoS One **13**(10), e0205447 (2018).
23. L. M. Huyett, R. Mittal, H. C. Zisser, E. S. Luxon, A. Yee, E. Dassau, F. J. Doyle, and D. R. Burnett, "Preliminary Evaluation of a Long-Term Intraperitoneal Glucose Sensor With Flushing Mechanism," J. Diabetes Sci. Technol. **10**(5), 1192–1194 (2016).
24. J. J. Kaneko, J. W. Harvey, and M. L. Bruss, *Clinical Biochemistry in Domestic Animals*, 6th ed (Academic Press, 2008).
25. M. Laposata, *Laposata's Laboratory Medicine Diagnosis of Disease in Clinical Laboratory*, 3rd ed (McGraw-Hill Education/Medical, 2018).
26. I. L. Jernelv, K. Strøm, D. R. Hjelme, and A. Aksnes, "Infrared Spectroscopy with a Fiber-Coupled Quantum Cascade Laser for Attenuated Total Reflection Measurements Towards Biomedical Applications," Sensors **19**(23), 5130 (2019).
27. I. L. Jernelv, K. Strøm, D. R. Hjelme, and A. Aksnes, "Mid-infrared spectroscopy with a fiber-coupled tuneable quantum cascade laser for glucose sensing," Proc. SPIE **1123**, 36 (2020).
28. Y. W. Shi, K. Ito, L. Ma, T. Yoshida, Y. Matsuura, and M. Miyagi, "Fabrication of a polymer-coated silver hollow optical fiber with high performance," Appl. Opt. **45**(26), 6736–6740 (2006).
29. K. Iwai, M. Miyagi, Y.-W. Shi, and Y. Matsuura, "Fabrication of silver-coated hollow fiber with an inner diameter of 100 μm or less," Proc. SPIE **7894**, 78940B (2011).
30. C. Vigano, J. M. Ruysschaert, and E. Goormaghtigh, "Sensor applications of attenuated total reflection infrared spectroscopy," Talanta **65**(5), 1132–1142 (2005).
31. H. Kirchsteiger, L. Heinemann, G. Freckmann, V. Lodwig, G. Schmelzeisen-Redeker, M. Schoemaker, and L. Del Re, "Performance comparison of CGM systems: MARD values are not always a reliable indicator of CGM system accuracy," J. Diabetes Sci. Technol. **9**(5), 1030–1040 (2015).
32. D. Rodbard, "Continuous Glucose Monitoring: A Review of Successes," Diabetes Technol. Ther. **18**(S2), 3–13 (2016).
33. I. L. Jernelv, J. Høvik, D. R. Hjelme, and A. Aksnes, "Signal enhancement in microstructured silicon attenuated total reflection elements for quantum cascade laser-based spectroscopy," Proc. SPIE **11359**, 9 (2020).
34. W. B. Martin, S. Mirov, and R. Venugopalan, "Middle infrared, quantum cascade laser optoelectronic absorption system for monitoring glucose in serum," Appl. Spectrosc. **59**(7), 881–884 (2005).
35. Y. Matsuura and T. Koyama, "Non-invasive blood glucose measurement using quantum cascade lasers," Proc. SPIE **39**(2), 105–110 (2018).
36. T. Wittek, A. Grosche, L. Locher, A. Alkaassem, and M. Fürll, "Biochemical constituents of peritoneal fluid in cows," Vet. Rec. **166**(1), 15–19 (2010).